V. 120, NO. 5
SEPTEMBER 2023

ACI MATERIALS JOURNAL

A JOURNAL OF THE AMERICAN CONCRETE INSTITUTE

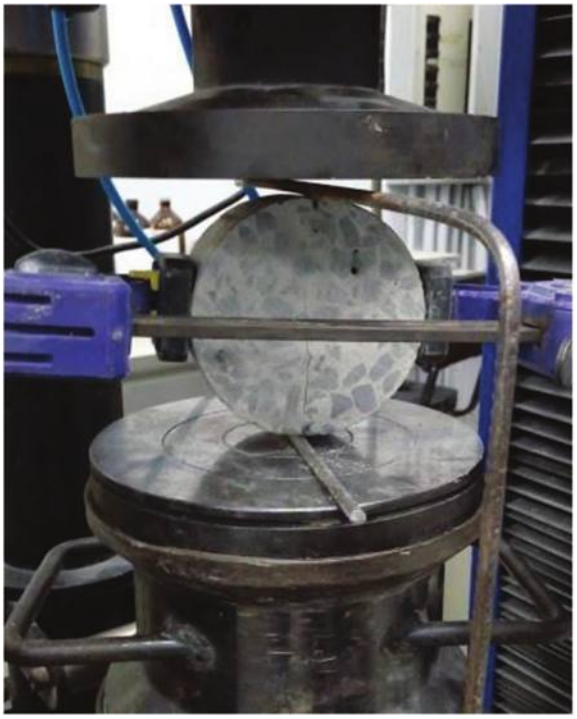

American Concrete Institute

CONTENTS

ACI Materials Journal

September 2023, V. 120, No. 5

A JOURNAL OF THE AMERICAN CONCRETE INSTITUTE
AN INTERNATIONAL TECHNICAL SOCIETY

Discussion is welcomed for all materials published in this issue and will appear ten months from this journal's date if the discussion is received within four months of the paper's print publication. Discussion of material received after specified dates will be considered individually for publication or private response. ACI Standards published in ACI Journals for public comment have discussion due dates printed with the Standard.

The *ACI Materials Journal* (ISSN 0889-325x) is published bimonthly by the American Concrete Institute. Publication office: 38800 Country Club Drive, Farmington Hills, MI 48331. Periodicals postage paid at Farmington, MI, and at additional mailing offices. Subscription rates: $192 per year, payable in advance. POSTMASTER: Send address changes to: *ACI Materials Journal*, 38800 Country Club Drive, Farmington Hills, MI 48331.

Canadian GST: R 1226213149.

Direct correspondence to 38800 Country Club Drive, Farmington Hills, MI 48331. Telephone: +1.248.848.3700.
Website: http://www.concrete.org.

PRINTED WITH SOY INK

MEETINGS

OCTOBER

6-9—2023 APA Annual Convention, Delray Beach, FL, www.archprecast.org/annual-convention

9-11—Dni Betonu 2023, Wisła, Poland, www.dnibetonu.com/en

12-14—National Academy of Construction Annual Meeting, Boston, MA, www.naocon.org/annual-meetings

12-14—NPCA 58th Annual Convention, Oklahoma City, OK, https://precast.org/convention/

16-21—CTBUH 2023 International Conference, Marina Bay, Singapore, and Kuala Lumpur, Malaysia, https://ctbuhconference.com

18-19—BUILDEX Alberta, Calgary, AB, Canada, www.buildexalberta.com

25-27—2023 Decarbonization Conference for the Built Environment, Washington, DC, www.ashrae.org/conferences/topical-conferences/2023-decarbonization-conference-for-the-built-environment

NOVEMBER

8-9—ASCC/TCA Safety Summit 2023, St. Louis, MO, https://ascconline.org/events

8-10—IMCYC 1st Concrete Sustainability Forum, Huatulco, Oaxaca, Mexico, www.imcyc.com

10—International Conference on Construction Science and Technology toward Sustainable Development, Hanoi, Vietnam, www.ibst.vn/tin-tuc/hnkh2018/hoi-nghi-quoc-te-khoa-hoc-vacong-nghe-xay-dung-huong-toi-phat-trien-ben-vung-263089.html

13-15—TRB's Transportation Resilience 2023: International Conference on Extreme Weather and Climate Change Challenges, Washington, DC, https://trb.secure-platform.com/a/page/TransportationResilience

DECEMBER

4-7—Big 5 Global, Dubai, UAE, www.big5global.com

8—ATC at 50: Celebrating the Past, Engaging the Present, and Envisioning the Future, San Francisco, CA, www.atcouncil.org

18-19—ICCET 2023: International Conference on Concrete Engineering and Technology, Cairo, Egypt, https://waset.org/concrete-engineering-and-technology-conference-in-december-2023-in-cairo

ACI CONCRETE CONVENTION: FUTURE DATES

2023—Oct. 29-Nov. 2, Westin Boston Seaport District & Boston Convention and Exhibition Center, Boston, MA
2024—March 24-28, Hyatt Regency New Orleans, New Orleans, LA
2024—November 3-7, Philadelphia Marriott Downtown, Philadelphia, PA
2025—Mar. 30-Apr. 3, Sheraton Centre Toronto Hotel, Toronto, ON, Canada

For additional information, contact:
Event Services, ACI
38800 Country Club Drive
Farmington Hills, MI 48331
Telephone: +1.248.848.3795
email: conventions@concrete.org

ON FRONT COVER: 120-M55, p. 82, Fig. 6—Crack opening procedure.

Contributions to *ACI Materials Journal*

The *ACI Materials Journal* is an open forum on concrete technology and papers related to this field are always welcome. All material submitted for possible publication must meet the requirements of the "American Concrete Institute Publication Policy" and "Author Guidelines and Submission Procedures." Prospective authors should request a copy of the Policy and Guidelines from ACI or visit ACI's website at **www.concrete.org** prior to submitting contributions.

Papers reporting research must include a statement indicating the significance of the research.

The Institute reserves the right to return, without review, contributions not meeting the requirements of the Publication Policy.

All materials conforming to the Policy requirements will be reviewed for editorial quality and technical content, and every effort will be made to put all acceptable papers into the information channel. However, potentially good papers may be returned to authors when it is not possible to publish them in a reasonable time.

Discussion

All technical material appearing in the *ACI Materials Journal* may be discussed. If the deadline indicated on the contents page is observed, discussion can appear in the designated issue. Discussion should be complete and ready for publication, including finished, reproducible illustrations. Discussion must be confined to the scope of the paper and meet the ACI Publication Policy.

Follow the style of the current issue. Be brief—1800 words of double spaced, typewritten copy, including illustrations and tables, is maximum. Count illustrations and tables as 300 words each and submit them on individual sheets. As an approximation, 1 page of text is about 300 words. Submit one original typescript on 8-1/2 x 11 plain white paper, use 1 in. margins, and include two good quality copies of the entire discussion. References should be complete. Do not repeat references cited in original paper; cite them by original number. Closures responding to a single discussion should not exceed 1800-word equivalents in length, and to multiple discussions, approximately one half of the combined lengths of all discussions. Closures are published together with the discussions.

Discuss the paper, not some new or outside work on the same subject. Use references wherever possible instead of repeating available information.

Discussion offered for publication should offer some benefit to the general reader. Discussion which does not meet this requirement will be returned or referred to the author for private reply.

Send manuscripts to:
http://mc.manuscriptcentral.com/aci

Send discussions to:
Journals.manuscripts@concrete.org

ACI MATERIALS JOURNAL TECHNICAL PAPER

Title No. 120-M49

Toughness Performance of Lightweight Aggregate Concrete Reinforced with Steel Fibers

by Hak-Young Kim, Keun-Hyeok Yang, and Hye-Jin Lee

The purpose of this study is to investigate the effect of steel fiber content and type on the compressive and flexural ductility capacities of lightweight aggregate concrete (LWAC). Fiber-reinforced LWAC specimens were divided into four groups according to the type of fibers, such as conventional macrosteel fibers (SFs) with hooked ends, straight copper-coated microsteel fibers (CMSFs), crimping-shaped CMSFs, and hooked-end CMSFs. The fiber-volume fractions (V_f) were 0.5, 1.0, and 1.5%. This study also modifies the ASTM C1018 method by using the initial crack point calculated from the elastic theorem to save a tedious and elaborated effort in determining the reference point at the load-deflection curve, particularly for beams with a strong hardening response. The test results revealed that the hooked-end CMSFs were better than SFs and crimping-shaped CMSFs with the same shape and length at decreasing the slope of the applied loads at descending branches of the compressive stress-strain and flexural load-deflection curves for the LWAC. Compressive and flexural toughness indexes were derived as functions of the fiber reinforcing index based on the regression analysis of test data to assess the ductility improvement of LWAC with steel fibers.

Keywords: ASTM C1018; fiber reinforcing index; lightweight aggregate concrete (LWAC); steel fibers; toughness.

INTRODUCTION

With the global attention to conserving natural resources and managing the depletion of natural aggregates, structural artificial lightweight aggregate concrete (LWAC) has been applied in the concrete industry since the 2000s. It is well known[1,2] that LWAC has a higher strength-to-weight ratio than conventional normalweight concrete (NWC). Hence, relatively smaller and lighter structural elements can be designed using LWAC. In addition, LWAC improves the seismic resistance of structures by reducing the mass dead loads and minimizing the transport and handling costs of precast concrete structures. However, the inadequate mechanical responses of LWAC are a drawback to its wide application to buildings and infrastructures.[3] Artificial lightweight aggregates typically exhibit lower stiffness, strength, and more porous structures than conventional natural aggregates, yielding concrete with lower tensile and crack resistance.[4,5] Moreover, LWAC shows a steeper descending branch of the stress-strain curve than NWC at the same compressive strengths.[6] Consequently, LWAC fracturing is typically characterized by poor ductility, accompanied by rapid crack propagation at localized failure zones.

The use of discontinuous fibers randomly distributed throughout the concrete matrix enhances the tensile strength and durability of hardened concrete by controlling crack propagation.[7,8] The proper addition of fibers is also promising for converting the brittleness of concrete into ductility with a good energy dissipation capacity. Hassanpour et al.[3] observed that the effectiveness of fibers in enhancing splitting tensile and flexural strengths is more significant for LWAC than NWC with the same compressive strength. Li et al.[9] proposed the optimal volume fraction of conventional steel fibers with a crimped shape as 2.0% based on the improvement effect on the flexural toughness of LWAC. In addition, they reported that the JSCE SF-4 method[10] yielded an inconsistent assessment of the pre-peak and post-peak behaviors of the load-deflection curve in determining the flexural toughness of LWAC. Guler[11] determined different mechanical properties of LWAC reinforced with micropolyamide and macropolyamide synthetic fibers at volumetric fractions ranging between 0.25 and 0.75%. The experimental results showed that polyamide fiber contents less than 0.5% by volume minimally influenced the improvement in the compressive and flexural toughness capacities of LWAC. The effect of fibers on the pre-peak and post-peak properties is more sensitive for LWAC than NWC owing to the weakened interfacial zone between the aggregate particles and the cement matrix and a more localized failure zone. Therefore, further experimental investigations are still required to develop a reliable design approach for fibers to enhance the toughness of LWAC.

Although fiber reinforcing techniques have been developed to complement the weakness of concrete, conventional macrosteel fibers (SFs) with different shapes are still the most widely used type because of their desirable performances, such as economic feasibility, availability of manufacturing facilities, and reinforcing effectiveness in improving the crack resistance and toughness of concrete.[12,13] However, SFs reduce the workability of concrete and may cause concrete spalling owing to their corrosion.[14] Recently, copper-coated microsteel fibers (CMSFs) have attracted significant attention as an alternative to SFs. Feng et al.[15] found that the addition of CMSFs with a volume fraction of 2.0% transformed the failure mode from brittle to ductile for sulfoaluminate cement composite specimens. Okeh et al.[16] observed that the partial replacement of SFs with CMSFs alleviated workability loss and maintained the hardening performance of self-consolidating concrete. Nahhab and

ACI Materials Journal, V. 120, No. 5, September 2023.

MS No. M-2021-291.R2, doi: 10.14359/51737185, received March 14, 2022, and reviewed under Institute publication policies.

Table 1—Physical properties of artificial lightweight aggregates

Classification	Maximum size, mm	Dry bulk density, kg/m^3	Specific gravity	Water absorption, %	Porosity, %	Fineness modulus
Coarse aggregate	19	990	1.4	14.1	44.5	6.4
Fine aggregate	4.75	1050	1.5	10.3	37.6	2.9

Note: 1 mm = 0.039 in.; 1 kg/m^3 = 0.062 lb/ft^3.

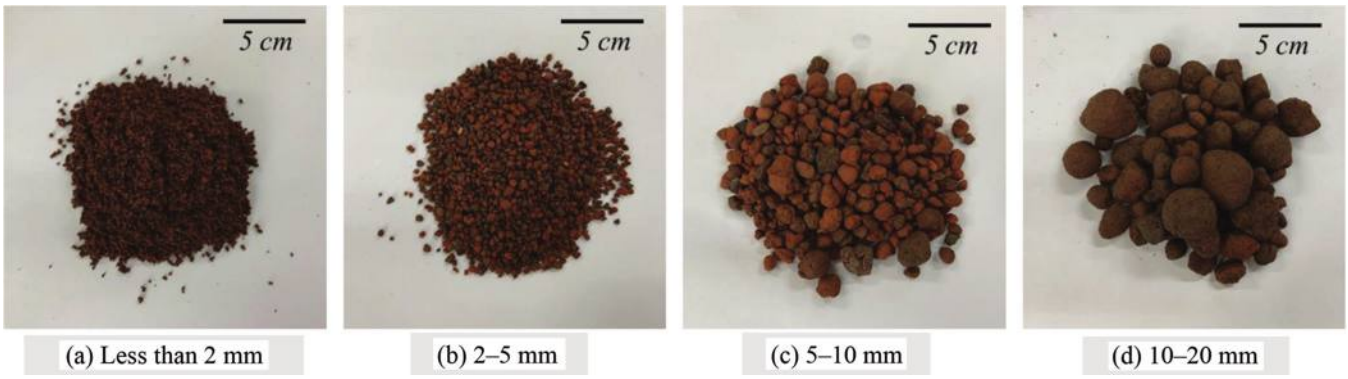

Fig. 1—Typical shapes of lightweight fine and coarse aggregates. (Note: 1 mm = 0.039 in.)

Ketab[17] performed experimental tests on 18 LWAC mixtures reinforced with CMSFs up to a volume fraction of 0.75% and ascertained that CMSFs improved the flexural strength more than the compressive strength. Li et al.[18] reported that the compressive strength of self-consolidating LWAC increased with the addition of CMSFs up to a specific volume fraction, beyond which a decrease occurred because of fiber clumping and insufficient compaction between the fibers and cement matrix. Based on previous studies, it can be concluded that CMSFs exhibit better dispersion in the cement matrix and drive more multiscale crack distribution in concrete than SFs. Thus, extensive experimental tests can be helpful for the practical and reliable application of CMSFs to improve the crack resistance and fracture toughness of LWAC.

In this study, 13 concrete mixtures were prepared to investigate the effectiveness of different steel fibers on compressive and flexural toughness indexes of LWAC. The ASTM C1018-97[19] method applied to calculate the flexural toughness indexes was modified to reliably assess the enhancement of the energy capacity of LWAC reinforced with SFs. The modification was performed by substituting the initial crack point measured in each beam specimen with the predictions obtained using the theory of elasticity as the reference point. Based on a regression analysis using the test data, the compressive and flexural toughness indexes were formulated as a function of the fiber reinforcing index to estimate the effects of steel fiber type and content on the ductility of LWAC.

RESEARCH SIGNIFICANCE

Although numerous studies have been conducted to investigate the mechanical properties and toughness of NWC reinforced with SFs, this study provides useful infrequent test data on the compressive and flexural toughness indexes of LWAC reinforced with different steel fiber types. This study generalizes the initial crack point at the load-deflection curve of beams based on the fundamental flexural theory to induce a good consistency in assessing the flexural toughness indexes of fiber-reinforced concrete in accordance with ASTM C1018. Moreover, original equations were formulated to straightforwardly determine the compressive and flexural toughness indices of concrete reinforced with different steel fibers.

EXPERIMENTAL PROCEDURE

Materials

All concrete mixtures contained ordinary portland cement (OPC) manufactured to ASTM C150 Type I[20] standards without any partial replacement with supplementary cementitious materials. The specific gravity and Blaine fineness of the OPC were 3.15 and 3340 cm^2/g, respectively. Locally available, artificially expanded granules with maximum sizes of 19 and 4.75 mm (0.75 and 0.19 in.) were used as structural lightweight coarse and fine aggregates, respectively. Bottom ash and dredged soils were calcined and expanded in rotary kilns at approximately 1200°C (2192°F) to produce the lightweight granules. The quality of the artificially expanded granules satisfied the requirements for structural lightweight aggregates specified in ASTM C330[21] (Table 1). Lightweight aggregates typically have a spherical shape and a porous core structure (Fig. 1). Because of the porous structures, the lightweight aggregate particles exhibited higher water absorption than the natural normalweight aggregates.

Different types of steel fibers were selected to reinforce the LWAC (Fig. 2). The straight CMSFs were further formed into crimped and hooked-end shapes to enhance their bond performance with the cement matrix. The nominal diameters were 0.2 mm (0.0079 in.) for straight and crimping-shaped CMSFs, 0.3 mm (0.019 in.) for hooked-end CMSFs, and 0.6 mm (0.024 in.) for SFs. The nominal lengths were 13 mm (0.51 in.) for straight and crimping-shaped CMSFs, 30 mm (1.18 in.) for hooked-end CMSFs, and 35 mm (1.38 in.) for SFs. Thus, fiber aspect ratios (S_f) of 65, 100, and 58 were obtained for straight and crimping-shaped CMSFs, hooked-end CMSFs, and SFs, respectively (Table 2). The CMSFs had a tensile strength of 2580 MPa (374.2 ksi),

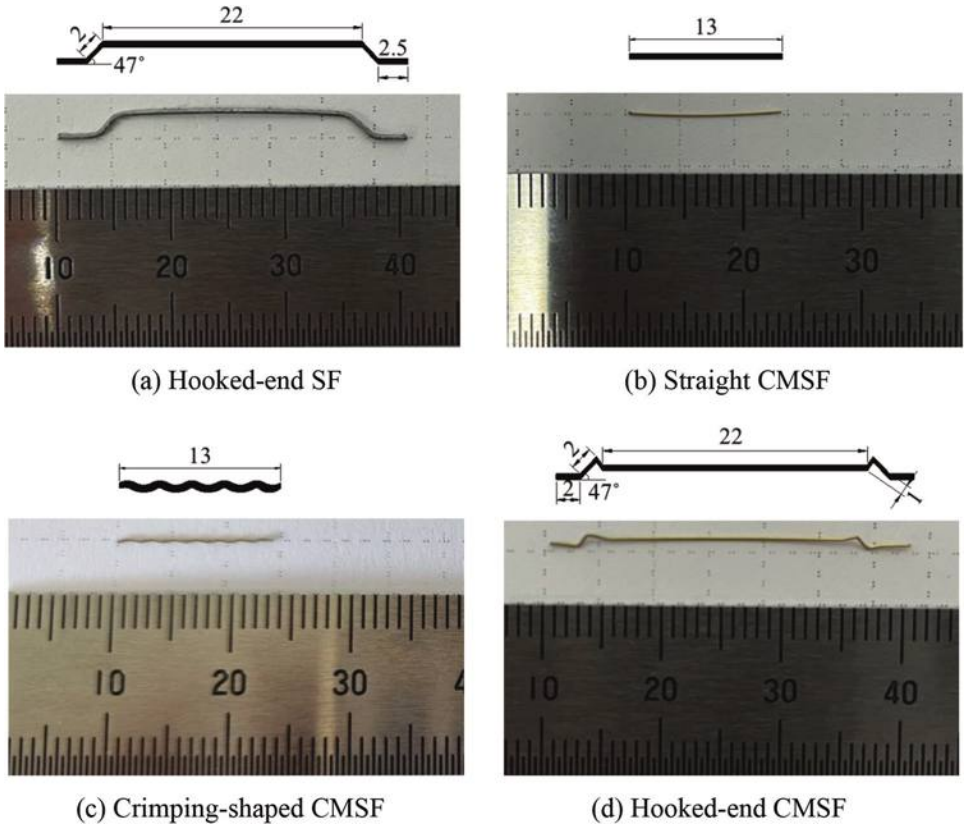

Fig. 2—Typical appearances of steel fibers used. (Note: 1 mm = 0.039 in.)

Table 2—Typical properties of steel fibers

Type		Physical properties				Mechanical properties	
		ρ_f, g/cm^3	L_f, mm	d_f, mm	S_f	F_f, MPa	τ, MPa
Hooked-end SF		7.85	35	0.6	58	2240	16.2
CMSF	Straight	7.8	13	0.2	65	1220	8.6
	Crimping shape		13	0.2	65		11.2
	Hooked-end shape		30	0.3	100		18.7

Note: ρ_f, L_f, d_f, S_f, F_f, and τ are density, length, diameter, aspect ratio, tensile strength, and interfacial bond strength between fiber and cement matrix, respectively; 1 g/cm^3 = 62.43 lb/ft^3; 1 mm = 0.039 in.; 1 MPa = 145 psi.

which was close to the SF values. The bond performance of the CMSFs with the cement matrix was significantly influenced by the additional treatment (Fig. 3). The straight-shaped CMSFs exhibited no post-peak bond resistance, indicating that they pulled out immediately after attaining the peak bond stress. Meanwhile, the crimping-shaped and hooked-end CMSFs exhibited improved pullout resistance and showed a distinct post-peak branch of the bond stress-slip curve of the fibers. Compared to the bond strength of the straight-shaped CMSFs, those of the hooked-end and crimping-shaped CMSFs were higher by 2.2 and 1.6 times, respectively. Additionally, the hooked-end CMSFs exhibited bond stress-slip performance similar to that of hooked-end SFs up to slippage of 4 mm (0.16 in.), beyond which slightly higher bond stresses were observed in the former than in the latter.

Details of specimens and concrete mixtures

Twelve fiber-reinforced LWAC mixtures and a fiberless control mixture were initially prepared, considering the type and V_f of steel fibers (Table 3). The LWAC mixtures containing hooked-end SFs, straight-shaped CMSFs, crimping-shaped CMSFs, and hooked-end CMSFs were classified into SH, CS, CC, and CH groups, respectively. The design values of V_f were 0.5%, 1.0%, and 1.5% for each group. Thus, the specimen notation for a fiber-reinforced LWAC mixture was identified using the group and fiber content notations. For example, CH-0.5 indicates an LWAC mixture reinforced using hooked-end CMSFs with V_f of 0.5%. It should be noted that Specimen C refers to the fiberless control mixture.

The target compressive strength of concrete was 40 MPa (5.80 ksi) based on the high-strength classification of LWAC. The mixture proportions (Table 4) of the LWAC were determined based on a mathematical procedure proposed by Yang et al.[22] A water-cement ratio (w/c) of 35% by weight and a fine aggregate-to-total aggregate ratio of 45% by volume were adopted for the concrete mixture to achieve the targeted strength. Furthermore, a commercially available polycarboxylate-based high-range water-reducing admixture (HRWRA) was added to maintain the initial

slump value of more than 80 mm (3.15 in.). The lightweight aggregates were prepared in a saturated surface-dry state to prevent excessive bleeding and segregation in fresh concrete owing to the high absorption of the lightweight aggregates. The amount of mixing water was adjusted to compensate for the changes in the moisture content of the aggregates because the absorbed surface water does not become part of the mixing water.

Casting, curing, and testing

All the prepared aggregates were dry-mixed with cement in a 0.35 m^3 (12.36 ft^3) capacity mixer for 1 minute, and water was then added and mixed for another minute. Steel fibers were added after mixing the concrete components in a wet state. A commercially available polycarboxylate-based HRWRA was added to each mixture with different contents to achieve the targeted minimum slump of LWAC. It was challenging to control the addition of the HRWRA because of the sensitive interfacial action between the lightweight aggregates and the cement matrix and the incomplete compaction between the steel fibers and the cement matrix. Hence, a minimum slump of 80 mm (3.15 in.) was targeted, considering the casting of the steel fiber-reinforced LWAC. After determining the initial slump and air content of the fresh concrete according to ASTM C143[23] and C231[24] recommendations, respectively, each fresh mixture was placed into various steel molds. All specimens were consolidated according to the vibration casting method specified in ASTM C31.[25] In addition, the specimens were cured in a steady temperature and relative humidity room of 23 ± 2°C (73.4 ± 3.6°F) and 70 ± 5%, respectively, until testing at 28 days. All steel molds were removed at an age of 3 days.

The compressive strength and dry density of concrete were determined using 100 x 200 mm (3.94 x 7.87 in.) cylinder specimens according to ASTM C39[26] and C138,[27] respectively. The stress-strain curves of concrete were measured using 100 x 200 mm (3.94 x 7.87 in.) cylinders according to ASTM C469[28] to determine the compressive toughness index. The incremental strains were obtained using a compressor meter with built-in 10 mm (0.39 in.) capacity dial gauges. Prismatic beams with section size of 100 x 100 mm (3.94 x 3.94 in.) were subjected to four-point bending tests using a fixed 3000 kN (674.43 kip) capacity testing machine according to ASTM C1018 to obtain the flexural toughness indexes from the load-deflection curve. A roller system was installed at both end supports to prevent restraint on the deformation of the specimens. Loading was steadily applied without a sudden shock under closed-loop control at a displacement rate of 0.002*D*/min at the midspan, where *D* is the section depth of the beam. The applied load value was recorded using a load cell fixed to the head of the testing machine. The deflection at the midspan of the beams was recorded using two 5 mm (0.20 in.) capacity linear variable differential transducers. Note that the aforementioned mechanical properties of concrete were calculated as an

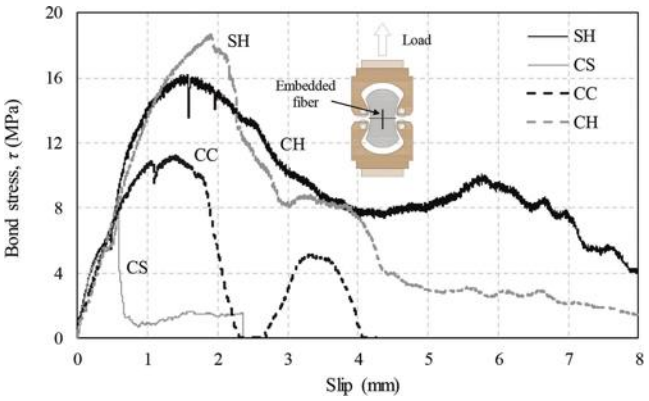

Fig. 3—Bond stress-slip response between steel fibers and cement matrix. (Note: 1 mm = 0.039 in.; 1 MPa = 145 psi.)

Table 3—Details of test specimens and summary of test results

Specimen	Details of fiber			R_{sp}, %	s_l, mm	A_c, %	ρ_c, kg/m^3	f_c', MPa	f_{cr}, MPa	f_r, MPa	E_c, MPa	$f_{cr}/\sqrt{f_c'}$	$f_r/\sqrt{f_c'}$	$E_c/\sqrt{f_c'}$
	Type	V_f, %	β_f											
C	N	0	—	0.2	165	3.8	1685	43.4	3.75	3.75	17,560	0.57	0.57	2666
SH-0.5	Hooked-end	0.5	0.70	0.25	150	3.5	1733	45.7	4.26	4.26	17,687	0.63	0.63	2616
SH-1.0		1.0	1.36	0.35	130	3.4	1752	48.3	5.78	5.78	18,180	0.83	0.83	2616
SH-1.5		1.5	2.05	0.4	120	3.0	1787	47.9	6.42	6.42	18,304	0.93	0.93	2645
CS-0.5	Straight	0.5	0.41	0.3	140	3.4	1743	46.4	3.96	3.96	17,756	0.58	0.58	2607
CS-1.0		1.0	0.77	0.4	120	3	1790	52.6	4.45	4.45	19,302	0.61	0.61	2661
CS-1.5		1.5	1.13	0.45	110	3.2	1803	55.1	5.05	5.75	20,145	0.68	0.77	2714
CC-0.5	Crimped	0.5	0.53	0.45	100	3.4	1740	46.4	4.22	4.22	17,757	0.62	0.62	2607
CC-1.0		1.0	1.01	0.65	70	3.5	1775	51.8	4.78	4.87	18,915	0.66	0.68	2628
CC-1.5		1.5	1.56	0.85	60	3.6	1792	48.8	5.12	5.12	18,610	0.73	0.73	2664
CH-0.5	Hooked-end	0.5	1.35	0.4	130	4.1	1729	48.1	4.54	4.85	18,139	0.65	0.70	2615
CH-1.0		1.0	2.67	0.65	90	3.8	1760	48.9	6.81	7.01	18,233	0.97	1.00	2607
CH-1.5		1.5	3.99	0.75	60	3.7	1790	49.2	6.64	7.25	18,940	0.95	1.03	2700

Note: V_f is volumetric fraction of fiber; β_f is reinforcing index of fiber; R_{sp} is ratio of HRWRA content to cement content; s_l is initial slump of concrete; A_c is air content of fresh concrete; ρ_c, f_c', f_{cr}, f_r, and E_c are dry density, 28-day compressive strength, initial cracking strength, ultimate flexural strength, and modulus of elasticity of hardened concrete, respectively; 1 mm = 0.039 in.; 1 MPa = 145 psi; 1 kg/m^3 = 0.062 lb/ft^3.

Table 4—Mixture proportions of LWAC

		Unit weight, kg/m^3			
w/c	*S/A*	Water	Cement	LWFA	LWCA
0.35	0.45	180	514	420	479

Note: *S/A* is fine-to-total aggregate ratio, by volume; LWFA and LWCA refer to lightweight fine and coarse aggregates, respectively.

average of test data obtained from three cylinders or prismatic beams prepared in each specimen.

EXPERIMENTAL RESULTS AND DISCUSSION

Workability of fresh concrete

The addition of steel fibers decreased the initial slump (s_l) of the LWAC (Table 3). Thus, the LWAC reinforced with a higher V_f required a higher HRWRA content than the conventional concrete to achieve the targeted minimum values of s_l. When V_f was increased from 0.5% to 1.5%, the HRWRA-cement ratio increased from 0.25% to 0.4% for the SH group, 0.3% to 0.45% for the CS group, 0.45% to 0.85% for the CC group, and 0.4% to 0.75% for the CH group. These trends indicated that the crimping-shaped and hooked-end CMSFs were more unfavorable than the straight-shaped CMSFs in minimizing the workability loss of LWAC because the geometric shape deformation of fibers could accelerate the ball bearing effect owing to increased interlocking friction between the fibers and aggregates. In addition, the specimens in the CC and CH groups exhibited a lower slump than those of SH mixtures, although more HRWRA was added to the former mixtures than the latter mixtures. This behavior probably occurred because CMSFs with a smaller diameter yielded a higher aspect ratio and more individual fibers than SFs with a larger diameter.

The air content ranged between 3.0% and 4.1% for all concrete mixtures. No distinct effect of the steel fiber type and content on the air content of LWAC was observed.

Compressive strength and dry density

All concrete mixtures satisfied the designed compressive strength of 40 MPa (5.80 ksi). Figure 4 shows the relative values of $f_c'/(f_c')_N$ and $\rho_c/(\rho_c)_N$ for steel-fiber reinforced LWAC, where subscript N refers to the control fiberless concrete. The control concrete with an oven-dried density (ρ_c) of 1685 kg/m^3 (105.20 lb/ft^3) exhibited a 28-day compressive strength (f_c') of 43.4 MPa (6.29 ksi). The relative $\rho_c/(\rho_c)_N$ value proportionally increased with the steel fiber content, and the increase rate was independent of the steel fiber type. The relative $f_c'/(f_c')_N$ value slightly increased with an increasing steel fiber content up to a V_f of 1.0%, beyond which the steel fiber effect on f_c' was negligible, although an increase in $f_c'/(f_c')_N$ up to a V_f of 1.5% was observed for CS group specimens. The CS group specimens had higher $f_c'/(f_c')_N$ values than the other group specimens with V_f of 1.0% and 1.5%. It is widely known[8,29] that the effectiveness of fibers on improving f_c' is minimal compared to the contribution of fibers in enhancing the tensile resistance of concrete. This might occur because macrocracks in concrete under compression develop mainly after reaching the peak strength. In addition, an increase in the steel fiber content can result in inadequate compaction along the interfacial

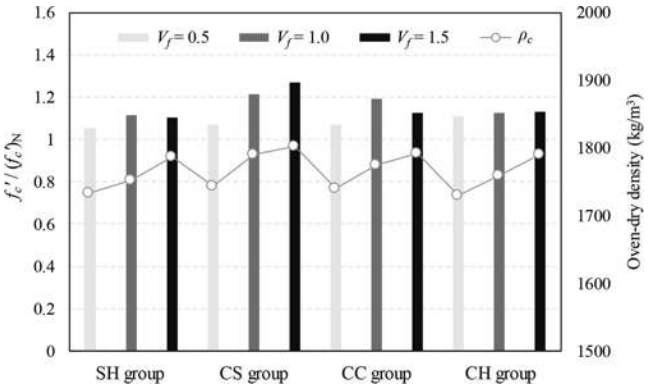

Fig. 4—Relative compressive strength and density values of steel fiber-reinforced LWAC. (Note: 1 kg/m^3 = 0.062 lb/ft^3.)

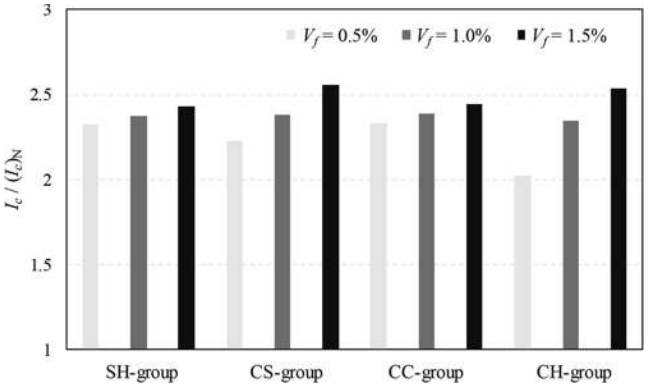

Fig. 5—Relative compressive toughness indexes of steel fiber-reinforced LWAC.

zone between the lightweight aggregates and cement matrix owing to the interference and poor dispersion of the fibers. Thus, the addition of steel fibers exceeding a specific limit adversely affects the compressive strength development of concrete. Considering the $f_c'/(f_c')_N$ values measured in this study, the steel fiber content in LWAC needs to be controlled to less than 1%. For LWAC specimens with a V_f of 1.0%, the $f_c'/(f_c')_N$ values obtained for the SH, CS, CC, and CH groups were 1.11, 1.21, 1.19, and 1.13, respectively.

Compressive toughness index

The compressive toughness index (I_c) of each concrete specimen was calculated using its compressive stress–strain curve based on the ASTM C1018 procedure. Figure 5 shows the relative $I_c/(I_c)_N$ of steel fiber-reinforced LWAC. Table 5 also lists the toughness indexes calculated in each specimen. It is challenging to compile the data for the fiberless high-strength LWAC beyond 85% peak load at the descending branch of the stress-strain curve because of the significant brittle failure characteristics of such concrete. Therefore, the approximate value of $(I_c)_N$ was obtained in this study using the generalized stress-strain model established by Yang et al.[6] to trace the descending branch of the curve. The obtained value of the I_c of the control concrete was 1.63. As expected, the relative $I_c/(I_c)_N$ values increased with increasing V_f, and they were 2.33 to 2.43, 2.23 to 2.56, 2.33 to 2.45, and 2.02 to 2.53 for the SH, CS, CC, and CH groups, respectively. These results implied that the addition of steel fibers enabled the

Table 5—Summary of compressive and flexural toughness indexes

Specimen	Compressive toughness index I_c	Flexural toughness indexes									
		Δ_0, mm		$I_f(5)$		$I_f(10)$		$I_f(20)$		$I_f(30)$	
		ASTM C1018	Modification	ASTM C1018	Modification	ASTM C1018	Modification	ASTM C1018	Modification	ASTM C1018	Modification
C	1.63	0.058	—	3.17	—	—	—	—	—	—	—
SH-0.5	3.79	0.077	0.044	3.81	4.27	7.03	8.51	12.60	15.11	16.78	21.78
SH-1.0	3.87	0.075	0.053	3.99	4.66	7.80	9.19	15.37	18.30	22.69	27.55
SH-1.5	3.96	0.070	0.059	4.01	4.71	7.68	9.01	15.64	18.46	23.87	28.15
CS-0.5	3.63	0.071	0.041	3.41	3.98	5.61	6.69	10.51	11.46	15.59	16.63
CS-1.0	3.88	0.065	0.044	4.41	4.38	7.40	7.81	12.92	13.37	18.60	18.70
CS-1.5	4.17	0.053	0.051	4.19	4.46	8.65	8.97	16.30	16.25	21.92	23.79
CC-0.5	3.80	0.073	0.046	3.60	4.24	7.04	8.27	13.02	14.03	17.55	19.88
CC-1.0	3.89	0.070	0.048	3.78	4.39	7.41	8.68	13.78	15.92	19.53	23.49
CC-1.5	3.99	0.060	0.056	4.02	4.51	7.96	8.99	15.71	16.55	22.59	24.09
CH-0.5	3.30	0.065	0.055	4.15	4.60	8.41	8.70	16.55	16.71	23.43	23.96
CH-1.0	3.83	0.064	0.063	4.57	5.00	9.13	10.17	18.24	19.24	26.66	28.68
CH-1.5	4.13	0.062	0.069	4.61	5.42	9.54	10.37	19.57	19.95	28.94	29.76

Note: Flexural toughness indexes specified by ASTM C1018 were calculated using experimental Δ_0, whereas modified procedure is applied to Δ_0 predicted using Eq. (3) to (8) as reference value for specified deflection of beams.

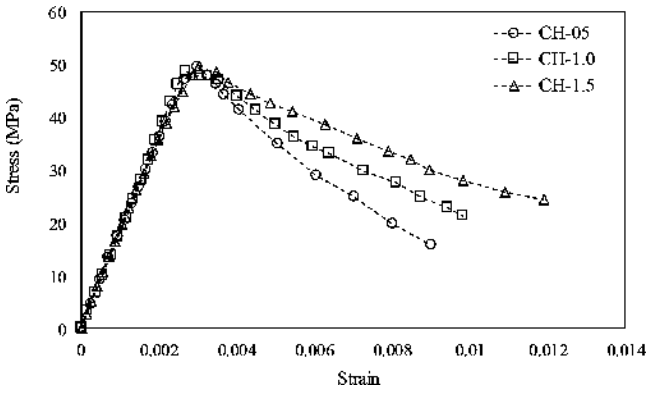

Fig. 6—Typical compressive stress-strain curves measured for CH group specimens. (Note: 1 MPa = 145 psi.)

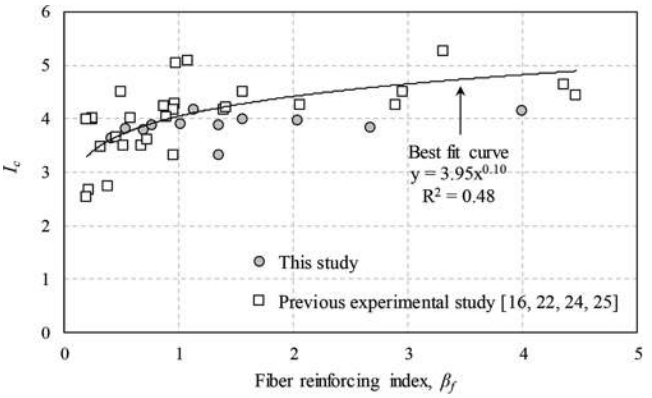

Fig. 7—Relationship between β_f and I_c of LWAC.

descending branch of the stress-strain curve of the LWAC to possess a less sharp slope (Fig. 6). It should be noted that the steel fibers minimally influenced the slope of the ascending branch. For the same V_f of 0.5% and 1.0%, higher $I_c/(I_c)_N$ values were obtained for SH group specimens than for the other group specimens. The specimens in all groups showed a consistent increase in I_c up to a V_f of 1.5%. Remarkably, the I_c values of CS and CH specimens increased significantly at a V_f of 1.5%. Thus, specimens reinforced using CMSFs with a V_f of 1.5% exhibited higher $I_c/(I_c)_N$ values than their counterpart SH specimens.

Yang[30] derived a fiber reinforcing index (β_f) to reflect the effects of the aspect ratio, reinforcing amount, and interfacial bond strength of the fibers on the crack resistance and tensile resistance of concrete. Generally, the enhancement effect of the crack and tensile resistances of concrete by fiber addition decreases with the increase in concrete brittleness. An increase in the concrete compressive strength leads to an increase in the brittleness of the concrete.[3] Hence, the fiber reinforcing index was modified in this study in the following form

$$\beta_f = \sum_{i=1}^{n} g_i \tau_i V_{f,i} S_{f,i} / \sqrt{f_c'} \quad (1)$$

where i is the fiber type in each concrete mixture; g is the efficiency factor of discontinuous fibers; and τ is the interfacial bond strength of the fiber. It is difficult to estimate the value of g reliably because the bridging action of the discontinuous fibers is significantly dependent on various parameters, such as the orientation and length of the fiber, workability of concrete, and interlocking friction between the fibers and aggregates or cement matrix. In addition, published papers reporting the values of g for different types of steel fibers are lacking. Hence, this study assumed the value of g as 1.0 for all steel fiber types. Figure 7 shows the relationship between the β_f and I_c of LWAC reinforced with steel fibers. Data sets compiled for LWAC specimens evaluated in previous studies[16,29,31,32] are also presented in Fig. 7. A distinct co-relationship between β_f and I_c was observed.

Based on the definition of β_f, a lower compressive toughness was expected for concrete with a higher f_c' at the same V_f. For high-strength concrete and LWAC subjected to axial compression, cracks typically penetrate the aggregate particles after the peak load is attained, resulting in the generation of broader crack widths and a more intensive failure zone.[33] From a regression analysis using the test data sets presented in Fig. 7, the I_c value of steel-fiber-reinforced LWAC could be optimally formulated as follows

$$I_c = 3.95 \cdot (\beta_f)^{0.1} \quad (2)$$

Flexural load-deflection curve

Figure 8 shows a typical midspan deflection (Δ) of beam specimens against the applied load under four-point bending. No data were obtained for the control fiberless LWAC beam beyond peak load because it failed with the development of initial flexural cracks. The outline of the load-deflection curve for concrete specimens was significantly influenced by the steel fiber content and shape. The load-deflection response of LWAC beams with V_f = 0.5%, except for beam CH-0.5, could be characterized in the following stages: 1) the applied load linearly increased until the initial crack appeared; 2) the load sharply dropped up to 60 to 80% of the peak load; and 3) the load then remained constant, yielding a plastic flow response. The slope for the decrease in the applied load after initial cracking decrease with increasing fiber content. The most sudden drop in the applied load immediately beyond the peak load was observed for Beam CS-0.5. LWAC beams with V_f = 1.5% exhibited slight hardening or plastic flow performance with no sharp decline in the applied load after initial cracking, although Beam CS-1.5 showed a very short hardening stage. Beams CC-1.0 and CH-1.0 also showed hardening performances similarly observed for beams with V_f = 1.5%. Moreover, all CH-group beams and beams CS-1.5 and CC-1.0 exhibited a higher ultimate load (P_n) than the initial cracking load (P_{cr}), indicating that the ultimate flexural strength (f_r) was 1.02 to 1.14 times higher than the initial cracking strength (f_{cr}) (Table 3). The beams that did not exhibit hardening performance had the same values of f_{cr} and f_r. The applied load on the LWAC beams with V_f = 1.5% started to decrease gradually at Δ/Δ_0 = 13.6 for SF-1.5, 4.4 for CS-1.5, 6.3 for CC-1.5, and 9.6 for CH-1.5, where Δ_0 is the midspan deflection corresponding to P_{cr}. The slope at the ascending branch of the load-deflection curve was minimally influenced by the steel fiber content and shape.

Apart from Beam CC-1.0, Beam CS-1.5, and the CH group beams, all other beams showed equal values of f_{cr} and f_r (Table 3), indicating that the hardening strength of those beams did not exceed f_{cr}. The normalized initial cracking strength ($f_{cr}/\sqrt{f_c'}$) tended to increase with an increase in V_f. The value of $f_{cr}/\sqrt{f_c'}$ measured in the fiberless concrete beam was 0.57, which was conservative compared to the predictions (0.465) obtained using the ACI 318-19 equation[34] for all LWAC. The values of $f_{cr}/\sqrt{f_c'}$ measured for the fiber-reinforced beams were 0.58 to 0.65, 0.61 to 0.97, and 0.68 to 0.95 when the V_f values were 0.5%, 1.0%, and 1.5%, respectively. At the same V_f, slightly higher $f_{cr}/\sqrt{f_c'}$ values were

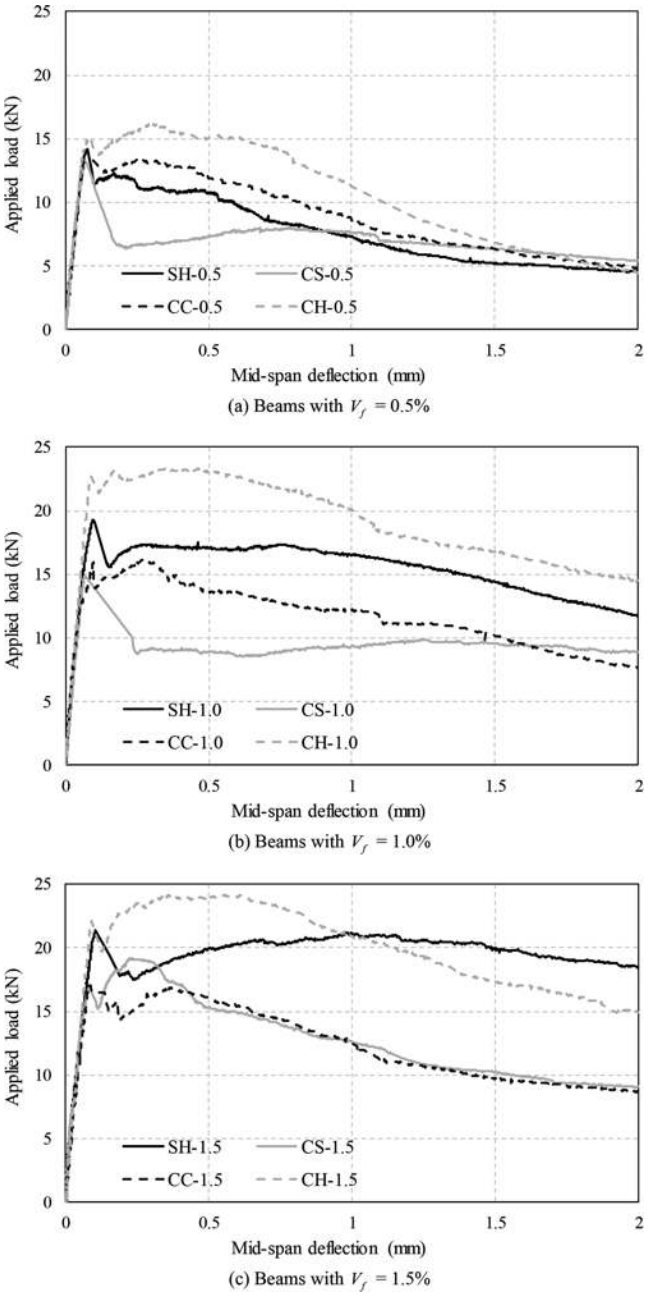

Fig. 8—Typical load-deflection curves of beams under four-point bending. (Note: 1 mm = 0.039 in.; 1 kN = 0.2248 kip.)

obtained for the CH group beams, followed by the SH group beams, whereas the CS group beams exhibited the lowest values. Because the CH group beams exhibited the most improved post-crack response, they yielded higher f_r values. The ratios between f_r and f_{cr} determined for Beams CH-0.5, CH-1.0, and CH-1.5 were 1.07, 1.03, and 1.09, respectively. These values indicated that the hooked-end CMSFs provided a stronger bridging restriction against crack propagation than the hooked-end macrosteel fibers. Generally, macrocrack propagation is more effectively restricted by a longer fiber than a shorter fiber.[3,32] Hence, the beams with hooked-end CMSFs of 30 mm (1.18 in.) long exhibited a stronger hardening response than those with crimping-shaped or straight-shaped CMSFs of 13 mm (0.51 in.) long. CS group beams exhibited a more rapid rate of decrease in the applied load

than CC group beams containing fibers of equal lengths. These results suggest that straight-shaped fibers are insufficient for restricting macrocrack propagation, owing to slip displacement between the fiber and the cement matrix.

Flexural toughness

Because flexural toughness indexes (I_f) were calculated from the load-deflection curve, higher I_f values were determined for CH group beams than beams of the other groups (Table 5). ASTM C1018 identifies $I_f(5)$, $I_f(10)$, $I_f(20)$, and $I_f(30)$ as the ratios of the areas under the load-deflection curve up to specified deflections of $3\Delta_0$, $5.5\Delta_0$, $10.5\Delta_0$, and $15.5\Delta_0$, respectively, relative to the area up to the referenced deflection of Δ_0. No values of $I_f(10)$ to $I_f(30)$ were determined for the control fiberless LWAC beam because of a rapid softening post-peak response. The steel fiber content and type marginally influenced the values of $I_f(5)$ and $I_f(10)$ because their effects on the calculated area below the load-deflection curve were minimal, up to $5.5\Delta_0$. A unique trend was observed for values of $I_f(20)$ and $I_f(30)$, particularly for the latter. Thus, this subsection focuses on the effects of the test parameters on the $I_f(30)$ values.

The value of $I_f(30)$ increased with an increase in V_f, indicating that it was 16.8 to 23.9, 12.5 to 20.9, 19.0 to 22.5, and 23.2 to 32.9 for the SH, CS, CC, and CH groups, respectively. These results proved that the steel fiber content up to V_f = 1.5% did not induce the incomplete compaction of cement matrix because of the ball bearing of the fibers, which enhanced the slope of the descending branch of the load-deflection curve. At an equal V_f, the highest $I_f(30)$ values were obtained for CH group beams, whereas the values determined for SH group beams were slightly lower than those for CC group beams but higher than those for CS group beams. For example, Beam CH-1.0 had a higher $I_f(30)$ value than the beams SH-1.0, CC-1.0, and CS-1.0 by 21.2%, 32.0%, and 28.1%, respectively. These findings demonstrated that the CMSFs were better than the conventional SFs in enhancing the flexural toughness of LWAC because CMSFs with a smaller diameter improved the dispersion in the cement matrix and strengthened the interlocking action across the crack. Although the straight-shaped and crimping-shaped CMSFs had the same length and aspect ratio, the CC group beams showed slightly higher $I_f(30)$ values than the CS group beams. This trend could be attributed to the slippage of the straight-shaped fibers against the cement matrix, reducing the interlocking action of the fibers across the cracks. Figure 9 shows typical images of the interaction between the cement matrix and steel fibers across a flexural macrocrack, captured for Beams CH-1.0 and CS-1.0. Most straight-shaped fibers were pulled out of the cement matrix (Stage III), resulting in a wider crack mouth opening displacement (CMOD) in the CS group beams than CH group beams. Thus, a shorter Stage III region was observed for CH group beams than the beams in the other groups. Hooked-end fibers across the macrocrack effectively restricted crack propagation even at the postpeak response because of their elongated and hooked appearance.

Modification of flexural toughness indexes

Two reference points are widely used for assessing the flexural toughness of fiber-reinforced concrete. ASTM C1018 is based on the initial crack-based deflection for calculating the relative energy dissipation capacities of beams, whereas JSCE-SF4[10] and ASTM C1609[35] provide the absolute energy dissipation up to a deflection of $L/150$, where L is the beam length between the centers of both end supports. Nataraja et al.[36] and Turk et al.[37] noted that the ASTM C1018 method has a critical weakness of determining the initial crack point at the load-deflection curve with difficulty, particularly for high-volume fiber concrete exhibiting a hardening response. Additionally, it takes significant time and effort to determine the initial crack point, even for beams exhibiting a softening response. Because the ASTM C1018 method results in the energy dissipation at different deflections relative to that at the initial crack, it is crucial to determine the initial crack point reliably. Li et al.[18] stated that the ASTM C1609 and JSCE-SF4 methods have an insufficient theoretical hypothesis and do not provide the crack resistance of concrete,

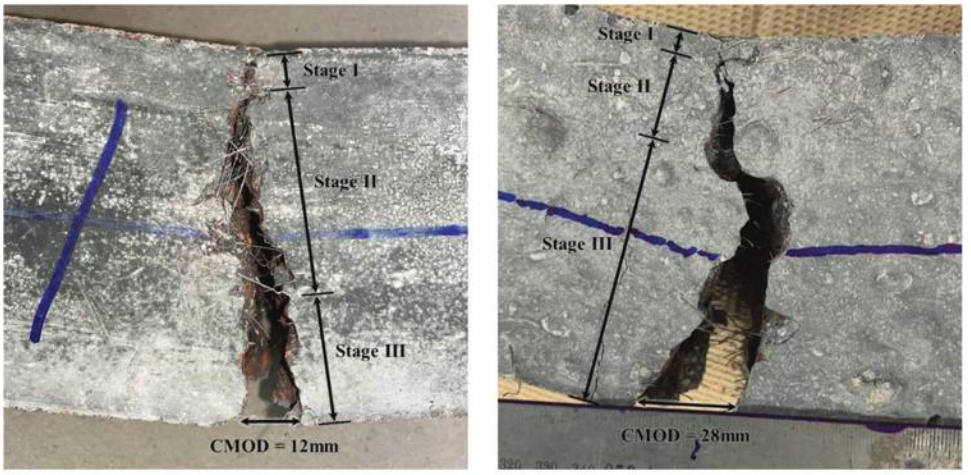

(a) CH-1.0 (b) CS-1.0

Fig. 9—Images showing interaction between crack plane and steel fibers. (Note: Stage I represents fiber action along microcracks; Stage II represents fiber action along macrocracks; and Stage III represents pulling out of fibers owing to significant opening of crack. 1 mm = 0.039 in.)

resulting in absolute energy dissipation, and they proposed an equivalent flexural strength ratio as a relative value. They also reported that the equivalent flexural strength does not practically reflect the improvement in flexural toughness with the addition of fibers. Thus, it is still unclear to evaluate the effect of fibers on enhancing the flexural toughness of concrete reliably.

The primary reason to assess the flexural toughness is to examine how the brittleness of fiberless concrete can be improved with the addition of different fiber types. Therefore, the ASTM C1018 method was modified in this study by substituting the initial crack point measured for each beam specimen with that calculated using the elastic theory. This modification has the following advantages: 1) the reference point can be mathematically and precisely determined with no tedious and elaborated effort, even for beams exhibiting strong hardening response; and 2) the reliability of beam tests in plotting the load-deflection curve is easily verified by comparing the experimental and calculated ascending branches of the slopes. Based on the elastic curve or virtual work method, the Δ_0 of beams under four-point loading conditions at equidistant intervals can be expressed as follows

$$\Delta_0 = 0.0177 P_{cr} L^3 / E_c I_g \quad (3)$$

where E_c is the elastic modulus of concrete; and I_g is the moment of the inertia of the uncracked section. Although steel fibers can slightly increase E_c because of the increase in ρ_c, the effect of fibers on E_c is insignificant because no fiber bridging action is expected until a crack develops. Most steel fiber-reinforced concrete specimens had normalized $E_c/\sqrt{f_c'}$ values similar to those of the fiberless concrete (Table 3). Hence, in this study, E_c was obtained using the generalized design equation of Lee et al.[4] for concrete with different compressive strengths and densities, as follows

$$E_c = 8090[(f_c')^{1/3}(\rho_c/\rho_0)]^{0.89} \quad (4)$$

where ρ_0 (= 2300 kg/m^3 [143.58 lb/ft^3]) is the reference value of the concrete density. Note that Eq. (4) was formulated from the regression analysis of the concrete test data that include f_c' range of 18 to 50 MPa (2610.7 to 7251.9 psi) and ρ_c range of 1200 to 2300 kg/m^3 (74.91 to 143.58 lb/ft^3). P_{cr} in Eq. (3) can be calculated using the fundamental flexural theory. For beams under four-point loading conditions at equidistant intervals, P_{cr} is expressed in the following generalized form

$$P_{cr} = f_{cr} bh^2 / L \quad (5)$$

where b and h are the width and overall depth of the beam section, respectively. The addition of steel fibers significantly enhances the crack resistance capacity of concrete. However, the f_{cr} of LWAC reinforced with steel fibers has been formulated in very few studies. Hence, the test data obtained in this study were compared with the design equation results of Lee et al.[4] and then used for a regression analysis to determine the f_{cr} of steel fiber-reinforced LWAC (Fig. 10). Lee et al.

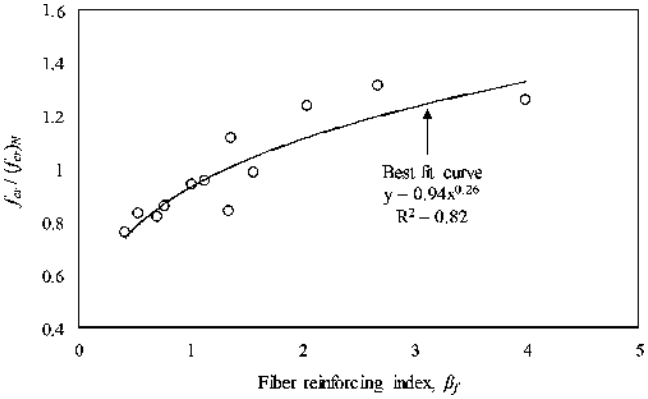

Fig. 10—Regression analysis of f_{cr} *of LWAC reinforced with steel fibers.*

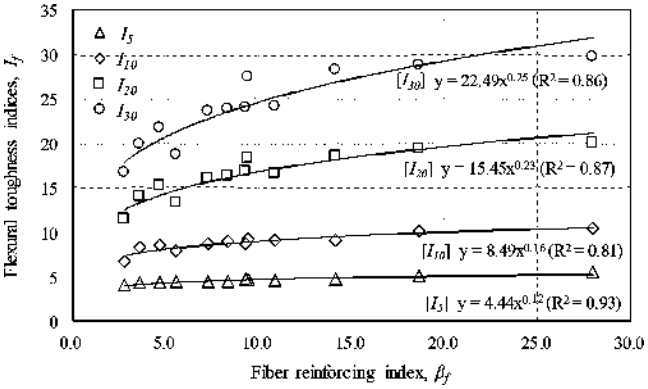

Fig. 11—Relationship between β_f *and* I_f *values. (Note:* I_f *values were calculated based on predicted* Δ_0*.)*

compiled extensive test data and empirically formulated the flexural strength $[(f_{cr})_N]$ of fiberless concrete with different compressive strengths and densities, as follows

$$(f_{cr})_N = 1.21[f_c'(\rho_c/\rho_0)^{1.5}]^{0.44} \quad (6)$$

The test data obtained for the experimental specimens in this study were normalized based on the predictions calculated using Eq. (6) to determine the f_{cr} of steel fiber-reinforced LWAC. Subsequently, a regression analysis was conducted with β_f as the main influencing parameter (Fig. 10). Thus, the f_{cr} of steel fiber-reinforced LWAC could be determined using Eq. (7)

$$f_{cr} = 0.94(\beta_f)^{0.26} \cdot (f_{cr})_N \quad (7)$$

Table 5 lists the Δ_0 values determined experimentally and using Eq. (3) for each beam specimen. In addition, different values of I_f were calculated using the predicted Δ_0 as a reference deflection and compared with values determined according to the ASTM C1018 method. The predicted Δ_0 values were slightly lower than the experimental values. Therefore, the I_f values calculated based on the predicted Δ_0 were slightly higher than those determined using the measured Δ_0. However, the I_f values calculated using the predicted Δ_0 satisfactorily reflected the effect of steel fiber content and type on the flexural ductility of the LWAC beams.

Overall, the different values of I_f based on the predicted Δ_0 could be formulated as a function of β_f, as follows (Fig. 11)

$$I_f(j) = \alpha_1 (\beta_f)^{\gamma_1} \quad (8)$$

The experimental coefficients α_1 could be set as 4.44, 8.49, 15.45, and 22.49; and γ_1 could be set as 0.12, 0.16, 0.23, and 0.25, when *j* corresponded to 5, 10, 20, and 30, respectively. Equation (8) indicates that the modified version yields good consistency with less effort in analyzing the enhancement of the energy capacity of LWAC containing steel fibers.

CONCLUSIONS

In this study, the effects of different steel fibers on the compressive and flexural responses of lightweight aggregate concrete (LWAC) were evaluated. The fiber-reinforced concrete specimens were classified into four groups: SH containing conventional SFs with hooked ends, CS containing straight-shaped copper-coated microsteel fibers (CMSFs), CC containing crimping-shaped CMSFs, and CH containing hooked-end CMSFs. Based on the test results, the following conclusions are drawn:

1. At V_f values of 0.5% and 1.0%, higher compressive toughness indexes were obtained for the SH group specimens than other group specimens. Meanwhile, specimens reinforced with CMSFs at a V_f of 1.5% exhibited a higher compressive toughness index than the specimens in the SH group.

2. The I_c value of the LWAC reinforced with steel fibers could be optimally formulated as a function of the fiber reinforcing index (β_f) using the following expression, $I_c = 3.95 \cdot (\beta_f)^{0.1}$.

3. LWAC beams with V_f = 1.0% and 1.5% exhibited slight hardening and plastic flow performances with no sharp decline in the applied load after the initial crack appeared. Moreover, all the CH group beams resisted a higher ultimate load (P_n) than the initial cracking load (P_{cr}), indicating that the ultimate flexural strength (f_r) was 1.02 to 1.14 times higher than the initial cracking strength (f_{cr}).

4. At the same V_f, the highest $I_f(30)$ values were obtained for CH group beams, whereas the values determined for the SH group beams were slightly lower than those for the CC group beams but higher than those for the CS group beams.

5. The hooked-end CMSFs were better than the conventional hooked-end macrosteel fibers in enhancing the flexural ductility of LWCA.

6. The ASTM C1018 method was modified by substituting the initial crack point measured for each beam specimen with that calculated using the elastic theory. The modified version yields a good consistency and requires less effort in assessing the improvement of the energy capacity of LWAC reinforced with steel fibers.

AUTHOR BIOS

Hak-Young Kim *is a Research Professor at Kyonggi University, Suwon, South Korea. He received his BS, MS, and PhD in architectural engineering from Dankook University, Seoul, South Korea, in 2004, 2009, and 2015, respectively. His research interests include the development of design models of sustainable concrete using various recycled materials.*

ACI member **Keun-Hyeok Yang** *is a Professor at Kyonggi University. He received his BS, MS, and PhD in architectural engineering from Chung-Ang University, Seoul, South Korea, in 1995, 1999, and 2002, respectively. His research interests include the development of sustainable concrete materials and structural technology.*

Hye-Jin Lee *is a Doctoral Student at Kyonggi University, where she received her MS in architectural engineering in 2018. Her research interests include examining the mechanical properties of lightweight aggregate concrete.*

ACKNOWLEDGMENTS

This study was supported by a Korea Agency for Infrastructure Technology Advancement (KAIA) grant funded by the Ministry of Land, Infrastructure, and Transport (Grant No. 21NANO-B156177-02).

REFERENCES

1. Chandra, S., and Berntsson, L., *Lightweight Aggregate Concrete: Science, Technology, and Applications*, Noyes Publications, New York, 2003.

2. Clarke, J. I., *Structural Lightweight Aggregate Concrete*, Blackie Academic & Professional, London, UK, 1993.

3. Hassanpour, M.; Shafigh, P.; and Mahmud, H. B., "Lightweight Aggregate Concrete Fiber Reinforcement—A Review," *Construction and Building Materials*, V. 37, 2012, pp. 452-461. doi: 10.1016/j.conbuildmat.2012.07.071

4. Lee, K. H.; Yang, K. H.; Mun, J. H.; and Kwon, S. J., "Mechanical Properties of Concrete Made from Different Expanded Lightweight Aggregates," *ACI Materials Journal*, V. 116, No. 2, Mar. 2019, pp. 9-19. doi: 10.14359/51712265

5. Li, J. J.; Niu, J. G.; Wan, C. J.; Jin, B.; and Yin, Y. L., "Investigation on Mechanical Properties and Microstructure of High-Performance Polypropylene Fiber Reinforced Lightweight Aggregate Concrete," *Construction and Building Materials*, V. 118, 2016, pp. 27-35. doi: 10.1016/j.conbuildmat.2016.04.116

6. Yang, K. H.; Mun, J. H.; Cho, M. S.; and Kang, T. H., "A Stress-Strain Model for Various Unconfined Concrete in Compression," *ACI Structural Journal*, V. 111, No. 4, July-Aug. 2014, pp. 819-826.

7. Balaguru, P., and Najm, H., "High-Performance Fiber-Reinforced Concrete Mixture Proportions with High Fiber Volume Fractions," *ACI Materials Journal*, V. 101, No. 4, July-Aug. 2004, pp. 281-286.

8. Shafei, B.; Kazemian, M.; Dopko, M.; and Najimi, M., "State-of-the-Art Review of Capabilities and Limitations of Polymer and Glass Fibers Used for Fiber-Reinforced Concrete," *Materials (Basel)*, V. 14, No. 2, 2021, pp. 409-453. doi: 10.3390/ma14020409

9. Li, J. J.; Wan, C. J.; Niu, J. G.; Wu, L. F.; and Wu, Y. C., "Investigation on Flexural Toughness Evaluation Method of Steel Fiber Reinforced Lightweight Aggregate Concrete," *Construction and Building Materials*, V. 131, 2017, pp. 449-458. doi: 10.1016/j.conbuildmat.2016.11.101

10. JSCE Standard SF-4, "Method of Test for Flexural Strength and Flexural Toughness of Fiber Reinforced Concrete," Japan Society of Civil Engineering, Tokyo, Japan, 1984.

11. Guler, S., "The Effect of Polyamide Fibers on the Strength and Toughness Properties of Structural Lightweight Aggregate Concrete," *Construction and Building Materials*, V. 173, 2018, pp. 394-402. doi: 10.1016/j.conbuildmat.2018.03.212

12. Mehta, P. K., and Monteiro, P. J. M., *Concrete: Microstructure Properties and Materials*, third edition, McGraw Hill, New York, 2006.

13. Barros, J. A. O., and Cruz, J. S., "Fracture Energy of Steel Fibre Reinforced Concrete," *Mechanics of Composite Materials and Structures*, V. 8, No. 1, 2001, pp. 29-45. doi: 10.1080/107594101459815

14. Nordström, E., "Durability of Sprayed Concrete: Steel Fibre Corrosion in Cracks," Department of Civil and Environmental Engineering, Lulea University of Technology, Lulea, Sweden, 2005.

15. Feng, H.; Chen, G.; Hadi, M. N. S.; Sheikh, M. N.; and Zhou, B., "Mechanical Behavior of Micro-Fine Steel Fibre Reinforced Sulphoaluminate Cement Composite," *Construction and Building Materials*, V. 170, 2018, pp. 91-100. doi: 10.1016/j.conbuildmat.2018.03.065

16. Okeh, C. A. O.; Begg, D. W.; Barnett, S. J.; and Nanos, N., "Behaviour of Hybrid Steel Fibre Reinforced Self-Compacting Concrete using Innovative Hooked-End Steel Fibres under Tensile Stress," *Construction and Building Materials*, V. 202, 2019, pp. 753-761. doi: 10.1016/j.conbuildmat.2018.12.067

17. Nahhab, A. H., and Ketab, A. K., "Influence of Content and Maximum Size of Light Expanded Clay Aggregate on the Fresh, Strength, and Durability Properties of Self-Compacting Lightweight Concrete Reinforced with Micro Steel Fibers," *Construction and Building Materials*, V. 233, 2020, p. 117922. doi: 10.1016/j.conbuildmat.2019.117922

18. Li, J. J.; Zhao, E. J.; Niu, J. G.; and Wan, C. J., "Study on Mixture Design Method and Mechanical Properties of Steel Fiber Reinforced Self-Compacting Lightweight Aggregate Concrete," *Construction and Building Materials*, V. 267, 2021, p. 121019. doi: 10.1016/j.conbuildmat.2020.121019

19. ASTM C1018-97, "Standard Test Methods for Flexural Toughness and First Crack Strength of Fibre Reinforced Concrete (Withdrawn 2006)," ASTM International, West Conshohocken, PA, 1997.

20. ASTM C150/C150M-12, "Standard Specification for Portland Cement," ASTM International, West Conshohocken, PA, 2012.

21. ASTM C330/C330M-09, "Standard Specification for Lightweight Aggregates for Structural Concrete," ASTM International, West Conshohocken, PA, 2009, 4 pp.

22. Yang, K. H.; Kim, G. H.; and Choi, Y. H., "An Initial Trial Mixture Proportioning Procedure for Structural Lightweight Aggregate Concrete," *Construction and Building Materials*, V. 55, 2014, pp. 431-439. doi: 10.1016/j.conbuildmat.2013.11.108

23. ASTM C143/C143M-12, "Standard Test Method for Slump of Hydraulic-Cement Concrete," ASTM International, West Conshohocken, PA, 2012, 4 pp.

24. ASTM C231/C231M-09b, "Standard Test Method for Air Content of Freshly Mixed Concrete by the Pressure Method," ASTM International, West Conshohocken, PA, 2009, 10 pp.

25. ASTM C31/C31M-12, "Standard Practice for Making and Curing Concrete Test Specimens in the Field," ASTM International, West Conshohocken, PA, 2012, 6 pp.

26. ASTM C39/C39M-12, "Standard Test Method for Compressive Strength of Cylindrical Concrete Specimens," ASTM International, West Conshohocken, PA, 2012, 7 pp.

27. ASTM C138/C138M-12a, "Standard Test Method for Density (Unit Weight), Yield, and Air Content (Gravimetric) of Concrete," ASTM International, West Conshohocken, PA, 2012, 4 pp.

28. ASTM C469/C469M-10, "Standard Test Method for Static Modulus of Elasticity and Poisson's Ratio of Concrete in Compression," ASTM International, West Conshohocken, PA, 2010, 5 pp.

29. Liu, X.; Wu, T.; and Liu, Y., "Stress-Strain Relationship for Plain and Fibre-Reinforced Lightweight Aggregate Concrete," *Construction and Building Materials*, V. 225, 2019, pp. 256-272. doi: 10.1016/j.conbuildmat.2019.07.135

30. Yang, K. H., "Tests on Concrete Reinforced with Hybrid or Monolithic Steel and PVA Fibers," *ACI Materials Journal*, V. 108, No. 6, Nov.-Dec. 2011, pp. 664-672.

31. Chen, B., and Liu, J. Y., "Contribution of Hybrid Fibers on the Properties of the High-Strength Lightweight Concrete Having Good Workability," *Cement and Concrete Research*, V. 35, No. 5, 2005, pp. 913-917. doi: 10.1016/j.cemconres.2004.07.035

32. Balaguru, P., "Contribution of Fibers to Crack Reduction of Cement Composites During the Initial and Final Setting Period," *ACI Materials Journal*, V. 91, No. 3, May-June 1994, pp. 280-288.

33. Matsumoto, T., and Li, V. C., "Fatigue Life Analysis of Fiber Reinforced Concrete with a Fracture Mechanics Based Model," *Cement and Concrete Composites*, V. 21, No. 4, 1999, pp. 249-261. doi: 10.1016/S0958-9465(99)00004-9

34. ACI Committee 318, "Building Code Requirements for Structural Concrete (ACI 318-19) and Commentary (ACI 318R-19) (Reapproved 2022)," American Concrete Institute, Farmington Hills, MI, 2019, 624 pp.

35. ASTM C1609/C1609M-12, "Standard Test Method for Flexural Performance of Fiber-Reinforced Concrete (Using Beam with Third-Point Loading)," ASTM International, West Conshohocken, PA, 2012, 9 pp.

36. Nataraja, M. C.; Dhang, N.; and Gupta, A. P., "Toughness Characterization of Steel Fiber-Reinforced Concrete by JSCE Approach," *Cement and Concrete Research*, V. 30, No. 4, 2000, pp. 593-597. doi: 10.1016/S0008-8846(00)00212-X

37. Turk, K.; Bassurucu, M.; and Bitkin, R. E., "Workability, Strength, and Flexural Toughness Properties of Hybrid Steel Fiber Reinforced SCC with High-Volume Fiber," *Construction and Building Materials*, V. 266, 2021, p. 120944. doi: 10.1016/j.conbuildmat.2020.120944

ACI Faculty Network

Why Join the Faculty Network?

The Faculty Network is a support group for educators interested in ACI and the concrete industry. Members receive notifications about classroom resources, fellowships and scholarships, funding for research, online learning, and calls for papers and presenters.

Free 1-Year Educator Membership

ACI offers complimentary membership to teaching professionals who have not been an ACI member within the past 5 years.

Free Desk Copies

Faculty Network members can request a complimentary print or PDF copy of:

- ACI CODE-318 Building Code Requirements for Structural Concrete and Commentary (includes a free subscription to ACI 318 PLUS)
- ACI CODE-530 Building Code Requirements and Specification for Masonry Structures and Companion Commentaries
- ACI CODE-562 Assessment, Repair, and Rehabilitation of Existing Concrete Structures—Code and Commentary
- MNL-3(20) Guide to the Code for Assessment, Repair, and Rehabilitation of Existing Concrete Structures
- MNL-5(19) Contractor's Guide to Quality Concrete Construction, 4th Edition
- MNL-17(21) ACI Reinforced Concrete Design Handbook (available digitally with ACI 318 PLUS subscription)
- MNL-66(20) ACI Detailing Manual (available digitally with ACI 318 PLUS subscription)

Networking

ACI hosts a Faculty Network Reception twice a year during the ACI Concrete Conventions, giving an opportunity to exchange ideas and network.

aci 318PLUS+ Faculty Network members receive a complimentary annual subscription that provides users with convenient digital interactive access to ACI CODE-318-19, the ACI Detailing Manual, and the numerous design examples in the ACI Reinforced Concrete Design Handbook. The platform allows professors to create custom user notes that can be distributed to the students to view alongside the Code. Student members are provided 1-year access to ACI 318 PLUS when they purchase their printed copy of ACI 318-19 at the student price of $99 (plus shipping).

aci Professors' Workshop
Materials | Pavements | Structures
Sponsor: aci Foundation

The Professors' Workshop is designed to provide instructors in civil engineering, architecture, architectural engineering, materials science, and construction management programs the tools to engage students in the latest developments in concrete design, construction, and materials.

aci Foundation
Building the Future

The Concrete Research Council (CRC) seeks concrete research projects that further the knowledge and sustainability of concrete materials, construction, and structures in coordination with ACI Committees. Annual Request for Proposals (RFP) are received annually between August 1 and December 1.

aci
American Concrete Institute
Always advancing

ADVANCE YOUR CLASSROOM WITH ACI

JOIN OR RENEW TODAY! concrete.org/educatorsandresearchers

ACI MATERIALS JOURNAL TECHNICAL PAPER

Title No. 120-M50

Effects of Different Fibers and Cement Substituting Minerals on Mechanical Properties of Ultra-High-Performance Fiber-Reinforced Concrete

by Nima Mohammadian Tabrizi, Davood Mostofinejad, and Mohammad Reza Eftekhar

This paper is aimed at investigating the effects of different fiber inclusion on the mechanical properties of ultra-high-performance concrete (UHPC) by adding mineral admixtures as cement replacement materials to reduce production costs and CO_2 emissions of UHPC. Throughout this research, 21 mixture designs containing four cement substitution materials (silica fume, slag cement, limestone powder, and quartz powder) and three fibers (steel, synthetic macrofibers, and polypropylene) under wet and combined (autoclave, oven, and water) curing were developed. To investigate the mechanical properties in this research, a total of 336 specimens were cast to evaluate compressive strength, the modulus of rupture (MOR), and the toughness index. The findings revealed that at the combined curing, regarded as a new procedure, all levels of cement replacement recorded a compressive strength higher than 150 MPa (21.76 ksi). Furthermore, the mechanical properties of the mixture design containing microsilica and slag (up to 15%) were found to be higher than other cement substitutes. Also, it was shown that all levels of the fiber presented the MOR significantly close together, and samples made of synthetic macrofibers and steel fibers exhibited deflection-hardening behavior after cracking. The mixture design containing microsilica, slag, limestone powder, and quartz powder, despite the significant replacement of cement (approximately 50%) by substitution materials, experienced a slight drop in strength. Therefore, the development of this mixture is optimal both economically and environmentally.

Keywords: cement replacement materials; curing; mechanical properties; synthetic fiber; ultra-high-performance concrete (UHPC).

INTRODUCTION

The advancement of modern civil engineering structures has created an increasing demand for new kinds of concrete requiring improved properties such as strength, toughness, and durability. In the early 1980s, the idea of producing concrete with a very dense and homogeneous microstructure became popular among researchers. Accordingly, scientists' research led to the emergence of a new type of fine-grained concrete with extraordinary properties, namely ultra-high-performance concrete (UHPC).[1] Unlike the extremely high compressive strength of UHPC, this concrete shows brittle behavior during failure, in comparison to normal-strength concrete (NSC). The ductility and brittleness of UHPC are improved by the addition of fibers.[2] This type of concrete indicating great compressive strength (>150 MPa [21.76 ksi]) and high tensile strength (>13 MPa [1.89 ksi]) is named ultra-high-performance fiber-reinforced concrete (UHPFRC).[3] UHPFRC is a cutting-edge cement-based composite with high strength and excellent durability. Due to its high potential, this concrete is regarded as a feasible solution to enhance the stability of buildings and other components of substructures.[4] The experimental results and a parametric study conducted with the numerical model showed that UHPFRC and normal-strength reinforced concrete are compatible in the long term, and the high potential of such composite elements can be used in the long-term rehabilitation and retrofitting of existing structures.[5]

Typically, to produce different types of UHPC, the materials—for example, cement—that are used have production processes that pollute the environment. In general, it is worth highlighting that construction materials are regarded as the third-largest sector of CO_2 production worldwide. Moreover, the production of cement entails 7% of total greenhouse gas emissions. The cement content applied in UHPC is approximately three times (900 to 1100 kg/m^3 [1517 to 1854 lb/yd^3]) more than ordinary concrete cement, causing higher CO_2 emissions. Hence, the design and production of concrete with less cement and decreasing greenhouse gas emissions with high efficiency and durability have remained major challenges facing sustainable development in the coming decades.[6,7] In the literature on UHPC, concerning the low water-cement ratio (w/c) (approximately 0.14 to 0.2), the rate of cement hydration is only between 30 and 40%, indicating the use of a considerable amount of nonhydrated clinker as a filler.[8] Therefore, to mitigate cement in UHPC, it is preferred to replace it with limestone powder, quartz powder, slag, fly ash, and so on. Concerning the advantages of such replacement, it could lead to the production of UHPC with a denser and more uniform cement matrix with high compatibility with the environment.[9,10]

In recent years, there have been several studies on the substitution of cement with pozzolans and fillers in UHPC leading to appropriate outcomes.[11-13] Achieving high flowability and minimizing compressive strength loss, Kim et al.[14] produced an eco-friendly UHPC through the use of industrial slag and limestone powder. The results revealed that the application of more limestone powder to replace cement yields higher flowability and less strength. Moreover, they also found that the specimen containing slag had a compressive strength higher than that of limestone powder. Abdulkareem et al.[15] investigated the effects of substituting

ACI Materials Journal, V. 120, No. 5, September 2023.

MS No. M-2021-483.R6, doi: 10.14359/51738888, received January 15, 2023, and reviewed under Institute publication policies.

30, 50, and 80% (by volume) of cement with slag cement on the early-age characteristics of UHPC in terms of workability, setting time, hydration temperature, and compressive strength. Their findings showed that the replacement of 30% cement with slag cement in UHPC accelerated its setting time by improving the granulation density, which enhanced the workability and hydration of cement, hence elevating the compressive strength of the concrete at an early age. Huang et al.[16] studied the effect of the cement replacement with limestone powder in various amounts (34, 54, and 74% by volume) on the rate of hydration and compressive strength of UHPC, which improved mechanical properties and hydration.

Recently, the effect of fibers on UHPC has received much attention.[17-20] Yoo et al.[21] analyzed the effects of various percentages of micro steel fibers on the mechanical properties of UHPFRC, which improved the compressive strength through the use of micro steel fibers up to 3%. Also, increasing the amount of steel fiber from 1 to 4% would consequently improve flexural strength. In another study, Meng and Khayat[22] investigated the effects of straight steel fibers, hooked-end steel fibers, and polyvinyl alcohol (PVA) fibers on key properties of UHPC. With a constant level of 2% fibers, different combinations of micro-macro steel and micro steel-PVA fibers were considered. At a fiber content of 2%, increasing the ratio of PVA or hooked steel fibers to straight steel fibers, plastic viscosity was enhanced. Also, the integration of 1% straight steel fibers and 1% hooked steel fibers improved flexural strength, toughness, and tensile strength in comparison to the reference UHPC mixture design with 2% straight steel fibers. The cross-influence of macro and micro steel fibers on the tensile behaviors of UHPC was studied by Chun and Yoo,[23] who found a reduction in the fiber efficiency ratios of specimens containing hooked and twisted fibers when the macrofibers were replaced with microfibers. Also, the replacement of 1.5% of hooked and twisted fibers with microfibers increased the post-cracking tensile strength and energy absorption capacity. Bahmani et al.[24,25] examined the impact of various types of fibers (synthetic and mineral) and partial cement substitution levels on the mechanical properties of UHPFRC. The results showed that samples containing synthetic fibers showed remarkable mechanical properties close to the samples with steel fibers.

Based on the literature review, this study aims to develop UHPC with mineral admixtures and investigates the concurrent effects of macro- and microfibers on the mechanical properties of UHPC. Furthermore, owing to the related role of curing conditions on the properties of concrete, diverse types of curing were examined in this investigation.

RESEARCH SIGNIFICANCE

In recent years, economic and environmental issues in the production of UHPC have gained momentum. However, many researchers have focused on the replacement of cement with pozzolanic materials, whereas the simultaneous effects of the combination of supplementary cementitious materials (SCMs) such as slag and fillers such as limestone and quartz powders on the mechanical properties of UHPC have not been scrutinized. Additionally, there has been no study on the effect of using synthetic fibers, such as synthetic macrofibers (a new kind of modified polypropylene fiber, which has the advantages of being lightweight, a simplified construction process, low cost, and few carbon emissions) and polypropylene fibers, as an alternative to steel fibers to reduce production costs, or on the mechanical properties of UHPC mixtures using the combination of cement substitute minerals. Therefore, the present study aimed to significantly replace cement with the optimal ratio of the combination of cement substitute minerals to lower the greenhouse gas emissions due to cement production and to investigate the effect of the addition of synthetic fibers (single and hybrid) on the properties of UHPFRC.

MATERIALS AND MIXTURE DESIGN

The constituent materials used in this study included ordinary portland cement (OPC) Type II under the standard specifications of ASTM C150/C150M-16,[26] which has a moderate Blaine fineness value (320 m^2/kg [174 yd^2/lb]). The silica fume or microsilica with a specific surface of 15,000 to 25,000 m^2/kg (8137 to 13,562 yd^2/lb) and a specific gravity of 2.2 has a particle size of less than 1 μm, which complies with ASTM C1240-15.[27] Silica sand (SS) and silica flour (the very fine-sized particles of silica sand) have particle sizes of less than 0.15 mm (0.006 in.) and 0.05 mm (0.002 in.), respectively. The slag cement (S) has a specific surface of 30,700 m^2/kg (16,655 yd^2/lb) and a specific gravity of 2.7. Limestone powder (LP) and quartz powder (QP) are used as fillers that can reduce the amount of cement. The chemical composition of the ingredients of UHPC as provided by the manufacturer are summarized in Table 1. Polycarboxylate-based high-range water-reducing admixture (HRWRA) with a density of 1050 kg/m^3 (1770 lb/yd^3) and 30% solid content was used as a water reducer conforming to ASTM C494/C494M-05a.[28] Hooked-end steel fibers, synthetic macrofibers, and polypropylene fibers, as illustrated in Fig. 1, were added to the concrete mixture. Table 2 demonstrates detailed information from the manufacturers about the fibers.

Mixture design of UHPC

There is no established mixture design to produce UHPC. Therefore, the literature review reveals a variety of methods used by researchers to produce UHPC. Based on the

Table 1—Chemical composition of ingredients of UHPC

Chemical composition, % by weight	OPC	SF(M)	Slag	LP	QP	SS
SiO_2	22	90 to 95	35.9	0.07	99	97 to 99
Al_2O_3	5	0.6 to 1.2	8.4	0.02	0.5	0.51 to 1.63
Fe_2O_3	4	1.2 to 1.8	0.6	0.02	0.3	0.2 to 0.7
CaO	64	0.5 to 1	37.9	56.7	0.02	0.07 to 0.2
MgO	1.7	0.6 to 1.2	8.9	0.49	—	—
SO_3	2.1	—	—	—	0.03	—
BaO	—	—	2.1	—	—	—
Loss on ignition (LOI)	1.66	0.4 to 3	1.5	43.36	0.1	0.2 to 0.6

(a)

(b)

(c)

Fig. 1—Photo of fibers used in this study: (a) steel; (b) synthetic macrofibers; and (c) polypropylene.

mixing, compaction, and curing methods, the comprehensive mixture design requires that materials be readily and abundantly available that yield high strength despite a reduction in the amount of cement. Therefore, as the first step, the basic mixture design was selected, because better results can be obtained using a more appropriate initial mixture design. The mixture design in this study is based on Mostofinejad et al.'s[29] study. A new mixture design was obtained by changing the size of the aggregates and the ratio of the materials used, which provides the best properties of UHPC. Due to the use of materials with different particle sizes and changes in flowability, the basic mixture design was modified with a slight change, as demonstrated in Table 3.

Table 2—Manufacturer-reported details of fibers

Fiber type	Diameter, mm	Length, mm	Specific density, kg/m^3	Tensile strength, MPa
Steel (ST)	0.6	35	7850	800 to 1200
Synthetic macrofiber (BA)	0.07	54	900 to 920	>600
Polypropylene (PP)	0.017 to 0.02	6	910	400

Note: 1 kg/m^3 = 1.6856 lb/yd^3; 1 mm = 0.039 in.; 1 MPa = 0.145 ksi.

Table 3—Basic UHPC mixture design, kg/m^3

Cement	Silica fume	Silica sand	Silica flour	Water	HRWRA	Compressive strength at 28 days, MPa
1000	295	745	185	185	37.5	133

Note: 1 kg/m^3 = 1.6856 lb/yd^3; 1 MPa = 0.145 ksi.

Experimental methodology

Mixture designs and samples naming—The final mixture proportioning of the UHPFRC mixtures used in this research is given in Table 4. In the current research, three levels of cement replacement materials—silica fume + slag, silica fume + limestone powder + quartz powder, and silica fume + slag + limestone powder + quartz powder—under wet and combined curings were studied. Also, fibers were added at a percentage of 2% (by volume of concrete) in all of the mixture designs. This was due to the observations that using more than 2% of synthetic fibers resulted in a conglobation phenomenon occurring in the UHPFRC mixture and making high-porosity concrete. Because the cement substitutes were used, each mixture design was named in such a way that the name of each mixture corresponded to the first letter of the materials used. For example, the mixture containing silica fume (microsilica) and slag is labeled MS, the mixture design containing microsilica + limestone powder + quartz powder is MLQ, and the mixture containing microsilica + slag + limestone powder + quartz powder is MSLQ. In addition, the first letter of the fibers used was designated in parentheses in front of the mixture design. Steel fibers are represented by ST, synthetic macrofibers are BA, and polypropylene fibers are PP. To find the workability of the fresh concrete, the slump test was carried out according to ASTM C1437-13[30] at a temperature of 20 ± 2°C (68 ± 35.6°F). The water-cementitious materials ratios (*w*/*cm*) were determined between 0.14 and 0.22, and the target flowability was 220 mm (7.87 in.) to achieve good workability with dense packing.

Mixing procedure and preparation of specimens

Regarding the studies conducted on UHPC, there have been various methods for mixing materials, because there are different types of materials and mixers employed. In this research, the concrete mixture design was prepared in a mixer with a capacity of 20 L according to the instructions for the preparation of the UHPFRC mixture,[31,32] with a slight difference due to the use of fibers in the following steps:

- All materials excluding water, HRWRA, and fibers, in all mixture designs, were first thoroughly mixed for

Table 4—Mixture designs and slump flow of UHPFRC

Designation	Mixture proportions, kg/m^3									Slump flow, mm
	Cement	Silica fume	Slag	Limestone powder	Quartz powder	Silica sand	Silica flour	Water	HRWRA	
MS	700	295	270	—	—	745	185	190	40	220
MS(ST)	700	295	270	—	—	745	185	190	42.5	211
MS(PP)	700	295	270	—	—	745	185	190	42.5	202
MS(BA)	700	295	270	—	—	745	185	190	42.5	206
MS(ST-PP)	700	295	270	—	—	745	185	190	42.5	207
MS(ST-BA)	700	295	270	—	—	745	185	190	42.5	208
MS(PP-BA)	700	295	270	—	—	745	185	190	42.5	203
MLQ	700	295	—	202.5	67.5	745	185	175	39	220
MLQ(ST)	700	295	—	202.5	67.5	745	185	175	42	213
MLQ(PP)	700	295	—	202.5	67.5	745	185	175	42	206
MLQ(BA)	700	295	—	202.5	67.5	745	185	175	42	208
MLQ(ST-PP)	700	295	—	202.5	67.5	745	185	175	42	209
MLQ(ST-BA)	700	295	—	202.5	67.5	745	185	175	42	211
MLQ(PP-BA)	700	295	—	202.5	67.5	745	185	175	42	206
MSLQ	550	295	270	102	33	745	185	180	38	220
MSLQ(ST)	550	295	270	102	33	745	185	180	40.5	212
MSLQ(PP)	550	295	270	102	33	745	185	180	40.5	205
MSLQ(BA)	550	295	270	102	33	745	185	180	40.5	207
MSLQ(ST-PP)	550	295	270	102	33	745	185	180	40.5	208
MSLQ(ST-BA)	550	295	270	102	33	745	185	180	40.5	210
MSLQ(PP-BA)	550	295	270	102	33	745	185	180	40.5	205

Note: 1 kg/m^3 = 1.6856 lb/yd^3; 1 mm = 0.039 in.

5 minutes at a low speed and then for 2 minutes at a high speed.

- Water and HRWRA were combined and gradually added to the materials; the mixer was turned on for approximately 10 minutes and the materials were allowed to get entirely mixed at a low speed.
- At the final step, the fibers were added to the mixer, first for 2 minutes at a low speed, and second for 3 minutes at a high speed to spread well in the mixer.

The curing method significantly affects the mechanical properties of UHPC. The researchers used different curing conditions considering time, place, and temperature. In this study, wet, autoclave, and combined curing were taken into consideration. The samples subjected to wet curing were extracted from the mold after 24 hours and then placed in water at approximately 22°C (71.6°F) for 7 and 28 days. This curing was chosen because of simplicity, commonality, and the benchmark. Also in this study, two combined curing conditions were performed as follows:

1. Autoclave-oven curing: The samples were extracted from the mold after 24 hours, placed in an autoclave at a temperature of 121°C (249.8°F) and under a pressure of 0.18 MPa (0.026 ksi) for 3 days, and finally placed in an oven at a temperature of 200°C (392°F) for 7 days.

2. Autoclave-water curing: The samples were taken out from the mold after 24 hours, placed in an autoclave at a temperature of 121°C (249.8°F) and under a pressure of 0.18 MPa (0.026 ksi) for 3 days, and placed in water at approximately 22°C (71.6°F) for 25 days afterward.

After placing the samples comprising synthetic macrofibers and polypropylene fibers in an oven at 200°C (392°F), they went through burns, and then the resistance was reduced. Hence, a combination of autoclave and water was used for these levels of fibers.

Experiments

To evaluate the outcomes, compressive strength and four-point flexural tests were employed. Regarding the compressive strength test based on ASTM C109/C109M-11b,[33] the cubic specimens with dimensions of 70 mm (2.76 in.) for all mixtures were tested through a compression-testing machine at a loading rate of 900 to 1800 N/s (202.33 to 404.66 lb/s). In addition, the cylindrical specimens with dimensions of 100 x 200 mm (3.94 x 7.87 in.) under wet curing for 28 days for all mixtures were used to compare with the results of the cubic specimens.

The four-point flexural test was carried out on the prismatic specimens with dimensions of 70 x 70 x 350 mm (2.76 x 2.76 x 13.78 in.). The flexural test was performed based on ASTM C78/C78M-10,[34] through the use of a four-point bending testing machine with a capacity of 50 kN (11.24 kip). Here two cylinders were employed to apply force, and the distance between the cylinders on both sides was equal to their close supports. In this method, the

specimens were placed on two supporting pins and the distance from the end of the specimen to the support was 25 mm (0.98 in.). Two linear variable differential transformers (LVDTs) on the supports and one LVDT at the center of the beam were applied to plot load-displacement diagrams. Figure 2 displays the testing apparatuses of the compression and the four-point flexural tests. In this study, each test was repeated at least twice to report the result.

RESULTS AND DISCUSSION

Workability of UHPFRC

Based on the flow values obtained for fresh UHPFRC in Table 4, a reduction is observed from the comparison drawn between UHPFRC mixtures in the workability of UHPC with fibers due to mechanical interaction between fibers and grains. In general, it is observed that the slump flow values of UHPFRC mixtures with polypropylene, synthetic macrofibers, and steel fibers decrease by up to 8%, 6%, and 4%, respectively. Also, to achieve the target flowability (220 mm [7.87 in.]), the amount of water used in the MLQ and MSLQ mixtures decreased by 9% and 6%, respectively, compared to the MS mixture.

(a)

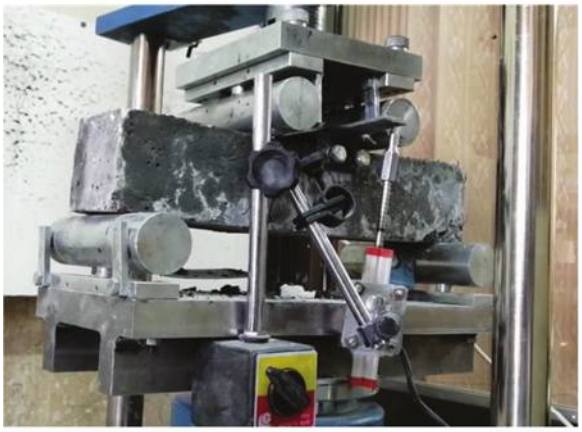

(b)

Fig. 2—(a) Compressive strength test; and (b) four-point flexural test.

Compressive strength

Effects of slag—To replace part of the cement with slag, different ratios of slag were applied, and the compressive strength of the specimens was calculated after 7 and 28 days (Table 5). As can be seen from the findings, 30% replacement of the cement with slag resulted in the greatest compressive strength at 28 days (129.5 MPa [18.78 ksi]), which is almost equal to the sample made of 100% cement. It was found that with growing curing age, the increase in the compressive strength of samples containing slag is greater than that of samples containing cement due to the higher reaction of slag.[1,35] Increasing the amount of slag to 40% in the mixture, the strength decreased by approximately 10% due to slower slag hydration and a lower rate of production of secondary calcium-silicate-hydrate.[36,37]

Figure 3 illustrates the compressive strength results in all cement replacement designs under wet and combined curing. It is apparent from Fig. 3(a) that the MS specimens with compressive strengths between 122 and 140.5 MPa (17.69 and 20.37 ksi) at a curing age of 28 days exhibit the best performance compared to the other levels of cement replacement. The combined curing improved the compressive strength (up to 35%) compared to the wet curing as a result of increasing hydration reactions, which created more hydration products. Also, all specimens containing silica fume and slag under the combined curing achieved a compressive strength of more than 150 MPa (21.7 ksi), highlighting the positive effect of combined curing on concrete. For example, samples reinforced with steel fibers recorded the highest compressive strength (184 MPa [26.69 ksi]) under this curing.

Effects of limestone and quartz powders—To find the best percentage of cement replacement with limestone powder and quartz powder, four ratios were probed. In this study, up to 40% of cement was replaced with limestone powder at 3:4 and quartz powder at 1:4 (Table 6). The highest compressive strength (111 MPa [16.1 ksi] at 28 days) was observed in the specimens with 30% limestone and quartz powders instead of cement, which resulted in a 13% drop in compressive strength compared to replacing cement with slag. By increasing the limestone powder-to-cement ratio (*L*/*C*) to 30%, fillers provide more space and water for cement hydration due to the dilution effect, absorbing more hydration products.[16] With higher percentages of limestone

Table 5—Mixture design of UHPFRC containing microsilica and slag, kg/m^3

S/*C*	Cement	Silica fume	Silica sand	Silica flour	Slag	Water	HRWRA	Compressive strength at 7 days, MPa	Compressive strength at 28 days, MPa
10	900	295	745	185	90	190	46	85	126.5
20	800	295	745	185	180	190	43	79	123
30	700	295	745	185	270	190	40	82	129.5
40	600	295	745	185	360	190	38	75	118

Note: *S*/*C* is slag-cement ratio; 1 kg/m^3 = 1.6856 lb/yd^3; 1 MPa = 0.145 ksi.

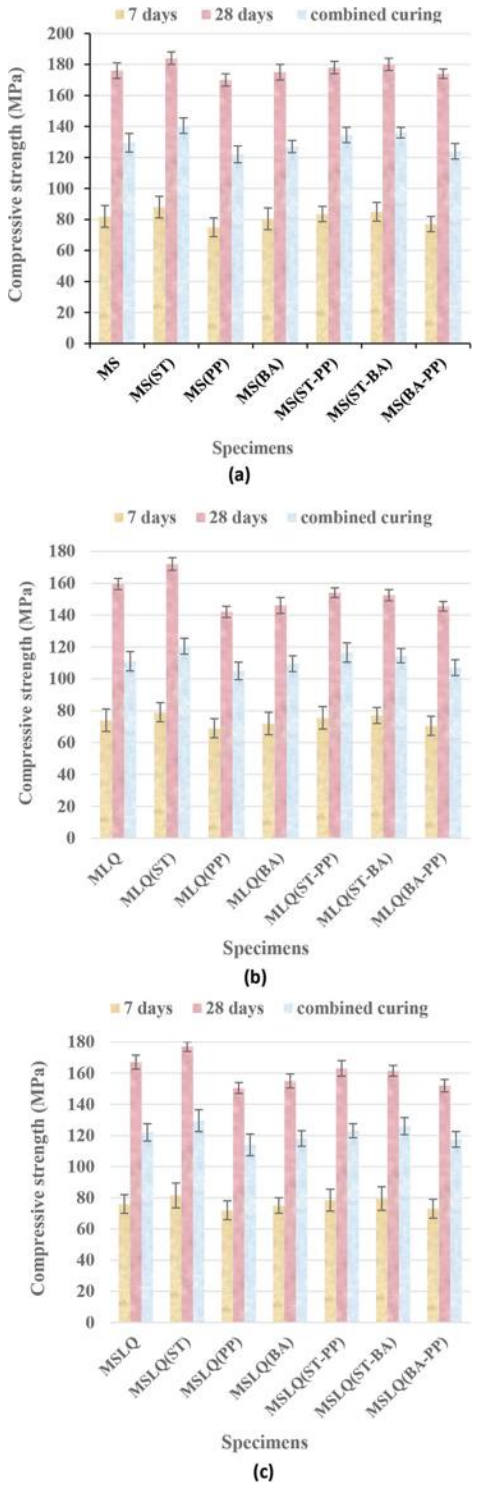

Fig. 3—Compressive strength of mixture designs: (a) MS specimens; (b) MLQ specimens; and (c) MSLQ specimens.

powder and quartz powder instead of cement, the volume of pores with smaller diameters expanded.[38] Thus, the pores became interconnected, which elevated the water absorption by immersion, capillarity, and porosity.[39]

Figure 3(b) demonstrates the compressive strength outcomes of mixtures containing silica fume, limestone powder, and quartz powder under wet and combined curing. The MLQ(ST) specimen with compressive strengths of 120.5 MPa (17.47 ksi) at a curing age of 28 days shows the greatest values compared to the other mixtures, whereas MLQ(PP) reveals the lowest compressive strength of 105 MPa (15.23 ksi) at a curing age of 28 days. The reduction between 13 and 16% in the compressive strength is perceived compared to the MS mixture design at a curing age of 28 days, because of generating fewer hydration products in response to water, whereas the mixtures cured under the combined curing show reductions between 6 and 16% in compressive strength. However, the samples with steel fibers achieved a strength above 150 MPa (21.76 ksi) under the combined curing.

Effects of slag, limestone powder, and quartz powder—To obtain the optimal percentage of cement replacement with slag and limestone powder, the slag replacement ratio was kept constant at 30%, and limestone powder and quartz powder were replaced in four percentages at 3:4 and 1:4 ratios (Table 7). As summarized in Table 7, a total of 45% cement replacement with 30% slag and 15% limestone and quartz powders led to the highest compressive strength (122 MPa [17.69 ksi] at 28 days), which is the most desirable mixture design without a notable drop (approximately 5%) compared to the MS samples. At this level of cement replacement, despite decreasing the use of cement up to 550 kg/m^3 (927.1 lb/yd^3), acceptable compressive strength and better behavior were observed in comparison with the MLQ specimens.

Figure 3(c) displays the compressive strength results of the third cement replacement design containing silica fume, slag, limestone powder, and quartz powder. As shown in Fig. 3(c), the MSLQ(ST) and MSLQ(PP) with compressive strengths of 129.5 and 114 MPa (18.78 and 16.53 ksi), respectively, under 28 days of wet curing recorded the maximum and minimum values. At combined curing, the compressive strength of the MSLQ samples increased up to 35%, and all the specimens had a strength above 150 MPa (21.76 ksi). It is likely that the binding interaction between SCMs under combined curing forms more hydration products, and as a result, leads to greater compressive strength. The cylinder/cube compressive strength ratios for the MS,

Table 6—Mixture design of UHPFRC containing microsilica, limestone powder, and quartz powder, kg/m^3

L/*C*	Cement	Silica fume	Silica sand	Silica flour	LP	QP	Water	HRWRA	Compressive strength at 7 days, MPa	Compressive strength at 28 days, MPa
10	900	295	745	185	67.5	22.5	175	46	77	108
20	800	295	745	185	135	45	175	43	70	104
30	700	295	745	185	202.5	67.5	175	39	74	111
40	600	295	745	185	270	90	175	37.5	66	95

Note: 1 kg/m^3 = 1.6856 lb/yd^3; 1 MPa = 0.145 ksi.

Table 7—Mixture design of UHPFRC containing microsilica, slag, limestone powder, and quartz powder, kg/m³

L/*C*	Cement	Silica fume	Silica sand	Silica flour	Slag	LP	QP	Water	HRWRA	Compressive strength at 7 days, MPa	Compressive strength at 28 days, MPa
5	650	295	745	185	270	34	11	180	42	79	120
10	600	295	745	185	270	68	22	180	40	72	117
15	550	295	745	185	270	102	33	180	38	76	122
20	500	295	745	185	270	136	44	180	36	70	111
25	450	295	745	185	270	170	55	180	34	64	98

Note: 1 kg/m³ = 1.6856 lb/yd³; 1 MPa = 0.145 ksi.

MLQ, and MSLQ specimens are 0.951, 0.950, and 0.952, respectively.

Effects of fibers—Table 8 shows the effect of different fibers individually or in combination with other fibers on the compressive strength of the mixture designs in comparison to non-fiber specimens. There is a stronger connection between the fibers and the matrix rises due to the increase in the matrix strength with growing age, which consequently enhances the performance of fibers in improving the strength. As shown in Table 8, the steel fibers, either as single or hybrids, enhance the compressive strength (up to 10%) as they effectively arrest microcracks and delay the formation and propagation of cracks. With reference to the polypropylene fibers, either as single or as polypropylene-synthetic macrofiber hybrids, with a significant increase in porosity, the compressive strength (approximately 8%) declined compared to the specimens without fibers under wet curing. On the contrary, the compressive strength of specimens containing synthetic macrofibers decreased slightly compared to specimens without fibers. In combined curing, other samples experienced a decrease in strength, except steel fibers, which increase the compressive strength relative to the non-fiber specimens. It may be noted that the melting point of synthetic macrofibers and polypropylene fibers is lower than the oven temperature. As a result, the samples containing these fibers were cured under autoclave water, which led to a drop in compressive strength.

Flexural strength

In the experimental samples, because the rupture occurs in the range of the middle third, Eq. (1) is used to calculate the modulus of rupture (MOR). The MOR is defined as the maximum stress that can be resisted by a member before rupture.

$$f_r = \frac{PL}{bd^2} \quad (1)$$

where f is the flexural strength of concrete; P is the applied load; L is the effective span of the beam; b is the width of the beam; and d is the height of the beam.

The results of the MOR in three different cement replacement levels under wet and combined curing are shown in Fig. 4. As observed in Fig. 4(a), the MOR of the MS mixtures is more than the other two levels of cement replacement, due to the creation of additional hydration products (by slag) in the mixtures by reacting with water.[14] For example, the

Table 8—Effect of fibers on variation of compressive strength in comparison to non-fibers specimens, %

Mixtures	7 days	28 days	Combined curing
MS(ST)	7.3↑	8.5↑	4.5↑
MS(ST-BA)	3.6↑	5.0↑	1.7↓
MS(ST-PP)	1.8↑	3.9↑	2.8↓
MS(BA)	1.8↓	1.9↓	4.5↓
MS(PP-BA)	6.1↓	4.2↓	6.5↓
MS(PP)	8.5↓	5.8↓	8.3↓
MLQ(ST)	6.8↑	8.6↑	7.8↑
MLQ(ST-BA)	2.0↑	2.7↑	4.4↓
MLQ(ST-PP)	4.1↑	5.0↑	3.4↓
MLQ(BA)	2.7↓	1.4↓	8.5↓
MLQ(PP)	6.8↓	5.4↓	11.0↓
MLQ(PP-BA)	4.7↓	3.6↓	9.0↓
MSLQ(ST)	7.2↑	6.1↑	6.0↑
MSLQ(ST-BA)	4.6↑	3.3↑	3.3↓
MSLQ(ST-PP)	3.3↑	1.0↑	2.4↓
MSLQ(BA)	1.3↓	3.3↓	7.2↓
MSLQ(PP)	5.3↓	6.6↓	9.9↓
MSLQ(PP-BA)	4.0↓	4.5↓	9.0↓

MS(ST) specimens at 7 and 28 days of wet curing showed the highest flexural strengths 14.91 and 24.31 MPa (2.16 and 3.52 ksi), respectively. Additionally, better outcomes were obtained for the mixture design with the combination of slag and limestone powder rather than replacing cement only with limestone and quartz powders. The flexural strength of the MLQ mixtures decreased by up to 14% compared to MS mixtures under wet conditions. However, MLQ(ST) specimens under 7 and 28 days of wet curing recorded σ_{MOR} of 12.81 and 22.79 MPa (2.24 and 3.99 ksi), respectively. The flexural strengths of the MSLQ(ST) specimens at curing ages of 7 and 28 days were recorded at 12.94 and 23.56 MPa (2.26 and 4.12 ksi), respectively, which were higher than those of the MLQ(ST) specimens.

Concerning the findings in the combined curing, all the mixture designs experienced a slight reduction in their MOR, because of weaker fiber adhesion, compared to the wet curing. Notably, the decrease in flexural strength under the combined curing of autoclave ovens for samples containing single steel fibers was approximately 5% higher

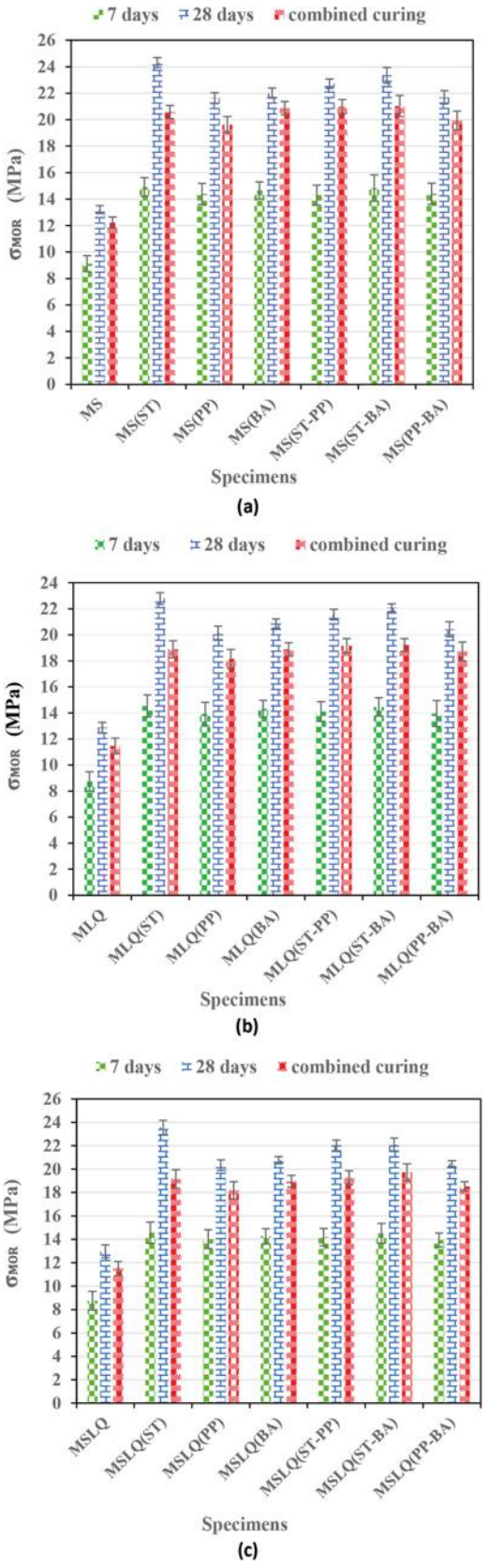

Fig. 4—Moduli of rupture (MOR) of mixture designs: (a) MS specimens; (b) MLQ specimens; and (c) MSLQ specimens.

than the combined curing of autoclave water for other specimens. As can be seen, the MS(ST-BA) specimens under combined curing had the highest flexural strength of 21.03 MPa (3.68 ksi) compared to other cement replacement designs, which is 72% higher than that recorded by those without fibers.

As demonstrated in Fig. 4, due to the greater tensile strength of steel fibers, the use of steel fibers (single and hybridized) in all cement replacement designs resulted in the highest flexural strength values, which are 70 to 80% greater than the mixtures without fibers. Furthermore, the obtained results of specimens reinforced with synthetic macrofibers were close to steel fibers, denoting the high ductility of samples in the presence of macrofibers.

Stress-deflection curves

The average stress-deflection diagrams at the midspan for all cement replacement designs under wet curing are provided in Fig. 5. As shown in Fig. 5, all three levels of cement substitute mixtures containing fibers presented identical deflection and flexural capacities close to each other before cracking. The first crack deflection for the MS, MLQ, and MSLQ mixtures at 7 and 28 days of wet curing occurred at approximately 0.36 and 0.48 mm (0.014 and 0.019 in.), respectively. The critical load to develop the first crack of the MS, MLQ, and MSLQ mixtures was 9.12, 8.74, and 8.76 MPa (1.32, 1.26, and 1.27 ksi), respectively, at 7 days, and 13.21, 12.87, and 12.98 MPa (1.92, 1.87, and 1.88 ksi), respectively, at 28 days. However, the MS specimens, in terms of deflection capacity and post-peak ductility beyond the cracking point, indicated better flexural performance by up to 20% compared to the MLQ specimens. Despite a significant reduction in cement, observed in Fig. 5(e) and (f), the MSLQ specimens showed acceptable flexural behavior such as deflection capacity and post-peak ductility close to the MS specimens. The development of this mixture is financially and environmentally justified. The average decreases in the 28-day peak loads for the MLQ and MSLQ specimens containing different fibers were 6% and 5%, respectively, compared to the MS specimens containing fibers.

As can be observed in Fig. 5, because of the longer fibers of steel and synthetic macrofibers, which develop greater matrix-fibers interaction, the post-cracking capacity of concrete was significantly elevated and caused more ductility compared to samples containing polypropylene fibers. The presence of polypropylene fibers, like other fibers, enhances the flexural strength of samples compared to specimens in the absence of fibers, indicating short strain-hardening behavior that is explained through the patching of microcracks after cracking. However, when the macrocracks have emerged in samples containing polypropylene fibers, these fibers cannot limit the multiplication of macrocracks. Furthermore, specimens containing macro and micro hybrid fibers such as MS(BA-PP) indicated acceptable flexural performance in terms of deflection capacity and post-peak ductility. This is mainly due to the involvement of polypropylene fibers in bridging and harnessing the microcracks surfaces, and also the synthetic macrofibers limiting the initiation and propagation of deep cracks. On the other hand, bending the specimens without fibers causes complete rupture immediately after the first crack. Thus, it can be inferred that concrete without fibers is brittle and has marginal ductility. Failure of specimens containing fibers after cracking causes the

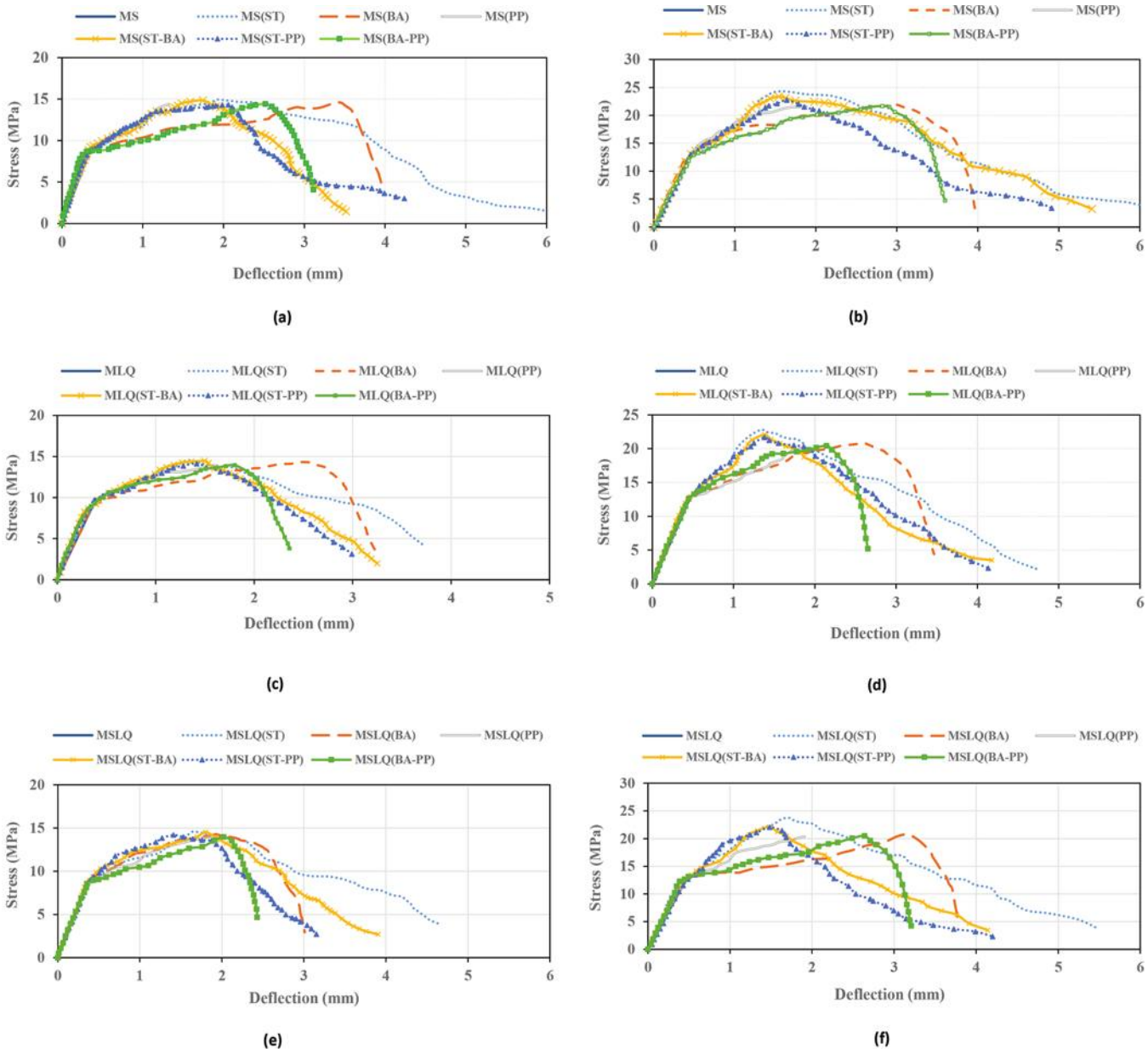

Fig. 5—Stress-deflection curves under wet curing: (a) MS (7 days); (b) MS (28 days); (c) MLQ (7 days); (d) MLQ (28 days); (e) MSLQ (7 days); and (f) MSLQ (28 days).

load-increasing slope to become smoother until it reaches the peak of load-bearing, and afterward, by lowering the load-bearing capacity, it reaches the complete rupture point of the sample.

The effect of combined curing on the flexural responses of all mixtures is represented in Fig. 6. According to Fig. 6, notwithstanding the remarkable increase in compressive strength, the use of an autoclave reduced by up to 15% the deflection capacity and post-peak ductility of specimens containing fibers relative to those under wet curing. It may be because the increasing temperature would consequently accelerate the hydration reaction of the cement and the hydration products of the cement, especially calcium hydroxide, surround the fibers, and reduce the tensile strength of the fibers by sticking the fibers together. In this case, the bearing capacity is reduced and the specimens become more brittle.

For the combined curing, it can be inferred from Fig. 6(a) that the MS specimens indicated better flexural responses (approximately 5 to 10%) compared to the MLQ and MSLQ mixtures. Furthermore, steel fibers and their combination with synthetic macrofibers presented the best displacement ductility capacity. The combined curing of autoclave ovens reduces the ductility of steel fiber-reinforced specimens further than the combined curing of autoclave water. It can be deduced that when the sample is exposed to heat, it intends to reshape and different strains are formed due to the discrepancy in the essence between the steel fibers and concrete materials.[40] As a consequence of this behavior, the stress between the steel fibers and the concrete will be formed, which itself is regarded as a factor in reducing the adhesion between the concrete and the steel fibers.[41] Figure 7 demonstrates typical cracking patterns and failure modes of UHPFRC specimens containing macro and hybrid fibers.

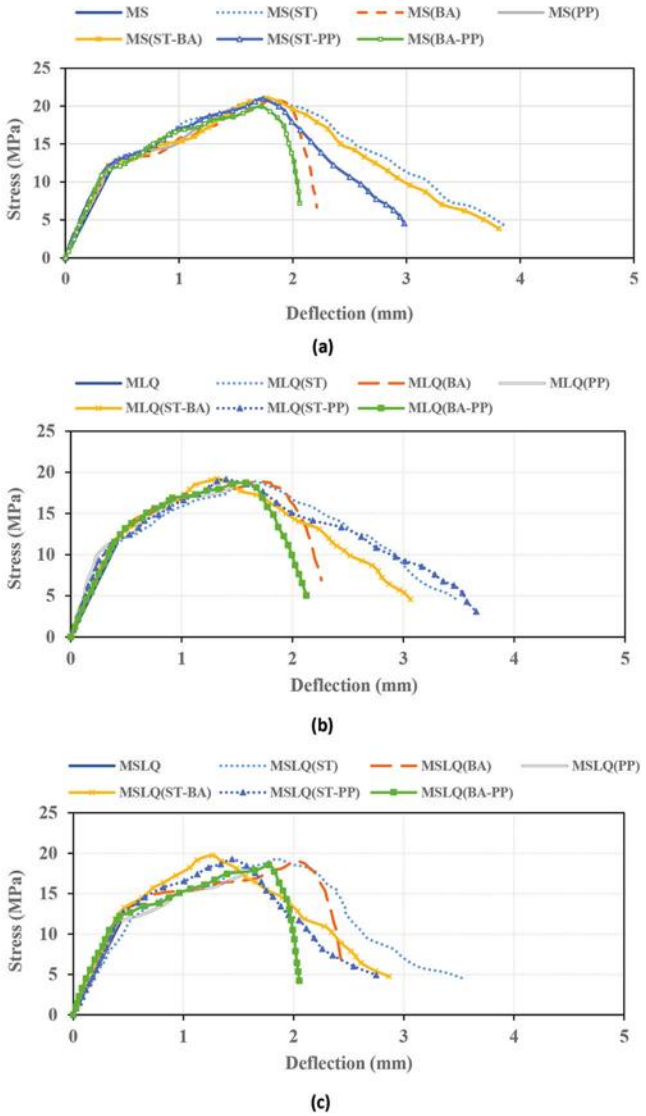

Fig. 6—Stress-deflection curves under combined curing: (a) MS; (b) MLQ; and (c) MSLQ.

Figure 8 shows the results of deflection at the MOR for all cement replacement designs containing fibers and without fibers under wet and combined curing. The use of fibers causes variation in the amount of MOR deflection. For instance, synthetic macrofibers in the MS mixture increase the post-cracking properties at the MOR point and show the highest difference in δ_{MOR} (3.4 mm [0.13 in.]). On the contrary, the specimens without fibers have the lowest δ_{MOR} value of 0.35 mm (0.014 in.). According to Fig. 8, combined curing decreased the values of δ_{MOR} (up to 40%) in all cement replacement designs.

Toughness

The surface area under the load-deflection diagram, which shows the amount of energy absorbed by the concrete specimens, is described as the flexural toughness of the concrete. The presence of fibers in the concrete improves continuity after cracking compared to the non-fiber sample, so considerable energy is required for complete rupture to occur in the concrete.

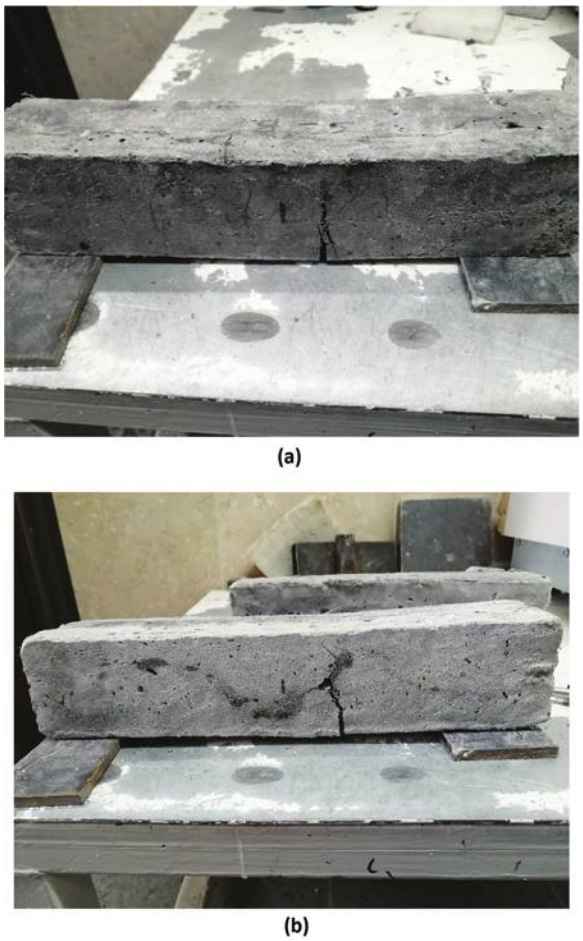

Fig. 7—Cracking patterns and failure modes of UHPFRC specimens: (a) MLQ(ST-BA); and (b) MSLQ(PP).

Based on ASTM C1018-97,[42] the dimensionless parameters were used to compare the flexibility and the absorbed energy of the samples. The toughness indexes of I_5, I_{10}, and I_{20} are obtained by dividing the area under the load-displacement diagram up to a deflection equal to 3δ, 5.5δ, and 10.5δ, respectively, by the surface area below the diagram up to the deflection at δ; where δ is the deflection measured at the incidence of first cracking. In Fig. 9, the calculation process of the toughness indexes according to ASTM 1018 can be found.

Figure 10 displays the toughness indexes for all cement replacement designs under wet curing. As shown in Fig. 10, in all of the cement replacement designs, the samples reinforced with fibers, excluding the polypropylene fibers, indicated "acceptable ductility" results at 7 and 28 days of curing—that is, a deflection equal to 3, 5.5, and 10.5 times the displacement corresponding to the incidence of first cracking was provided by all levels of fibers, except the polypropylene fiber. The MS specimens containing the different fibers recorded the best I_5, I_{10}, and I_{20} values at 7 and 28 days of curing compared to the MLQ and MSLQ mixtures with fibers. For example, the MS(ST) specimen under 28 days of curing recorded I_5, I_{10}, and I_{20} at 6.12, 13.33, and 24.07, respectively, while the indexes for the MLQ(ST) and MSLQ(ST) specimens decreased to 5.71, 12.68, and 22.11 and 5.92, 13.01, and 23.06, respectively.

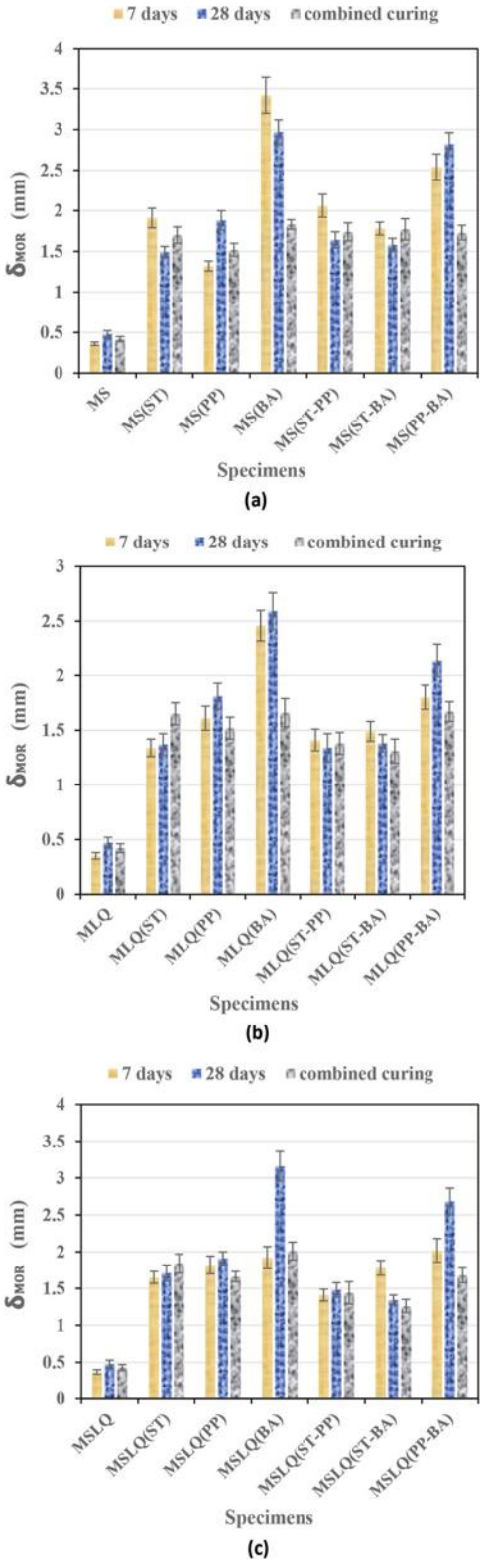

Fig. 8—Deflection capacity at MOR: (a) MS specimens; (b) MLQ specimens; and (c) MSLQ specimens.

Samples containing polypropylene fibers were the only level of fibers that could not provide the 10.5 times displacement corresponding to the first crack occurrence because these fibers bridged the cracks in the first cracking stage. The worst I_{10} values belong to the mixtures with polypropylene fibers. This index for the MS(PP), MLQ(PP), and MSLQ(PP) specimens under 28 days of wet curing was recorded at 9.96, 11.35, and 10.37, respectively.

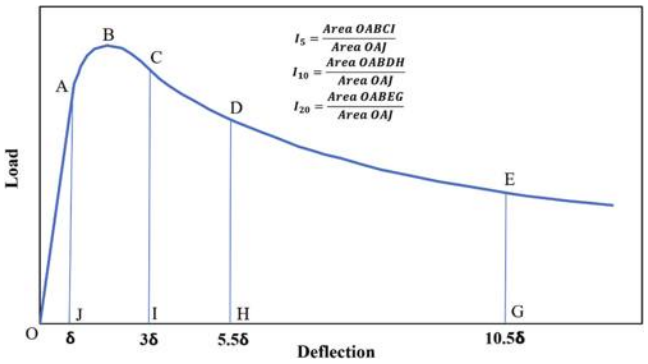

Fig. 9—Calculation process of toughness indexes.

Figure 11 displays the toughness indexes for the MS, MLQ, and MSLQ samples treated under the combined curing method. Here, although all the specimens achieved I_5 and I_{10} toughness indexes, they exhibited disappointing I_{20} results. This decrease in flexural strength is because the autoclave weakened the bond strength between the matrix and the fibers. The I_{20} values for the MS, MLQ, and MSLQ mixtures under combined curing fell between 10 and 15% relative to wet curing. However, the MS(ST) specimen recorded the best I_{20} at 18.12.

Financial and environmental evaluation of designed UHPC mixtures

Table 9 shows the costs of 1 m^3 of the UHPFRC mixtures. The cost of 1 m^3 of concrete in the the sample made of 100% cement without fibers was equal to $61. The cost of the production of 1 m^3 of the MS, MLQ, and MSLQ mixtures decreased by 8, 12, and 15%, respectively, compared to the sample made of 100% cement. The comparison between the three levels of cement replacement materials shows that the highest cost of production belonged to the MS specimens. Also, polypropylene and synthetic macrofibers have a lower price than steel fibers, and adding these fibers decreases the production cost by up to 25%. Therefore, the mixtures containing synthetic macrofibers, hybrid fibers of steel-synthetic macrofiber, and steel-polypropylene are more economical according to the results close to steel fibers. Based on the embodied CO_2 values for each component of concrete provided by the previous studies,[11,43-45] it can be inferred that the UHPC mixtures made with 100% cement have higher embedded CO_2 emissions and environmental impact. The CO_2 emissions significantly decreased for the specimens containing slag, limestone powder, and quartz powder compared to mixtures made with 100% cement. The percentage values of the reduction in CO_2 emissions for the MS, MLQ, and MSLQ mixtures are equal to 27, 29, and 43%, respectively. Therefore, it is environmentally justified to use mineral admixtures as cement replacement materials.

CONCLUSIONS

In this study, the mechanical properties of ultra-high-performance concrete (UHPC) were scrutinized by reducing cement and replacing it with the optimal ratio of silica fume,

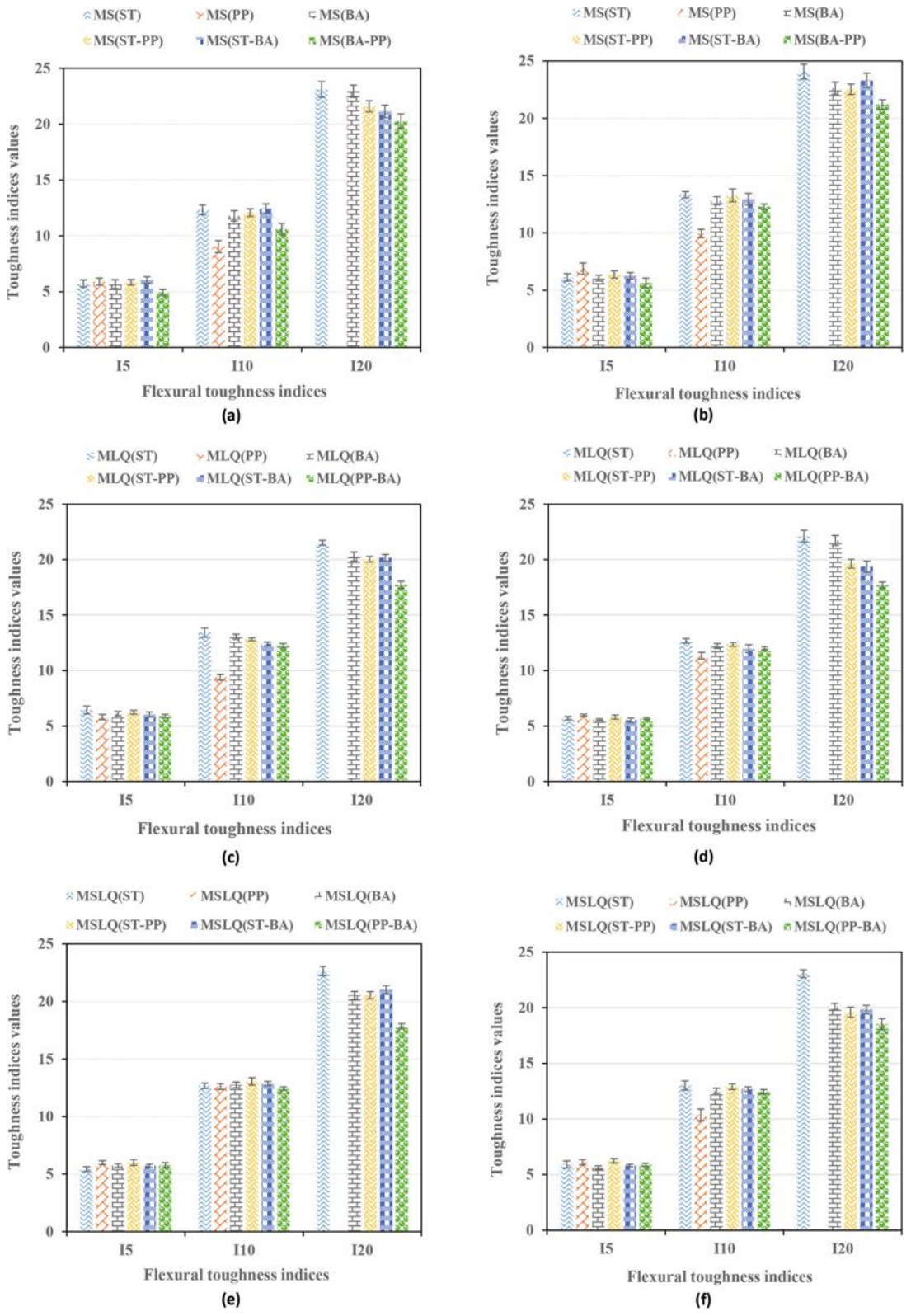

Fig. 10—Toughness indexes of mixtures under wet curing: (a) MS (7 days); (b) MS (28 days); (c) MLQ (7 days); (d) MLQ (28 days); (e) MSLQ (7 days); and (f) MSLQ (28 days).

slag, limestone powder, and quartz powder. Moreover, the effects of steel, polypropylene, and synthetic macrofibers either used singly or as a hybrid on the mechanical properties of UHPC were examined. A total of 21 mixture designs were selected, and 336 specimens were treated for 7 and 28 days under wet and combined curing as a modern technique. To evaluate the mechanical properties of ultra-high-performance fiber-reinforced concrete (UHPFRC), compression and flexural tests were performed on the specimens. The following conclusions can be drawn from this study:

1. Combined curing increased compressive strength by approximately 40% compared to wet curing. With this

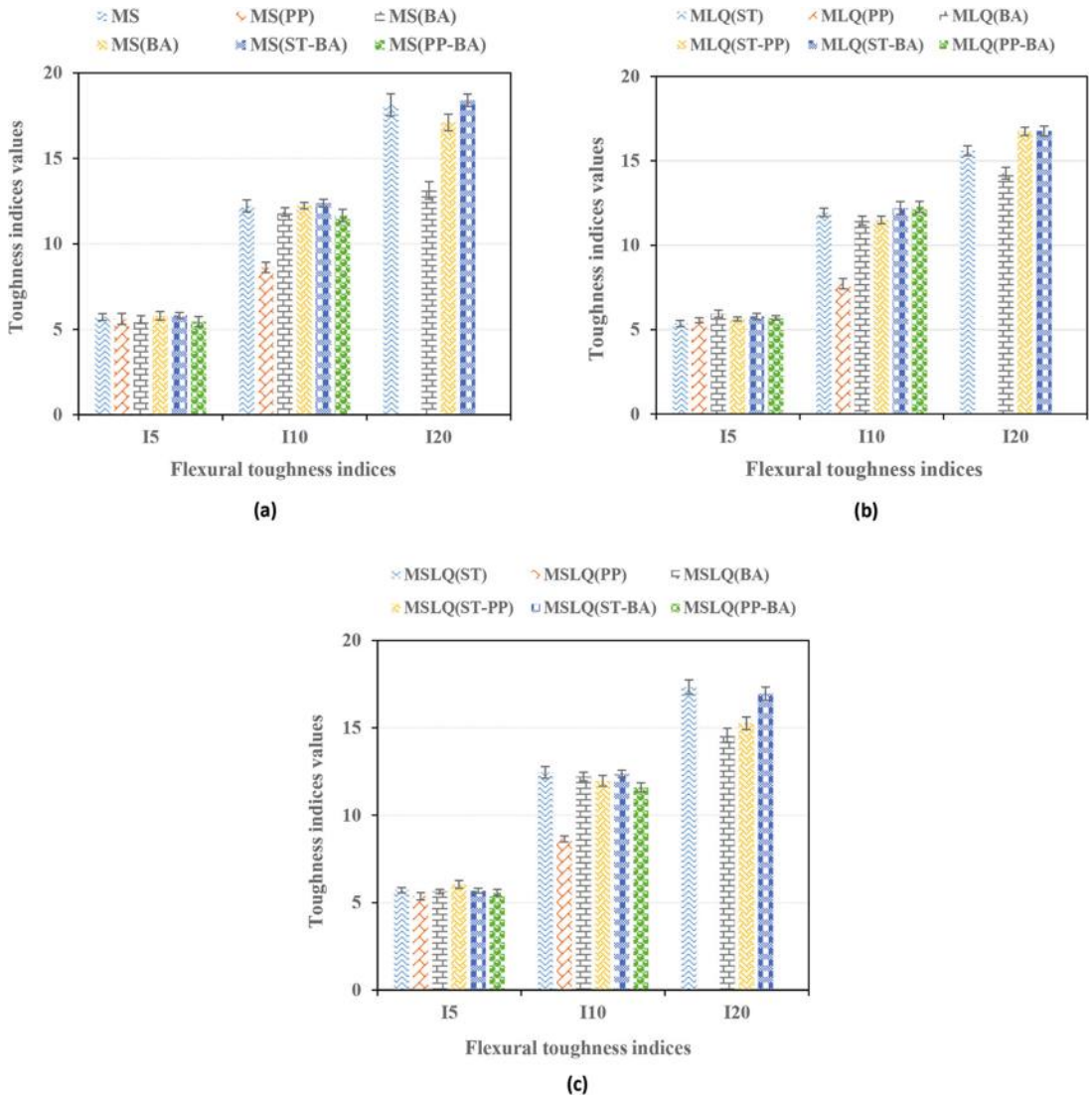

Fig. 11—Toughness indexes of mixtures under combined curing: (a) MS specimens; (b) MLQ specimens; and (c) MSLQ specimens.

curing, the compressive strength of more than 150 MPa (21.76 ksi) was obtained in most specimens. For example, the MS(ST) specimen cured by this method recorded compressive strength of 184 MPa (26.69 ksi). On the other hand, combined curing reduced flexural behavior and ductility indexes compared to wet curing. The specimens under the combined curing experienced approximately a 35% reduction in their deflection capacity compared to those cured under wet conditions.

2. The specimens containing slag achieved the best results in terms of compressive strength and flexural strength, indicating the feasibility of cement replacement with slag, without significantly reducing the strength of this type of concrete. For example, samples containing steel fibers displayed a compressive strength of 140 MPa (20.30 ksi), 10% more than those specimens without fibers.

3. The specimens containing limestone powder and quartz powder reduced the compressive strength (by approximately 15%) compared to the MS specimens, while the overall flexural behavior is almost similar to the mixture containing slag with identical fibers. However, it appeared as an acceptable strength, which is cost-effective and environmentally friendly.

4. The simultaneous use of microsilica, slag, limestone powder, and quartz powder showed better results compared to the MLQ mixture. The compressive strength of the MSLQ mixture is reduced (by approximately 7%) compared to specimens containing slag, while the flexural performance is similar to the MS specimens. Due to the significant reduction in cement and the replacement of approximately 50% of cement with slag and limestone powder, the development of this mixture design is justified both economically and environmentally.

5. The best results as regards flexural strength and energy absorption were recorded by the samples containing steel fibers and synthetic macrofibers with a slight difference. Using synthetic macrofibers in the mixtures in comparison to steel fibers obtained the largest strain-hardening area. The I_5, I_{10}, and I_{20} indexes were acceptable in all specimens containing macrofibers, which indicates that the macrofibers have appropriate flexural toughness.

Table 9—Cost per cubic meter of UHPFRC mixtures

Mixtures	Production cost, USD
MS	412
MS(ST)	776
MS(ST-BA)	691
MS(ST-PP)	634
MS(BA)	605
MS(PP-BA)	548
MS(PP)	491
MLQ	401
MLQ(ST)	767
MLQ(ST-BA)	682
MLQ(ST-PP)	625
MLQ(BA)	596
MLQ(PP)	482
MLQ(PP-BA)	539
MSLQ	386
MSLQ(ST)	681
MSLQ(ST-BA)	664
MSLQ(ST-PP)	608
MSLQ(BA)	579
MSLQ(PP)	465
MSLQ(PP-BA)	522

AUTHOR BIOS

Nima Mohammadian Tabrizi *is a Research Assistant in the Department of Civil Engineering at the Isfahan University of Technology (IUT), Isfahan, Iran, where he received his MSc in 2020. His research interests include concrete technology, specifically ultra-high-performance concrete.*

Davood Mostofinejad *is a Distinguished Professor in the Department of Civil Engineering at IUT. He received his BSc from the University of Tehran, Tehran, Iran, in 1985; his MSc from IUT in 1987; and his PhD from Carleton University, Ottawa, ON, Canada, in 1997. His research interests include the application of fiber-reinforced polymer composites in concrete and masonry structures, repair and rehabilitation of damaged reinforced concrete (RC) structures, ductility of RC beam-column joints, advanced concrete technology, and biological treatment of concrete.*

Mohammad Reza Eftekhar *is an Assistant Professor in the Department of Civil Engineering at IUT. He received his MSc from Shiraz University, Shiraz, Iran, in 1992, and his PhD from IUT in 2010. His research interests include concrete technology and the application of fiber-reinforced polymer composites in concrete and masonry structures.*

REFERENCES

1. Fehling, E.; Schmidt, M.; Walraven, J.; Leutbecher, T.; and Fröhlich, S., *Ultra-High Performance Concrete UHPC: Fundamentals, Design, Examples*, John Wiley & Sons, Inc., New York, NY, 2015, 198 pp.

2. Kim, S.-K.; Kim, W.; and Han, S.-M., "Behavior Evaluation of Ultrahigh-Performance Concrete Beam Containing Para-Aramid Fibers," *Advances in Civil Engineering*, V. 2019, 2019, Article No. 5187630, 17 pp. doi: 10.1155/2019/5187630

3. Kang, S.-T.; Lee, Y.; Park, Y.-D.; and Kim, J.-K., "Tensile Fracture Properties of an Ultra High Performance Fiber Reinforced Concrete (UHPFRC) With Steel Fiber," *Composite Structures*, V. 92, No. 1, Jan. 2010, pp. 61-71. doi: 10.1016/j.compstruct.2009.06.012

4. Schmidt, M., and Fehling, E., "Ultra-High-Performance Concrete: Research, Development and Application in Europe," *Seventh International Symposium on the Utilization of High-Strength/High-Performance Concrete*, SP-228, American Concrete Institute, Farmington Hills, MI, 2005, pp. 51-78.

5. Habel, K.; Denarié, E.; and Brühwiler, E., "Time Dependent Behavior of Elements Combining Ultra-High Performance Fiber Reinforced Concretes (UHPFRC) and Reinforced Concrete," *Materials and Structures*, V. 39, No. 5, June 2006, pp. 557-569. doi: 10.1007/s11527-005-9045-0

6. Habert, G.; Denarié, E.; Šajna, A.; and Rossi, P., "Lowering the Global Warming Impact of Bridge Rehabilitations by Using Ultra High Performance Fibre Reinforced Concretes," *Cement and Concrete Composites*, V. 38, Apr. 2013, pp. 1-11. doi: 10.1016/j.cemconcomp.2012.11.008

7. Friedlingstein, P.; Houghton, R. A.; Marland, G.; Hackler, J.; Boden, T. A.; Conway, T. J.; Canadell, J. G.; Raupach, M. R.; Ciais, P.; and Le Quéré, C., "Update on CO_2 Emissions," *Nature Geoscience*, V. 3, No. 12, Dec. 2010, pp. 811-812. doi: 10.1038/ngeo1022

8. Korpa, A.; Kowald, T.; and Trettin, R., "Phase Development in Normal and Ultra High Performance Cementitious Systems by Quantitative X-Ray Analysis and Thermoanalytical Methods," *Cement and Concrete Research*, V. 39, No. 2, Feb. 2009, pp. 69-76. doi: 10.1016/j.cemconres.2008.11.003

9. Huang, W.; Kazemi-Kamyab, H.; Sun, W.; and Scrivener, K., "Effect of Replacement of Silica Fume with Calcined Clay on the Hydration and Microstructural Development of Eco-UHPFRC," *Materials & Design*, V. 121, May 2017, pp. 36-46. doi: 10.1016/j.matdes.2017.02.052

10. Bahmani, H., and Mostofinejad, D., "Microstructure of Ultra-High-Performance Concrete (UHPC)—A Review Study," *Journal of Building Engineering*, V. 50, June 2022, Article No. 104118. doi: 10.1016/j.jobe.2022.104118

11. Randl, N.; Steiner, T.; Ofner, S.; Baumgartner, E.; and Mészöly, T., "Development of UHPC Mixtures from an Ecological Point of View," *Construction and Building Materials*, V. 67, Part C, Sept. 2014, pp. 373-378. doi: 10.1016/j.conbuildmat.2013.12.102

12. Ganesh, P., and Murthy, A. R., "Tensile Behaviour and Durability Aspects of Sustainable Ultra-High Performance Concrete Incorporated with GGBS as Cementitious Material," *Construction and Building Materials*, V. 197, Feb. 2019, pp. 667-680. doi: 10.1016/j.conbuildmat.2018.11.240

13. Bahmani, H.; Mostofinejad, D.; and Dadvar, S. A., "Fiber Type and Curing Environment Effects on the Mechanical Performance of UHPFRC Containing Zeolite," *Iranian Journal of Science and Technology, Transactions of Civil Engineering*, V. 46, No. 6, Dec. 2022, pp. 4151-4167. doi: 10.1007/s40996-022-00911-z

14. Kim, H.; Koh, T.; and Pyo, S., "Enhancing Flowability and Sustainability of Ultra High Performance Concrete Incorporating High Replacement Levels of Industrial Slags," *Construction and Building Materials*, V. 123, Oct. 2016, pp. 153-160. doi: 10.1016/j.conbuildmat.2016.06.134

15. Abdulkareem, O. M.; Ben Fraj, A.; Bouasker, M.; and Khelidj, A., "Mixture Design and Early Age Investigations of More Sustainable UHPC," *Construction and Building Materials*, V. 163, Feb. 2018, pp. 235-246. doi: 10.1016/j.conbuildmat.2017.12.107

16. Huang, W.; Kazemi-Kamyab, H.; Sun, W.; and Scrivener, K., "Effect of Cement Substitution by Limestone on the Hydration and Microstructural Development of Ultra-High Performance Concrete (UHPC)," *Cement and Concrete Composites*, V. 77, Mar. 2017, pp. 86-101. doi: 10.1016/j.cemconcomp.2016.12.009

17. Yu, R.; Tang, P.; Spiesz, P.; and Brouwers, H. J. H., "A Study of Multiple Effects of Nano-Silica and Hybrid Fibres on the Properties of Ultra-High Performance Fibre Reinforced Concrete (UHPFRC) Incorporating Waste Bottom Ash (WBA)," *Construction and Building Materials*, V. 60, June 2014, pp. 98-110. doi: 10.1016/j.conbuildmat.2014.02.059

18. Pourbaba, M.; Asefi, E.; Sadaghian, H.; and Mirmiran, A., "Effect of Age on the Compressive Strength of Ultra-High-Performance Fiber-Reinforced Concrete," *Construction and Building Materials*, V. 175, June 2018, pp. 402-410. doi: 10.1016/j.conbuildmat.2018.04.203

19. Ghasemzadeh Mosavinejad, S. H.; Langaroudi, M. A. M.; Barandoust, J.; and Ghanizadeh, A., "Electrical and Microstructural Analysis of UHPC Containing Short PVA Fibers," *Construction and Building Materials*, V. 235, Feb. 2020, Article No. 117448. doi: 10.1016/j.conbuildmat.2019.117448

20. Mostofinejad, D.; Moosaie, I.; Eftekhar, M.; and Hesami, E., "Ultra-High Performance Hybrid Polyvinyl Alcohol-Polypropylene Fiber-Reinforced Cementitious Composites with Augmented Toughness and Strain-Hardening Behavior," *Iranian Journal of Science and Technology, Transactions of Civil Engineering*, V. 46, No. 3, June 2022, pp. 1997-2009. doi: 10.1007/s40996-021-00815-4

21. Yoo, D.-Y.; Shin, H.-O.; Yang, J.-M.; and Yoon, Y.-S., "Material and Bond Properties of Ultra High Performance Fiber Reinforced Concrete with Micro Steel Fibers," *Composites Part B: Engineering*, V. 58, Mar. 2014, pp. 122-133. doi: 10.1016/j.compositesb.2013.10.081

22. Meng, W., and Khayat, K. H., "Effect of Hybrid Fibers on Fresh Properties, Mechanical Properties, and Autogenous Shrinkage of Cost-Effective UHPC," *Journal of Materials in Civil Engineering*, ASCE, V. 30, No. 4, Apr. 2018, p. 04018030. doi: 10.1061/(ASCE)MT.1943-5533.0002212

23. Chun, B., and Yoo, D.-Y., "Hybrid Effect of Macro and Micro Steel Fibers on the Pullout and Tensile Behaviors of Ultra-High-Performance Concrete," *Composites Part B: Engineering*, V. 162, Apr. 2019, pp. 344-360. doi: 10.1016/j.compositesb.2018.11.026

24. Bahmani, H.; Mostofinejad, D.; and Dadvar, S. A., "Effects of Synthetic Fibers and Different Levels of Partial Cement Replacement on Mechanical Properties of UHPFRC," *Journal of Materials in Civil Engineering*, ASCE, V. 32, No. 12, Dec. 2020, p. 04020361. doi: 10.1061/(ASCE)MT.1943-5533.0003462

25. Bahmani, H.; Mostofinejad, D.; and Dadvar, S. A., "Mechanical Properties of Ultra-High-Performance Fiber-Reinforced Concrete Containing Synthetic and Mineral Fibers," *ACI Materials Journal*, V. 117, No. 3, May 2020, pp. 155-168. doi: 10.14359/51724596

26. ASTM C150/C150M-16, "Standard Specification for Portland Cement," ASTM International, West Conshohocken, PA, 2016, 10 pp.

27. ASTM C1240-15, "Standard Specification for Silica Fume Used in Cementitious Mixtures," ASTM International, West Conshohocken, PA, 2015, 7 pp.

28. ASTM C494/C494M-05a, "Standard Specification for Chemical Admixtures for Concrete," ASTM International, West Conshohocken, PA, 2005, 10 pp.

29. Mostofinejad, D.; Nikoo, M. R.; and Hosseini, S. A., "Determination of Optimized Mix Design and Curing Conditions of Reactive Powder Concrete (RPC)," *Construction and Building Materials*, V. 123, Oct. 2016, pp. 754-767. doi: 10.1016/j.conbuildmat.2016.07.082

30. ASTM C1437-13, "Standard Test Method for Flow of Hydraulic Cement Mortar," ASTM International, West Conshohocken, PA, 2013, 2 pp.

31. Habel, K., and Gauvreau, P., "Response of Ultra-High Performance Fiber Reinforced Concrete (UHPFRC) to Impact and Static Loading," *Cement and Concrete Composites*, V. 30, No. 10, Nov. 2008, pp. 938-946. doi: 10.1016/j.cemconcomp.2008.09.001

32. Máca, P.; Sovják, R.; and Konvalinka, P., "Mix Design of UHPFRC and Its Response to Projectile Impact," *International Journal of Impact Engineering*, V. 63, Jan. 2014, pp. 158-163. doi: 10.1016/j.ijimpeng.2013.08.003

33. ASTM C109/C109M-11b, "Standard Test Method for Compressive Strength of Hydraulic Cement Mortars (Using 2-in. or [50-mm] Cube Specimens)," ASTM International, West Consohocken, PA, 2011, 10 pp.

34. ASTM C78/C78M-10, "Standard Test Method for Flexural Strength of Concrete (Using Simple Beam with Third-Point Loading)," ASTM International, West Conshohocken, PA, 2010, 4 pp.

35. Yu, R.; Spiesz, P.; and Brouwers, H. J. H., "Development of an Eco-Friendly Ultra-High Performance Concrete (UHPC) with Efficient Cement and Mineral Admixtures Uses," *Cement and Concrete Composites*, V. 55, Jan. 2015, pp. 383-394. doi: 10.1016/j.cemconcomp.2014.09.024

36. Gupta, S., "Effect of Content and Fineness of Slag as High Volume Cement Replacement on Strength and Durability of Ultra-High Performance Mortar," *Journal of Building Materials and Structures*, V. 3, No. 2, 2016, pp. 43-54. doi: 10.34118/jbms.v3i2.23

37. Chidiac, S. E., and Panesar, D. K., "Evolution of Mechanical Properties of Concrete Containing Ground Granulated Blast Furnace Slag and Effects on the Scaling Resistance Test at 28 Days," *Cement and Concrete Composites*, V. 30, No. 2, Feb. 2008, pp. 63-71. doi: 10.1016/j.cemconcomp.2007.09.003

38. Kang, S.-H.; Jeong, Y.; Tan, K. H.; and Moon, J., "High-Volume Use of Limestone in Ultra-High Performance Fiber-Reinforced Concrete for Reducing Cement Content and Autogenous Shrinkage," *Construction and Building Materials*, V. 213, July 2019, pp. 292-305. doi: 10.1016/j.conbuildmat.2019.04.091

39. Liu, S.-H., and Yan, P., "Influence of Limestone Powder on Filling Effect of Cement Paste and Pore Structure of Sand Grout," *Journal of the Chinese Ceramic Society*, V. 36, No. 1, 2008, pp. 69-72, 77.

40. Haddad, R. H.; Al-Saleh, R. J.; and Al-Akhras, N. M., "Effect of Elevated Temperature on Bond between Steel Reinforcement and Fiber Reinforced Concrete," *Fire Safety Journal*, V. 43, No. 5, July 2008, pp. 334-343. doi: 10.1016/j.firesaf.2007.11.002

41. Abdallah, S.; Fan, M.; and Cashell, K. A., "Bond-Slip Behaviour of Steel Fibres in Concrete after Exposure to Elevated Temperatures," *Construction and Building Materials*, V. 140, June 2017, pp. 542-551. doi: 10.1016/j.conbuildmat.2017.02.148

42. ASTM C1018-97, "Standard Test Method for Flexural Toughness and First-Crack Strength of Fiber-Reinforced Concrete (Using Beam With Third-Point Loading) (Withdrawn 2006)," ASTM International, West Conshohocken, PA, 1997, 7 pp.

43. Kuruşcu, A. O., and Girgin, Z. C., "Efficiency of Structural Materials in Sustainable Design," *Journal of Civil Engineering and Architecture*, V. 8, No. 10, Oct. 2014, pp. 1260-1265.

44. Long, G.; Gao, Y.; and Xie, Y., "Designing More Sustainable and Greener Self-Compacting Concrete," *Construction and Building Materials*, V. 84, June 2015, pp. 301-306. doi: 10.1016/j.conbuildmat.2015.02.072

45. Turner, L. K., and Collins, F. G., "Carbon Dioxide Equivalent (CO_2-e) Emissions: A Comparison between Geopolymer and OPC Cement Concrete," *Construction and Building Materials*, V. 43, June 2013, pp. 125-130. doi: 10.1016/j.conbuildmat.2013.01.023

We're Building the Future

Mission: We make strategic investments in ideas, research, and people to create the future of the concrete industry

Through its councils and programs, the ACI Foundation helps to keep the concrete industry at the forefront of advances in material composition, design, and construction. Our focus:

Our Concrete Innovation Council identifies technologies and innovation that are aligned with ACI and industry strategies and helps facilitate their use when appropriate

Our Concrete Research Council advances the knowledge and sustainable aspects of concrete materials, construction, and structures by soliciting, selecting, financing, and publishing research

Our Scholarship Council supports our future concrete innovators and leaders by administering fellowships and scholarships to help bridge the financial gap for students

Our Veterans Rebate for ACI Certification program helps honorably discharged veterans and increases skills in the industry's workforce. ACICertification.org/veteranrebate

aci Foundation
Building the Future

ACI MATERIALS JOURNAL TECHNICAL PAPER

Title No. 120-M51

Carbon Dioxide Conversion and Use as Admixture for Calcined Clay Blended Pastes

by Run-Sheng Lin and Xiao-Yong Wang

This study proposed using carbon dioxide (CO_2) as an indirect admixture for calcined clay blended pastes. By injecting CO_2 gas into limewater, solid nano-$CaCO_3$ particles were synthesized and used to partially replace the binder at ratios of 2, 4, and 6%. Various tests and analyses were performed on the calcined clay blended pastes. After adding nano-$CaCO_3$, the strength, ultrasonic pulse velocity, hydration heat, and electrical resistivity were improved; monocarboaluminate and hemicarboaluminate were formed; and CO_2 emissions were lowered. The electrical resistivity was improved more significantly than the strength. The reduction ratio in CO_2 emissions was higher than the replacement ratio of nano-$CaCO_3$. In summary, based on the transformation of gaseous CO_2 to solid nano-$CaCO_3$ particles, the proposed technique shows a similar concept to limestone calcined clay cement (LC3) concrete and can overcome the limitations of carbonation curing.

Keywords: calcined clay blended concrete; carbon dioxide (CO_2) conversion; durability; nano-$CaCO_3$; strength.

INTRODUCTION

Concrete is the most commonly used construction material in modern society. Cement is an essential binder material in concrete production and has been used to build various infrastructures. However, a large quantity of carbon dioxide (CO_2) is emitted during the production of cement, which accounts for approximately 7% of the world's total CO_2 emissions.[1] Reducing the carbon emissions of the cement industry while meeting engineering demands is an urgent problem to be solved.

Supplementary cementitious materials (SCMs) such as fly ash, slag cement, silica fume, and various natural pozzolans (clay, shale, and diatomaceous earth)[2] have been used to partially replace cement in concretes. SCM-blended concrete involves less CO_2 emissions than ordinary portland cement (OPC)-based concrete. At the same time, the secondary reaction of SCMs can also generate calcium silicate hydrates (C-S-H), improving the long-term strength of the concrete.[3] Many studies have estimated the CO_2 emissions of SCM-blended concrete. Vargas and Halog[4] constructed a system dynamics model and found that upgrading processes of fly ash could reduce CO_2 emissions. Wang et al.[5] performed a life cycle analysis of fly ash composite concrete and proposed that fly ash could alleviate the social burden and save long-term costs. Berndt[6] showed that mixing 65% slag in cement could reduce CO_2 emissions by approximately 44% without compromising performance or strength. Similarly, Shin et al.[7] showed that using 56% slag could improve the performance and release less CO_2. Cancio Díaz et al.[8] proposed that limestone calcined clay cement (LC3) could provide a low-carbon solution by reducing greenhouse gas emissions by 20% and cost by 15%. Pillai et al.[9] reported that LC3 had fewer CO_2 emissions than OPC concrete per year during the service life.

In addition, as a new carbon capture technology, carbonation curing has been employed to manufacture concrete products. Concrete can absorb CO_2 to achieve high strength through carbonation curing.[10] There are many studies on the carbonation curing of concrete mixed with SCMs. Monkman and Shao[11] reported the benefits of carbonation curing of slag-blended concretes, such as reduced shrinkage and improved strength and resistance to deicing salt. Qin et al.[12] demonstrated that fly ash presented a more significant promoting effect than slag on carbonation curing. Zhang et al.[13] found that fly ash concrete had higher early strength, comparable late strength, and fewer CO_2 emissions after carbonation curing. Mo et al.[14] proposed that carbonation curing increased the strength of fly ash-MgO-cement blends. Wang et al.[15] reported that carbonation could be used for surface treatment to densify the surface microstructure and reduce the permeability of concrete.

Despite the aforementioned advantages of carbonation curing, some limitations are also evident:

1. Due to the requirements of curing equipment, carbonation curing is more suitable for precast concrete than cast-in-place concrete.[13]

2. The effects of carbonation curing on chloride resistance are complicated. On the positive side, carbonation curing reduces the number of pores and lowers the diffusion coefficient. On the negative side, carbonation-cured concretes cannot bind with chloride ions effectively, reducing the service life of concrete in marine environments.[16]

3. Carbonation curing of large specimens is very challenging. In the process of carbonation curing, by increasing the CO_2 concentration or pressure, CO_2 enters the interior of the concrete through the surface. When the specimen size is relatively small, CO_2 can reach the central zone of the specimen. However, it is difficult for the CO_2 to reach the central zone of large specimens.[17] In the current research on carbonation curing, small specimens (100 x 200 mm cylinders) are often used. However, in actual engineering, the sizes of reinforced concrete are much larger than these cylinders.

4. Carbonation curing consumes calcium hydroxide (CH) in the concrete and reduces the quantity of CH available for the reactions of SCMs. In other words, carbonation curing

ACI Materials Journal, V. 120, No. 5, September 2023.

MS No. M-2022-011.R4, doi: 10.14359/51738889, received January 18, 2023, and reviewed under Institute publication policies.

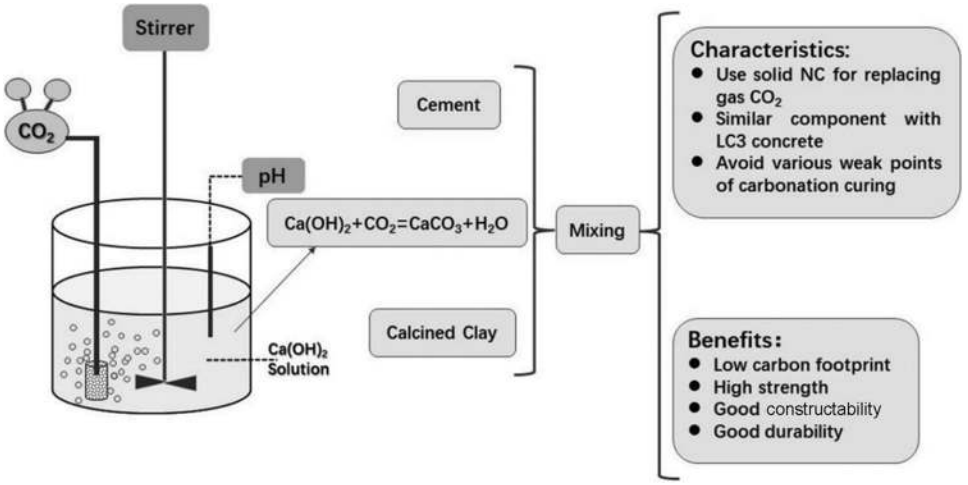

Fig. 1—Technical road map of proposed method.

Table 1—Chemical compositions of cement and calcined clay

Samples	SiO_2	Al_2O_3	Fe_2O_3	CaO	MgO	Na_2O	SO_3	R_2O	LOI
Cement	20.44	3.16	3.19	64.06	2.44	0.45	2.51	3.29	0.46
Calcined clay	63.72	25.58	6.17	0.16	0.67	—	—	2.87	0.83

Note: LOI is loss on ignition.

may lower the reaction degree of SCMs and impair the concrete performance.[18] Zhang et al.[13] found that compared with standard curing methods, carbonation curing reduced the reactivity of fly ash.

To overcome these limitations of carbonation curing, this paper proposes a technology that uses CO_2 as an indirect admixture to produce concrete. The technical road map is shown in Fig. 1.

First, by injecting CO_2 gas into limewater, a suspension of nano-$CaCO_3$ (NC) can be prepared. This reaction realizes the transformation of gaseous CO_2 into solid nano-$CaCO_3$ particles.

Second, the synthesized nano-$CaCO_3$ particles were used to replace a part of the binder material of concrete, and samples with different substitution ratios were prepared.

Through a series of tests and analyses such as strength, heat of hydration, electrical resistivity, ultrasonic pulse velocity (UPV), X-ray powder diffraction (XRD), thermogravimetric analysis (TGA), scanning electron microscopy (SEM), and CO_2 emissions, the benefits of the proposed method were clarified in terms of mechanical properties, durability, and environmental performance.

The flow of this paper is as follows: the first section provides the literature review, research significance, and an outline of the study. In the second section, the experimental details including raw materials, mixture preparation, and methods are presented, and the third section provides the experimental results. Finally, the last section presents the conclusions.

RESEARCH SIGNIFICANCE

A feasible way to reduce CO_2 emissions without compromising concrete performance is urgently required. The CO_2 conversion method proposed in this paper converts gaseous CO_2 into solid nano-calcium carbonate, which is used as a mineral admixture for concrete. The aim of CO_2 elimination is not fully reached because the proposed method only reduces the CO_2 emissions for unit strength, and the ability of CO_2 elimination is weaker compared with the carbonation curing method. Through experimental studies at the macro and micro levels, this paper clarifies the mechanism of the carbon conversion method to improve the performance of concrete mixed with calcined clay. The advantages of the proposed method in reducing carbon emissions and its engineering significance are analyzed in detail.

EXPERIMENTAL DETAILS

Raw materials

Type I OPC obtained from the domestic market of Korea was calcined at 800°C with a kaolinite content of 27.0%.[18] It is worth mentioning that the family of "clay materials" is large. For different countries, the clay materials may be different. This study only used clay materials from Korea. The median particle size (Dv(50)) values of OPC and calcined clay were determined as 18.2 and 12.4 µm, respectively, through particle-size distribution analysis. The chemical compositions of OPC and calcined clay are shown in Table 1. Commercial calcium hydroxide (purity 98%), deionized water, and commercially available CO_2 gas with a 100% concentration were used in this study.

Synthesis of nano-calcium carbonate

Before preparing the cement samples, nano-calcium carbonate was synthesized. According to the formulation in Table 2, $Ca(OH)_2$ was dissolved in deionized water. Then CO_2 was introduced to the limewater at a flow rate of 20 L/min with continuous mechanical stirring at 300 rpm/min. The reaction ended when the pH of the solution was between 7 and 8. The reaction is shown as follows

$$Ca(OH)_2 + CO_2 \rightarrow CaCO_3 + H_2O \quad (1)$$

where CO_2 on the left is a gaseous reactant; and $CaCO_3$ on the right is a solid product. Through this reaction, the conversion of CO_2 from gas to solid is achieved. According to the life cycle inventory of CO_2 in Korea,[19] the embodied CO_2 of 1 g $Ca(OH)_2$ is 0.53 g. Based on Eq. (1), to produce 1 g of nano-$CaCO_3$, 0.44 g of CO_2 is consumed. In other words, the CO_2 emissions to produce nano-$CaCO_3$ are $(74 \times 0.53 - 44)/100 = -0.0478$ g/g, where 74 and 44 are the molar weights of $Ca(OH)_2$ and CO_2, respectively. That is, the CO_2 uptake to produce 1 g of nano-$CaCO_3$ is negative—that is, –0.0478 g.

Mixture preparation

The mixture proportions of the binder pastes are listed in Table 3. The water in the specimens consists of the mixing water and the water generated in Eq. (1). For various specimens, the contents of total water are the same—that is, 50%. The mixing water shown in Table 3 is the initial volume of water for the synthesis. For most LC3 specimens, the sum of calcined clay and limestone powder is approximately 45 to 50%, and the mass ratio of calcined clay to limestone powder is approximately 2:1. The replacement rate of calcined clay in LC3 is approximately 30%. Hence, in this study, the replacement rate of calcined clay was set at 30%. For all specimens, the mass ratio of cement to calcined clay is kept constant at 7:3, which is widely used in current engineering practices.[20] Specimens NC0, NC2, NC4, and NC6 were prepared by adding various quantities of calcium carbonate—that is, 0, 2, 4, and 6% of the binder content (cement and calcined clay)—into the pastes, respectively. A water-binder ratio (*w*/*b*) of 0.5 was used for all the mixtures. This *w*/*b* is widely used in engineering practices and can represent the concrete widely used in construction sites. It is worth noting that because the reaction of CO_2 and $Ca(OH)_2$ will produce additional water, the total amount of water is the sum of the mixing water and the water produced by the reaction of CO_2 and $Ca(OH)_2$.

Table 2—Amounts of reactant $Ca(OH)_2$ and produced water and calcium carbonate, wt.% of binder

Sample	$Ca(OH)_2$	Water (produced by $Ca(OH)_2 + CO_2$ reaction)	$CaCO_3$
NC0	0	0	0
NC2	1.48	0.36	2
NC4	2.96	0.72	4
NC6	4.44	1.08	6

Methods

The paste specimens were mixed by a mechanical stirrer and placed into molds. The molds were removed after the first day, and the specimens were wrapped with a film for sealed curing in a curing chamber (20°C) for 1, 3, 7, and 28 days.

Compressive strength, ultrasonic pulse velocity, and isothermal calorimetry—The compressive strength of the specimens were tested according to ASTM C349. The compressive strength specimens are cubes (40 x 40 x 160 mm). The UPV tester used a portable nondestructive digital indicator tester in accordance with ASTM C597. The UPV specimens are prisms (40 x 40 x 160 mm). For the UPV test, the measurements were performed along the long axis, and for the compressive test, the measurements were performed on the lateral side to avoid the influence of the placement of the specimens.

The hydration heats of the samples were tested at 20°C on an isothermal calorimeter following the experimental method in the literature.[21]

Microstructure characterization—To characterize the microstructure, hydration was terminated for all samples using a solvent exchange method before characterization.[21] TGA of the pastes was performed using a simultaneous differential scanning calorimetry (DSC)/differential thermal analysis (DTA)/TGA system. The heating rate was 10°C/min, and the temperature range was 20 to 1050°C. XRD analysis was carried out with a diffractometer with Cu Kα radiation (λ = 1.5406 Å). The attenuated total reflectance-Fourier-transform infrared spectroscopy (ATR-FTIR) measurements were conducted using a spectrometer with a resolution of 0.4 cm^{-1}. Microscopic morphologies of the sheet samples were observed using ultra-high-resolution SEM (UHR-SEM). Prior to the observations, the surfaces of the samples were coated with platinum on an ion sputter system. High-resolution transmission electron microscopy (TEM) images were obtained using a TEM system equipped with a Schottky-type field-emission source. The accelerating voltage was 200 kV, and the point resolution and lattice resolution were 0.19 and 0.10 nm, respectively.

Electrical resistivity—The electrical resistivities of the samples were measured according to RILEM TC154-EMC on a resistivity meter.[21]

RESULTS

Structure and morphology of nano-$CaCO_3$

As shown in the SEM images (Fig. 2(a) and (b)), the nano-calcium carbonate particles had a regular diamond shape with a uniform size of approximately 100 to 300 nm, which was significantly smaller than the cement particles

Table 3—Mixture proportions of blended cement pastes

Sample	OPC, wt.% of binder	Calcined clay, wt.% of binder	Synthesized nano-$CaCO_3$, wt.% of binder	Mixing water, wt.%	Water (produced by $Ca(OH)_2 + CO_2$ reaction), wt.%	Total water, wt.%	*w*/*b*
NC0	70	30	0	50	0	50	0.50
NC2	68.6	29.4	2	49.64	0.36	50	0.50
NC4	67.2	28.8	4	49.28	0.72	50	0.50
NC6	65.8	28.2	6	48.92	1.08	50	0.50

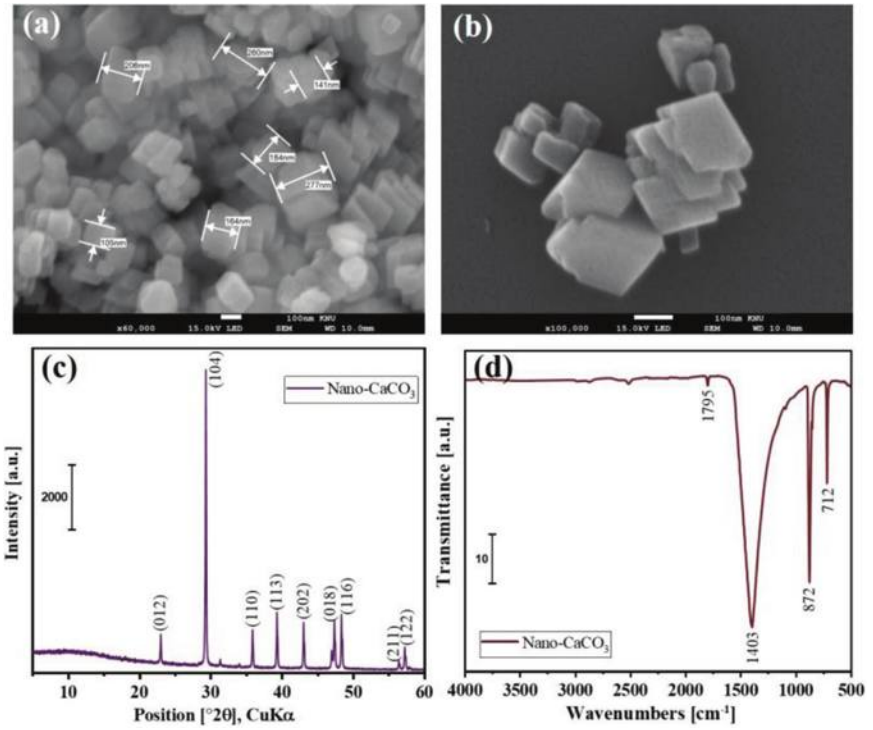

Fig. 2—Characterization of synthesized nano-$CaCO_3$: (a) and (b) SEM images; (c) XRD pattern; and (d) ATR-FTIR spectrum.

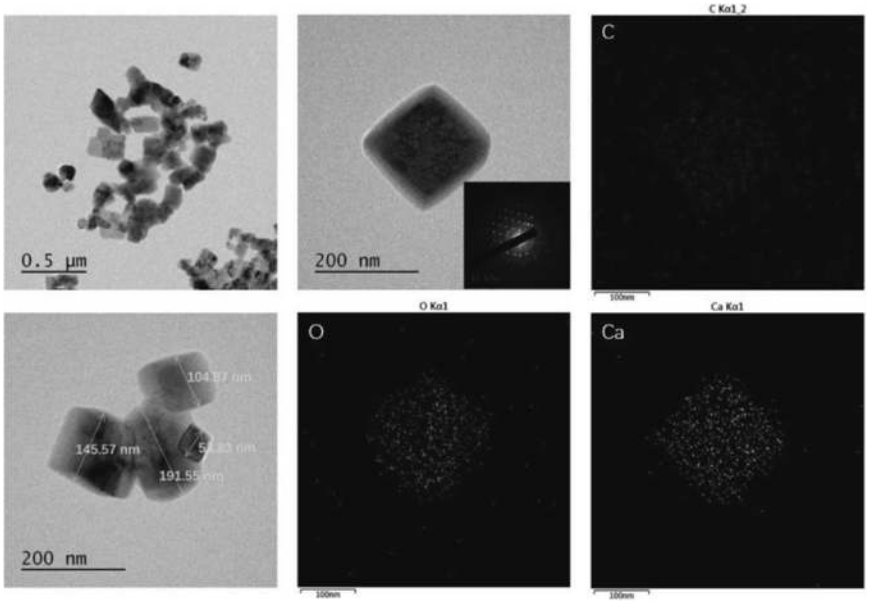

Fig. 3—TEM images of synthesized nano-$CaCO_3$.

(10 to 20 μm). In other words, the produced calcite was apprixmately 100 times finer than the cement. To emphasize the size effect of the produced calcite, the current research uses the terminology of nano-calcium carbonate. Figure 2(c) shows the XRD pattern of nano-calcium carbonate. Diffraction peaks at 2θ = 23.0, 29.4, 36.0, 39.4, 43.1, 47.5, and 48.5 degrees were assigned to the $CaCO_3$ (012), (104), (110), (113), (202), (018), and (116) planes, respectively, confirming the rhombohedrons calcite structure (Joint Committee on Powder Diffraction Standards [JCPDS] card number).[21] Figure 2(d) shows the FTIR spectrum of nano-calcium carbonate, wherein the asymmetric stretching vibration of CO_3^{2-} occurs at 1419 cm^{-1}, and the peaks at 873 and 712 cm^{-1} indicate the out-of-plane bending vibration of CO_3^{2-}. In the TEM image (Fig. 3), the synthesized nano-calcium carbonate had a rhombus shape. In addition, the selected area electron diffraction (SAED) pattern of calcium carbonate showed sharp diffraction spots, indicating a high crystal orientation.

Strength

Concrete is a composite material consisting of the paste, aggregate, and interfacial transition zone phases. The concrete strength is highly dependent on the properties of the paste phase. Figure 4(a) shows the compressive strength after curing for 1, 3, 7, and 28 days. Figure 4(b) shows the

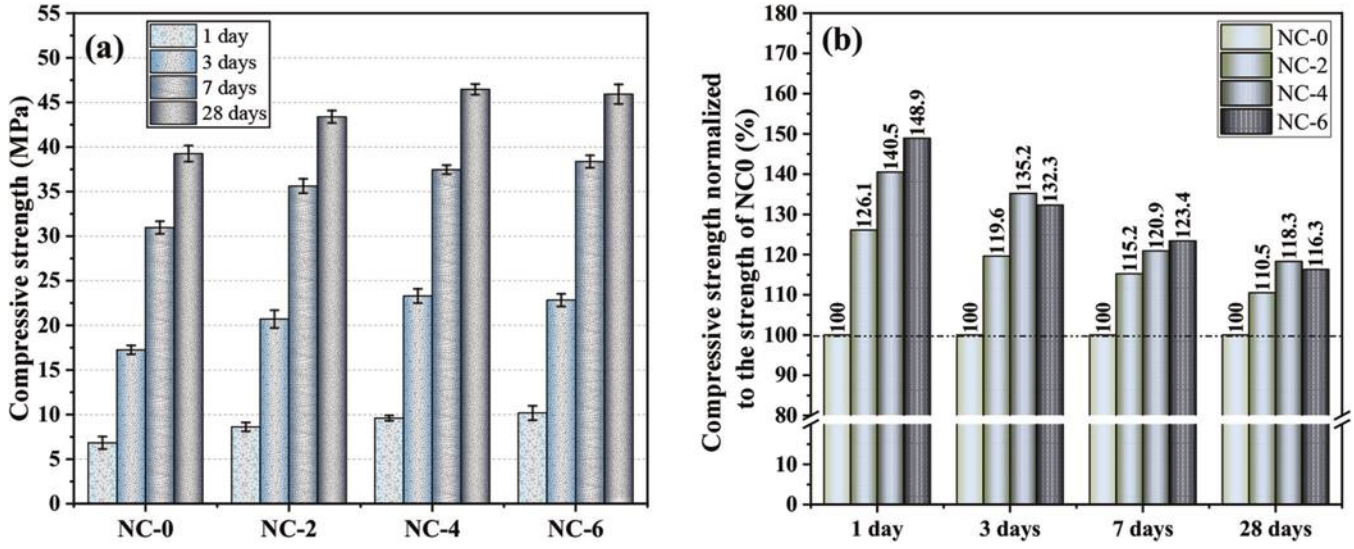

Fig. 4—(a) Compressive strength; and (b) compressive strength normalized to strength of NC0.

compressive strength normalized to the strength of NC0. The calculation equation of the relative strength (R) is shown as follows

$$R = fc_1/fc_2 \quad (2)$$

where fc_1 is the strength of the specimen containing nano-calcite (NC2, NC4, and NC6); and fc_2 is the strength of the control specimen (NC0).

From the first to seventh days, the strength increased rapidly. From the seventh to 28th days, the increase in strength was relatively slow. This was similar to the development trend due to hydration reported by Lin et al.[21] In addition, on the first day, as the nano-$CaCO_3$ content increased, the relative strength of the specimens increased. Compared with NC0, the 1-day strength of NC2, NC4, and NC6 increased by 126.1, 140.5, and 148.9%, respectively. On day 28, as the nano-$CaCO_3$ content increased, the relative strength of the specimens first increased and then slightly decreased. The 28-day strength of NC2, NC4, and NC6 increased by 110.5, 118.3, and 116.3% compared with specimen NC0, respectively.

The effects of nano-$CaCO_3$ on hydration include three aspects:

1. Nano-$CaCO_3$ can provide additional nucleation sites for hydration products, accelerating the hydration of cement and improving the strength.[22]

2. Nano-$CaCO_3$ can react with the aluminate in cement and calcined clay to form hemicarboaluminate (Hc) and monocarboaluminate (Mc), filling the pores and increasing the strength.[22]

3. When nano-$CaCO_3$ is used to partially replace the cementitious material, the content of cement and calcined clay is reduced due to a dilution effect, which can also reduce the strength.[22]

It was reported that the properties of the limestone powders depended on three effects—that is, the nucleation effect, chemical reaction, and dilution effect. In this study, nano-calcite was prepared with a diameter between 100 and 300 nm. Similar to the previous work,[18] the three effects also existed for the produced nano-calcite. In short, after adding nano-$CaCO_3$, the three factors acted synergically to impact the paste strength. Moreover, the influence of these factors also changed with curing ages.

By comparing the relative strengths on day 1 and day 28, nano-$CaCO_3$ had a more significant effect on the early strength due to its nucleation effect. The nano-$CaCO_3$ particles could provide additional precipitation sites for the hydrates and accelerate the hydration of cement.[18] On the other hand, on day 28, the strength of NC6 was slightly lower than that of NC4, mainly due to a decreased amount of cement (dilution effect of nano-$CaCO_3$).

Hydration heat

Figure 5 shows the effect of nano-$CaCO_3$ on the release rate of hydration heat. As the content of nano-$CaCO_3$ increased, the dormant period of the hydration decreased (Fig. 5(a)) because the nucleation effect of nano-$CaCO_3$ accelerated the hydration of cement. In addition, as the content of nano-$CaCO_3$ increased, the reaction peak of C_3S and the redissolution peak of C_3A increased significantly. The sulfate ions were adsorbed in the C-S-H precipitates due to the ongoing hydration of C_3S.[23] The reaction rate of C_3S increased as the filler effect accelerated the precipitation rate of C-S-H, increasing the adsorbed amount of sulfate. The depletion of gypsum occurred at an early stage and consequently shifted the aluminate peak to the left.[24] Moreover, after 20 hours, with the increase in nano-$CaCO_3$ content, the release rate of hydration heat did not increase significantly for all specimens. This suggested that the acceleration effect of nano-$CaCO_3$ mainly occurred in the early stage (before 1 day) of hydration, and its impact on the later hydration (after 1 day) was limited.

Moreover, Hu et al.[25] showed that the initial and final setting times determined by isothermal calorimetry were consistent with the setting times determined according to ASTM C403/C403M. The initial setting time corresponds to the time when the rapid temperature rise starts after the induction period of the exothermic curve, and the final setting time corresponds to the time when the cement exotherm reaches

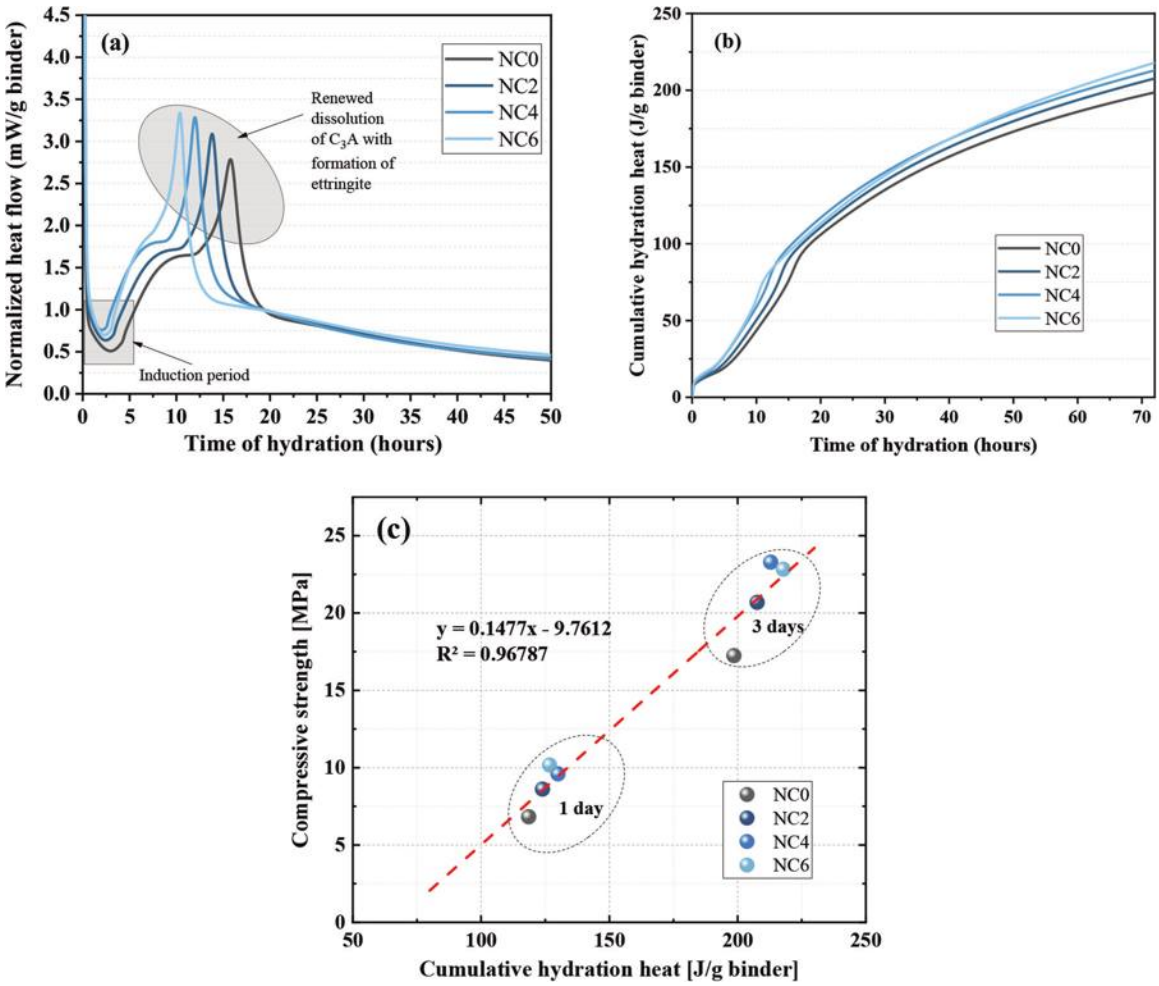

Fig. 5—Hydration heat of specimens: (a) heat rate; (b) cumulative hydration heat; and (c) strength versus cumulative hydration heat.

the maximum rate in the acceleration period. As shown in Fig. 5(a), adding nano-$CaCO_3$ could significantly shorten the initial setting time (NC0 is 3.23 hours; NC2 is 2.95 hours; NC4 is 2.63 hours; NC6 is 2.31 hours) and final setting time (NC0 is 6.63 hours; NC2 is 5.24 hours; NC4 is 4.10 hours; NC6 is 3.94 hours).

Figure 5(b) shows the effect of nano-$CaCO_3$ on the accumulated hydration heat. As the nano-$CaCO_3$ content increased, more hydration heat was generated. It suggested that in the early stage of hydration (3 days), the promotion effect of nano-$CaCO_3$ was more significant than the dilution effect.

Figure 5(c) shows the relationship between the compressive strength and cumulative hydration heat on days 1 and 3. The compressive strength and hydration heat showed a linear relationship for different specimens. The regression equation was strength = 0.1477 × heat – 9.7612, and the coefficient of determination was 0.968. In addition, according to the regression, the hydration heat was 67.71 J/g when the compressive strength was 0. When cement came into contact with water, the mixture began to generate hydration heat.[22] However, no compressive strength was observed until the hydration heat exceeded a threshold (67.71 J/g in this study).

On the SEM and TEM images (Fig. 6), a large number of needle-like ettringite (AFt) crystals and flocculent calcium aluminate silicate hydrate (C-A-S-H) were formed during the first day of hydration. In addition, the growth of C-A-S-H on the surface of nano-calcium carbonate could be observed in the TEM images.

XRD

Figure 7(a) shows the XRD results of the specimens on day 1. First, the formation of AFt crystals was found. Compared with NC0, the specimens containing nano-calcium carbonate generated more AFt, consistent with the dissolution peak of C_3A observed in the hydration heat experiment. In addition, the monocarboaluminate (Mc) peak was observed. Mc is the reaction product of calcium carbonate and the aluminate phase in the binder (cement and calcined clay). As the content of nano-$CaCO_3$ increased from 4 to 6%, the Mc peak was more obvious, suggesting more Mc was formed. Moreover, for the NC0 specimen, calcium carbonate peaks were also observed because the cement contained 2 to 3% calcium carbonate.[26] However, compared to NC6, the Mc content in NC0 was lower. The calcium carbonate particles in NC0 were from the cement and had a micron size. In contrast, the calcium carbonate particles in NC6 were in the nano-size range and mainly from the synthesis. Nanoscale calcium carbonate was more reactive than the micron-sized one.

Figure 7(b) shows the XRD results of the curing specimens on day 28. For NC2, NC4, and NC6, the transformation

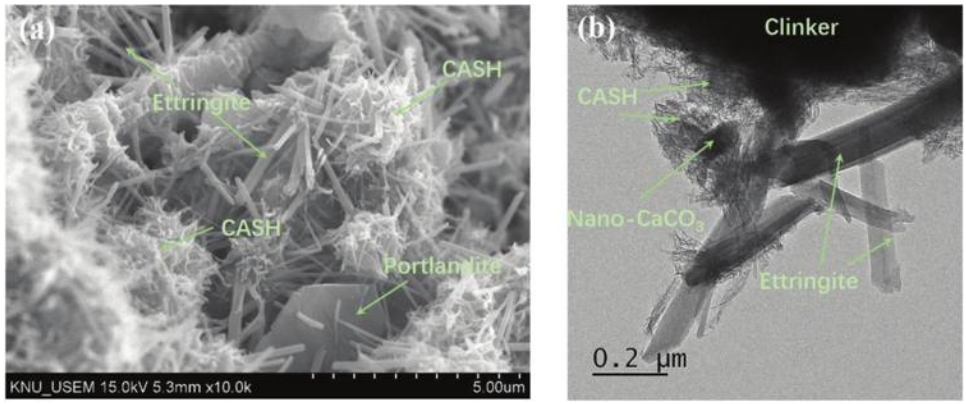

Fig. 6—(a) SEM; and (b) TEM images of NC6 on day 1.

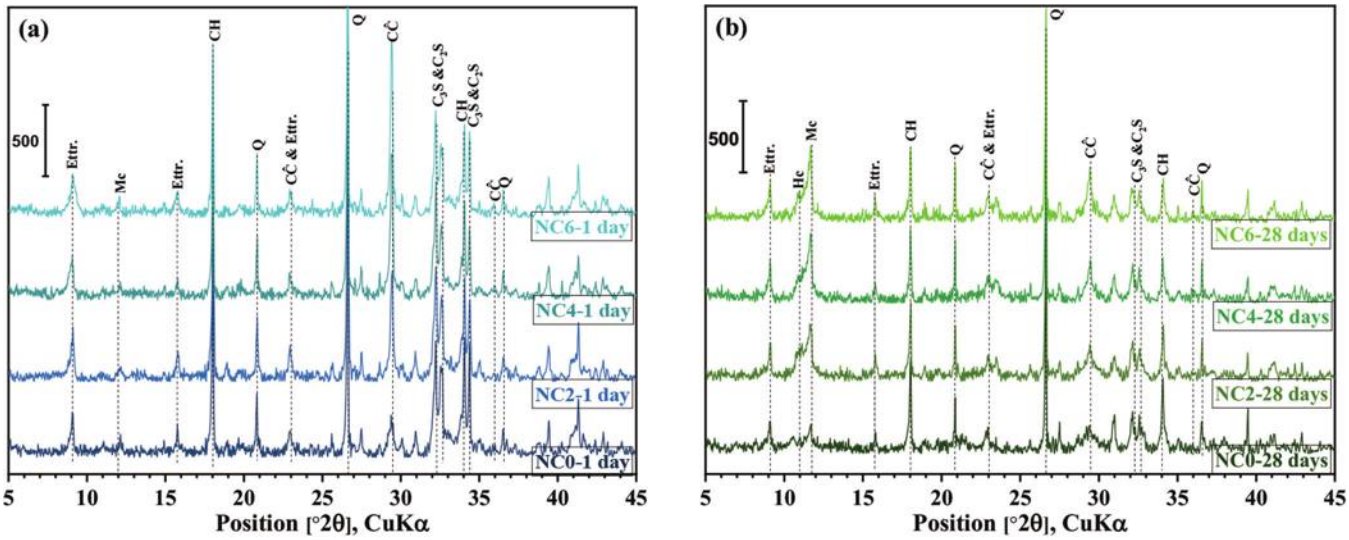

Fig. 7—XRD patterns of specimens at: (a) 1 day; and (b) 28 days. (Note: Ettr. is ettringite; CH is portlandite; Q is quartz; CĈ is calcium carbonate; Hc is hemicarboaluminate; and Mc is monocarboaluminate.)

of hemicarboaluminate (Hc) to monocarboaluminate (Mc) was dependent on the content of aluminate in the binder.[21,22] Increasing the content of aluminate was favorable to produce Hc but unfavorable to produce Mc.[21] For NC0, Mc did not convert to Hc. In addition, from day 1 to day 28, the AFt content decreased in NC0 due to the conversion of AFt to monosulfate (AFm). For NC2, NC4, and NC6, the AFt contents did not decrease significantly,[27] because nano-$CaCO_3$ stabilized the AFt and prevented the conversion of AFt to AFm.[21] Finally, as the nano-$CaCO_3$ content increased, the CH content decreased because the chemical reaction of nano-$CaCO_3$ consumed CH.[21] In addition, the dilution effect of nano-$CaCO_3$ could also reduce the content of CH.

FTIR

Figure 8 shows the FTIR spectra of the 1-day (Fig. 8(a)) and 28-day specimens (Fig. 8(b)) in the scan range of 500 to 2000 cm^{-1}. First, the absorption band at 1416 cm^{-1} corresponded to the CO_3^{2-} asymmetric stretching vibration in calcium carbonate.[18] The out-of-plane bending vibration of CO_3^{2-} produced a sharp absorption peak at 872 cm^{-1}.[18] After 28 days of hydration, the absorption bands of NC2, NC4, and NC6 at 872 and 1416 cm^{-1} were weaker than those on day 1. This might be due to the reaction between calcined clay and limestone to form carboaluminate hydrate,[21] consistent with the XRD analysis (Fig. 7(b)). In addition, after 28 days of curing (Fig. 8(b)), the absorption peak at 1368 cm^{-1} was attributed to the CO_3^{2-} asymmetric stretching vibration of Hc and Mc.[18] With the increased content of nano-$CaCO_3$, the absorption peak was more prominent. Second, the absorption bands of asymmetric stretching and bending vibrations of the Si-O bond were located at approximately 950 to 960 cm^{-1} and 630 to 680 cm^{-1}, respectively.[18] From day 1 to day 28, the strength of the absorption band corresponding to the Si-O bond increased, indicating an increased C-S-H content with the progress of hydration. The absorption peak on day 28 shifted to higher wavenumbers compared to that on day 1, indicating that the Si-O bonds gradually transformed to Si-O-Si bonds. In other words, from day 1 to day 28, the degree of polymerization of C-S-H increased.[18] Moreover, the stretching vibration absorption band of the Si-O bond at approximately 798 cm^{-1} reflected the quartz phase in calcined clay.[18] Third, the absorption band at approximately 1105 cm^{-1} corresponded to the SO_4^{2-} asymmetric stretching vibration of gypsum.[18] After 28 days of hydration, the strength of the absorption band of SO_4^{2-} was weakened due to the consumption of gypsum, consistent with the results of the previous studies.[21]

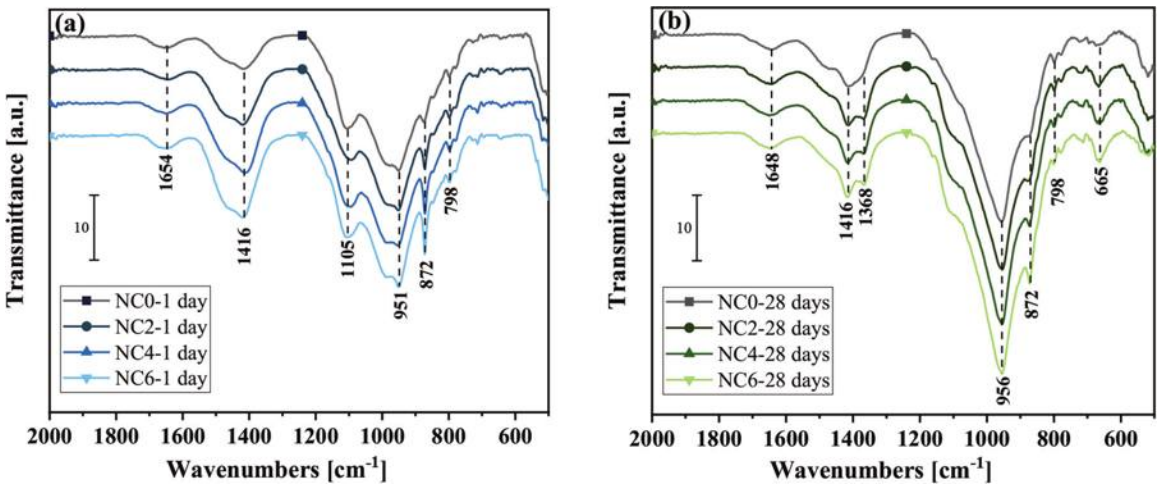

Fig. 8—FTIR spectra of all pastes on: (a) day 1; and (b) day 28.

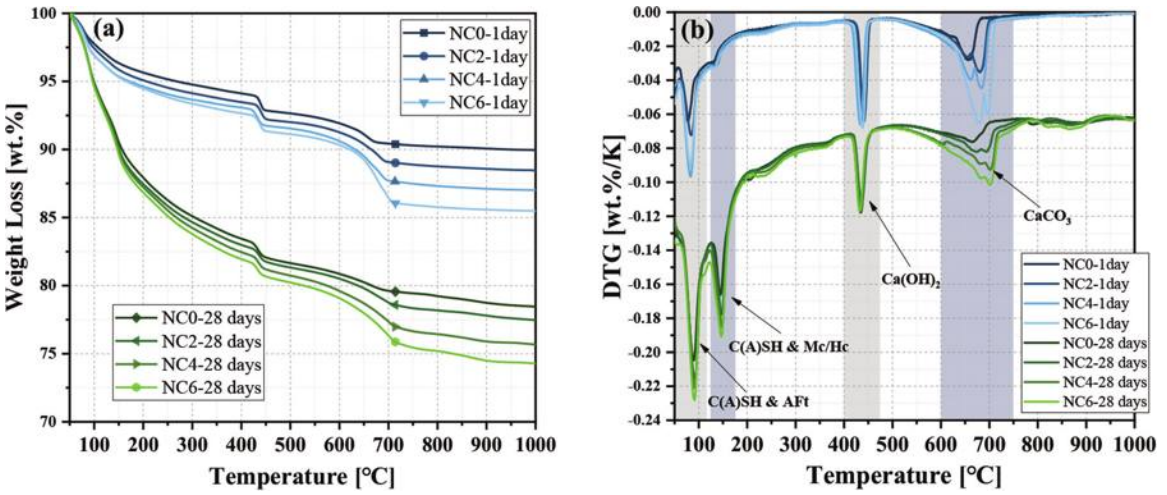

Fig. 9—(a) TGA curves of specimens; and (b) DTG curves of specimens.

TGA

Figure 9 shows the results of the TGA (Fig. 9(a)) and differential thermogravimetric (DTG) (Fig. 9(b)) tests. As the temperature increased, the hydrated products started to decompose.[28] The notable mass loss below 700°C was mainly attributed to dehydration of C-S-H gel. Thermal decomposition of pure calcite (Fig. 9) occurred between 720 and 820°C with a peak at 790 to 800°C. In this study, the calcite was not pure, and these temperatures increased slightly. The weak peaks were observed between 770 and 900°C in Fig. 9(b) on day 28.

The contents of combined water were calculated between 40 and 550°C as follows[29]

$$\text{Combined water} = \frac{(w40 - w550)}{w550} \quad (3)$$

where $w40$ and $w550$ are the weights of specimens at the temperatures of 40 and 550°C, respectively.

The contents of calcium hydroxide were calculated between 400 and 500°C as follows[29]

$$CH = (w400 - w500)/w550 \times 74/18 \quad (4)$$

where $w400$ and $w500$ are the weights of specimens at the temperatures of 400 and 500°C, respectively.

The calculation results of combined water and calcium hydroxide are shown in Table 4. First, from day 1 to day 28, the content of chemically bound water increased due to continuous hydration. As the content of nano-$CaCO_3$ increased, its chemical reaction produced Hc and Mc containing more chemically bound water. In addition, more chemically bound water implied more hydration products, consistent with the results of the strength and hydration heat.

Second, as the content of nano-$CaCO_3$ increased, the content of CH also increased on day 1 because the nucleation effect of nano-$CaCO_3$ accelerated the hydration of cement and produced more CH. On day 28, the CH contents in NC2, NC4, and NC6 were lower than that in NC0. The dilution effect of nano-$CaCO_3$ reduced the amount of cement and produced less CH. Moreover, the chemical reaction of nano-$CaCO_3$ could consume CH, further reducing the content of CH.

Third, from day 1 to day 28, the content of CH decreased for all specimens because CH was consumed in the chemical reaction of calcined clay. This was similar to the experimental studies on fly ash and metakaolin.[21,30]

Figure 10 shows the relationship between the compressive strength and chemically bound water. For all specimens

at different ages (day 1 and day 28), a linear relationship was found with a coefficient of determination of 0.997. This finding was consistent with Lin et al.'s research.[18] In other words, the chemically bound water was a good indicator of compressive strength. When the chemically bound water was 0, compressive strength was not observed. In this study, the intercept of the regression line on the x-axis was 5.483 in the plot of strength and chemically bound water.

Table 4—Amounts of combined water and calcium hydroxide

Specimen	Combined water content, wt.% binder mass	$Ca(OH)_2$ content, wt.% binder mass
NC0-1 day	8.25	4.19
NC2-1 day	8.99	4.43
NC4-1 day	9.64	4.69
NC6-1 day	10.01	4.72
NC0-28 days	22.98	4.15
NC2-28 days	23.48	3.64
NC4-28 days	24.55	3.92
NC6-28 days	25.35	3.75

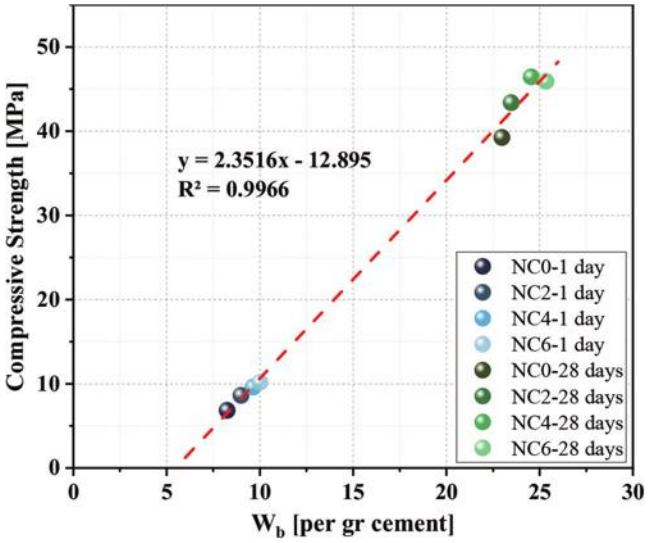

Fig. 10—Strength versus combined water of specimens.

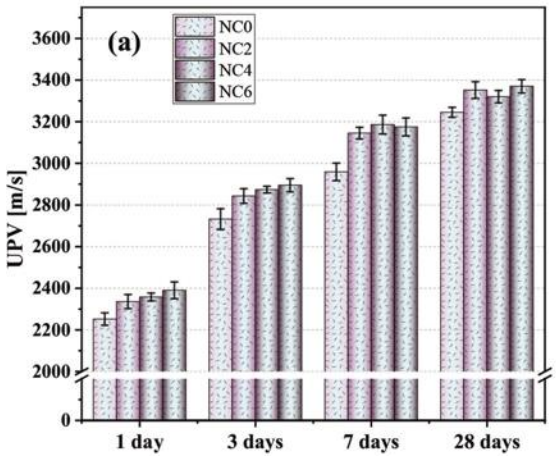

Fig. 11—(a) UPV development; and (b) strength versus UPV.

When the chemically bound water was greater than 5.483, compressive strength was detected. This was consistent with the concept of the final setting, wherein the final setting time corresponds to the start time of the development of compressive strength.

UPV

As shown in Fig. 11(a), the development trend of UPV was the same as that of compressive strength. In the early period (days 1 to 7), the UPV increased rapidly. From days 7 to 28, the increases in UPV were not obvious. In addition, between days 1 and 3, the UPV increased as the nano-$CaCO_3$ contents increased because the nano-$CaCO_3$ promoted hydration and produced more hydration products.

Figure 11(b) shows the relationship between the compressive strength and the UPV. For different specimens, the compressive strength and UPV showed an exponential relationship at different ages with a coefficient of determination of 0.974. The compressive strength depended on the number of hydration products, and the UPV mainly relied on the amount of solid matter in the system. In other words, the development trend of the compressive strength was consistent with that of the UPV, and the UPV could be used as a nondestructive test method to measure the development of strength.

Electrical resistivity

Resistivity tests and other porosity analyses are relevant for all cement-based materials, such as paste, mortar, and concrete. Table 5 shows the electrical resistivity measurement results. At each age, as the nano-$CaCO_3$ content increased, the electrical resistivity increased. On day 28, the electrical resistivity of the specimen was 2.85 times that of the specimen without nano-$CaCO_3$ (NC0 specimen) (88.7/31.1 = 2.85). The electrical resistivity is mainly related to the pore-size distribution and water content of the paste. Nano-$CaCO_3$ particles could react with aluminate to refine the pores, significantly enhancing the electrical resistivity and further increasing the durability of the paste structures.

In addition, from day 1 to day 28, the resistivity of NC0 increased 19.44 times (31.1/1.6 = 19.44), and the resistivity of NC6 increased 35.48 times (88.7/2.5 = 35.48), confirming

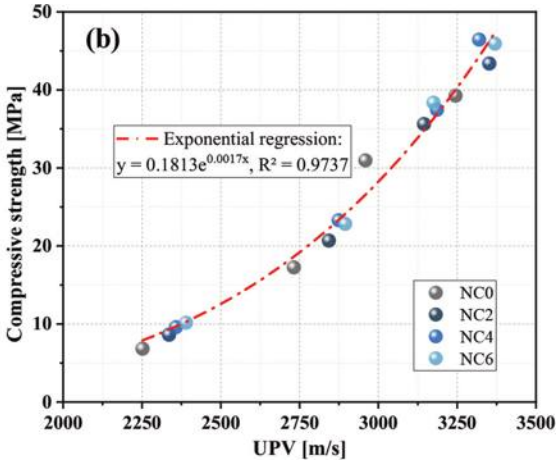

Table 5—Electrical resistivity on different days, kΩ·cm

Curing ages	NC0	NC2	NC4	NC6
1 day	1.6	1.7	2.2	2.5
3 days	3.2	4.4	6.4	7.8
7 days	8.9	26.2	35.6	40.1
28 days	31.1	71.6	84.2	88.7

that the chemical reaction of nano-$CaCO_3$ prompted the pore structure refinement.

After adding nano-$CaCO_3$, the UPV, compressive strength, and electrical resistivity all increased. Moreover, the increase in electrical resistivity was more significant than the increases in UPV and strength. This was mainly because the UPV and strength were more related to the content of solid hydration products, while the electrical resistivity also depended on the paste pore-size distribution and water content.

CO_2 emissions analysis

For paste specimens, the volumetric sum of their components, such as cement, calcined clay, nano-$CaCO_3$, and water, should be 1 m^3 as follows

$$\sum_{i=1}^{4}\frac{m_i}{\rho_i} = 1 \quad (5)$$

where m_i and ρ_i are the mass and density of component i, respectively. Using Eq. (2) and the mixture ratio of the specimens, the mass of the paste component was calculated. The densities of cement, calcined clay, nano-$CaCO_3$, and water are 3150, 2600, 2700, and 1000 kg/m^3, respectively.[18]

The CO_2 emissions of 1 m^3 of paste can be determined as follows

$$CO_{2T} = \sum_{i=1}^{4} m_i CO_{2i} \quad (6)$$

where CO_{2T} and CO_{2i} are the CO_2 emissions of the paste and the components of the paste, respectively. The CO_2 emissions of 1 kg of cement, calcined clay, nano-$CaCO_3$, and water are 0.86, 0.27, –0.0478, and 0.0003 kg, respectively.[3]

The normalized CO_2 emissions value is the ratio of the CO_2 emissions to the strength of the paste. The normalized CO_2 emissions indicate the amount of CO_2 emissions for 1 MPa of strength and can be determined as follows

$$NCO_2 = \frac{CO_{2T}}{f_c} \quad (7)$$

where NCO_2 and f_c are the normalized CO_2 emissions and the strength, respectively. Based on Eq. (2), (3), and (4), the normalized CO_2 emissions for specimens NC0, NC2, NC4, and NC6 were determined as 20.74, 18.37, 16.79, and 16.58 kg/m^3/MPa, respectively. The calculation results showed that as the nano-$CaCO_3$ replacement rate increased, the CO_2 emissions per unit strength decreased. Compared with NC0, the CO_2 emissions were reduced by 20% in NC6. The reduction rate in CO_2 emissions was significantly higher than the replacement rate of nano-$CaCO_3$. This was because nano-$CaCO_3$ improved the late strength and had a negative CO_2 emissions value. Therefore, nano-$CaCO_3$ can improve cement paste's strength to meet engineering applications' needs and reduce CO_2 emissions to enhance sustainability.

CONCLUSIONS

This study proposed a novel method to use carbon dioxide (CO_2) as an indirect admixture of calcined clay blended pastes. By injecting CO_2 gas into limewater, CO_2 gas was transformed into a nano-$CaCO_3$ solid. Moreover, this nano-calcium carbonate was used to partially replace the binder at the ratios of 2, 4, and 6%. Various tests and analyses were performed on the strength, hydration heat, microstructure, electrical resistivity, and CO_2 emissions. The results are summarized as follows:

1. During the first day of curing, as the nano-$CaCO_3$ content increased, the relative strength of the specimens increased. The relative strengths of NC2, NC4, and NC6 were 126.1, 140.5, and 148.9% higher than that of NC0, respectively. On day 28, nano-$CaCO_3$ blended specimens presented higher strength than the control specimens.

2. The hydration heat tests showed that as the content of nano-$CaCO_3$ increased, the dormant period of the hydration decreased. The reaction peak of C_3S and the redissolution peak of C_3A increased significantly, suggesting that more cumulative hydration heat was generated.

3. X-ray diffraction (XRD) analysis showed that monocarboaluminate (Mc) was formed on day 1 as the reaction product of the calcium carbonate and aluminate phases in the binder (cement and calcined clay). As the content of nano-$CaCO_3$ increased from 4 to 6%, the Mc peak was more obvious. On day 28, part of the Mc was transformed into hemicarbonaluminate (Hc).

4. Fourier-transform infrared spectroscopy (FTIR) analysis showed that after 28 days of hydration, the absorption bands of NC2, NC4, and NC6 at 872 cm^{-1} and 1416 cm^{-1} were weaker than those on day 1. This might be due to the reaction between calcined clay and limestone to form carboaluminate hydrate.

5. Thermogravimetric analysis (TGA) showed that the content of chemically bound water increased with nano-$CaCO_3$ because the chemical reaction of nano-$CaCO_3$ produced Hc and Mc. On day 1, as the content of nano-$CaCO_3$ increased, the CH content increased, while on day 28, as the content of nano-$CaCO_3$ increased, the CH content decreased.

6. For different specimens, the compressive strength and ultrasonic pulse velocity (UPV) showed an exponential relationship at different curing ages, and the coefficient of determination was 0.974. The UPV could be used as a nondestructive testing method to measure strength development.

7. At each age, the electrical resistivity increased as the nano-$CaCO_3$ content increased. After curing for 28 days, the electrical resistivity of NC6 was 2.85 times higher than that of NC0 as the chemical reaction of nano-$CaCO_3$ prompted pore refinement.

8. Compared with NC0, the CO_2 emissions from NC6 were reduced by 20%. The reduction rate of CO_2 emissions

was significantly higher than the replacement rate of nano-$CaCO_3$. This was because nano-$CaCO_3$ increased the late strength and also had a negative CO_2 emissions value.

In summary, by transforming gaseous CO_2 to solid nano-calcium carbonate and using nano-calcium carbonate in concrete, this study proposed a concept similar to limestone calcined clay cement (LC3) concrete. The reported method showed various benefits, such as improved early and late strengths, high electrical resistivity, and good construction adaptability for both precast and cast-in-place concretes. However, only paste specimens were used in this study. For mortar and concrete specimens, more work is required to consider the effect of fine and coarse aggregates.

AUTHOR BIOS

Run-Sheng Lin *is a Lecturer at Kunming University of Science and Technology, Xishan, Kunming, China. He received his PhD from Kangwon National University, Chuncheon, Korea. His research interests include carbon neutrality in cement-based materials, the durability of building materials, and the microstructure and hydration of cement composite materials.*

Xiao-Yong Wang *is a Professor in the Department of Architectural Engineering and Department of Integrated Energy and Infra System at Kangwon National University. He received his PhD from Hanyang University, Seoul, South Korea. His research interests include concrete materials and composite structures.*

ACKNOWLEDGMENTS

This work has supported by the National Research Foundation of Korea (NRF) grant funded by the Korea government (MSIT) (No. RS-2023-00208720). This work was also supported by Yunnan Fundamental Research Projects (Grant No. 202201BE070001-010).

REFERENCES

1. Yang, K.-H.; Jung, Y.-B.; Cho, M.-S.; and Tae, S.-H., "Effect of Supplementary Cementitious Materials on Reduction of CO_2 Emissions from Concrete," *Journal of Cleaner Production*, V. 103, 2015, pp. 774-783. doi: 10.1016/j.jclepro.2014.03.018

2. Lothenbach, B.; Scrivener, K.; and Hooton, R. D., "Supplementary Cementitious Materials," *Cement and Concrete Research*, V. 41, No. 12, 2011, pp. 1244-1256. doi: 10.1016/j.cemconres.2010.12.001

3. Miller, S. A.; John, V. M.; Pacca, S. A.; and Horvath, A., "Carbon Dioxide Reduction Potential in the Global Cement Industry by 2050," *Cement and Concrete Research*, V. 114, 2018, pp. 115-124. doi: 10.1016/j.cemconres.2017.08.026

4. Vargas, J., and Halog, A., "Effective Carbon Emission Reductions from Using Upgraded fly Ash in the Cement Industry," *Journal of Cleaner Production*, V. 103, 2015, pp. 948-959. doi: 10.1016/j.jclepro.2015.04.136

5. Wang, J.; Wang, Y.; Sun, Y.; Tingley, D. D.; and Zhang, Y., "Life Cycle Sustainability Assessment of Fly Ash Concrete Structures," *Renewable & Sustainable Energy Reviews*, V. 80, 2017, pp. 1162-1174. doi: 10.1016/j.rser.2017.05.232

6. Berndt, M. L., "Influence of Concrete Mix Design on CO_2 Emissions for Large Wind Turbine Foundations," *Renewable Energy*, V. 83, 2015, pp. 608-614. doi: 10.1016/j.renene.2015.05.002

7. Shin, H.-O.; Yang, J.-M.; Yoon, Y.-S.; and Mitchell, D., "Mix Design of Concrete for Prestressed Concrete Sleepers Using Blast Furnace Slag and Steel Fibers," *Cement and Concrete Composites*, V. 74, 2016, pp. 39-53. doi: 10.1016/j.cemconcomp.2016.08.007

8. Cancio Díaz, Y.; Sánchez Berriel, S.; Heierli, U.; Favier, A. R.; Sánchez Machado, I. R.; Scrivener, K. L.; Martirena Hernández, J. F.; and Habert, G., "Limestone Calcined Clay Cement as a Low-Carbon Solution to Meet Expanding Cement Demand in Emerging Economies," *Development Engineering*, V. 2, 2017, pp. 82-91. doi: 10.1016/j.deveng.2017.06.001

9. Pillai, R. G.; Gettu, R.; Santhanam, M.; Rengaraju, S.; Dhandapani, Y.; Rathnarajan, S.; and Basavaraj, A. S., "Service Life and Life Cycle Assessment of Reinforced Concrete Systems with Limestone Calcined Clay Cement (LC3)," *Cement and Concrete Research*, V. 118, 2019, pp. 111-119. doi: 10.1016/j.cemconres.2018.11.019

10. Liu, Z., and Meng, W., "Fundamental Understanding of Carbonation Curing and Durability of Carbonation-Cured Cement-Based Composites: A Review," *Journal of CO2 Utilization*, V. 44, 2021, p. 101428.

11. Monkman, S., and Shao, Y., "Carbonation Curing of Slag-Cement Concrete for Binding CO_2 and Improving Performance," *Journal of Materials in Civil Engineering*, ASCE, V. 22, No. 4, 2010, pp. 296-304. doi: 10.1061/(ASCE)MT.1943-5533.0000018

12. Qin, L.; Gao, X.; and Chen, T., "Influence of Mineral Admixtures on Carbonation Curing of Cement Paste," *Construction and Building Materials*, V. 212, 2019, pp. 653-662. doi: 10.1016/j.conbuildmat.2019.04.033

13. Zhang, D.; Cai, X.; and Shao, Y., "Carbonation Curing of Precast Fly Ash Concrete," *Journal of Materials in Civil Engineering*, ASCE, V. 28, No. 11, 2016, p. 04016127. doi: 10.1061/(ASCE)MT.1943-5533.0001649

14. Mo, L.; Zhang, F.; and Deng, M., "Effects of Carbonation Treatment on the Properties of Hydrated Fly Ash-MgO-Portland Cement Blends," *Construction and Building Materials*, V. 96, 2015, pp. 147-154. doi: 10.1016/j.conbuildmat.2015.07.193

15. Wang, Y.; Lu, B.; Hu, X.; Liu, J.; Zhang, Z.; Pan, X.; Xie, Z.; Chang, J.; Zhang, T.; Nehdi, M. L.; and Shi, C., "Effect of CO_2 Surface Treatment on Penetrability and Microstructure of Cement-Fly Ash–Slag Ternary Concrete," *Cement and Concrete Composites*, V. 123, 2021, p. 104194. doi: 10.1016/j.cemconcomp.2021.104194

16. Shen, X.-H.; Jiang, W.-Q.; Hou, D.; Hu, Z.; Yang, J.; and Liu, Q.-F., "Numerical Study of Carbonation and its Effect on Chloride Binding in Concrete," *Cement and Concrete Composites*, V. 104, 2019, p. 103402. doi: 10.1016/j.cemconcomp.2019.103402

17. Chen, T., and Gao, X., "Use of Carbonation Curing to Improve Mechanical Strength and Durability of Pervious Concrete," *ACS Sustainable Chemistry & Engineering*, V. 8, No. 9, 2020, pp. 3872-3884. doi: 10.1021/acssuschemeng.9b07348

18. Lin, R.-S.; Wang, X.-Y.; and Yi, H., "Effects of Cement Types and Addition of Quartz and Limestone on the Normal and Carbonation Curing of Cement Paste," *Construction and Building Materials*, V. 305, 2021, p. 124799. doi: 10.1016/j.conbuildmat.2021.124799

19. E.D. Office, "LCI DB," Korea Environmental Industry & Technology Institute, Seoul, Korea, 2022.

20. Scrivener, K.; Martirena, F.; Bishnoi, S.; and Maity, S., "Calcined Clay Limestone Cements (LC3)," *Cement and Concrete Research*, V. 114, 2018, pp. 49-56. doi: 10.1016/j.cemconres.2017.08.017

21. Lin, R.-S.; Lee, H.-S.; Han, Y.; and Wang, X.-Y., "Experimental Studies on Hydration–Strength–Durability of Limestone-Cement-Calcined Hwangtoh Clay Ternary Composite," *Construction and Building Materials*, V. 269, 2021, p. 121290. doi: 10.1016/j.conbuildmat.2020.121290

22. Bentz, D. P.; Ardani, A.; Barrett, T.; Jones, S. Z.; Lootens, D.; Peltz, M. A.; Sato, T.; Stutzman, P. E.; Tanesi, J.; and Weiss, W. J., "Multi-Scale Investigation of the Performance of Limestone in Concrete," *Construction and Building Materials*, V. 75, 2015, pp. 1-10. doi: 10.1016/j.conbuildmat.2014.10.042

23. Lin, R.-S.; Park, K.-B.; Wang, X.-Y.; and Zhang, G.-Y., "Increasing the Early Strength of High-Volume Hwangtoh–Cement Systems Using Bassanite," *Journal of Building Engineering*, V. 30, 2020, p. 101317. doi: 10.1016/j.jobe.2020.101317

24. Zunino, F., and Scrivener, K., "The Influence of the Filler Effect on the Sulfate Requirement of Blended Cements," *Cement and Concrete Research*, V. 126, 2019, p. 105918. doi: 10.1016/j.cemconres.2019.105918

25. Hu, J.; Ge, Z.; and Wang, K., "Influence of Cement Fineness and Water-to-Cement Ratio on Mortar Early-Age Heat of Hydration and Set Times," *Construction and Building Materials*, V. 50, 2014, pp. 657-663. doi: 10.1016/j.conbuildmat.2013.10.011

26. Jeong, Y.; Kang, S.-H.; Kim, M. O.; and Moon, J., "Acceleration of Cement Hydration from Supplementary Cementitious Materials: Performance Comparison between Silica Fume and Hydrophobic Silica," *Cement and Concrete Composites*, V. 112, 2020, p. 103688. doi: 10.1016/j.cemconcomp.2020.103688

27. Zunino, F., and Scrivener, K., "The Reaction between Metakaolin and Limestone and its Effect in Porosity Refinement and Mechanical Properties," *Cement and Concrete Research*, V. 140, 2021, p. 106307. doi: 10.1016/j.cemconres.2020.106307

28. Lin, R.-S.; Han, Y.; and Wang, X.-Y., "Macro–Meso–Micro Experimental Studies of Calcined Clay Limestone Cement (LC3) Paste Subjected to Elevated Temperature," *Cement and Concrete Composites*, V. 116, 2021, p. 103871. doi: 10.1016/j.cemconcomp.2020.103871

29. De Weerdt, K.; Haha, M. B.; Le Saout, G.; Kjellsen, K. O.; Justnes, H.; and Lothenbach, B., "Hydration Mechanisms of Ternary Portland Cements Containing Limestone Powder and Fly Ash," *Cement and Concrete Research*, V. 41, No. 3, 2011, pp. 279-291. doi: 10.1016/j.cemconres.2010.11.014

30. Papadakis, V. G., "Effect of Supplementary Cementing Materials on Concrete Resistance against Carbonation and Chloride Ingress," *Cement and Concrete Research*, V. 30, No. 2, 2000, pp. 291-299. doi: 10.1016/S0008-8846(99)00249-5

CALL FOR ACTION

ACI Invites You To...

Share your expertise

Do you have EXPERTISE in any of these areas?

- BIM
- Chimneys
- Circular Concrete Structures Prestressed by Wrapping with Wire and Strand
- Circular Concrete Structures Prestressed with Circumferential Tendons
- Concrete Properties
- Demolition
- Deterioration of Concrete in Hydraulic Structures
- Electronic Data Exchange
- Insulating Concrete Forms, Design, and Construction
- Nuclear Reactors, Concrete Components
- Pedestal Water Towers
- Pipe, Cast-in-Place
- Strengthening of Concrete Members
- Sustainability

Then become a REVIEWER for the *ACI Structural Journal* or the *ACI Materials Journal*.

Become a Reviewer for the ACI Journals

How to become a Reviewer:

1. Go to: **http://mc.manuscriptcentral.com/aci**;
2. Click on "Create Account" in the upper right-hand corner; and
3. Enter your E-mail/Name, Address, User ID and Password, and Area(s) of Expertise.

Update your Manuscript Central user account information

Did you know that the database for MANUSCRIPT CENTRAL, our manuscript submission program, is separate from the ACI membership database?

How to update your user account:

1. Go to **http://mc.manuscriptcentral.com/aci**;
2. Log in with your current User ID & Password; and
3. Update your E-mail/Name, Address, User ID and Password, and Area(s) of Expertise.

QUESTIONS?

E-mail any questions to Journals.Manuscripts@concrete.org.

American Concrete Institute

Always advancing

ACI MATERIALS JOURNAL TECHNICAL PAPER

Title No. 120-M52

Practical Measurement of Pore Solution Resistivity in Fresh Mixtures

by Joseph H. Biever, Krishna Siva Teja Chopperla, O. Burkan Isgor, and W. Jason Weiss

This study compares techniques to extract pore solution from fresh mixtures to measure the resistivity of the extracted solution. The centrifuge approach for extracting pore solution and conductivity probe for determining pore solution resistivity are practical and have the potential to be used in the field. Pore solution extraction can be done between 30 and 90 minutes after mixing without a statistically significant difference in the measured resistivity. A practical method is proposed to determine the pore solution resistivity from the diluted cement paste samples when the extracted pore solution quantity is not adequate for accurate measurements with a conductivity probe.

Keywords: conductivity; fresh paste; fresh properties; pore solution; pore solution extraction; resistivity.

INTRODUCTION

Over 30 billion tons of concrete is produced worldwide each year.[1] In the United States alone, approximately 75,000 concrete trucks are used to deliver approximately 371 million yd^3 (284 million m^3) of concrete.[2] The concrete mixtures that are delivered to the construction site are often checked for their slump, unit weight, air content, and temperature as part of a contractual process defined by ASTM C94/C94M-16.[3] These measures are often used to demonstrate that the mixture delivered is consistent with the concrete that was purchased.

Compressive strength and water-cementitious materials ratio (*w*/*cm*) are often used as surrogate indicators of a concrete's durability to various exposure states (corrosion, freezing-and-thawing damage, and salt attack), as demonstrated by ACI 318-19.[4] While this is common in construction, the use of strength and *w*/*cm* may be insufficient in many cases to address durability issues. This is becoming increasingly challenging, as mixture proportions are being altered to address concerns for economy, sustainability, and new material constituents. Simply stated, rules of thumb that have worked in the past that relate compressive strength and durability may need to be reconsidered with more complicated mixture designs and materials. As such, the quality control/quality assurance (QC/QA) protocols that have been used in the past may need to be updated to account for concrete durability and performance. The American Association of State Highway and Transportation Officials (AASHTO) took a major step in this direction by developing a model specification, AASHTO R 101-22.[5] Both AASHTO R 101 and the CEB-FIP Model Code[6] identify transport processes of concrete as critical factors.

It should be noted that the compressive strength of hardened concrete is measured after a specific period of time, such as 7 or 28 days, which is not helpful to make quick decisions on the acceptance of delivered concrete at the site. Measuring factors such as *w*/*cm* on site as part of QC/QA protocols could be useful. Approaches such as the AASHTO T 318-15 microwave oven-drying method[7] and the Phoenix method[8] use evaporation techniques to determine the *w*/*cm* of fresh concretes. Additionally, fresh concrete resistivity properties to determine *w*/*cm* have been explored by several authors.[9-12] However, no standard methods exist to determine *w*/*cm* of fresh concrete using electrical properties.

Another durability indicator that is typically measured on hardened concrete and has become a part of specifications such as AASHTO R 101 (previously noted as PP 84),[5,13] "Standard Practice for Developing Performance Engineered Concrete Pavement Mixtures," is the formation factor (*F*) of concrete. For example, AASHTO R 101 specifies the minimum formation factor for mature concrete for limiting transport in concrete such as chloride ingress. Similar approaches were proposed for the use of concrete resistivity; however, one limitation of using resistivity is it can be heavily influenced by the chemistry of the fluid in the pores.[14] To overcome this, *F* can be used to eliminate the pore solution effects as it can be determined from the bulk resistivity (ρ_b) and pore solution resistivity (ρ_o)[15-20] as shown in Eq. (1).

$$F = \frac{\rho_b}{\rho_o} \cong \frac{1}{\beta \cdot \varphi} \quad (1)$$

where *F* is inversely related to the product of porosity, φ, and pore connectivity factor, β. While the formation factor has been used to assess transport properties such as water absorption,[21] permeability,[22] or chloride ingress[23,24] of hardened concrete, it may also have value for fresh concrete.

Recently, several studies[25,26] have focused on determining the formation factor of fresh cement pastes and its properties. Sallehi et al.[26] calculated the formation factor of a variety of cementitious pastes containing ordinary portland cement (OPC) and supplementary cementitious materials (SCMs) such as fly ash, silica fume, and slag. They found that the formation factor of fresh cement pastes is correlated to the porosity, tortuosity, and *w*/*cm* of cement pastes.[14] It was shown that for a given paste mixture, the formation factor decreases with an increase in porosity or *w*/*cm*.[16] Sant et al.[27] evaluated the variations in the electrical response of fresh systems. Castro et al.[28] and Kompare[29] examined

ACI Materials Journal, V. 120, No. 5, September 2023.

MS No. M-2022-084.R1, doi: 10.14359/51738903, received August 15, 2022, and reviewed under Institute publication policies.

the early-age electrical measurements in fresh concrete as a potential QC/QA tool by testing the ability of the tool to determine water added or admixture variations. A pore solution sensor was developed and evaluated by Rajabipour et al.[30] Castro et al.[28] noticed specifically that the conductivity was able to pick up both changes in the paste volume and the pore solution.

Practical methods exist to measure bulk resistivity of fresh cementitious systems[12,31-36]; however, no standardized methods exist to measure the properties of the pore solution in fresh cementitious materials. The National Institute of Standards and Technology's (NIST) calculator,[34] which uses mixture proportions and oxide compositions to calculate pore solution resistivity provides a good starting point; however, it may not be accurate for fresh cementitious systems, as it does not consider sulfate-ion concentrations to calculate pore solution conductivity and assumes 75% of alkalies dissolve into pore solution at early ages.[37] Rajabipour et al.[30] developed pore solution sensors; however, these have a time lag, which is not a concern at later ages, although it may be an issue in measuring fresh concrete. Further, these sensors have yet to be mass-produced. Thermodynamic modeling is another tool that has been successfully used for long-term properties; however, these models struggle to provide strong predictions for fresh mixtures as they are based on long-term equilibrium calculations and early ages are dominated by kinetic effects and dissolution properties.[38-49] Direct measurement methods that use chemical composition to calculate resistivity such as ion chromatography,[50] titration,[51] or inductively coupled plasma spectroscopy (ICP)[52,53] take significant time and require multiple samples, making them expensive and impractical for field applications. Pore solution resistivity has been able to be calculated using chemical compositions obtained using X-ray fluorescence (XRF) with an error of 3.75%.[54,55] This, however, requires the solution to be extracted and tested in a laboratory environment. As such, a need exists for a practical method to extract pore solution from fresh cementitious systems. Further, a need exists to rapidly determine the resistivity of this pore solution.

Table 1—Chemical composition of OPC

	OPC
Cement oxides and loss on ignition (LOI)	Percent by mass, %
Silicon dioxide (SiO_2)	19.9
Aluminum oxide (Al_2O_3)	4.6
Ferric oxide (Fe_2O_3)	3.2
Calcium oxide (CaO)	62.0
Magnesium oxide (MgO)	3.8
Sulfur trioxide (SO_3)	2.8
Alkalies ($Na_2O + 0.658 \cdot K_2O$)	0.57
LOI	1.6
Bogue phase composition	Percent by mass, %
Tricalcium silicate (C_3S)	57.0
Dicalcium silicate (C_2S)	14.0
Tricalcium aluminate (C_3A)	7.0
Tetracalcium aluminoferrite (C_4AF)	10.0

This paper investigates procedures to extract pore solution and to measure pore solution resistivity for use in the field. In addition, this study includes the determination of the effect of time from mixing on the pore solution resistivity. This paper also investigates a practical method to determine the pore solution conductivity/resistivity from the diluted cement paste sample when the extracted pore solution quantity is not adequate to make accurate measurements.

RESEARCH SIGNIFICANCE

Obtaining the pore solution of a delivered concrete could have QC/QA benefits. For example, it may be used to assess if an admixture has been added or as a step in determining the *w/cm* of the delivered concrete. This paper outlines a technique to obtain the pore solution and to measure its electrical resistivity in the field. This approach is compared with the existing methods. This paper also discusses predicting the pore solution resistivity from diluted cementitious pastes in cases when a limited solution can be extracted. This may provide a method for its eventual use as a part of a QC/QA program for determining the water-cement ratio (*w/c*) of delivered concrete.

MATERIALS AND METHODS

Materials

An ASTM C150/C150M-19a Type I OPC was used in this study.[56] The specific gravity of this cement was 3.15, and the Blaine fineness was 420 m^2/kg. The water used in all mixtures was ASTM D1193 Type II deionized (DI) water. Table 1 lists the chemical composition of the OPC used in this study.

This study examines cement pastes prepared at three different *w/cm* (0.35, 0.45, and 0.55). The cement pastes were mixed in a 1000 mL tabletop vacuum mixer for a total of 3 minutes at 400 rpm and 70% vacuum to minimize entrapped air, and they were agitated by mixing them for 90 seconds every 15 minutes until the testing time.

Pore solution extraction methods

The two most prevalent techniques to extract fresh-paste pore solution used previously are the nitrogen pressure extraction device and the vacuum pump.[54,57] Both use applied pressure and a filter to extract the pore solution from a fresh cement paste. The reference method used in this study was nitrogen pressure extractor, as it is the easier of the two methods, which also minimizes carbonation.[54] The method introduced in this study to obtain pore solution was centrifuge extraction, and the solution obtained with this approach is compared with the nitrogen pressure extraction method.

Nitrogen pressure extraction—Figure 1 provides a labeled diagram of the nitrogen pressure extraction apparatus used in this study. It consists of several parts, including a main chamber that holds the cement paste, a steel filter, and a 0.45 µm cellulose filter to filter any solids; a funnel that collects the extracted pore solution to transfer to a vial; and a part to attach the nitrogen gas cylinder to the main chamber using a connector. To extract the pore solution, the cement paste is placed in the main chamber, which is pressurized with nitrogen at 200 kPa. This pressure causes the solution

to be separated from the paste and it passes through the filter and is collected below the funnel.

The nitrogen pressure method of extraction takes approximately 5 minutes to obtain a sufficient amount of pore solution, which is approximately 8 mL. Between each measurement, the apparatus must be taken apart, cleaned, rinsed with DI water, dried, and a new filter must be inserted. It is only capable of testing one sample at a time. It also requires a nitrogen gas source, which makes it more cumbersome for field applications. To avoid these concerns, an alternative method—centrifuge extraction of pore solution—is studied.

Centrifuge extraction—In this method, a centrifuge spins the samples at high speed, creating an acceleration that separates particles from the liquid phase according to their densities. A centrifuge can separate the pore solution from cement paste because cement particles are denser than the pore solution, causing them to separate due to centrifugal force. The benefits of using a centrifuge are portability, ease of use, and the number of samples it can run. The process requires very little space, low effort, needs only electrical power to operate, and requires no cleaning between the uses as the tubes are self-contained and disposable.

In this work, centrifuge tubes (50 mL capacity) are filled with cement pastes, and 5 minutes later, four pore solutions are extracted from the cementitious materials. The pore solution is then decanted into another vessel for storage or immediate testing. The 50 mL centrifuge tubes are disposed of after decanting the pore solution. The apparatus used in this study can centrifuge four samples simultaneously, with potential to have additional samples tested in larger setups, allowing for testing to be performed much faster. The centrifuge method also yields more pore solution from a single cycle. An image of the centrifuge used in this study is pictured in Fig. 2(a), along with an image of the separated pore solution in Fig. 2(b).

Pore solution resistivity measurement methods

Two pore solution resistivity measurement methods were considered in this study. The two methods include the resistivity cell[54,58-61] and conductivity probe.[62,63] Measurement using a resistivity cell was used as a reference to compare and investigate the measurement using a conductivity probe.

Cell resistivity measurement—Electrical measurements of pore solution were taken by using a concrete resistivity meter and running a current through a cell of known dimensions filled with the pore solution.[58,64] Figures 3(a) and (b) show the details of the resistivity cell and brass plates.

To perform a measurement, the acrylic cell is inserted into the indentation on either side of the brass plates. Pore solution is then injected with the syringe through the holes on the top of the acrylic cell. Alligator clips are attached to the connection points for the resistivity meter, and the impedance in ohms is recorded. Resistivity is then calculated by multiplying the impedance by the cosine of the phase angle and the geometry factor for the acrylic cell. For this resistivity cell, the geometry factor was found to be 2.76 mm, which was calculated by dividing the cross-sectional area of the cell (69.84 mm^2) by the length of the cell (25.35 mm). To correct the measurement to standard temperature 23°C,

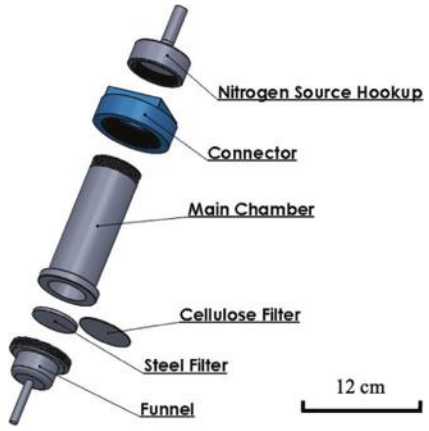

Fig. 1—Illustration of nitrogen pressure extraction apparatus (assembly diagram).

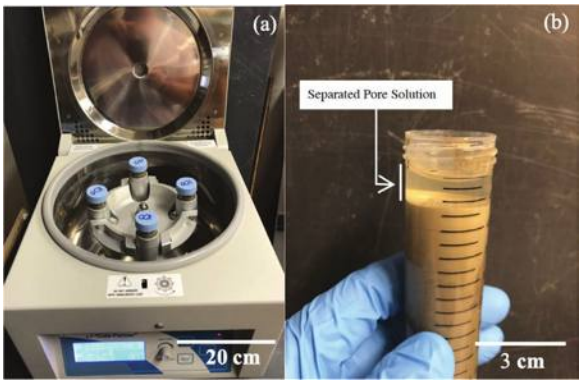

Fig. 2—(a) Picture of centrifuge with 50 mL centrifuge tubes; and (b) image of specimen after cycled in centrifuge.

the Arrhenius equation (Eq. (2)) was used with an activation energy of 13.9 kJ/mol.[65-67]

$$\rho_0 = \rho_T e^{\left[\frac{-E_{a,\rho}}{R}\left(\frac{1}{T}-\frac{1}{T_0}\right)\right]} \quad (2)$$

where ρ_T is the resistivity measured at temperature T (K); ρ_0 is the resistivity measured at the reference temperature (298.15 K); $E_{a,\rho}$ is the activation energy for resistivity (kJ/mol); and R is the gas constant (kJ). This cell method is preferred for measuring pore solution properties of cured concrete, as it requires less than 2 mL of pore solution. Many times, only approximately 2 mL of fluid can be extracted from fully hydrated concrete samples.[58-61] There are several steps that must be taken with this method of electrical measurement to ensure accuracy. Cross-contamination between pore solution samples, oxidation of the brass plates, and air trapped in the acrylic cell must be minimized for an accurate measurement. The plates, syringe, and cell were rinsed with DI water between uses to prevent cross-contamination of pore solution samples. Wires need to be securely fastened, and connection points are cleaned to ensure proper current flow. The brass plates need to be cleaned and polished with a scouring product to remove the oxidized surface and rubbed with isopropyl alcohol to remove any chemical residue.

Probe resistivity measurement—An alternative to the cell method of measuring resistivity uses a commercial

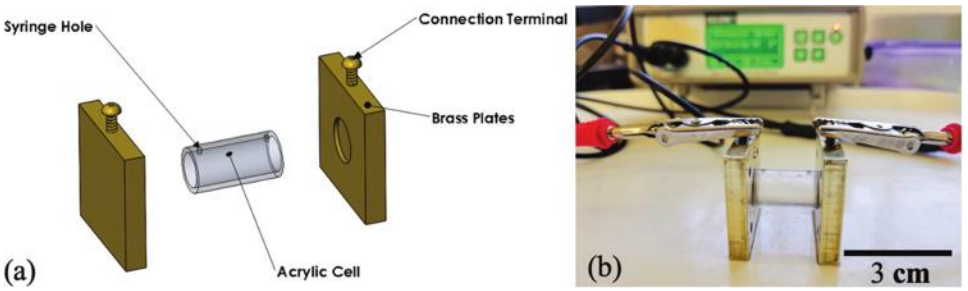

Fig. 3—(a) Resistivity cell with conductive metal plates at both ends for circuit connections; and (b) assembled cell with resistivity meter.

conductivity probe. The probe chosen for this study is a three-pole platinum conductivity electrode for a benchtop meter. The experimental setup can be seen in Fig. 4.

Probes can also contain a temperature sensor such as the one used in this study to adjust the reading to room temperature (23°C). The conductivity probe was calibrated with a standard solution of 25 mS/cm before testing the pore solution samples. Measured conductivities of the solutions were later converted to resistivities. Conductivity probes are not commonly used to measure concrete pore solution, as they require more than 2 mL of pore solution. However, sufficient pore solution can be extracted from fresh concretes and pastes as they are mostly unhydrated at an early age. Therefore, for early-age studies, a conductivity probe is more desirable for its faster measurement times. A single reading took 1 minute to obtain, which was significantly faster than the cell resistivity method.

Investigation of effect of time from initial mixing on pore solution resistivity

To analyze the possible effect of time from mixing on fresh pore solution resistivity, 0.35, 0.45, and 0.55 *w/cm* paste mixtures were prepared, and their pore solution resistivities were measured after 30, 60, and 90 minutes from initial mixing. Each mixture was agitated by mixing it every 15 minutes for 90 seconds prior to extraction and measurement of pore solution resistivity. The centrifuge method of extraction and probe method of resistivity measurement were used for all the samples.

Prediction of original pore solution resistivity from diluted cement paste

One of the possible challenges for the resistivity measurement of fresh cement paste pore solution (or concrete) is obtaining an adequate amount of pore solution from fresh mixtures. For these cases, a method is proposed that can be used to back-calculate the original pore solution resistivity (or conductivity) by measuring the conductivities of the extracted pore solutions of diluted fresh cement pastes (that is, serial dilution). As additional water is added to dilute the fresh cement paste, more pore solution is yielded upon extraction by a centrifuge. Diluted fresh cement paste pore solution conductivity can be related to the original pore solution conductivity using the relationship between ion concentrations and solution conductivity that was discussed by Snyder et al.[68]

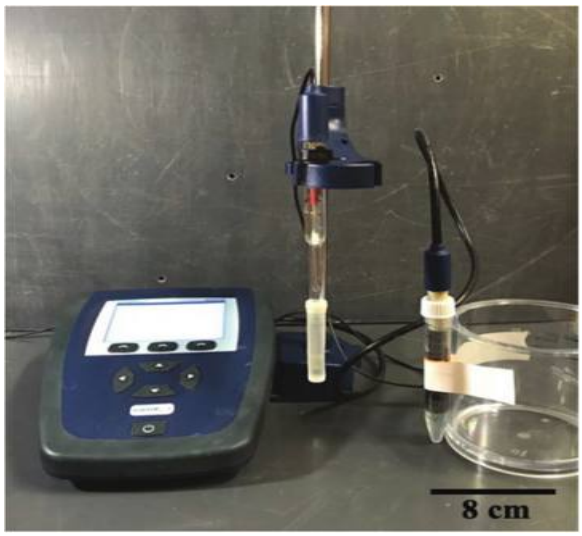

Fig. 4—Benchtop meter with pH probe (left); and resistivity probe testing specimen (right).

For diluting the fresh cement pastes, 60 g of fresh cement paste was measured into two different 50 mL centrifuge tubes. Different quantities of DI water were added to the centrifuge tubes to create different dilutions. Dilutions were calculated in terms of added water and were quantified using the dilution percentage shown in Eq. (3). Seven different dilution points were tested for each paste sample, and all combinations of two points were examined to find the best selection of dilution points to predict the original pore solution conductivity with the least difference. The procedure to choose the two dilution points measurements for the prediction of pore solution conductivity is further discussed in the "Results and Discussion" section.

$$D_P = \left[\frac{V_{OS} + V_{Aw}}{V_{OS}}\right]100 \quad (3)$$

where D_P is the dilution percentage; V_{OS} represents the volume of original pore solution in the sample; and V_{Aw} represents the volume of added water to the system for the dilution.

The centrifuge tubes with the added water and the cement paste were shaken for 60 seconds to sufficiently combine the added water with the paste, and they were run through the centrifuge to extract the pore solutions. The conductivity of each sample was then measured using the conductivity probe.

The conductivity of an undiluted sample for each trial was also measured to act as a control for the experiment, which allowed percent error to be calculated (difference between the measured and predicted pore solution conductivities). Using these measurements along with solution conductivity-ion concentration relationships from Snyder et al.,[68] a relationship was found to theoretically predict the original pore solution conductivity. This relationship is represented as shown by Eq. (4).

$$\sigma_{calc} = \sum_i C_i z_i \lambda_i \tag{4}$$

where C_i represents the molar concentration of each ion i; z_i is the valence number of each ion i; and λ_i is the equivalent conductivity of each ion i. The equivalent conductivity of an ionic species can be calculated in a number of ways, but can be simplified by a single parameter model that is accurate to within 10% for pore solutions, as shown in Eq. (5).[68]

$$\lambda_i = \frac{\lambda_i^\circ}{1 + G_i I_M^{1/2}} \tag{5}$$

where λ° is the equivalent conductivity of an ionic species at infinite dilution; and G_i is the conductivity coefficient. The values of these coefficients can be found in the literature.[69] The value I_M is the ionic strength on a molar basis and is described by Eq. (6).[68]

$$I_M = \frac{1}{2}\sum_i z_i^2 C_i \tag{6}$$

Equations (3) through (6) can be combined to create an equation that relates the conductivities of the two pore solutions as a function of ion concentration. While the original ion concentrations are unknown, multiple data points allow these unknowns to be solved with a system of equations. To create a function of pore solution conductivity in terms of concentration of pore solutions for diluted cement pastes, a new term for ion concentration was required in terms of the volume of added water for dilution. For each quantity of added water, it would quantify its change to the original concentration C_i. The following relationship was developed for determining the ion concentration at the dilution point

$$C_{i.dilution} = \frac{C_i}{1 + \frac{V_{Aw}}{V_{OS}}} \tag{7}$$

Pore solution of fresh cement paste (in the 30 to 90 minutes from initial mixing window) primarily consists of sodium (Na^+), potassium (K^+), hydroxide (OH^-), and sulfate (SO_4^{2-}) ions.[52] Because little to no hydration is expected to take place, calcium (Ca^{2+}) concentration was assumed as insignificant at this early of an age. These ion concentrations were included in the function to solve for the original (undiluted cement paste sample) pore solution conductivity. The resulting function using Eq. (3) through (6) is shown in simplified form as Eq. (8).

$$\sigma_{dilution(x)} = \sum_i \left[\frac{C_i z_i}{1 + \frac{V_{Aw}}{V_{OS}}}\right]\left[\frac{\lambda_i^\circ}{1 + G_i\sqrt{\frac{1}{2}\cdot\frac{C_K + C_{Na} + C_{OH} + 4C_{SO4}}{1 + \frac{V_{Aw}}{V_{OS}}}}}\right] \tag{8}$$

To solve Eq. (8), five unknown constants (C_K, C_{Na}, C_{OH}, C_{SO4}, V_{OS}) must be determined. While these constants can be found by fitting the function to the five dilution points, the process can be simplified by reducing the number of unknown constants. For example, C_{OH} can be estimated using pH, which was measured for one of the two pore solutions from the diluted samples, and the volume of added water of that pH measurement was noted for C_{OH} measurements that would be required. The activity of OH^- was then used to estimate the C_{OH} in the pore solution. In this work, the activity coefficient for OH^- was assumed as 0.7 based on the literature,[70,71] but this assumption can be revised with additional information about the mixtures. C_{SO4} was approximated using an equation developed by Taylor,[72] as shown in Eq. (9).

$$C_{SO_4} = \left(0.06\frac{1}{\text{mol}}\right)(C_{Na} + C_K)^2 \tag{9}$$

An assumption was made that the ratio of Na_2O to K_2O of OPC would be equal to C_{Na}/C_K in the pore solution. Table 2 shows average percent by mass quantities of Na_2O and K_2O for a variety of portland cements[73] and SCMs.[74]

For the Type I cement used in this study, a ratio of 0.3 was used to develop the following relationship between ion concentrations, as shown in Eq. (10).

$$C_{Na} = 0.3 C_K \tag{10}$$

A MATLAB code was prepared to solve Eq. (7) through (9) and relate the measured conductivities of the two solutions from the diluted samples and the pH of one of the solutions of diluted samples to find the original pore solution conductivity. This function solves for two unknowns (C_{Na} and V_{OS}) to provide the conductivity of the pore solution of the undiluted sample. To quantify the accuracy of the predictions generated by the MATLAB code, the percent difference in predicted and measured conductivity ($\Delta\sigma$ %) was calculated. This calculation is represented by Eq. (11).

$$\Delta\sigma\ \% = \left[\frac{\sigma_m - \sigma_p}{\sigma_m}\right]100 \tag{11}$$

where σ_m is the measured conductivity of the undiluted pore solution sample; and σ_p represents the predicted pore solution conductivity based on the fitted function to the points.

RESULTS AND DISCUSSION

Extraction methods analysis

Table 3 shows the measured resistivity values of pore solution extracted using both the nitrogen pressure and centrifuge extraction methods. Statistical analysis was done using

a *t*-test of two means to compare the extraction methods at each *w*/*cm*. Table 3 also shows the results of the analysis.

The calculated *p*-values across all three *w*/*cm* tests were greater than 0.05, implying that no statistically significant difference exists between the extraction test methods. The centrifuge method samples were easier to prepare, and disposable centrifuge tubes eliminated cleanup. It also yielded 3 mL more pore solution in the 0.35 *w*/*cm* samples compared to the nitrogen pressure method. The centrifuge method provides flexibility to choose sample sizes. Additionally, four samples were extracted in 5 minutes using the centrifuge method, whereas only one sample was extracted using the nitrogen pressure method in 5 minutes. For these reasons, the centrifuge extraction method was found to be a more practical method for extracting pore solution from fresh cement pastes compared to the nitrogen pressure extraction method.

Table 2—Mean of typical Na_2O and K_2O compositions in portland cements and SCMs, % by mass[70]

Cement/SCM type	Statistic	Na_2O	K_2O
Type I	Mean	0.18	0.67
	SD	0.08	0.34
Type II	Mean	0.17	0.57
	SD	0.07	0.22
Type III	Mean	0.16	0.60
	SD	0.07	0.22
Type V	Mean	0.15	0.47
	SD	0.06	0.13
Undensified silica fume	Mean	0.41	0.34
	SD	0.55	0.27
Densified silica fume	Mean	0.32	0.63
	SD	0.39	0.14
Class F fly ash	Mean	1.88	1.34
	SD	2.17	0.78
Class C fly ash	Mean	1.98	0.58
	SD	1.45	0.26
Slag	Mean	0.32	0.45
	SD	0.12	0.13
Calcinated clays	Mean	0.81	0.85
	SD	2.02	1.82

Note: SD is standard deviation.

Resistivity methods analysis

Table 4 shows resistivity measurements made using both the resistivity cell and conductivity probe methods. The centrifuge method of extraction was used for this comparison for consistency in results. Statistical analysis was done using a *t*-test to compare the resistivity measurement methods. Table 4 also shows the results of the analysis.

Reported *p*-values of 0.059, 0.233, and 1.023 all indicated that there was no statistically significant difference between the mean resistivity measurements existing at a significance level of 0.05. The cell method of resistivity measurement was found to take approximately 3 minutes to make a single measurement, compared to approximately 1 minute for the probe to complete a resistivity measurement. Therefore, using the probe method for determining the resistivity of pore solution is recommended for making faster and more accurate measurements.

Effect of time from initial mixing on pore solution resistivity

Table 5 shows the pore solution resistivity measurements measured on 0.35, 0.45, and 0.55 *w*/*cm* cement pastes pore

Table 3—*t*-test statistical comparison of differences in resistivity measurement means due to different pore solution extraction methods (sample size = 3)

w/*cm*	Extraction method	Resistivity, ohm·m	Standard deviation, ohm·m	Coefficient of variation	*p*-value
0.35	Nitrogen	0.222	0.004	0.019	0.241
	Centrifuge	0.225	0.003	0.015	
0.45	Nitrogen	0.258	0.004	0.017	0.145
	Centrifuge	0.262	0.002	0.006	
0.55	Nitrogen	0.294	0.002	0.008	0.372
	Centrifuge	0.295	0.001	0.003	

Table 4—*t*-test statistical comparison of differences in resistivity measurement means using cell and probe methods (sample size = 3)

w/*cm*	Resistivity measurement method	Resistivity measurement, ohm·m	Standard deviation, ohm·m	Coefficient of variation	*p*-value
0.35	Cell	0.265	0.002	0.008	0.059
	Probe	0.257	0.003	0.013	
0.45	Cell	0.300	0.010	0.033	0.233
	Probe	0.292	0.008	0.026	
0.55	Cell	0.350	0.010	0.027	1.023
	Probe	0.341	0.008	0.023	

Table 5—Statistical analysis of differences between resistivities of pore solutions extracted after 30, 60, and 90 minutes from initial mixing (sample size = 3)

w/cm	Time from initial mixing, minutes	Resistivity, ohm·m	Standard deviation, ohm·m	Coefficient of variation	*p*-values (ANOVA results)
0.35	30	0.206	0.0179	0.0869	0.604
	60	0.199	0.0127	0.0638	
	90	0.198	0.0124	0.0626	
0.45	30	0.253	0.0099	0.0391	0.621
	60	0.259	0.0014	0.0054	
	90	0.254	0.0028	0.0110	
0.55	30	0.289	0.0122	0.0422	0.606
	60	0.285	0.0041	0.0144	
	90	0.284	0.0032	0.0113	

solutions at 30, 60, and 90 minutes after initial mixing. Analysis of variance (ANOVA) tests were performed to find if there was a statistically significant difference in the mean measured resistivities. The ANOVA results reported *p*-values greater than the significance interval of 0.05. Therefore, there is no statistically significant difference in pore solution resistivity at 30, 60, and 90 minutes after initial mixing. A similar observation was made in previous studies[11,26,27] where no noticeable difference in pore solution resistivity of fresh cement pastes was observed during the induction period of cement hydration.

This observation has practical implications. Concrete trucks typically arrive on site between 30 and 90 minutes after the mixture is first prepared at a batching plant. Because the statistical analysis shows the pore solution resistivity does not significantly change in this fresh state of concrete, testing can be simplified. All pore solution resistivity measurements taken within the 30- to 90-minute window from initial mixing will not require time adjustments.

Prediction of pore solution conductivity

Seven dilutions were tested in this study for each *w/cm* mixture. As the prepared MATLAB program uses resistivities of pore solutions of pastes at two dilutions to make a prediction of original pore solution resistivity, there were 21 combinations of two dilution points for the input to the function. To determine the best two dilution points in terms of predicting original pore solution conductivity accurately, all 21 combinations were tested. Table 6 shows the percent difference in predicted and measured conductivities of the samples with 0.35, 0.45, and 0.55 *w/cm* of the three best dilution combinations of all 21 combinations.

The two dilution points that predicted the original pore solution conductivities most accurately were 120 and 144%. This is probably because these dilution levels were the most concentrated among the tested dilutions. However, if the 120% dilution point is unattainable due to the water content of the sample, 144 and 176% dilutions could also be used as the predictions did not change significantly (the difference in average predicted and original pore solution conductivity was 0.8%).

Figure 5 shows the graphical output for each *w/cm*. The figure demonstrates using an average of 144 and 176% dilutions to back-calculate for the original pore solution conductivity. Percent dilutions differ slightly for each *w/cm*, as each mixture has a different original water content.

Table 6—Percent difference in predicted and original pore solution conductivity for 0.35, 0.45, and 0.55 *w/cm* samples when different combinations of two dilution points are chosen

w/cm	Percent difference in predicted and original pore solution conductivity		
0.35	1.31*	–0.26†	3.52‡
0.45	–1.35*	–1.11†	–1.27‡
0.55	0.62*	4.34†	1.59‡

*Conductivities of diluted solutions with average D_p of 120 and 144% were used for prediction of original pore solution conductivity.

†Conductivities of diluted solutions with average D_p of 144 and 176% were used for prediction of original pore solution conductivity.

‡Conductivities of diluted solutions with average D_p of 120 and 176% were used for prediction of original pore solution conductivity.

For 0.35, 0.45, and 0.55 *w/cm* pastes, the predicted pore solution conductivity values were 50.13, 39.62, and 33.47 mS/cm, respectively. These predicted pore solution conductivity values translate to 0.199 ohm·m for the 0.35 *w/cm* mixture, 0.252 ohm·m for the 0.45 *w/cm* mixture, and 0.299 ohm·m for the 0.55 *w/cm* mixture. The measured values for 0.35, 0.45, and 0.55 *w/cm* pastes were 50.00, 39.18, and 34.99 mS/cm, respectively. The percent difference in the predicted and measured conductivity for 0.35 *w/cm* was –0.26%. For the 0.45 and 0.55 *w/cm* samples, the percent difference in the predicted and measured conductivities were –1.11% and 4.34%, respectively. The higher error observed for the 0.55 *w/cm* sample could be due to an overall higher dilution of the system due to the high water content of the cement paste. This method of resistivity determination has an error less than or similar to the average error of 3.75% reported by resistivity calculation from ion concentrations determined using XRF.[55] Also, the proposed approach is practical, more direct, and less expensive to use when compared to the resistivity calculated using the XRF method.

If an assumption that the ratio of Na_2O to K_2O of OPC is equal to the ratio of C_K and C_{Na} of the pore solution cannot be made, both constants (C_K, C_{Na}) can be left as unknowns. The same function can be used to solve for the original pore solution conductivity. Figure 6 is the output for the MATLAB function with three unknowns (C_K, C_{Na}, V_{OS}).

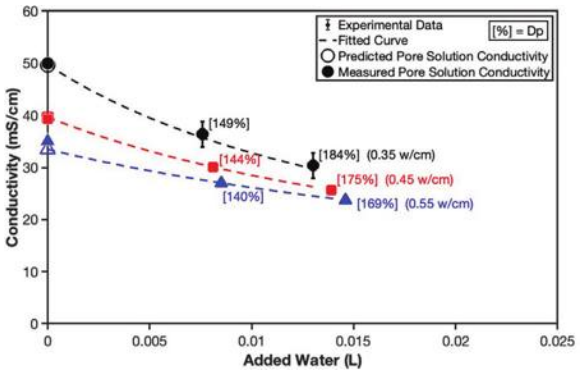

Fig. 5—Predicted conductivity from two diluted cement paste pore solution samples, unknowns: C_{Na} *and* V_{OS}*. For 0.35* w/cm*, difference in predicted and measured conductivities = –0.26%; for 0.45* w/cm*, difference in predicted and measured conductivities = –1.1%; for 0.55* w/cm*, difference in predicted and measured conductivities = 4.3%.*

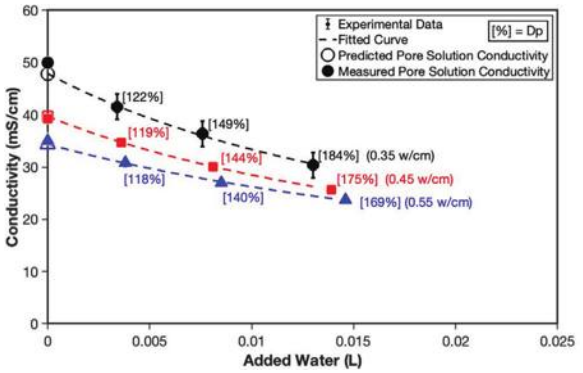

Fig. 6—Predicted conductivity from three diluted 0.35 w/cm *cement paste pore solution samples, unknowns:* C_K*,* C_{Na}*, and* V_{OS}*. For 0.35* w/cm*, difference in predicted and measured conductivities = 4.3%; for 0.45* w/cm*, difference in predicted and measured conductivities = –1.3%; for 0.55* w/cm*, difference in predicted and measured conductivities = 1.7%.*

This time, three dilution points were used, as there are three unknown constants.

Predicting pore solution conductivity using only one dilution was also explored. To do this, another assumption was made in addition to the previous assumptions to make the number of unknowns equal to 1. V_{OS} was assumed to be same as the amount of water added during the mixing process but calculated for the volume of the sample used. Therefore, the function only solves for one unknown: C_{Na}. Figure 7 shows the predicted and measured conductivities of the original solution and the measured conductivities of the diluted solution of all three mixtures. It was observed that the percent difference in measured and predicted conductivities using the single dilution approach ranges from 5 to 9%, which was higher when compared to the approach using two or three dilutions.

While this study used a constant 60 g of cement paste with added water for dilutions between 10 and 25 g, this can be upscaled for larger quantities for application to concrete or mortar. In the event of an insufficient amount of pore solution extraction to accurately measure conductivity using a probe, the proposed dilution approach allows the user to predict

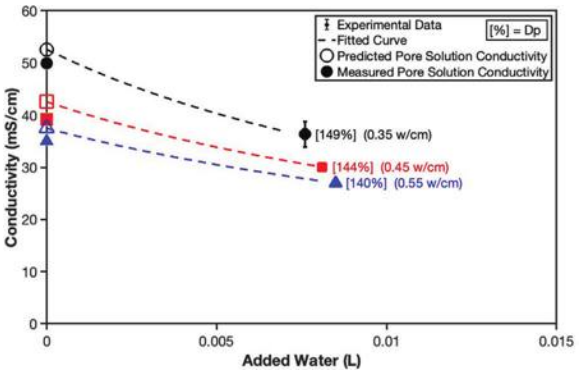

Fig. 7—Predicted conductivity from one diluted cement paste pore solution sample, unknown: C_{Na}*. For 0.35* w/cm*, difference in predicted and measured conductivities = –5.2%; for 0.45* w/cm*, difference in predicted and measured conductivities = –8.7%; for 0.55* w/cm*, difference in predicted and measured conductivities = –7.1%.*

the original pore solution conductivity using the equations relating the ion concentrations and solution conductivity. It was observed that the proposed serial dilution method predicts the pore solution conductivity within 5% of the measured conductivity value.

CONCLUSIONS

This paper discussed a method for extracting fresh cement paste pore solution and determining its resistivity. The proposed method was compared using statistical methods to both existing methods for extraction and pore solution resistivity/conductivity measurements. This paper also discussed the effect of time from initial mixing on the pore solution resistivity, and finally proposed a method of predicting pore solution conductivity by the dilution of cement paste that can be used in the event of less pore solution extraction. The conclusions that were drawn from the study are summarized as follows.

There was no statistically significant difference in the pore solution resistivities when a centrifuge is used for extraction as compared to nitrogen pressure extraction. The centrifuge method can perform multiple tests at a time rather than one, is easier to operate, and is more portable than the nitrogen pressure extractor. This approach has the potential to be scaled to mortar or concrete with a larger centrifuge.

Analysis of variance (ANOVA) showed statistically similar results between pore solution resistivity measured using a resistivity cell and conductivity probe. The probe method of measuring resistivity was found to be faster and more user-friendly (especially for field application) compared to the cell method of measurement.

Statistical analysis of the measured pore solution resistivity showed that times from initial mixture of 30, 60, and 90 minutes were statistically similar, suggesting that the pore solution resistivity measurements can be done at any time between 30 and 90 minutes from mixing. This makes the measurements in the field more practical, as it allows pore solution resistivity tests to be calculated without factoring in corrections for the time from initial mixing. However, the change in pore solution resistivity from 30 to 90 minutes has

to also be studied for mixtures with admixtures and supplementary cementitious materials (SCMs).

This study also demonstrated that in the event of too little pore solution extracted for a pore solution resistivity measurement, a dilution procedure can be used to find the original pore solution resistivity. By preparing two dilutions of the fresh cement paste samples, measuring their pore solution conductivities, and using the ion concentration-solution conductivity relationship discussed by Snyder et al.,[68] the pore solution conductivity of the undiluted sample can be predicted within 5% of the measured pore solution conductivities.

AUTHOR BIOS

ACI member **Joseph H. Biever** *is an MS student at Oregon State University, Corvallis, OR, where he received his BS. His research interests include fresh concrete properties and pore solution chemistry.*

ACI member **Krishna Siva Teja Chopperla** *is a Postdoctoral Scholar at Oregon State University. His research interests include concrete durability and the characterization of cementitious materials.*

O. Burkan Isgor, *FACI, is a Professor in the School of Civil and Construction Engineering at Oregon State University. He is Chair of ACI Committee 222, Corrosion of Metals in Concrete. His research interests include corrosion of steel in concrete, service life modeling of concrete, and thermodynamic modeling of cementitious systems.*

W. Jason Weiss, *FACI, is the Edwards Distinguished Professor in Engineering in the School of Civil and Construction Engineering at Oregon State University. He is Editor-in-Chief of the* ACI Materials Journal*, a member of the ACI Technical Activities Committee, and a member of the ACI Board of Direction.*

ACKNOWLEDGMENTS

The authors would like to acknowledge that this study was partly funded by the Transportation Pooled Fund—TPF-5(368): Performance-Engineered Concrete Paving Mixtures.

REFERENCES

1. "Concrete Needs to Lose Its Colossal Carbon Footprint," *Nature*, V. 597, No. 7878, 2021, pp. 593-594. doi: 10.1038/d41586-021-02612-5

2. Kotzea, D. G.; Brekken, M.; Morris, T.; Ho, W.; Walgenbach, K.; and Mullings, G. M., "2020 NRMCA Fleet Benchmarking and Costs Survey," *Concrete InFocus*, 2020, 4 pp.

3. ASTM C94/C94M-16, "Standard Specification for Ready-Mixed Concrete," ASTM International, West Conshohocken, PA, 2016, 14 pp.

4. ACI Committee 318, "Building Code Requirements for Structural Concrete (ACI 318-19) and Commentary (ACI 318R-19) (Reapproved 2022)," American Concrete Institute, Farmington Hills, MI, 2019, 624 pp.

5. AASHTO R 101-22, "Standard Practice for Developing Performance Engineered Concrete Pavement Mixtures," American Association of State Highway and Transportation Officials, Washington, DC, 2022, 14 pp.

6. *fib*, "CEB-FIP Model Code 1990," *fib* Bulletin No. 213/214, International Federation for Structural Concrete, Lausanne, Switzerland, 1993, 460 pp.

7. AASHTO T 318-15 (2019), "Standard Method of Test for Water Content of Freshly Mixed Concrete Using Microwave Oven Drying," American Association of State Highway and Transportation Officials, Washington, DC, 2019, 6 pp.

8. Robertson, J. B.; Ley, M. T.; and Cook, M. D., "Measuring the Change in Water-to-Cement Ratio in Fresh and Hardened Concrete," *Journal of Materials in Civil Engineering*, ASCE, V. 34, No. 4, 2022, 11 pp.

9. Li, Z.; Xiao, L.; and Wei, X., "Determination of Concrete Setting Time Using Electrical Resistivity Measurement," *Journal of Materials in Civil Engineering*, ASCE, V. 19, No. 5, 2007, pp. 423-427. doi: 10.1061/(ASCE)0899-1561(2007)19:5(423)

10. Mancio, M.; Moore, J. R.; Brooks, Z.; Monteiro, P. J. M.; and Glaser, S. D., "Instantaneous In-Situ Determination of Water-Cement Ratio of Fresh Concrete," *ACI Materials Journal*, V. 107, No. 6, Nov.-Dec. 2010, pp. 586-592.

11. Wei, X., and Li, Z., "Early Hydration Process of Portland Cement Paste by Electrical Measurement," *Journal of Materials in Civil Engineering*, ASCE, V. 18, No. 1, 2006, pp. 99-105. doi: 10.1061/(ASCE)0899-1561(2006)18:1(99)

12. Whittington, H. W.; McCarter, J.; and Forde, M. C., "The Conduction of Electricity through Concrete," *Magazine of Concrete Research*, V. 33, No. 114, 1981, pp. 48-60. doi: 10.1680/macr.1981.33.114.48

13. AASHTO PP 84-20, "Standard Practice for Developing Performance Engineered Concrete Pavement Mixtures," American Association of State Highway and Transportation Officials, Washington, DC, 2020, 14 pp.

14. Bu, Y., and Weiss, J., "The Influence of Alkali Content on the Electrical Resistivity and Transport Properties of Cementitious Materials," *Cement and Concrete Composites*, V. 51, 2014, pp. 49-58. doi: 10.1016/j.cemconcomp.2014.02.008

15. Archie, G. E., "The Electrical Resistivity Log as an Aid in Determining Some Reservoir Characteristics," *Transactions of the AIME*, V. 146, 1942, pp. 54-62.

16. Dullien, F. A. L., *Porous Media: Fluid Transport and Pore Structure*, second edition, Academic Press, Cambridge, MA, 1991.

17. McCarter, W. J.; Starrs, G.; and Chrisp, T. M., "Electrical Conductivity, Diffusion, and Permeability of Portland Cement-Based Mortars," *Cement and Concrete Research*, V. 30, No. 9, 2000, pp. 1395-1400. doi: 10.1016/S0008-8846(00)00281-7

18. Tumidajski, P. J.; Schumacher, A. S.; Perron, S.; Gu, P.; and Beaudoin, J. J., "On the Relationship between Porosity and Electrical Resistivity in Cementitious Systems," *Cement and Concrete Research*, V. 26, No. 4, 1996, pp. 539-544. doi: 10.1016/0008-8846(96)00017-8

19. Gu, P.; Xie, P.; Beaudoin, J. J.; and Brousseau, R., "A.C. Impedance Spectroscopy (I): A New Equivalent Circuit Model for Hydrated Portland Cement Paste," *Cement and Concrete Research*, V. 22, No. 5, 1992, pp. 833-840. doi: 10.1016/0008-8846(92)90107-7

20. Christensen, B. J.; Coverdale, T.; Olson, R. A.; Ford, S. J.; Garboczi, E. J.; Jennings, H. M.; and Mason, T. O., "Impedance Spectroscopy of Hydrating Cement-Based Materials: Measurement, Interpretation, and Application," *Journal of the American Ceramic Society*, V. 77, No. 11, 1994, pp. 2789-2804. doi: 10.1111/j.1151-2916.1994.tb04507.x

21. Moradllo, M. K.; Qiao, C.; Isgor, O. B.; Reese, S.; and Weiss, W. J., "Relating Formation Factor of Concrete to Water Absorption," *ACI Materials Journal*, V. 115, No. 6, Nov. 2018, pp. 887-898. doi: 10.14359/51706844

22. Rajabipour, F., "Insitu Electrical Sensing and Material Health Monitoring in Concrete Structures," PhD dissertation, Purdue University, West Lafayette, IN, 2006, 193 pp.

23. Jafari Azad, V.; Erbektas, A. R.; Qiao, C.; Isgor, O. B.; and Weiss, W. J., "Relating the Formation Factor and Chloride Binding Parameters to the Apparent Chloride Diffusion Coefficient of Concrete," *Journal of Materials in Civil Engineering*, ASCE, V. 31, No. 2, 2019, p. 04018392. doi: 10.1061/(ASCE)MT.1943-5533.0002615

24. Qiao, C.; Coyle, A. T.; Isgor, O. B.; and Weiss, W. J., "Prediction of Chloride Ingress in Saturated Concrete Using Formation Factor and Chloride Binding Isotherm," *Advances in Civil Engineering Materials*, V. 7, No. 1, 2018, pp. 206-220. doi: 10.1520/ACEM20170141

25. McCarter, W. J., and Puyrigaud, P., "Water Content Assessment of Fresh Concrete," *Proceedings of the Institution of Civil Engineers—Structures and Buildings*, V. 110, No. 4, 1995, pp. 417-425. doi: 10.1680/istbu.1995.28059

26. Sallehi, H.; Ghods, P.; and Isgor, O. B., "Formation Factor of Fresh Cementitious Pastes," *Cement and Concrete Composites*, V. 91, 2018, pp. 174-188. doi: 10.1016/j.cemconcomp.2018.05.011

27. Sant, G.; Rajabipour, F.; Fishman, P.; Lura, P.; and Weiss, W. J., "Electrical Conductivity Measurements in Cement Paste at Early Ages: A Discussion of the Contribution of Pore Solution Conductivity, Volume, and Connectivity to the Overall Electrical Response," International RILEM Workshop on Advanced Testing of Fresh Cementitious Materials, Stuttgart, Germany, 2006, 9 pp.

28. Castro, J.; Spragg, R.; Kompare, P.; and Weiss, W. J., "Portland Cement Concrete Pavement Permeability Performance," Report No. FHWA/IN/JTRP-2010/29, Joint Transportation Research Program, Indiana Department of Transportation and Purdue University, West Lafayette, IN, 2010, 258 pp.

29. Kompare, P., "Electrical and Relative Humidity Measurements of Concrete and Their Relation to Transport Properties," master's thesis, Purdue University, West Lafayette, IN, 2015, 124 pp.

30. Rajabipour, F.; Sant, G.; and Weiss, W. J., "Development of Electrical Conductivity-Based Sensors for Health Monitoring of Concrete Materials," Transportation Research Board 86th Annual Meeting, 2007, 16 pp.

31. Chrisp, T. M.; Starrs, G.; McCarter, W. J.; Rouchotas, E.; and Blewett, J., "Temperature-Conductivity Relationships for Concrete: An Activation Energy Approach," *Journal of Materials Science Letters*, V. 20, No. 12, 2001, pp. 1085-1087. doi: 10.1023/A:1010926426753

32. Liu, Y., and Presuel-Moreno, F. J., "Normalization of Temperature Effect on Concrete Resistivity by Method Using Arrhenius Law," *ACI Materials Journal*, V. 111, No. 4, July-Aug. 2014, pp. 433-442. doi: 10.14359/51686725

33. McCarter, W. J.; Chrisp, T. M.; Starrs, G.; Basheer, P. A. M.; and Blewett, J., "Field Monitoring of Electrical Conductivity of Cover-Zone Concrete," *Cement and Concrete Composites*, V. 27, No. 7-8, 2005, pp. 809-817.

34. Morsy, M. S., "Effect of Temperature on Electrical Conductivity of Blended Cement Pastes," *Cement and Concrete Research*, V. 29, No. 4, 1999, pp. 603-606. doi: 10.1016/S0008-8846(98)00198-7

35. Villagrán Zaccardi, Y. A.; Fullea García, J.; Huélamo, P.; and Di Maio, Á. A., "Influence of Temperature and Humidity on Portland Cement Mortar Resistivity Monitored with Inner Sensors," *Materials and Corrosion*, V. 60, No. 4, 2009, pp. 294-299. doi: 10.1002/maco.200805075

36. Obla, K.; Kong, R.; Sherman, S.; Bentz, D. P.; and Jones, S. Z., "Relating the Electrical Resistance of Fresh Concrete to Mixture Proportions," *Advances in Civil Engineering Materials*, V. 7, No. 1, 2018, pp. 71-86.

37. NIST, "Estimation of Pore Solution Conductivity," online calculator, National Institute of Standards and Technology, Gaithersburg, MD, 2019.

38. Bharadwaj, K.; Chopperla, K. S. T.; Choudhary, A.; Glosser, D.; Ghantous, R. M.; Vasudevan, G. D.; Ideker, J. H.; Isgor, O. B.; Trejo, D.; and Weiss, W. J., "CALTRANS: Impact of the Use of Portland-Limestone Cement on Concrete Performance as Plain or Reinforced Material - Final Report," Oregon State University, Corvallis, OR, 2021, 320 pp.

39. Bharadwaj, K.; Ghantous, R. M.; Sahan, F.; Isgor, O. B.; and Weiss, W. J., "Predicting Pore Volume, Compressive Strength, Pore Connectivity, and Formation Factor in Cementitious Pastes Containing Fly Ash," *Cement and Concrete Composites*, V. 122, 2021, Article No. 104113. doi: 10.1016/j.cemconcomp.2021.104113

40. Bharadwaj, K.; Glosser, D.; Moradllo, M. K.; Isgor, O. B.; and Weiss, W. J., "Toward the Prediction of Pore Volumes and Freeze-Thaw Performance of Concrete Using Thermodynamic Modelling," *Cement and Concrete Research*, V. 124, 2019, Article No. 105820. doi: 10.1016/j.cemconres.2019.105820

41. Bharadwaj, K.; Isgor, O. B.; and Weiss, W. J., "Supplementary Cementitious Materials in Portland-Limestone Cements," *ACI Materials Journal*, V. 119, No. 2, Mar. 2022, pp. 141-154.

42. Bharadwaj, K.; Isgor, O. B.; and Weiss, W. J., "Pozzolanic Reactivity of Supplementary Cementitious Materials," *ACI Materials Journal*, V. 120, No. 4, July 2023, pp. 63-76.

43. Bharadwaj, K.; Isgor, O. B.; and Weiss, W. J., "A Simplified Approach to Determine Pozzolanic Reactivity of Commercial Supplementary Cementitious Materials," *Concrete International*, V. 44, No. 1, Jan. 2022, pp. 27-32.

44. Bharadwaj, K.; Isgor, O. B.; Weiss, W. J.; Chopperla, K. S. T.; Choudhary, A.; Vasudevan, G. D.; Glosser, D.; Ideker, J. H.; and Trejo, D., "A New Mixture Proportioning Method for Performance-Based Concrete," *ACI Materials Journal*, V. 119, No. 2, Mar. 2022, pp. 207-220.

45. Lothenbach, B., and Winnefeld, F., "Thermodynamic Modelling of the Hydration of Portland Cement," *Cement and Concrete Research*, V. 36, No. 2, 2006, pp. 209-226. doi: 10.1016/j.cemconres.2005.03.001

46. Lothenbach, B.; Matschei, T.; Möschner, G.; and Glasser, F. P., "Thermodynamic Modelling of the Effect of Temperature on the Hydration and Porosity of Portland Cement," *Cement and Concrete Research*, V. 38, No. 1, 2008, pp. 1-18. doi: 10.1016/j.cemconres.2007.08.017

47. Choudhary, A.; Bharadwaj, K.; Ghantous, R. M.; Isgor, O. B.; and Weiss, W. J., "Pozzolanic Reactivity Test of Supplementary Cementitious Materials," *ACI Materials Journal*, V. 119, No. 2, Mar. 2022, pp. 255-268.

48. Lothenbach, B.; Le Saout, G.; Gallucci, E.; and Scrivener, K., "Influence of Limestone on the Hydration of Portland Cements," *Cement and Concrete Research*, V. 38, No. 6, 2008, pp. 848-860. doi: 10.1016/j.cemconres.2008.01.002

49. Isgor, O. B., and Weiss, W. J., "A Nearly Self-Sufficient Framework for Modelling Reactive-Transport Processes in Concrete," *Materials and Structures*, V. 52, No. 1, 2019, Article No. 3. doi: 10.1617/s11527-018-1305-x

50. Zanella, R.; Primel, E. G.; and Martins, A. F., "Determination of Chloride and Sulfate in Pore Solutions of Concrete by Ion Chromatography," *Journal of Separation Science*, V. 24, No. 3, 2001, pp. 230-231. doi: 10.1002/1615-9314(20010301)24:3<230::AID-JSSC230>3.0.CO;2-8

51. Byfors, K.; Hansson, C. M.; and Tritthart, J., "Pore Solution Expression as a Method to Determine the Influence of Mineral Additives on Chloride Binding," *Cement and Concrete Research*, V. 16, No. 5, 1986, pp. 760-770. doi: 10.1016/0008-8846(86)90050-5

52. Caruso, F.; Mantellato, S.; Palacios, M.; and Flatt, R. J., "ICP-OES Method for the Characterization of Cement Pore Solutions and Their Modification by Polycarboxylate-Based Superplasticizers," *Cement and Concrete Research*, V. 91, 2017, pp. 52-60. doi: 10.1016/j.cemconres.2016.10.007

53. Bonta, M.; Eitzenberger, A.; Burtscher, S.; and Limbeck, A., "Quantification of Chloride in Concrete Samples Using LA-ICP-MS," *Cement and Concrete Research*, V. 86, 2016, pp. 78-84. doi: 10.1016/j.cemconres.2016.05.002

54. Tsui-Chang, M.; Suraneni, P.; Montanari, L.; Muñoz, J. F.; and Weiss, W. J., "Determination of Chemical Composition and Electrical Resistivity of Expressed Cementitious Pore Solutions Using X-Ray Fluorescence," *ACI Materials Journal*, V. 116, No. 1, Jan. 2019, pp. 155-164. doi: 10.14359/51712242

55. Tsui Chang, M.; Suraneni, P.; Isgor, O. B.; Trejo, D.; and Weiss, W. J., "Using X-Ray Fluorescence to Assess the Chemical Composition and Resistivity of Simulated Cementitious Pore Solutions," *International Journal of Advances in Engineering Sciences and Applied Mathematics*, V. 9, No. 3, 2017, pp. 136-143. doi: 10.1007/s12572-017-0181-x

56. ASTM C150/C150M-19a, "Standard Specification for Portland Cement," ASTM International, West Conshohocken, PA, 2019, 10 pp.

57. Sallehi, H.; Ghods, P.; and Isgor, O. B., "Formation Factor of Fresh Cementitious Pastes," *Cement and Concrete Composites*, V. 91, 2018, pp. 174-188. doi: 10.1016/j.cemconcomp.2018.05.011

58. Barneyback, R. S. Jr., and Diamond, S., "Expression and Analysis of Pore Fluids from Hardened Cement Pastes and Mortars," *Cement and Concrete Research*, V. 11, No. 2, 1981, pp. 279-285. doi: 10.1016/0008-8846(81)90069-7

59. Cyr, M.; Rivard, P.; Labrecque, F.; and Daidié, A., "High-Pressure Device for Fluid Extraction from Porous Materials: Application to Cement-Based Materials," *Journal of the American Ceramic Society*, V. 91, No. 8, 2008, pp. 2653-2658. doi: 10.1111/j.1551-2916.2008.02525.x

60. Spragg, R.; Bu, Y.; Snyder, K.; Bentz, D.; and Weiss, J., "Electrical Testing of Cement-Based Materials: Role of Testing Techniques, Sample Conditioning, and Accelerated Curing," Report No. FHWA/IN/JTRP-2013/28, Joint Transportation Research Program, Indiana Department of Transportation and Purdue University, West Lafayette, IN, 2013, 27 pp.

61. Longuet, P.; Burglen, L.; and Zelwer, A., "The Liquid Phase of Hydrated Cement," *Revue des Matériaux de Construction et de Travaux Publics*, V. 676, 1973, pp. 35-41.

62. Moret-Fernández, D.; Vicente, J.; Aragüés, R.; Peña, C.; and López, M. V., "A New TDR Probe for Measurements of Soil Solution Electrical Conductivity," *Journal of Hydrology*, V. 448-449, 2012, pp. 73-79. doi: 10.1016/j.jhydrol.2012.04.042

63. Scudiero, E.; Berti, A.; Teatini, P.; and Morari, F., "Simultaneous Monitoring of Soil Water Content and Salinity with a Low-Cost Capacitance-Resistance Probe," *Sensors*, V. 12, No. 12, 2012, pp. 17588-17607. doi: 10.3390/s121217588

64. Tsui Chang, M., "The Evaluation of Cementitious Pore Solution Composition and Electrical Resistivity Using X-ray Fluorescence (XRF)," master's thesis, Oregon State University, Corvallis, OR, 2017.

65. Spragg, R.; Villani, C.; Snyder, K.; Bentz, D.; Bullard, J. W.; and Weiss, J., "Factors That Influence Electrical Resistivity Measurements in Cementitious Systems," *Transportation Research Record: Journal of the Transportation Research Board*, V. 2342, No. 1, 2013, pp. 90-98. doi: 10.3141/2342-11

66. Coyle, A. T.; Spragg, R. P.; Suraneni, P.; Amirkhanian, A. N.; Tsui-Chang, M.; and Weiss, W. J., "Activation Energy of Conduction for Use in Temperature Corrections on Electrical Measurements of Concrete," *Advances in Civil Engineering Materials*, V. 8, No. 1, 2019, pp. 158-170. doi: 10.1520/ACEM20180045

67. Coyle, A. T.; Spragg, R. P.; Suraneni, P.; Amirkhanian, A. N.; and Weiss, W. J., "Comparison of Linear Temperature Corrections and Activation Energy Temperature Corrections for Electrical Resistivity Measurements of Concrete," *Advances in Civil Engineering Materials*, V. 7, No. 1, 2018, pp. 174-187. doi: 10.1520/ACEM20170135

68. Snyder, K. A.; Feng, X.; Keen, B. D.; and Mason, T. O., "Estimating the Electrical Conductivity of Cement Paste Pore Solutions from OH^-, K^+ and Na^+ Concentrations," *Cement and Concrete Research*, V. 33, No. 6, 2003, pp. 793-798. doi: 10.1016/S0008-8846(02)01068-2

69. Horvath, A. L., *Handbook of Aqueous Electrolyte Solutions: Physical Properties, Estimation, and Correlation Methods*, Halsted Press, New York, 1985, 631 pp.

70. Samson, E.; Lemaire, G.; Marchand, J.; and Beaudoin, J. J., "Modeling Chemical Activity Effects in Strong Ionic Solutions," *Computational Materials Science*, V. 15, No. 3, 1999, pp. 285-294. doi: 10.1016/S0927-0256(99)00017-8

71. Lura, P.; Friedemann, K.; Stallmach, F.; Mönnig, S.; Wyrzykowski, M.; and Esteves, L. P., "Kinetics of Water Migration in Cement-Based Systems Containing Superabsobent Polymers," *Application of Super Absorbent Polymers (SAP) in Concrete Construction: State-of-the-Art Report Prepared by Technical Committee 225-SAP*, V. Mechtcherine and H.-W. Reinhardt, eds., Springer, Dordrecht, the Netherlands, 2012, pp. 21-37.

72. Taylor, H. F. W., "A Method for Predicting Alkali Ion Concentrations in Cement Pore Solutions," *Advances in Cement Research*, V. 1, No. 1, 1987, pp. 5-17. doi: 10.1680/adcr.1987.1.1.5

73. Tennis, P., *Chemical and Physical Characteristics of U.S. Hydraulic Cements*, Portland Cement Association, Skokie, IL, 2016, 27 pp.

74. Bharadwaj, K.; Isgor, O. B.; and Weiss, W. J., "A Dataset Containing Statistical Compositions and Reactivities of Commercial and Novel Supplementary Cementitious Materials," Dataset Version 1.0, Oregon State University, Corvallis, OR, 2022, 24 pp.

ACI MATERIALS JOURNAL TECHNICAL PAPER

Title No. 120-M53

Recycled Aggregate Mortar Content and Composition Using Handheld X-Ray Fluorescence

by Arindam Dey, Tara L. Cavalline, Miras Mamirov, and Jiong Hu

The use of recycled concrete aggregates (RCAs) in lieu of natural aggregates improves the sustainability of the built environment. Barriers to the use of RCA include its variable composition, including the residual mortar content (RMC), chemical composition, and its potential to contain contaminants, which can negatively affect the properties of concrete or present environmental concerns. In this study, a rapid, economical method to estimate the RMC and provide the chemical characterization of RCA was developed using a portable handheld X-ray fluorescence (PHXRF) device. Models were developed using reference tests (RMC test based on the thermal shock method and chemical composition from whole-rock analysis) to correlate PHXRF results to measured values. The PHXRF shows strong potential for estimating the RMC and chemical composition of RCA. Paired with locally calibrated reference samples, the test method could be used in laboratory or field applications to characterize RCA and increase its use in bound and unbound applications.

Keywords: chemical composition; recycled concrete aggregate (RCA); residual mortar; X-ray fluorescence.

INTRODUCTION

The use of recycled concrete aggregate (RCA) from construction and demolition (C&D) waste as either a partial or complete replacement of natural aggregates (NA) is an economically viable and sustainable choice.[1] RCAs are obtained by crushing concrete from construction waste such as demolished buildings, highways, and other structures. RCA is currently primarily used in unbound applications such as pavement base courses, fill material, and soil stabilization.[2,3] However, RCA is being increasingly used as aggregates in hot-mixture asphalt or portland cement concrete.[4] The underuse of RCA in new concrete is primarily attributed to its material properties that can, if not properly accounted for in mixture design and proportioning, negatively affect the fresh and hardened properties of concrete.[5] Potential users often cite a lack of knowledge about its composition and suitability for use.[6,7]

The physical, mechanical, and chemical properties and characteristics of RCA can vary widely based upon the quality of the source concrete and production techniques used, and it is important to characterize the RCA prior to use in unbound or bound applications.[2-4,8] The variability of RCA, particularly when produced from crushed concrete obtained from multiple sources, is considered a barrier to increased use in new concrete.[3,4,7] Knowing the residual mortar content (RMC) of RCA is useful in predicting its performance. The residual mortar adhered to the coarse aggregates in RCA affects the characteristics of the RCA, including its absorption, specific gravity (SG), abrasion resistance, strength, and crushing value.[3,4,7,8] If the RCA is to be used in an unbound application, such as a roadbase, a higher mortar fraction will result in abrasion loss that may be unacceptable for use.[2,3] If the RCA is to be used in a bound application such as in new concrete mixtures, the mortar fraction will cause increased water demand, potentially resulting in issues with workability, finishing, strength, and permeability.[3,4,7-10] Adequate quality control (QC) in production and subsequent characterization testing is essential when producing RCAs and concrete containing RCA.[3,4,8,9]

The chemical composition of RCA will depend on the materials used in the aggregates and paste comprising the source concrete. Therefore, most RCAs are calcium- and silica-rich (primarily from aggregate sources), with aluminates, alkalies, and ferrous materials contributed by the cement. Chemical contaminants may also be present, including organic and inorganic chemicals.[4] Other contaminants may be present as entire particles from the crushing process, or as contaminants adhered to or contained within particles primarily consisting of RCA.[3] The presence of deleterious chemicals such as alkalies, sulfates, chlorides, organic impurities, and so on can negatively influence the properties of RCA concrete and its durability.[3,8,9] The ability to detect these impurities and contaminants could provide confidence in RCA use.

To date, no rapid methods for chemical characterization of RCA or estimation of its RMC have been developed and accepted. Nondestructive analytical testing techniques capable of determining the chemical and mineralogical characterization of RCA, such as inductively coupled plasma mass spectrometry (ICP-MS),[11] inductively coupled plasma-atomic emission spectrometry (ICP-AES),[12] infrared spectroscopy (IR),[12] conventional X-ray fluorescence, semi-quantitative X-ray diffraction, and thermogravimetric analysis (TGA-DTG)[13-15] each require a high investment cost, are time-consuming, and use a very small sample size, which may not allow accurate representation of contaminant materials in an RCA stockpile.

To overcome the shortcomings of these methods, this study proposed the use of a portable handheld X-ray fluorescence (PHXRF) device to chemically characterize and estimate the RMC of RCA.[16] XRF is an elemental analysis technique where a material excited by high-energy X-rays

ACI Materials Journal, V. 120, No. 5, September 2023.

MS No. M-2022-124.R2, doi: 10.14359/51738890, received February 15, 2023, and reviewed under Institute publication policies.

emits secondary X-rays of characteristic energy or wavelength. PHXRF devices are relatively simple to use, provide accurate analyses of a range of elements, and can be used in either field or laboratory settings.

Recently, studies have also focused on the analysis of geotechnical materials using PHXRF. Many transportation projects use stabilizers to improve the mechanical properties of soil. Previous studies have concluded PHXRF can be used to determine the stabilizer content in the subgrade, aiding geotechnical inspections by detecting irregularities.[17-19] Procedures developed by Cerato and Miller[18] and Cerato et al.[19] were used to guide work in the present study, and are presented herein in some detail to support the approach used for RCA characterization and to facilitate comparison of the findings of this work.

The study by Cerato et al.[19] was conducted on five sites where soils were stabilized with quicklime or high-calcium fly ash (Class C). Two PHXRF devices were used, and the stabilizer content readings of these devices were compared to laboratory readings using the whole-rock analysis technique to identify sample preparation and analysis techniques producing accurate PHXRF results. Whole-rock analysis is a geochemical technique widely used in the mining and geochemical fields to analyze rock samples to determine the composition of major and trace elements.[20-22] A composite chemical analysis approach, this technique involves tests including ICP-MS,[11] ICP-AES,[12] IR,[12] and loss on ignition (LOI).[23] Although each of these tests have limitations in determining the weight percent of certain elements, they are used together in whole-rock analysis to determine the weight percent of all major and trace elements comprising an entire rock sample. Samples are pulverized to the size of a few microns and are fused. Major and trace elements are quantified on a weight percent basis using the most appropriate approach (ICP-MS, ICP-AES, IR, or LOI).[20-23]

Cerato et al.[19] used statistical techniques including analysis of variance (ANOVA) and regression analysis to evaluate the accuracy of the PXHRF on determining sample composition. The influence of variables, including scan duration, scan technique, particle size, and the type of sampling on PHXRF results was also evaluated. A 60-second scan duration was determined to be appropriate for stabilized soil materials because longer scanning durations did not yield significant benefits in terms of precision. Scanning techniques (standard and quartering) were also evaluated to assess the homogeneity of the sample.[19] Particle size was found to play a prominent role in the accuracy of PHXRF to measure stabilizer contents, and the authors noted that significant benefits in terms of PHXRF accuracy are observed when particle sizes are reduced from passing No. 4 to No. 40, yet the benefits are less significant when particle sizes are reduced further. The effect of particle size on the root-mean-squared deviation (RMSD) and the coefficient of variation of the RMSD (COV_{RMSD}) revealed that milling samples to smaller particle sizes improved the accuracy of PHXRF readings, with the authors recommending that field preparation should be limited to milling samples passed on a No. 40 sieve for the sake of feasibility. With differences in design specified stabilizer content (typically 3 to 15% by weight) and PHXRF-determined stabilizer content ranging from approximately 1 to 2%, Cerato et al.[19] demonstrated that the PHXRF could be a useful tool to improve quality assurance (QA) and QC capabilities in future roadway inspections. More importantly, for the present work on RCA characterization, this study demonstrated the capability of PHXRF to successfully characterize granular, silicate, and calcareous materials.

With lesser success, PHXRF was used to estimate the mixture proportions of concrete.[24] The individual chemical composition of cementitious materials (slag cement, silica fume, Class C fly ash, Class F fly ash, and Type I portland cement) used in concrete mixtures was initially tested using the PHXRF. Paste mixtures with different combinations of the cementitious materials and mortar samples (1:3 cement-to-sand ratio by mass) were prepared and evaluated using the PHXRF. Results were averaged after testing three samples from each mixture. The researchers determined the PHXRF was reasonably accurate in determining the supplementary cementitious material (SCM) dosages of paste mixtures, but the inhomogeneity of the mortar samples affected the analysis of mortar, which increased errors.[24]

RESEARCH SIGNIFICANCE

Currently, no rapid test method exists to support chemical characterization and RMC determination for RCA. The inability to know this information about RCA from different sources is often cited as a barrier to use of RCA in bound and unbound applications. As a rapid, easy-to-use technology, PHXRF has been successfully used in construction applications, including the analysis of granular soil materials and cementitious/pozzolanic binders. Therefore, PHXRF shows promise for use in the analysis and characterization of RCA. In this study, an established sampling method and testing protocol to support the use of PHXRF for the characterization of RCA was developed. This method will support quality assurance and increased confidence in RCA for use in unbound and bound applications, including new concrete. Increased beneficial reuse of RCA will assist many entities in meeting their sustainability goals, and will provide environmental benefits associated with reduced virgin material use, decreased landfill use, and potentially reduced greenhouse gas emissions associated with transport and production.[1,3]

EXPERIMENTAL DESIGN AND PROCEDURE

A variety of different RCAs in terms of type of source and quality of parent concrete were collected from multiple U.S. states: Nebraska (NE), North Carolina (NC), Iowa (IA), and Texas (TX). Table 1 presents the nine aggregates used in this study with photographs and crushing methods provided in Hu et al.[16] and Mamirov et al.[25] The aggregate identification scheme is XX_YYa, where XX indicates the state abbreviation, YY indicates the type of source (where CT refers to municipal crushing and grading plant, HW refers to highway pavement project, and AP refers to airport pavement project), and a is a number used when different samples were obtained from the same state and type of source. Each RCA was characterized for SG, absorption, crushing value, and RMC (Table 2). Because many of these characteristics vary by the

size fraction tested, the values reported in Table 2 are the average value for the sample, with the RMC value reported for the No. 67 gradation of aggregate per ASTM C33/C33M-18.[28] Test results for properties of various size fractions of each RCA are presented in Mamirov et al.[25]

Laboratory-measured RMC values were needed for reference and comparison to PHXRF test results. Historically, RMC has been determined using several methods, including image analysis,[5,29] mortar disintegration by chemical methods,[30-34] and thermal shock methods, which use changes in temperature and moisture to separate the mortar fraction from aggregates.[29,33-35] Based on the efficiency in terms of time, equipment, and relative simplicity, the thermal shock method was selected for determining the RMC for RCA in this study. However, in previous studies using the thermal shock method, each researcher's approach varied slightly, and several limitations were identified. For example, in work by de Juan and Gutiérrez,[35] Butler et al.,[33] and Pepe et al.,[29] consistent, detailed procedures including important parameters such as sample size, amount of sample tested, temperature of water used for the soaking process, and soaking duration were not consistently used, described, or verified to provide the best results. Therefore, one aim of the larger study supporting this work was to develop a rapid method to quantify RMC, including a detailed, repeatable procedure. To identify the temperature and grinding procedure most effective in separating the RMC from the aggregate without abrading original natural aggregate, a series of tests were performed using temperatures ranging from 500 to 750°C (in 50°C increments) and grinding times ranging from 2 to 220 minutes (at a variety of intervals). Development of this procedure, including specimen preparation, temperature selection, the soaking process, and mortar removal through jar mill, is detailed in Mamirov et al.[25] The optimal heating temperature was identified as 650°C and the optimal grinding time was identified as 100 minutes.[25] These parameters were used in the thermal shock method approach used to support the work to develop the PHXRF test approach described herein.

In summary, the thermal shock method procedure[25] used to determine the RMC began with the preparation of 500 ± 25 g (1.10 ± 0.055 lb) of a single-sized coarse RCA by removing any visible contaminants. The sample was soaked in 23 ± 2°C (73.4 ± 3.6°F) water for 2 hours, then placed into a preheated furnace and allowed to heat at 650°C (1202°F) for 2 hours. The heated RCA sample was then removed from the furnace and immediately submerged in 23°C (73.4°F) water (with a water-to-RCA ratio of 2.70 by mass) for 0.5 hours. The sample was then drained and then oven-dried at 110 ± 5°C (43.3 ± 9°F) for 24 ± 4 hours, and subsequently placed in a jar mill with 20.63 x 20.63 mm (0.8125 x 0.8125 in.) cylindrical alumina grinding media (approximately 1:1 sample-to-grinding medium ratio, by mass) and ground at 70 rpm speed for 100 minutes. The sample was then sieved using a 4.75 mm (No. 4) sieve to separate residual mortar from the original NA. The RMC (%) was then calculated using Eq. (1).

$$\text{RMC (\%)} = \frac{\text{Mass of material passed No. 4 sieve}}{\text{Total mass}} \times 100 \quad (1)$$

The results of the SG, absorption, crushing value, and RMC are presented in Table 2. SG values for RCA included in this study ranged from 2.20 to 2.52, where higher values correspond to RCA crushed from a higher-quality concrete, such as highway or airport pavement. Results showed that for the RCA specimens included in this

Table 1—Sources and information about RCA samples

Aggregate ID	U.S. state	Source	Parent concrete use
NC_CT1	NC	C&D waste processing facility	Not known
NC_CT2	NC	C&D waste processing facility	Not known
NC_AP1	NC	Airport pavement project	Airfield pavement
NC_HW1	NC	Pavement contractor	Highway pavement
NE_HW1	NE	Pavement contractor	Highway pavement
NE_HW2	NE	Pavement contractor	Highway pavement
NE_CT2	NE	C&D waste processing facility	Not known
IA_CT1	IA	C&D waste processing facility	City-owned pavement
TX_CT1	TX	C&D waste processing facility	Not known

Table 2—RCA physical characteristics

	Test and test method			
	SG (oven-dried)	Absorption, %	Crushing value, %	RMC, %
Aggregate ID	ASTM C127[26]	ASTM C127[26]	Modified BS 812-110[27]	Procedure presented in Mamirov et al.[25]
NC_CT1	2.32	5.52	15.02	41.93
NC_CT2	2.20	6.28	16.37	55.75
NC_AP1	2.52	4.10	11.47	33.67
NC_HW1	2.25	6.09	13.06	43.93
NE_HW1	2.30	4.25	17.53	63.77
NE_HW2	2.25	5.17	20.07	68.12
NE_CT2	2.22	5.80	25.15	72.23
IA_CT1	2.25	5.63	16.15	53.62
TX_CT1	2.20	7.14	18.31	34.86

study, the RMC varied from 33.67 to 72.23%. It should be noted that the Nebraska RCA exhibited most of the high RMC values, which is due to their unique mixture designs for concrete where the major proportion of aggregate is a combination of sand and gravel aggregate that is mostly fine aggregate, yet includes a small fraction with a typical coarse aggregate size range.

Reference samples for each of the four NC RCA samples were prepared and then sent to an external laboratory to determine the chemical composition by whole-rock analysis. Based on the laboratory-measured RMC, and using the RMC and aggregate fractions produced during testing, a 20 g composite sample (residual mortar and original virgin aggregate contained in the RCA) of each RCA was prepared, comprised of X% of 20 g and (100-X)% of 20 g, where X is the mortar content and 100-X is the original virgin aggregate content. Results of the whole-rock analysis for elements found significant in this study are provided in Table 3, with all elements (65 in total) presented in Hu et al.[16] and Dey.[36] Results from the whole-rock analysis for many elements were provided by the analytical laboratory in oxide weight percent form, and were converted to elemental weight percent using atomic weights.

Several studies have published the chemical composition of RCA from a wide range of sources. Relative percent weights of each RCA used in this study tended to relatively align with the chemical compositions of RCAs characterized in other studies,[13-15] with relatively high (often ranging from 20 to 50%) elemental contents of Si and Ca; moderate elemental contents (approximately 0.5 to 10%) of Al, Fe, Mg, K, and Na; and far lower elemental contents (typically less than 1%) of other elements.

As expected, the specimens primarily comprise elements including Si, Ca, Al, and Fe, which are present in aggregates and cementitious materials. NC_CT1, NC_HW1, and NC_AP1 contained granitic gneiss as coarse aggregate in the source concrete, and therefore had elemental weights of Si close to 30%. NC_CT2 was sourced from closer to the Atlantic Ocean coast, and contained a marine limestone as the coarse aggregate of the source concrete. The elemental weight of Ca for NC_CT2 was approximately 30%, while the elemental weight of Si was only approximately 10%. Other elements that could be expected to be contained in smaller (or trace) amounts in either the cementitious materials or the aggregate were also measured, often at elemental weights significantly below 1%.

The PXHRF cannot determine chemical composition directly. Instead, the device measures chemical composition by penetrating the sample with an X-ray beam to relatively shallow depths that vary depending on the element being measured and on particle characteristics such as density and surface texture. Therefore, PXHRF data was used to develop models to estimate the RMC and chemical composition of each RCA sample. Model predictions were compared to reference values obtained through laboratory testing. By comparing PHXRF results to values determined by outside laboratories using more extensive, time-consuming techniques, the accuracy and repeatability of the results obtained from the PHXRF could be evaluated, and sample preparation and analysis techniques could be refined into a recommended testing protocol. This approach is shown in Fig. 1.

A handheld PHXRF (rhodium target with a silicon drift detector system) was used, with the manufacturer-prepared mudrock/ceramic calibration file. The calibration has two parts: the first part is to quantify major (lighter)

Table 3—Element weight percent or ppm obtained through whole-rock analysis

Element	Units	Limit of detection	Element weight, % (or ppm as noted)			
			NC_CT1	NC_CT2	NC_HW1	NC_AP1
Si	% weight	0.01	29.82	10.05	29.45	27.25
Ca			7.90	30.45	7.50	7.57
Al			5.45	0.56	6.30	6.96
Fe			3.18	0.62	1.97	6.29
Na			1.37	0.09	2.27	1.62
Mg			1.26	0.49	0.37	2.51
K			1.02	0.16	2.78	0.45
Ti			0.31	0.05	0.16	0.77
S			0.17	0.21	0.14	0.16
P			0.06	0.14	0.05	0.13
Mn			0.05	0.03	0.04	0.10
Ba			0.04	0.01	0.08	0.04
Cr			0.00	0.01	0.00	0.01
V	ppm	5	105	21	42	215
Zn		0.2	71.7	43.4	63.2	72
Cu		0.02	40.8	5.62	12.9	65.2
Ni		0.08	20.9	15.3	10.25	64.2

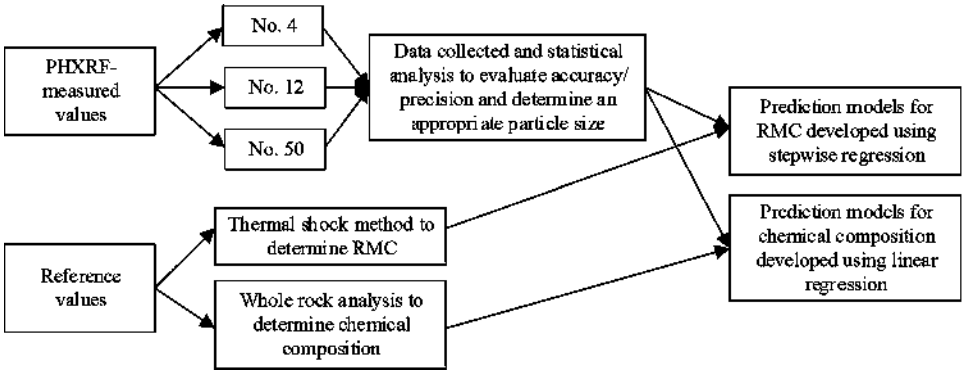

Fig. 1—Approach used to develop models for RMC and chemical characterization of RCA using PHXRF measurements.

(2a) PHXRF used in benchtop mode, connected to a vacuum pump, with sample cup protected by shield

(2b) Sample cup placed on table mounted to nose of PHXRF

(2c) Figure 31 PHXRF samples in cups secured with polyester film (left, rear) and inverted (right)

Fig. 2—PHXRF device setup.

elements—that is, Na to Fe (atomic numbers 11 to 26)—and the second part is the quantification of trace (heavier) elements—that is, Co to U (atomic numbers 27 to 92). It is noted that the device cannot detect elements lighter than Na (atomic numbers less than 11), so elements such as H, O, and C likely present in the RCA will not be detected and the total weight percent will not add to 100%.

The PHXRF can be operated as either a handheld device or in a bench-top setup (configuration used for this work). The instrument was mounted on a stand, and a sample table was fixed to the nose of the instrument to provide a flat working surface (Fig. 2(b)). To test each sample, a sample cup is placed on the sample table in an inverted fashion. A shield is placed over the sample (Fig. 2(a)) to prevent radiation exposure to the user. The PHXRF is connected to a computer, which controls the instrument and analyzes the spectrum generated using the S1PXRF software. Detecting major elements requires use of a vacuum pump provided with the device (Fig. 2(a) and (b)). The instrument requires different settings for the quantification of major and trace elements, and recommendations for the use of the mudrock/ceramic calibration file guided the setting selection. The voltage used was 15 kV for major elements and 40 kV for trace elements, as recommended by the manufacturer. The scan duration was 180 seconds for major elements and 60 seconds for trace elements. Use of a filter is recommended to optimize the excitation conditions for a group of elements (heavy elements) when used with a certain voltage setting. A yellow filter, composed of Ti and Al, was used for trace elemental analysis.[37]

In the development of a proposed PHXRF testing protocol for RCA, several variables must be considered to obtain accurate measurements,[16,36] including: 1) sample type and preparation, including size and containment vessel; 2) particle size: Cerato et al.[19] and Imanishi[38] observed that the grain size of soil samples influenced XRF intensity; 3) sample thickness: PHXRF intensities are influenced by the thickness of the sample, and the minimum thickness for each element is correlated to its characteristic X-ray energy[39]; 4) duration of each scan; and 5) scanning technique, including sample size, location of scans, and number of replicates.

To ensure the procedure was practical to perform in both field and laboratory settings, loose aggregate samples were used. The samples of RCA as received from the producers were sieved and the particle size fractions retained on sieve sizes 4.75 mm (No. 4), 1.70 mm (No. 12), and 300 µm (No. 50) were separated for analysis. These particle sizes were selected due to their presence in both fine and coarse RCA and their alignment with the particle sizes investigated successfully in the work by Cerato et al.[19] Each sample was placed into a cylindrical sample cup with an internal diameter of 38.1 mm (1.5 in.) and an internal height of 15.24 mm (0.6 in.) and was secured using a 6 µm (0.000236 in.) thick mylar film over the opening of the sample cup (Fig. 2(c)). Based on the minimum depth requirements for each element, the sample cup chosen for this analysis had a depth of 15.24 mm (0.6 in.) to mitigate the inaccuracies caused due to the

infinite thickness phenomenon. It is noted that larger particle sizes could be used for this work, but additional research would be needed to investigate the impact on the results.

For the scan technique, a quartering approach was used, similar to the approach developed by Cerato et al.[19] Cerato et al.[19] found that the quartering approach, where each quarter of a sample cup is scanned three times (a total of 12 measurements per sample), provided "a unique opportunity to assess sample homogeneity" because PHXRF typically have a small X-ray beam footprint. Each sample cup was divided into four quadrants (shown in Fig. 2(b)), with each quadrant scanned three times at three different locations for a total of 12 scans per sample cup. The average value of the 12 scans was computed for both major and trace elements.

Statistical analysis of the data obtained using the PHXRF began with a one-way ANOVA performed on the data sets to prove a statistically significant difference between the test results obtained for different size fractions of RCA (of the same type) and RCA obtained from different sources (using the same size fraction).

To determine the most appropriate particle size for testing, the approach was to identify the lowest value of RMSD at the largest particle size. Beyond this value, the effects of particle size on RMSD would level off.[19] The RMSD is defined as the standard deviation of the residuals and indicates the dispersion of the data points from the regression line, with RMSD values closer to 0 suggesting higher accuracy. Other statistical parameters were used to assess the accuracy and precision of the measurements and are detailed in Dey[36] as well as the final project report.[16]

Models were constructed using the PXHRF-measured chemical composition to predict the laboratory-measured RMC using stepwise regression. To predict the laboratory-measured chemical composition of RCA samples, a simple linear regression was performed using the PHXRF elemental weight percent and the weight percent of elements obtained from whole-rock analysis.

RESULTS AND DISCUSSION

Evaluating particle size influence for PHXRF characterization of RCA

Initial work to identify the most appropriate particle size for analysis focused on the four RCAs from NC. Table 4 provides the average weight percent of elements from the RCA samples tested using the PHXRF. Note that elements that were present at levels below the detection levels of the instrument (or were detected at 0.0000%) were removed from the table to aid in clarity. Elements found significant in this study are provided in Table 4, with all elements (65 in total) presented in Hu et al.[16] Results are provided for the three particle sizes of interest, 4.75 mm (No. 4), 1.70 mm (No. 12), and 300 µm (No. 50), with the value reported being the mean computed from 12 measurements (three measurements taken randomly from each of the four quadrants of the sample). Details of all PHXRF measurements are provided in Dey[36] and in the project final report.[16]

Using Minitab software, ANOVA tests were performed to prove a statistically significant difference between the test results for different sizes (4.75 mm [No. 4], 1.70 mm [No. 12], and 300 µm [No. 50]) within each RCA sample

Table 4—Average element concentrations in weight percent from PHXRF

	NC_AP1			NC_CT1			NC_HW1			NC_CT2		
Element	4.75 mm	1.75 mm	300 µm	4.75 mm	1.75 mm	300 µm	4.75 mm	1.75 mm	300 µm	4.75 mm	1.75 mm	300 µm
Si	4.2152	4.3376	5.1253	3.8349	4.2804	6.7317	4.5482	4.1852	4.8632	2.3525	2.2261	3.0400
Ca	4.1318	4.4303	4.0024	6.3559	7.3314	5.8792	4.4733	4.7039	5.1282	13.3876	14.0301	13.0233
Al	1.1005	1.1205	1.4142	0.3400	0.4525	0.4540	0.5891	0.8335	0.9614	0.0000	0.0042	0.0084
Fe	2.0522	1.0289	0.9035	0.3143	1.5305	0.8296	0.9243	0.9277	1.3025	0.2938	0.3408	0.4266
Na	0.0809	0.0000	0.0516	0.0008	0.0112	0.0000	0.0000	0.0329	0.0000	0.2808	0.2490	0.1556
K	0.2779	0.2708	0.2967	0.2366	0.3005	0.2588	0.5808	0.6666	0.9526	0.1108	0.1468	0.1474
Ti	0.2132	0.0970	0.0812	0.0246	0.1109	0.0701	0.0519	0.0645	0.0883	0.0192	0.0198	0.0325
S	0.5025	0.4984	0.5051	0.5628	0.5662	0.5866	0.5608	0.5012	0.5017	0.2613	0.2855	0.3591
P	0.0190	0.0040	0.0109	0.0069	0.0147	0.0012	0.0117	0.0014	0.0005	0.0188	0.0091	0.0000
Mn	0.0284	0.0275	0.0282	0.0223	0.0243	0.0281	0.0248	0.0239	0.0240	0.0215	0.0226	0.0224
Ba	0.3778	0.6236	0.8227	0.2238	0.0098	0.0966	0.0480	0.0769	0.0027	0.0000	0.0287	0.0103
Cr	0.0047	0.0063	0.0066	0.0045	0.0039	0.0060	0.0043	0.0054	0.0052	0.0023	0.0025	0.0034
V	0.0000	0.0000	0.0000	0.0013	0.0019	0.0055	0.0033	0.0042	0.0063	0.0049	0.0038	0.0054
Zn	0.0027	0.0056	0.0061	0.0053	0.0097	0.0025	0.0027	0.0062	0.0026	0.0031	0.0006	0.0025
Cu	0.0019	0.0072	0.0083	0.0042	0.0083	0.0032	0.0006	0.0043	0.0023	0.0038	0.0049	0.0011
Ni	0.0017	0.0036	0.0031	0.0026	0.0024	0.0012	0.0012	0.0022	0.0012	0.0021	0.0026	0.0018
Pb	0.0012	0.0012	0.0009	0.0010	0.0011	0.0011	0.0014	0.0012	0.0015	0.0010	0.0010	0.0011
Rb	0.0010	0.0010	0.0015	0.0019	0.0022	0.0007	0.0040	0.0102	0.0060	0.0005	0.0004	0.0005
Sr	0.0374	0.0818	0.0554	0.0357	0.0354	0.0108	0.0156	0.0392	0.0240	0.0404	0.0358	0.0290

and for each size across the four RCA samples. Tests were performed at a significance level of 5% ($\alpha = 0.05$), with tests returning a *p*-value of less than or equal to 0.05 considered statistically significant (shaded in Table 5). The test results (output) obtained from Minitab software are presented in Dey[36] and in the project final report.[16]

ANOVA test results revealed that for each particle size within each sample, the majority of the elements are statistically significant, indicating that the PHXRF results were affected by particle sizes for major and trace elements. A few elements were insignificant, indicating that the results were not affected by particle size, at least for the samples used in this analysis. ANOVA tests performed across samples of the same particle size revealed that many of the elements were statistically significant, indicating that the results were often affected by the source concrete of the samples obtained. It is noted that results differed for each source, with NC_CT1 having 13 of 18 elements significant, NC_AP1 having 10 of 18 elements significant, NC_HW1 having nine of 18 elements significant, and NC_CT2 having only six of 18 elements significant.

To understand the effects of particle size on PHXRF results, RMSD values were computed for each element present in the sample. The RMSD was calculated by determining the sample standard deviation of the difference between the whole-rock analysis results and PHXRF measurements. Figures 3(a) and (b) show the relationship between the particle size and the RMSD values for NC_CT1, which exhibited results that could be considered typical of the other three samples (results shown along with other statistics in Dey[36] and Hu et al.[16]) As can be observed in Fig. 3, the RMSD values for Si (NC_AP1, NC_CT1, and NC_HW1) and the Ca (NC_CT2) were high and in the unacceptable range (far greater than 1), whereas the rest of the elements were reasonable. One reason for this could be the fact that these elements were the primary elements present in each sample. The difference could be attributed to the fact that whole-rock analysis measures a pulverized sample from the whole RCA specimens, while PHXRF measures to a certain depth from the surface that could be influenced by the location of the aggregate particles in RCA.

Most of the trace elements showed RMSD values less than 1, indicating that the measured values for trace elements are close to the whole-rock analysis values and that the data is concentrated around the line of best fit. Contrary to what was observed in a similar analysis of soils,[18,19] the RMSD values for RCA samples did not decrease with a decrease in particle size. This could be attributed to RCA's heterogeneous composition due to the presence of adhered mortar and other contaminants, whereas the sample under consideration in the literature review was soil that had a more homogenous composition. Therefore, based on the RMSD values, it can be concluded that the particle size may not have a significant impact on the elemental concentrations of the majority of the elements for the samples tested in this research study using PHXRF.

Development of models to predict RMC using PHXRF

To predict the RMC of RCA from the PHXRF data, models were developed using the stepwise regression

Table 5—ANOVA tests for 4.75 mm (No. 4), 1.70 mm (No. 12), and 300 µm (No. 50) RCA samples

Major/ trace elements	Across RCA sources				Across particle sizes		
	p-value				*p*-value		
	NC_AP1	NC_CT1	NC_HW1	NC_CT2	4.75 mm	1.70 mm	300 µm
Si	0.001	0.000	0.189	0.000	0.000	0.000	0.000
Ca	0.233	0.008	0.311	0.535	0.000	0.000	0.000
Al	0.000	0.182	0.005	—	—	0.000	0.000
Fe	0.034	0.000	0.054	0.333	0.000	0.000	0.000
K	0.236	0.171	0.000	0.090	0.000	0.000	0.000
Ti	0.010	0.000	0.007	0.032	0.000	0.000	0.000
S	0.928	0.471	0.226	0.000	0.000	0.000	0.000
P	0.169	0.007	0.023	—	0.381	0.025	0.008
Mn	0.864	0.013	0.562	0.092	0.004	0.001	0.000
Ba	0.212	0.005	0.276	—	—	0.027	0.002
Cr	0.007	0.012	0.020	0.001	0.000	0.000	0.000
V	—	0.058	0.075	0.064	—	—	—
Zn	0.000	0.000	0.000	0.023	0.018	0.000	0.000
Cu	0.000	0.000	0.000	0.073	0.055	0.001	0.000
Ni	0.007	0.000	0.002	0.078	0.000	0.000	0.000
Pb	0.020	0.788	0.248	0.830	0.063	0.683	0.001
Rb	0.058	0.003	0.000	0.834	0.000	0.000	0.000
Sr	0.000	0.000	0.000	0.007	0.000	0.000	0.000

Note: "—" indicates that no *p*-value was computed; RMSD and COV_{RMSD} could not be determined because element weight percent was 0.

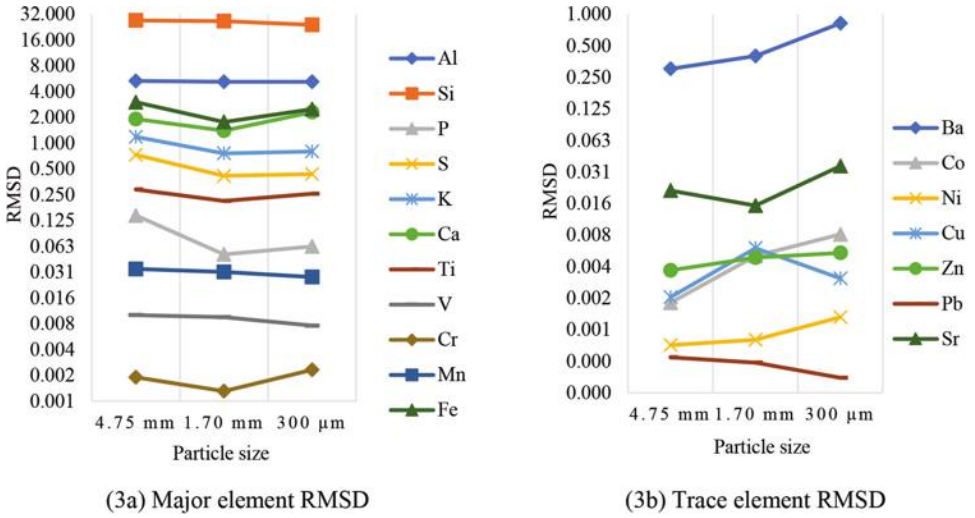

(3a) Major element RMSD

(3b) Trace element RMSD

Fig. 3—Major and trace element RMSD of RCA from NC_CT1.

Table 6—Regression equations for 4.75 mm (No. 4), 1.70 mm (No. 12), and 300 µm (No. 50)

Particle size	Model to predict mortar content	R^2
4.75 mm (No. 4)	RCA mortar content (weight %) = 54.52 + 3787 × V − 16,911 × Pb	0.999
1.70 mm (No. 12)	RCA mortar content (weight %) = 189.97 − 524.0 × P − 124,820 × Pb	0.998
300 µm (No. 50)	RCA mortar content (weight %) = 78.66 − 6588 × Cr	0.958

Table 7—Assessment of RMC prediction models for each particle size fraction

	4.75 mm (No. 4) size			1.70 mm (No. 12) size			300 µm (No. 50) size		
RCA sample	Measured RMC	Predicted RMC	% Diff.	Measured RMC	Predicted RMC	% Diff.	Measured RMC	Predicted RMC	% Diff.
NC_AP1	33.7	33.9	–0.66	33.7	33.4	1.02	33.7	35.5	–5.18
NC_CT1	41.9	41.6	0.62	41.9	42.1	–0.55	41.9	39.3	6.27
NC_HW1	43.9	43.8	0.25	43.9	44.3	–0.88	43.9	44.6	–1.57
NC_CT2	55.8	55.9	–0.24	55.8	55.5	0.52	55.8	56.0	–0.32

method. Both forward selection and backward elimination approaches were used to build a best-fitted combination of the independent and dependent variables. During each step, the least significant variables were removed and the most significant ones were added to the model. Variables were added and deleted from the model based on the selected alpha-to-enter and alpha-to-remove values (0.15 was used for both alpha values). The software systematically adds and removes the variables based on the *p*-values of the variables at each step. Models were developed for particle sizes 4.75 mm (No. 4), 1.70 mm (No. 12), and 300 µm (No. 50) (Table 6) with supporting data published in Dey[36] and the project final report.[16]

The laboratory-measured RMC was compared to the RMC predicted based on PHXRF data, and the models for all three particle sizes were fairly strong predictors of the mortar content (Table 7). However, the model for the 4.75 mm (No. 4) size fraction provided the closest prediction. Somewhat greater differences exist between measured and predicted values for the 300 µm (No. 50) and the 4.75 mm (No. 4) and 1.70 mm (No. 12) models. This greater difference could be attributed to the changes in proportion of mortar and aggregate components, which vary by particle size. With the increase in the nominal size of RCA, the adhered mortar fraction tends to decrease.[3] The result is also confirmed by Mamirov et al.[25] It is noted that two models included Pb, which was not detectable using the whole-rock analysis procedure. Users of this approach could choose to limit the variables included in the regression to those obtainable in the reference samples through whole-rock analysis.

Using PHXRF to predict mortar content—expanded data set and evaluation of models

After demonstrating that models could be developed to predict mortar content, the research team desired to improve the model with, and validate the effectiveness of the developed model with, an expanded data set. To do so, PHXRF data for the 4.75 mm (No. 4) size fraction of the five additional RCA sources TX_CT1, IA_CT1, NE_HW1, NE_HW2, and NE_CT2 (shown in Table 8) was combined with the 4.75 mm (No. 4) particle size PHXRF data from the four NC sources (Table 4) to produce an expanded data set. Note that in Table 8, similar to Table 4, elements that were present at levels below the detection levels of the instrument (or were detected at 0.0000%) were removed from the table to aid in clarity. Improved models were developed to predict laboratory-measured RMC from the PHXRF data using the stepwise regression method described previously. To

accomplish this, PHXRF data for three of the five additional RCA sources (IA_CT1, NE_HW2, and NE_CT2) were added to the data for NC_CT1, NC_HW1, NC_HW2, and NC_AP1 and used to train the models. PHXRF data for two of the five additional RCA sources (TX_CT1 and NE_HW1) were not used to train the models and instead were used to evaluate the models.

Minitab software's stepwise regression tool was used to build the regression model equation with the best predictor variables for the mortar content, with variables added and deleted from the model based on the selected alpha-to-enter and alpha-to-remove values of 0.15. The improved model to predict mortar content using PHXRF data from the 4.75 mm (No. 4) particle size of seven sources is shown in Eq. (2). The R^2 value for this equation was 0.999.

$$\text{RMC (weight \%)} = 77.687 - 12.683 \times \text{Ba} - 5805.13 \times \text{Cr} - 520.77 \times \text{U} + 29.49 \times \text{Sr} - 52606 \times \text{Sn} \quad (2)$$

As shown in Table 7, preliminary models for predicting mortar content using the four NC RCA sources of three different sizes included the elements of V, Pb, Cr, and P. Of note, the improved model using No. 4 PHXRF data from seven sources again included Cr, along with other trace elements, including Ba, U, Sr, and Sn. The R^2 of the preliminary 4.75 mm (No. 4) model was 0.999, while the improved model R^2 was also 0.999. The variance inflation factor (VIF) for each of the five predictor variables was lower than 10, indicating an acceptably low degree of multicollinearity. A review of the stepwise regression outputs indicated that models with four predictor variables (Cr, U, Sn, and Ba) and three predictor variables (Cr, U, and Sn) would also be suitable for use, with R^2 values for these models being 0.995 and 0.973, respectively.[16]

The improved model was evaluated using the 4.75 mm (No. 4) PHXRF data from TX_CT1 and NE_HW1, which was not used in model development, with the percent difference between the laboratory-measured RMC and predicted RMC shown in Table 9. The improved model, which uses a broad range of RCA samples, appears to provide a reasonable prediction for both a low-RMC RCA (TX_CT1) and an RCA with a very high RMC (NE_HW1). This additional analysis reaffirmed that the PHXRF could be used to predict the mortar content of RCA, using the elemental concentrations of trace elements, often heavy metals, as predictor variables. It also illustrated how the approach could be used by practitioners developing and assessing their own models using locally available RCA sources.

Stepwise regression resulted in the selection of trace elements, often heavy metals, as the strongest predictors of mortar content. Depending on the RCA, these elements could be present in the paste only due to their relatively higher presence in cement and fly ash, or may be present in very low quantities in the aggregate alone. From the PHXRF data obtained for aggregate only[9,25] as part of this work, it was observed that these metals were actually present in low concentrations in the aggregates, which made them good predictors. On the other hand, major elements such as Ca, Si, Fe, and Al, which were initially thought to be strong potential predictors of mortar content, were not identified as predictor variables, likely due to the fact that they were present in both the aggregate and the cement paste in significant quantities.

Table 8—Average element concentrations in weight percent from PHXRF for 4.75 mm (No. 4) size of five additional RCA samples

Element	TX_CT1	IA_CT1	NE_HW1	NE_HW2	NE_CT2
Si	2.4394	2.2996	5.3198	2.3845	3.8575
Ca	7.8630	6.9057	3.3849	7.2596	3.4007
Al	0.0292	0.0143	0.0825	0.0000	0.2568
Fe	0.5345	0.6695	0.2352	0.4746	0.4520
Na	0.0000	0.0000	0.0000	0.0000	0.0000
K	0.0610	0.0994	0.2807	0.1539	0.4813
Ti	0.1307	0.4140	0.2416	0.4081	0.2927
S	0.8788	0.5161	0.5397	0.4063	0.5283
P	0.0002	0.0000	0.0000	0.0000	0.0000
Mn	0.0185	0.0193	0.0205	0.0187	0.0198
Ba	2.4785	0.1702	0.1325	0.1710	0.1192
Cr	0.0000	0.0000	0.0000	0.0000	0.0000
V	0.0000	0.0000	0.0000	0.0000	0.0000
Zn	0.0027	0.0057	0.0010	0.0013	0.0045
Cu	0.0019	0.0035	0.0004	0.0026	0.0013
Ni	0.0017	0.0029	0.0021	0.0027	0.0020
Pb	0.0012	0.0014	0.0011	0.0012	0.0012
Rb	0.0010	0.0022	0.0089	0.0037	0.0123
Sr	0.0374	0.0321	0.0244	0.0495	0.0235

Table 9—Assessment of improved RMC prediction model for 4.75 mm (No. 4) size

RCA sample	Measured RMC	Predicted RMC	% Difference
TX_CT1	34.86	34.54	–0.32
NE_HW1	63.77	70.99	7.23

One barrier to the use of RCA in unbound uses is the potential for heavy metals from the RCA to leach into waters flowing around/over the RCA.[3,40,41] Although this approach appears to provide a readily implementable method to predict the mortar content of RCA, it may call attention to a negative aspect of RCA, which could also be a detractor to its use. It is noted, however, that many state transportation agencies allow RCA as unbound base, where it is commonly used. In these unbound applications, metals in leachate have not been found to be problematic in most situations.[3]

Prediction of chemical composition of RCA using PHXRF data

Because the PHXRF only detects material to a certain depth (ranging from 0.000001 to 0.4 cm [3.9×10^{-7} to 0.16 in.]) depending on the element, for the mudrock/ceramic calibration file used, it was not anticipated that the weight percent value reported by the PHXRF would be directly comparable to the weight percent value determined through whole-rock

analysis, where the sample is pulverized and more extensive testing is performed on the full volume of the sample. Therefore, a simple linear regression analysis was performed to develop models capable of predicting the laboratory-measured chemical composition using the PXHRF data. A particle-size-based simple regression model for each element was created to estimate the relationship between the whole-rock analysis values and the PHXRF values from the four RCA samples. For each particle size and each major and trace element, the laboratory-measured content (x-axis) versus PHXRF-measured content (y-axis) was plotted. A trend line with an R^2 value was produced for each plot. All regression models are presented in Dey,[36] and a summary is provided in this paper. In Table 10, the R^2 value for the particle sizes 4.75 mm (No. 4), 1.70 mm (No. 12), and 300 μm (No. 50) for each element have been indicated with text and table styling, where shaded values represent stronger models (R^2 above 0.70), underlined values represent less strong models (with R^2 between 0.40 and 0.69), and italicized values represent weak models (R^2 lower than 0.40).

Based on the R^2 values, particle sizes 4.75 mm (No. 4) (14 elements out of 27) and 1.70 mm (No. 12) (13 elements out of 27) show a strong relationship between the whole-rock analysis and PHXRF results for major and trace elements. Elements including Si, Ca, K, V, Th, and Rb showed exceptional R^2 values, implying that they were more predictable compared to the other elements. Overall, stronger models tended to be observed for elements present in greater amounts (higher weight percent) than trace elements. This improved predictability could be attributed to the fact that the relative quantities of these elements present in the samples were significant. It is worth noting that major elements commonly exist in cement paste, particularly Si, Ca, and Al; all exhibit high R^2 in all three sizes. Whole-rock analysis is a fairly costly laboratory test, and in this work, only one analysis was run per RCA sample, which likely limited the findings. Developing a reference sample for each size of RCA, as well as testing additional samples of RCA, would likely give more accurate results. In practice, a user could allocate sufficient resources to perform whole-rock analysis on a suitably broad range of locally available RCA to expand the reference values and provide additional confidence in the regression models for elements of interest.

Table 10—R^2 values for models predicting major and trace elements

Element	R^2 value		
	4.75 mm (No. 4)	1.70 mm (No. 12)	300 μm (No. 50)
Si	0.885	0.972	0.748
Ca	0.971	0.922	0.968
Al	0.576	0.858	0.783
Fe	0.728	*0.268*	*0.075*
K	0.908	0.975	0.938
Ti	0.869	0.461	*0.261*
S	0.813	0.634	0.472
Mn	0.730	0.978	0.642
Ba	0.500	0.614	*0.052*
Cr	0.542	*0.225*	*0.247*
V	0.880	0.948	0.827
Zn	*0.105*	0.782	0.221
Cu	*0.000*	0.620	0.879
Ni	*0.002*	0.946	0.849
Pb	*0.364*	*0.024*	0.768
Rb	0.990	0.978	0.874
Sr	*0.181*	0.907	0.635

Note: Shaded values represent stronger models (R^2 above 0.70); underlined values represent less strong models (with R^2 between 0.40 and 0.69); *italicized* values represent weak values (R^2 lower than 0.40).

Recommendation for particle size for PHXRF analysis

The 4.75 mm (No. 4) size exhibited the strongest model used to predict the laboratory-measured RMC. Although results were more variable in the elemental analysis, there was not a significant improvement in predictions between the 4.75 mm (No. 4) and 1.70 mm (No. 12) particle size, and the 300 μm (No. 50) size had the least strong correlations of the three particle sizes tested. Regression analysis indicated that the PHXRF results show reasonable accuracy for most of the major and trace elements detected and quantified by the PHXRF using the 4.75 mm (No. 4) size. Therefore, to simplify a recommended test method, the 4.75 mm (No. 4) size is suggested for future use of the PHXRF to analyze RCA because it shows reasonable accuracy for the elements under consideration. It should be noted that use of the 4.75 mm (No. 4) size would provide an advantage over the smaller sizes because the 4.75 mm (No. 4) size is typically present in both the coarse RCA and fine RCA produced from a given source concrete.

Recommended procedure for PHXRF analysis

1. Sampling: Care should be taken during sampling to ensure that representative RCA material is selected from the stockpile. ASTM D75/D75M-19[42] can be followed for guidance.

2. Physical characterization tests: Characterize RCA samples using sieve analysis (ASTM C136/C136M-19[43]), density, relative density (specific gravity), absorption (ASTM C127-15[26]), and bulk density and voids in aggregates (ASTM C29/C29M-17a[44]).

3. Determination of RMC

(a) Apparatus: Standard sieves (25.0 mm [1 in.], 19.0 mm [0.75 in.], 12.5 mm [0.5 in.], 9.5 mm [0.375 in.], and 4.75 mm [No. 4]), a furnace capable of heating to 650°C (1200°F), and a jar mill with cylindrical alumina grinding media of size 20.6 x 20.6 mm (0.8125 x 0.8125 in.).

(b) A representative sample of coarse RCA weighing 500 g (1.1 lb), retained on the 4.75 mm (No. 4) sieve and above, shall be prepared after removal of any visible contaminants from the sample. The RMC of the bulk sample of RCA should be determined using the thermal shock method as described in Mamirov et al.[25] to separate the mortar and aggregate and calculate the RMC percent.

4. Whole-rock analysis

(a) Whole-rock analysis should be performed on reference samples representative of the types of RCA expected to be analyzed in future work. To prepare the reference sample, the mortar and aggregate separated through the thermal shock method should be used.

(b) Once separated, each reference sample should be developed as a composite sample using the computed RMC from the thermal shock method. The weight distribution of the reference sample should be: X% of total weight of the sample plus (100-X)% of total weight of the sample, where X is the mortar content and 100-X is the aggregate content.

(c) Use the whole-rock analysis technique to obtain measurements of major and trace elements present in the sample.

5. PHXRF sample preparation and testing procedure

(a) Apparatus: PHXRF and supporting software, vacuum pump, desktop stand, sample cups, polyethylene terephthalate film, and computer.

(b) A representative sample weighing 10 kg shall be sieved through selected sieves. The portion of the sample retained on sieve sizes of interest should be set aside for PHXRF analysis. Samples shall be placed in cups that have a depth of at least 10 mm (0.40 in.). Secure the sample into the cup with polyethylene terephthalate film and mark the film into four quadrants. Place the cup on the nose of the PHXRF device per the manufacturer's instructions.

(c) Select an appropriate PHXRF manufacturer's calibration file capable of detecting and quantifying elements present in concrete aggregates. If an appropriate calibration file is unavailable, develop one by preparing a fresh reference sample or augment an existing calibration file by adding additional reference samples relevant to the existing file.

(d) The scanning duration should be as per the calibration file provided by the manufacturer. Use a vacuum for elemental analysis if recommended by the manufacturer.

(e) For each sample, take three measurements for each quadrant and calculate the average of 12 readings for each element concentration.

6. Statistical analysis (Note: This step should be performed if multiple sizes are being evaluated for use. If a single size fraction is selected for use, this step can be omitted.)

(a) Using the measurements from PHXRF and whole-rock analysis, perform an ANOVA test to test statistical significance between the particle sizes of the same sample and across samples of the same size. Compute parameters including standard deviation, COV, RMSD, and COV_{RMSD} to evaluate the accuracy and precision of measurements.

(b) Plot the RMSD versus size graph for the trace elements to observe a trend between both the parameters. The particle size with the lowest RMSD will be the most efficient size.

(c) To make an accurate comparison, use regression analysis and create a size-based regression model for each element of all the samples tested with whole-rock analysis values and PHXRF values. Observe the R^2 values for each size. An R^2 value closer to 1 suggests a stronger correlation between the whole-rock analysis and PHXRF results, thereby showing higher accuracy. Based on the R^2 values for the major (Si, Ca, Al, Fe) and trace elements (such as heavy metals), select the best particle size and use the regression equation for that particle size to compute the predicted values for all elements.

7. Residual mortar content

(a) Perform a stepwise regression analysis to develop models that predict the RMC. Use the RMC computed from the thermal shock method as the response variable and the major and trace elements as the predictor variables. Input the values of variables in the model equation to obtain the predicted values of mortar for each size. Users of this approach could choose to limit the variables included in the regression to those obtainable in the reference samples through whole-rock analysis. If multiple particle sizes are being tested, compare the percentage difference between the values obtained from experiments and the predicted ones to determine the best predictor based on size.

8. Chemical composition

(a) Use linear regression analysis to develop models to predict the chemical composition of the samples. For each particle size, plot the laboratory-measured value from the whole-rock analysis on the x-axis versus measured element content through PHXRF on the y-axis. Plot a best-fit curve that can be used to predict the laboratory-measured chemical composition from the PHXRF measured element content. The R^2 value can be used to assess each model. Stronger models will have higher R^2 values. Testing of additional RCA samples through whole-rock analysis and PHXRF could be performed to improve the models.

CONCLUSIONS

The portable handheld X-ray fluorescence (PHXRF) device shows strong potential for use for the chemical characterization of recycled concrete aggregates (RCAs), as well as for estimating the residual mortar content (RMC). As a rapid, easy-to-use technology, PHXRF can aid in the quality assurance (QA) and quality control (QC) requirements for qualifying an RCA source for use in concrete. The ability to rapidly determine the RMC and chemical composition of RCA should allow practitioners to better predict the performance of RCA in bound and unbound applications, potentially increasing its use.

The recommended test method developed as part of this research could serve as the basis for use by a technical procedure for agencies, contractors, and other users interested in this type of characterization of RCA. Additional research, broadening the range of RCAs tested and equipment used, would be needed to help develop this into an American Association of State Highway and Transportation Officials (AASHTO) or ASTM International standard. However, using the approaches described, practitioners should be able to develop efficient models for use with their own RCA sources and PHXRF equipment. The method may be most useful if a database of PHXRF measurements (laboratory-measured RMC and chemical composition) for a range of locally sourced reference RCAs is established by the user, supporting the development of locally calibrated models. In lieu of a manufacturer-provided calibration file for the PHXRF, an improved calibration file could be developed, capturing a broader range

of elements from high to low concentrations, especially for critical elements present in RCA.

Models for both the 4.75 mm (No. 4) and 1.70 mm (No. 12) size showed reasonable R^2 values for major and trace element composition. However, because the models used to predict RMC suggested the 4.75 mm (No. 4 size) to be the most appropriate, it is the size recommended for this test as well, primarily to save time by performing characterization testing on a single particle size. Use of the 4.75 mm (No. 4) particle size should allow testing of both fine and coarse RCA samples because this particle size is often present in both gradations. However, testing of other sources of RCA to develop locally calibrated models may suggest another particle size is more suitable.

Several heavy metals were the strongest predictor variables for RMC due to their relatively higher presence in cement paste, as compared to aggregate. Although these elements supported teh development of strong models, they are also negatively linked to human health effects, and their use may bring unwanted attention to RCA as a material containing these substances.

AUTHOR BIOS

Arindam Dey *is an MS Student in the Department of Engineering Technology and Construction Management at the University of North Carolina (UNC) at Charlotte, Charlotte, NC.*

ACI member **Tara L. Cavalline** *is an Associate Professor in the Department of Engineering Technology and Construction Management at UNC at Charlotte, where she received her PhD. She received her BS and MS in civil engineering from Penn State University, Centre County, PA. She is a member of ACI's Educational Activities Committee (EAC) and ACI Committees S801, Student Competitions; 121, Quality Assurance Systems for Concrete; 201, Durability of Concrete; and 555, Concrete with Recycled Materials. Her research interests include durable and sustainable concrete, quality assurance for concrete construction, and asset management systems.*

ACI member **Miras Mamirov** *is a PhD Candidate and works in the Department of Civil and Environmental Engineering at the University of Nebraska-Lincoln, Lincoln, NE.*

Jiong Hu *is an Associate Professor and works in the Department of Civil and Environmental Engineering at the University of Nebraska-Lincoln. He received his BEng and MEng in construction materials from Southeast University, Nanjing, China, and his PhD in geotechnical and materials engineering from Iowa State University, Ames, IA. Hu is a member of ACI Committees 236, Material Science of Concrete; 237, Self-Consolidating Concrete; 544, Fiber Reinforced Concrete; 555, Concrete with Recycled Materials; and 564, 3-D Printing with Cementitious Materials. His research interests include eco-efficient concrete; multi-state concrete behavior; high-performance, ultra-high performance, self-consolidating, and fiber-reinforced concretes; and concrete with recycled materials.*

ACKNOWLEDGMENTS

The authors thank the ACI Foundation for funding this work (Grant No. CRC 2019 P0027), and the Advisory Panel members (M. Snyder, K. Obla, C. Jones, and M. Adams) for their support. Thanks also to W. Maxwell, A. Bansal, and entities donating recycled aggregate.

REFERENCES

1. Van Dam, T. J.; Harvey, J.; Muench, S. T.; Smith, K. D.; Snyder, M. B.; Al-Qadi, I. L.; Ozer, H.; Meijer, J.; Ram, P.; and Roesler, J. R., "Towards Sustainable Pavement Systems: A Reference Document," Federal Highway Administration, Washington, DC, 2015, 456 pp.

2. American Concrete Pavement Association, "ACPA Concrete Pavement Technology Series: Recycled Concrete in Subbases: A Sustainable Choice," Skokie, IL, 2008, 102 pp.

3. Snyder, M.; Cavalline, T.; Fick, G.; Taylor, P.; Klokke, S.; and Gross, J., "Recycling Concrete Pavement Materials: A Practitioner's Reference Guide," National Concrete Pavement Technology Center, Iowa State University, Ames, IA, 2018, 88 pp.

4. American Concrete Paving Association, "Recycling Concrete Pavements," Skokie, IL, 2009, 100 pp.

5. Abbas, A.; Fathifazl, G.; Fournier, B.; Isgor, O. B.; Zavadil, R.; Razaqpur, A. G.; and Foo, S., "Quantification of the Residual Mortar Content in Recycled Concrete Aggregates by Image Analysis," *Materials Characterization*, V. 60, No. 7, 2009, pp. 716-728. doi: 10.1016/j.matchar.2009.01.010

6. Cackler, T., "Recycled Concrete Aggregate Usage in the US," National Concrete Pavement Technology Center, Iowa State University, Ames, IA, 2018, 34 pp.

7. McNeil, K., and Kang, T. H.-K., "Recycled Concrete Aggregates: A Review," *International Journal of Concrete Structures and Materials*, V. 7, No. 1, 2013, pp. 61-69. doi: 10.1007/s40069-013-0032-5

8. ACI Committee 555, "Removal and Reuse of Hardened Concrete (ACI 555R-01)," American Concrete Institute, Farmington Hills, MI, 2001, 26 pp.

9. Cavalline, T. L.; Snyder, M. B.; and Taylor, P. C., "Use of Recycled Concrete Aggregate in Concrete Paving Mixtures," Tech Brief FHWA-HIF-20-020, National Concrete Pavement Technology Center, Iowa State University, Ames, Iowa, 2022, 15 pp.

10. Silva, R. V.; de Brito, J.; and Dhir, R. K., "Properties and Composition of Recycled Aggregates From Construction and Demolition Waste Suitable for Concrete Production," *Construction and Building Materials*, V. 65, 2014, pp. 201-217. doi: 10.1016/j.conbuildmat.2014.04.117

11. Thermo Fisher Scientific, "Inductively Coupled Plasma Mass Spectrometry (ICP-MS) Information," 2022, https://www.thermofisher.com/us/en/home/industrial/spectroscopy-elemental-isotope-analysis/spectroscopy-elemental-isotope-analysis-learning-center/trace-elemental-analysis-tea-information/inductively-coupled-plasma-mass-spectrometry-icp-ms-information.html. (last accessed Sept. 15, 2023)

12. Barron, A. R., and Raja, P. M. V., *Physical Methods in Chemistry and Nanocience*, Rice University, Houston, TX.

13. Limbachiya, M. C.; Marrocchino, E.; and Koulouris, A., "Chemical-Mineralogical Characterization of Coarse Recycled Concrete Aggregate," *Waste Management*, V. 27, No. 2, 2007, pp. 201-208. doi: 10.1016/j.wasman.2006.01.005

14. Angulo, S. C.; Ulsen, C.; John, V. M.; Kahn, H.; and Cincotto, M. A., "Chemical-Mineralogical Characterization of C&D Waste Recycled Aggregates from Sao Paulo, Brazil," *Waste Management*, V. 29, No. 2, 2009, pp. 721-730. doi: 10.1016/j.wasman.2008.07.009

15. Sánchez-Cotte, E. H.; Pacheco-Bustos, C. A.; Fonseca, A.; Triana, Y. P.; Mercado, R.; Yepes-Martínez, J.; and Lagares Espinoza, R. G. "The Chemical-Mineralogical Characterization of Recycled Concrete Aggregates from Different Sources and Their Potential Reactions in Asphalt Mixtures," *Materials (Basel)*, V. 13, No. 24, 2020, p. 5592. doi: 10.3390/ma13245592

16. Hu, J.; Cavalline, T. L.; Mamirov, M.; and Dey, A., "Effective Characterization of Recycled Concrete Aggregate (RCA) for Concrete Applications," Final Report, ACI Concrete Research Council, Farmington Hills, MI, 2021, 173 pp.

17. Ferraro, N., "Validation of Portable Handheld X-Ray Fluorescence (PHXRF) for Construction Quality Control and Forensic Geotechnical Investigations in Stabilized Subgrade Projects," MS thesis, University of Oklahoma, Norman, OK, 2016, 119 pp.

18. Cerato, A. B., and Miller, G. A., "Determination of Soil Stabilizer Content Using X-Ray Fluorescence," *Geotechnical Testing Journal*, V. 36, No. 5, 2013, pp. 1-5. doi: 10.1520/GTJ20120186

19. Cerato, A. B.; Miller, G. A.; Ferraro, N.; and Collins, R., "Validating Field Employed X-Ray Fluorescence (XRF) on Stabilized Subgrade Projects to Assess Impact of Extreme Precipitation Events, Improve Construction Quality Control, and Facilitate Geotechnical Forensic Investigations," Final Report SPTC14.2-02-F, Southern Plains Transportation Center, Norman, OK, 2017, 37 pp.

20. SGS Group, Whole Rock Analysis, Geneva, Switzerland, 2022, www.sgsgroup.com.

21. Twelker, E.; Wypych, A.; Sicard, K. R.; Naibert, T. J.; Werdon, M. B.; Athey, J.E.; Willingham, A.L.; and Lockett, A.C., "New Geologic Investigations of Northeast Tanacross," Alaska Department of Natural Resources and Geological and Geophysical Surveys, Fairbanks, AK, 2017.

22. Bourke, A., and Ross, P.-S., "Portable X-Ray Fluorescence Measurements on Exploration Drill-Cores: Comparing Performance on Unprepared Cores and Powders for 'Whole-Rock' Analysis," *Geochemistry Exploration Environment Analysis*, V. 16, No. 2, 2016, pp. 147-157. doi: 10.1144/geochem2014-326

23. Dean, W. E., "Determination of Carbonate and Organic Matter in Calcareous Sediments and Sedimentary Rocks by Loss on Ignition: Comparison with Other Methods," *Journal of Sedimentary Research*, V. 44, No. 1, 1974, pp. 242-248.

24. Taylor, P.; Yurdakul, E.; and Ceylan, H., "Concrete Pavement Mixture Design and Analysis (MDA): Application of a Portable X-Ray Fluorescence Technique to Assess Concrete Mix Proportions," National Concrete Pavement Technology Center, Iowa State University, Ames, IA, 2012, 35 pp.

25. Mamirov, M.; Hu, J.; and Cavalline, T. L., "Geometrical, Physical, Mechanical, and Compositional Characterization of Recycled Concrete Aggregate," *Journal of Cleaner Production*, V. 339, 2022, p. 130754. doi: 10.1016/j.jclepro.2022.130754

26. ASTM C127-15, "Standard Test Method for Relative Density (Specific Gravity) and Absorption of Coarse Aggregate," ASTM International, West Conshohocken, PA, 2015.

27. BS 812-110:1990, "Testing Aggregates. Methods for Determination of Aggregate Crushing Value (ACV)," British Standards Institution, London, UK, 1990.

28. ASTM C33/C33M-18, "Standard Specification for Concrete Aggregates," ASTM International, West Conshohocken, PA, 2018.

29. Pepe, M.; Toledo Filho, R. D.; Koenders, E. A.; and Martinelli, E., "Alternative Processing Procedures for Recycled Aggregates in Structural Concrete," *Construction and Building Materials*, V. 69, 2014, pp. 124-132. doi: 10.1016/j.conbuildmat.2016.06.061

30. Nagataki, S.; Gokce, A.; Saeki, T.; and Hisada, M., "Assessment of Recycling Process Induced Damage Sensitivity of Recycled Concrete Aggregates," *Cement and Concrete Research*, V. 34, No. 6, 2004, pp. 965-971. doi: 10.1016/j.cemconres.2003.11.008

31. Afroughsabet, V.; Biolzi, L.; and Ozbakkaloglu, T., "Influence of Double Hooked-End Steel Fibers and Slag on Mechanical and Durability Properties of High Performance Recycled Aggregate Concrete," *Composite Structures*, V. 181, 2017, pp. 273-284. doi: 10.1016/j.compstruct.2017.08.086

32. Tam, V. W.; Tam, C. M.; and Le, K. N., "Removal of Cement Mortar Remains from Recycled Aggregate Using Pre-Soaking Approaches," *Resources, Conservation and Recycling*, V. 50, No. 1, 2007, pp. 82-101. doi: 10.1016/j.resconrec.2006.05.012

33. Butler, L.; West, J. S.; and Tighe, S. L., "Quantification of Recycled Concrete Aggregate (RCA) Properties for Usage in Bridges and Pavements: An Ontario Case Study," Presentation at the Innovative Developments in Sustainable Pavements Session of the 2011 Annual Conference of the Transportation Association of Canada, Edmonton, AB, Canada, 2011.

34. Butler, L., "Evaluation of Recycled Concrete Aggregate Performance in Structural Concrete," PhD dissertation, University of Waterloo, Waterloo, ON, Canada, 2012, 475 pp.

35. de Juan, M. S., and Gutiérrez, P. A., "Study on the Influence of Attached Mortar Content on the Properties of Recycled Concrete Aggregate," *Construction and Building Materials*, V. 23, No. 2, 2009, pp. 872-877. doi: 10.1016/j.conbuildmat.2008.04.012

36. Dey, A., "Chemical Characterization of Recycled Concrete Aggregates Using a Handheld X-Ray Fluorescence Device," MS thesis, University of North Carolina at Charlotte, Charlotte, NC, 2020, 268 pp.

37. Speakman, S., "Using the Bruker Tracer III-SD Handheld X-Ray Fluorescence Spectrometer Using PC Software for Data Collection," Center for Materials Science and Engineering at Massachusetts Institute of Technology, Cambridge, MA, 2015.

38. Imanishi, Y.; Bando, A.; and Komatani, S., Wada, S.; and Tsuji, K., "Experimental Parameters for XRF Analysis of Soils," *Advances in X-Ray Analysis*, V. 53, 2010, pp. 248-255.

39. Markowicz, A., "An Overview of Quantification Methods in Energy-Dispersive X-ray Fluorescence Analysis," *Pramana Journal of Physics*, V. 76, No. 2, 2011, pp. 321-329. doi: 10.1007/s12043-011-0045-z

40. Cavalline, T. L., "Concrete Pavement Recycling Series - Protecting Water Quality Through Planning and Design Considerations," Technical Brief, National Concrete Pavement Technology Center, Iowa State University, Ames, IA, 2018.

41. Cavalline, T. L., "Concrete Pavement Recycling Series – Protecting the Environment During Construction," Technical Brief, National Concrete Pavement Technology Center, Iowa State University, Ames, IA, 2018.

42. ASTM D75/D75M-19, "Standard Practice for Sampling Aggregates," ASTM International, West Conshohocken, PA, 2019.

43. ASTM C136/C136M-19, "Standard Test Method for Sieve Analysis of Fine and Coarse Aggregates," ASTM International, West Conshohocken, PA, 2019.

44. ASTM C29/C29M-17a, "Standard Test Method for Bulk Density ("Unit Weight") and Voids in Aggregate," ASTM International, West Conshohocken, PA, 2017.

ARE YOU A RESEARCHER?

SIGN UP FOR ORCID TODAY!

ORCID provides a persistent digital identifier that distinguishes you from every other researcher and, through integration in key research workflows such as manuscript and grant submission, supports automated linkages between you and your professional activities, ensuring that your work is recognized.

Individuals may use ORCID services freely and it's as easy as **1-2-3**:

1. REGISTER
2. ADD YOUR INFO
3. USE YOUR ORCID ID

For more information and to register, visit:

WWW.ORCID.ORG

ACI MATERIALS JOURNAL TECHNICAL PAPER

Title No. 120-M54

Long-Term Creep and Shrinkage of Alkali-Activated Concrete Incorporating Fly Ash and Rice Husk Ash

by S. Fernando, C. Gunasekara, D. W. Law, M. C. M. Nasvi, S. Setunge, and R. Dissanayake

The creep and drying shrinkage of two alkali-activated concretes produced with low-calcium fly ash and rice husk ash (RHA) were investigated over a period of 1 year. The compressive strength of 100% low-calcium fly ash (100NFA) concrete and the concrete having 10% RHA replacement (10RHA) decreased from 49.8 to 37.7 MPa (7.22 to 5.47 ksi) and 30.2 to 18.3 MPa (4.38 to 2.65 ksi), respectively, between 28 and 365 days. The imbalance in the dissolution rate of the raw materials in the blended system (10RHA) could negatively influence the strength properties, which leads to poor matrix integrity and a highly porous structure when compared with 100NFA. The presence of the micro-aggregates due to the block polymerization provides the effect of increasing the aggregate content in the 100NFA concrete compared with the 10RHA concrete, which is hypothesized as one of the reasons creep and shrinkage properties deteriorated in 10RHA.

Keywords: alkali-activated concrete; creep; drying shrinkage; fly ash; microstructure; rice husk ash (RHA).

INTRODUCTION

Portland cement (PC) is the most widely used construction material, with global PC production recorded at 4.4 billion metric tonnes in 2022[1] and predicted to rise in the future. The production of PC is an energy-intensive process that emits large amounts of greenhouse gases (GHGs), mainly carbon dioxide (CO_2). PC production accounts for 4% of human-made global warming and contributes between 5 and 7% of global anthropogenic CO_2 emissions.[2,3] The development of concrete solely using waste by-products is a promising technique to address the issues that arise with traditional PC production. Alkali-activated binders have been found to be mechanically efficient and an eco-friendly concrete using waste by-products such as fly ash, slag cement, rice husk ash (RHA), and metakaolin. The GHG emissions of alkali-activated binders have been reported to be comparatively lower compared to PC concrete.[4] Furthermore, the use of waste for concrete production leads to the conservation of landfills and storage lagoons and converts a waste product into a useful by-product.[5] Alkali-activation technology involves the chemical reaction between aluminosilicate species with an alkaline activator to form amorphous to semicrystalline polymer structures.[6,7]

Low-calcium Class F fly ash is a widely used aluminosilicate-rich by-product for alkali-activated concrete. RHA is an agricultural waste product, rich in silica, which contributes to numerous environmental and health issues.[8] Low-calcium fly ash and RHA are considered waste industrial and agricultural by-products, respectively, that can be used in alkali-activated concrete as a precursor material.[9] Hence, the production of alkali-activated binders using fly ash and RHA will have added benefits in terms of environmental impacts by conserving landfills and water sources. The major challenge in adopting alkali-activated concrete as a construction material is the variability of source materials (that is, fly ash from different sources), leading to variability in its engineering properties.[10] To date, limited research has been conducted to investigate the long-term creep and shrinkage behavior of low-calcium fly ash alkali-activated binders. A study by Wallah[11] showed that heat-cured Australian-based low-calcium fly ash alkali-activated concrete undergoes low creep, which is 50% less than the creep usually observed for traditional PC concrete. Creep varied from 15 to 29 με for compressive strengths ranging between 67 and 40 MPa (9.72 and 5.80 ksi). Furthermore, heat-cured specimens displayed lower values for shrinkage, with only 100 με after 3 months. Hardjito et al.[12] reported that the specific creep (creep strain normalized by creep stress) of alkali-activated concrete decreased as the compressive strength increased. In addition, a 45% lower basic creep coefficient (the ratio between creep strain and elastic strain) was found by Sagoe-Crentsil et al.[13] for 100% fly ash alkali-activated concrete when compared with an equivalent PC concrete. Gunasekara et al.[3] noted similar creep behavior for two 100% fly ash alkali-activated concretes (Gladstone and Port Augusta, Australia; creep coefficients ranging between 1.8 and 2.0) compared to PC concrete (creep coefficient of approximately 3). However, alkali-activated concrete prepared using another fly ash type (Tarong, Australia) showed a very high creep strain (approximately 1900 με) and drying shrinkage (615 με) compared to both PC (475 με drying shrinkage) and the other two fly ash concretes (approximately 700 με creep and 175 to 190 με drying shrinkage). Thus, significant variation in creep and shrinkage behavior is observed between alkali-activated fly ash and PC as well as between different types of alkali-activated materials.

Hence, a clear understanding of the influence of different source materials on long-term creep and shrinkage behavior in alkali-activated concrete is required to enable their use as a construction material for structural elements. To address this, the present study investigated the creep and drying shrinkage of alkali-activated concrete incorporating

ACI Materials Journal, V. 120, No. 5, September 2023.

MS No. M-2022-200.R2, doi: 10.14359/51738891, received February 6, 2023, and reviewed under Institute publication policies.

Table 1—Chemical composition of low-calcium fly ash and RHA

Source material	Chemical composition, %										
	SiO_2	Al_2O_3	Fe_2O_3	CaO	P_2O_5	TiO_2	MgO	K_2O	SO_3	MnO	Na_2O
Fly ash	45.1	33.22	3.33	9.26	1.3	2.08	2.27	0.74	0.56	0.06	1.07
RHA	91.55	0.42	0.47	1.25	1.43	0.04	1.28	2.87	0.21	0.23	0

low-calcium fly ash and RHA. A detailed microscopic and pore structure analysis was conducted to investigate the factors influencing the creep and shrinkage behavior for a period of up to 1 year.

RESEARCH SIGNIFICANCE

Alkali-activated concrete incorporating low-calcium fly ash and RHA is potentially beneficial in terms of environmental impacts. However, the long-term effect of adding RHA in alkali-activated fly ash concrete has not been extensively studied. To date, research conducted to investigate the long-term creep and shrinkage of the blended low-calcium fly ash-RHA alkali-activated concretes is still limited. The present research addresses this gap in knowledge by investigating the creep and shrinkage of blended fly ash-RHA alkali-activated concrete together with the compressive strength development for up to 1 year. Hence, the research data presented herein will be extremely useful to comprehend the long-term behavior of structural members made with this concrete.

METHODOLOGY

Materials

Low-calcium (Class F) fly ash conforming to Australian standard AS 3582.1-1998[14] was obtained from the Lakvijaya Coal Power Plant, Sri Lanka, while RHA was obtained from a local rice mill in Sri Lanka. The chemical composition of the fly ash and RHA source materials was determined by X-ray fluorescence (XRF) analysis, and the results are summarized in Table 1. The RHA was ground into fine particles and sieved to attain particles 75 µm and below. Although previous literature[15,16] has reported that the particle size of the material should have at least 80% below 45 µm to obtain optimum strength, a 75 µm limit was used to address practical difficulties in the grinding process with respect to industry application. The particle-size distribution of selected source materials was determined by a laser-diffraction particle-size analyzer, using the wet (hydro) laser-diffraction technique with water as a dispersant. The Brunauer-Emmett-Teller (BET) method under high-vacuum conditions was used for specific surface area analysis. Nitrogen was used as a cold bath (77.15 K). The results are summarized in Table 2.

A combination of 15 M sodium hydroxide (NaOH) and sodium silicate (Na_2SiO_3) was used as the alkaline activator. The sodium silicate solution consisted of 14.7% Na_2O, 29.4% SiO_2, and 55.9% H_2O by mass. The coarse aggregate was in the saturated surface-dry condition, while the fine aggregate was in a dried condition. The fine aggregate was river sand in the uncrushed form with a specific gravity of 2.5 and a fineness modulus of 2.75. Two grain sizes of crushed granite coarse aggregate were used: 7 mm aggregate with a 2.55 specific gravity and 1.63% water absorption, and 10 mm aggregate with a 2.60 specific gravity and 0.76% water absorption.

Table 2—Physical properties of low-calcium fly ash and RHA

		Fly ash	RHA
Particle passing, %, at x µm sieve	x = 5	11.9	8.4
	x = 10	23.7	16.2
	x = 20	40.1	32.6
	x = 45	62.6	67.6
	x = 75	74.1	91.0
	x = 90	77.5	96.8
BET surface area, m^2/kg		1495.1	4091.0
Specific gravity		2.12	1.95

Note: 1 m^2/kg = 4.88 ft^2/lb.

Mixture design

Alkali-activated concrete with fly ash (100NFA) was developed based on the optimization of the activator modules (AM) (SiO_2/Na_2O in alkaline activator) of the mixture. An optimum AM for 100NFA was obtained to be 1.375 based on 28-day compressive strength data for 100NFA concrete.[17] Hence, an AM of 1.375 was adopted for blended fly ash-RHA concrete (10RHA); this corresponds to 10% RHA replacement with fly ash. The absolute volume method was used to calculate the components of each material in the mixture design. The water-to-solid ratio was kept at 0.37, while the total aggregate in the concrete mixture was kept at 64% of the entire mixture by volume for both concretes. The mass of the water was considered as the sum of the mass of the water contained in sodium silicate, sodium hydroxide, and added water. The mass of the solid was considered as the sum of the binder (fly ash or RHA), the mass of the solid in sodium silicate, and sodium hydroxide. Table 3 summarizes the mixture proportions for 100NFA and 10RHA concrete.

Mixing, casting, and curing

The mixing of concrete was conducted using a 120 L capacity concrete mixer. The dry materials, fly ash, RHA (in the 10RHA mixture), and fine and coarse aggregate were mixed continuously for 5 minutes. The activator and water were added to the dry mixture and mixed for another 8 minutes until the mixture was well combined. The concrete was placed into the mold and vibrated using a vibrating table for 1 minute to remove air bubbles. All samples were kept at room temperature for 1 day and cured in an oven for 24 hours at 80°C in accordance with previous research in optimizing the mixture design and curing regime. Research has shown that heat curing is required to enhance the reactivity to

Table 3—Mixture proportions for fly ash and RHA alkali-activated concrete

Mixture	Fly ash	RHA	Combined aggregates			Water	Sodium silicate	Sodium hydroxide	*w/b*
			43% sand	19% 7 mm	38% 10 mm				
100NFA	411	0	691	305	611	7	289	64	0.37
10RHA	369.9	41.1	691	305	611	7	289	64	0.37

Note: *w/b* is water-binder ratio; 1 kg/m^3 = 0.0624 lb/ft^3; 1 mm = 0.0393 in.

achieve higher compressive strength.[9,18,19] Specimens were removed from the oven and left to cool to room temperature before demolding. Samples were kept at room temperature until being tested.

Testing

The compressive strength test was performed by a universal testing machine with a loading rate of 20 MPa/min (2.901 ksi/min) according to AS 1012.9:2014.[20] The creep test was performed in compliance with the Australian standard AS 1012.16-1996.[21] Strain gauges were attached on two opposite sides on the surface of six cylinders (28-day cured) from each mixture. Specimens were loaded with a load equivalent to 40% of the 28-day mean compressive strength using the load cell. The load was maintained throughout the 365-day period, the strain gauge readings were monitored every 6 hours, and the data were extracted weekly. Three loaded test specimens and the three control specimens (non-loaded) were monitored. The long-term readings of the two gauges fixed to each of the three cylinders loaded on the creep rig and the unloaded control cylinders were recorded throughout the 365-day period. The average of the two gauge readings of each cylinder was employed for the creep calculations. The average long-term strain was obtained by subtracting the mean strain of the control (unloaded) specimens, which corresponds to the drying shrinkage of the specimens, from the average strain of the loaded cylinders. To obtain the creep strain, the instant strain value (initial reading), which corresponds to the initial elastic strain due to the loading, was deducted from each strain value to obtain the long-term creep strain. The loading arrangement of the creep tests is illustrated in Fig. 1. Shrinkage testing was carried out in accordance with AS 1012.13:2015[22] after 7 days of curing. Length change measurements were recorded continuously using a horizontal comparator at 1-week intervals for 365 days. The specimens were kept in a controlled environment chamber at a temperature of 23 ± 1°C and relative humidity of 50%.

Microstructure development was evaluated using scanning electron microscopy (SEM) imaging employing a backscattered electron detector with 15 eV energy. To determine the chemical composition of the alkali-activated binder, energy-dispersive X-ray spectroscopy (EDS) analysis was performed using nanoanalysis software. Specimens were cut into a size of 4 mm in height and 10 mm in diameter using a diamond saw and embedded into epoxy resin. All the samples were carbon coated to avoid charge buildup during the test and mounted on the SEM sample stage with conductive double-sided carbon tape. An X-ray micro-computed tomography (micro-CT) scanner was used to examine the pore structure of the alkali-activated concrete samples. A 10 x 10 x 10 mm specimen was scanned at 12 mm resolution at 90 kV, and 720 images were recorded during a complete rotation.

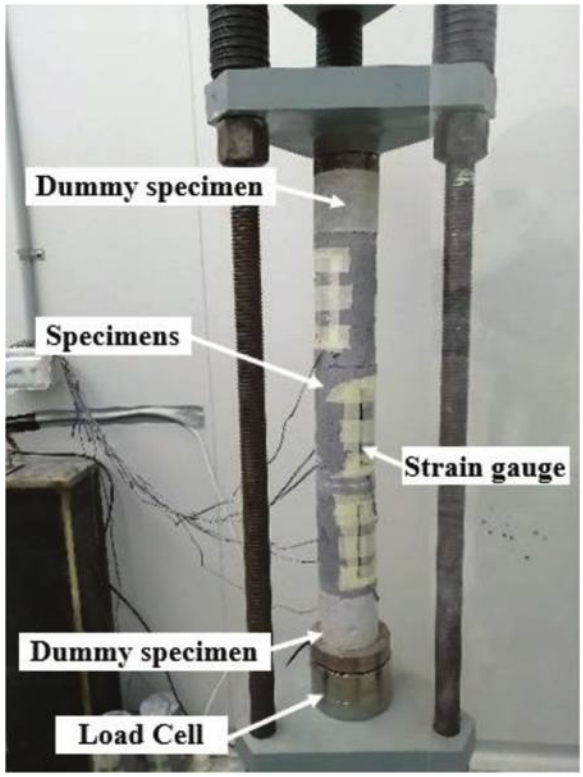

Fig. 1—Loading arrangement for creep test.

RESULTS

Compressive strength development

Table 4 shows the compressive strength and creep strength of the 100NFA and 10RHA concretes for up to 1 year. The compressive strength of the 100NFA and 10RHA concretes decreased from 49.8 to 37.7 MPa (7.22 to 5.41 ksi) and 30.2 to 18.3 MPa (4.38 to 2.65 ksi), respectively, between 28 and 365 days. The 100NFA displayed the highest compressive strength at all ages when compared to the 10RHA. Reductions in strength of 39% (19.6 MPa [2.84 ksi]), 49% (19.5 MPa [2.83 ksi]), and 52% (19.4 MPa [2.81 ksi]) were observed for 10RHA at 28, 180, and 365 days, respectively, compared with 100NFA. This indicates that the addition of RHA negatively affects the compressive strength development of the 100NFA concrete. In 100NFA, a 20% strength reduction (9.8 MPa [1.42 ksi]) was observed between 28 and 180 days, while a 6% reduction in compressive strength was noted (2.3 MPa [0.33 ksi]) from 180 to 365 days. The 10RHA alkali-activated concrete demonstrated a similar trend to 100NFA for long-term strength behavior.

Table 4—Compressive strength of 100NFA and 10RHA concrete

Type	Slump flow, mm	Compressive strength, MPa			Creep strength*, MPa	Strength increment	
		28 days	180 days	365 days	365 days	Strength, MPa	Percentage, %
100NFA	530	49.8 ± 2.5	40.0 ± 3.7	37.7 ± 1.9	34.0 ± 1.4	–3.7	–9.8
10RHA	456	30.2 ± 2.1	20.5 ± 4.0	18.3 ± 3.3	15.9 ± 2.0	–4.6	–13.1

*Compressive strength test conducted on specimens subjected to creep test for 1 year.

Note: 1 MPa = 0.145 ksi.

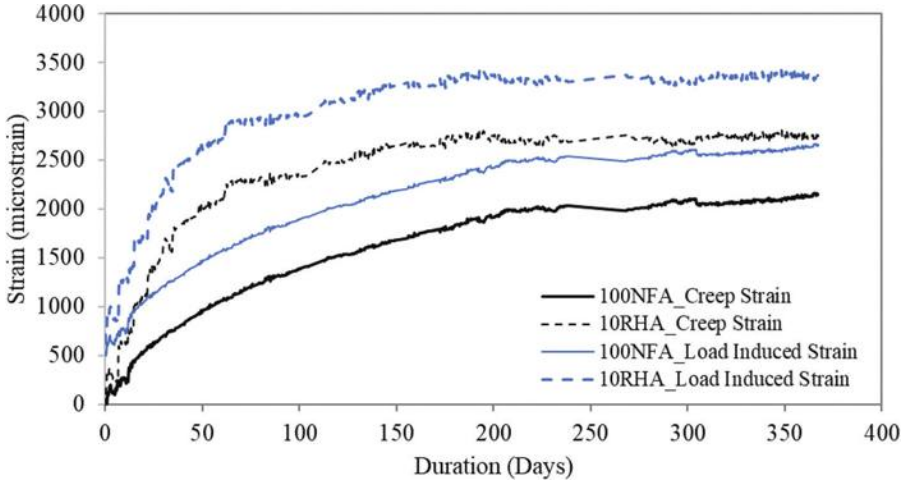

Fig. 2—Experimental creep strain and total load-induced strain of 100NFA and 10RHA alkali-activated concretes.

Approximately a 32% and 11% reduction (9.7 and 2.2 MPa [1.41 and 0.32 ksi]) was observed for 28 to 180 days and 180 to 365 days, respectively. The compressive strength of the specimens subjected to long-term creep loading was also tested at 365 days. The recorded creep compressive strength for the 100NFA and 10RHA concretes were 34.0 and 15.9 MPa (4.93 and 2.31 ksi), respectively. This correlated to a 9.8% and 13.1% strength reduction compared to the 365-day compressive strength of the unloaded 100NFA and 10RHA specimens.

Long-term creep

Long-term creep is a critical parameter for the durability and long-time serviceability of concrete structures. Creep is defined as the time-dependent increase in strain under sustained stress for a given material.[23] The deformation of concrete due to creep is a complex phenomenon, which is influenced by many factors, including the mixture design, environmental conditions (that is, temperature and relative humidity), load conditions, and the size of the structure or member.[24] At the application of a load, the instantaneous strain includes the elastic strain and some creep strain. The experimental creep strain ($\varepsilon_{ec(t)}$) is calculated (Eq. (1)) as the increase in strain above the initial elastic strain under sustained loading, minus shrinkage strains over the same time period.

$$\varepsilon_{ec(t)} = \varepsilon_{bc(t)} - \varepsilon_{es} - \varepsilon_{ss(t)} \quad (1)$$

where, at any time t after loading, $\varepsilon_{ec(t)}$ is the experimental creep strain; $\varepsilon_{bc(t)}$ is the measured creep strain; ε_{es} is the instantaneous elastic strain upon loading; and $\varepsilon_{ss(t)}$ is the shrinkage strain over time. Figure 2 illustrates the measured creep strain and total load-induced strain variation of the 100NFA and 10RHA concretes.

According to the creep strain curves, the 10RHA concrete has a higher gradient than 100NFA. This indicates a higher rate of creep development over the period. The 100NFA concrete specimens showed a creep strain of 2139 μm, while the 10RHA specimens had a creep strain of 2713 μm at 365 days. In the 100NFA concrete, the rate of creep increase is considerably reduced after 14 days, while in the 10RHA concrete, a similar reduction was observed after 65 days, as shown in Fig. 2. Furthermore, the total load-induced strain reached 2651 and 3333 με in the 100NFA and 10RHA concretes at 365 days, respectively. The results show that the creep data fluctuated slightly over the period of sustained loading. This might be due to the variations in the relative humidity of the laboratory where the creep test rig was housed.[25]

The creep coefficient is the ratio of the time-dependent basic creep strain to that of the instantaneous elastic strain. The instantaneous elastic strain is the strain measured immediately following the application of the sustained load. The creep coefficient is calculated using Eq. (2),[26] based on the experimental creep strain, and compared with the existing models (that is, AS 3600:2018[27] in Eq. (3), CEB-FIP[28] in Eq. (4), and ACI 209.2R-08[29] in Eq. (5)), as shown in Fig. 3.

$$\varphi(t, t_0) = \frac{\varepsilon_{cc}(t, t_0)}{\varepsilon_e} \quad (2)$$

where $\varphi(t, t_0)$ is the creep coefficient at a given time t (days); t_0 is the initial age at first loading; $\varepsilon_{cc}(t, t_0)$ is the creep strain

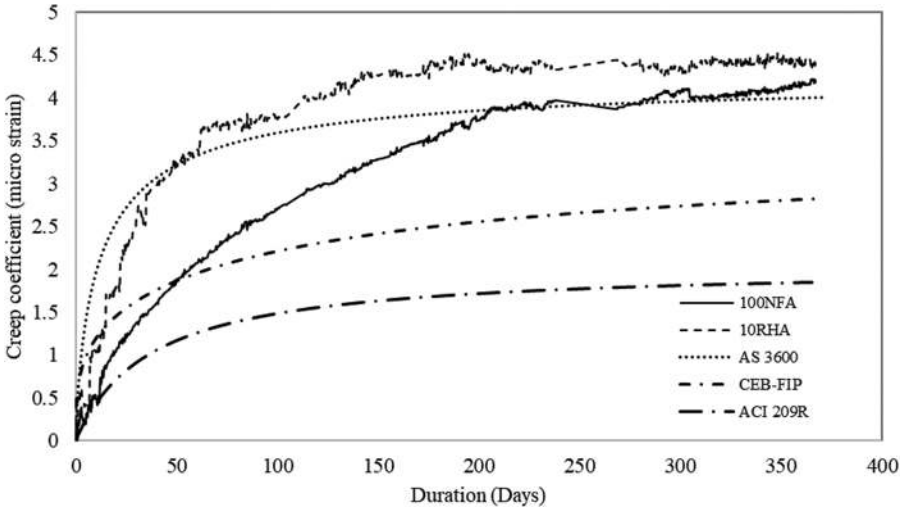

Fig. 3—Creep coefficient of 100NFA and 10RHA alkali-activated concretes.

of concrete as a function of time; and ε_e is the instantaneous elastic strain at the initial loading time.

$$\varphi_{cc} = K_2K_3K_4K_5K_6\varphi_{ccb} \quad (3)$$

where φ_{cc} is the creep coefficient; φ_{ccb} is the basic creep coefficient; and K_2, K_3, K_4, K_5, and K_6 are specific coefficients that depend on the time and thickness of the member, the age of concrete and time of loading, the environment, a modification factor for high-strength concrete, and account for nonlinear creep, respectively.

$$\varphi(t,t_0) = \frac{(t-t_0)^{\omega}}{d+(t-t_0)^{\omega}}\varphi_u \quad (4)$$

$$\varphi(t, t_0) = \varphi_0\beta_c(t-t_0) \quad (5)$$

where d and ω are constants for a given member shape/size; φ_u is the ultimate creep coefficient; φ_0 is the notional creep coefficient; and β_c is the coefficient to describe the development of creep with time.

After being subjected to continuous loading for 365 days, the calculated creep coefficient values were 4.2 and 4.4 for the 100NFA and 10RHA concretes. The creep coefficient at 365 days is higher than the creep coefficient value calculated based on the standards (as shown in Fig. 3).

It is noted that 100NFA has higher creep coefficients in the first 50 days when compared with ACI 209.2R-08[29] and lower values than predicted by CEB-FIP.[28] Beyond 206 days, the creep coefficient of the 100NFA concrete was greater than the values predicted by AS 3600.[27] The 10RHA concrete showed a considerably higher creep coefficient than 100NFA up to 365 days. The creep coefficient values were below the CEB-FIP[28] model for up to 14 days. Beyond 52 days, 10RHA displayed a higher creep coefficient, which remains above the values predicted by AS 3600.[27] Hence, both AS 3600[27] and CEB-FIP[28] could be conservatively used to predict creep of 100NFA up to 206 and 50 days, respectively, while AS 3600[27] could only be used to accurately predict the creep coefficient over a short-term period for the 10RHA concrete (52 days). Overall, both the CEB-FIP[28] model (from 14 to 365 days) and ACI 209.2R-08[29] (up to 365 days) underestimate the creep of 10RHA concrete.

The specific creep is defined as the creep strain per unit stress, which is used to compare the creep variation of different concrete types. The specific creep data for the 100NFA and 10RHA test specimens are shown in Fig. 4. The 100NFA concrete showed lower specific creep values compared to the 10RHA concrete up to 365 days. The 365-day specific creep values of the 100NFA and 10RHA concretes were 91.1 and 42.9 με/MPa. Overall, the specific creep of the 100NFA and 10RHA specimens increased as the compressive strength decreased, which correlates well with PC-based concrete.[30] Similar observations have been reported for a number of Class F fly ash alkali-activated concretes.[3,12,13]

Drying shrinkage

Drying shrinkage refers to the contraction of hardened concrete due to the loss of capillary water.[31] This generally leads to cracking (due to an increase in tensile stress), durability problems are generally increased, and it is one of the potentially most deleterious properties of concrete.[31] Drying shrinkage is associated with the ambient conditions and the material proportions of the concrete mixture.[32] In the present study, prism specimens from both the 100NFA and 10RHA concrete mixtures were investigated based on length change after 7 days.

The variation in average drying shrinkage of the 100NFA and 10RHA alkali-activated concretes and predicted drying shrinkage based on standard models[27-29] are illustrated in Fig. 5 up to 365 days. The age "zero" in Fig. 5 indicates 7-day aged concrete specimens at which time the initial measurements were taken. During the initial 7 days, the alkali-activated specimens were kept at 50% relative humidity and 23 ± 2°C temperature. The drying shrinkage during this period is reported to be minimal and is denoted as zero.[3]

The 10RHA alkali-activated concrete has higher shrinkage strain compared to the 100NFA alkali-activated concrete, with the early shrinkage strain of the 10RHA concrete specimens showing a rapid increment. The observed drying

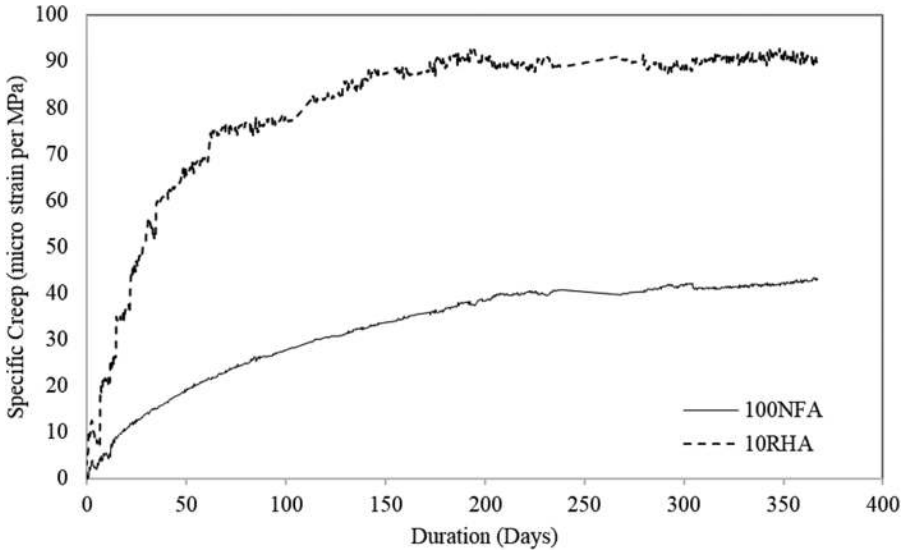

Fig. 4—Specific creep of 100NFA and 10RHA alkali-activated concretes.

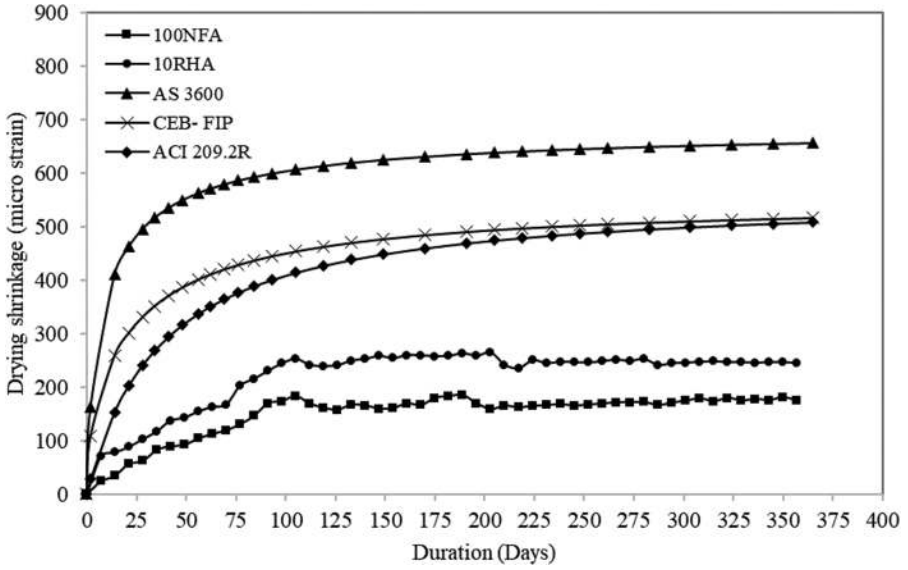

Fig. 5—Drying shrinkage of alkali-activated concrete—experimental versus standard drying shrinkage.

shrinkage values of the 100NFA and 10RHA concretes at 365 days are 181 and 264 με. These are significantly lower than the maximum permitted value for concrete recommended by the AS 3600 standard in Australia[27] and the CEB-FIP model,[28] as shown in Fig. 5. Furthermore, the values obtained for 100NFA and 10RHA are much lower compared to the values of 400 to 450 με observed by Hardjito et al.[23] for heat-cured fly ash-based geopolymer concrete after 1 year. Gunasekara et al.[3] observed drying shrinkage of 175 and 190 με for low-calcium fly ash (obtained from the Gladstone and Port Augusta Power Stations, respectively) geopolymer concretes at 365 days, which are considerably lower than the reported values for 10RHA and similar to the 100NFA alkali-activated concrete.

The drying shrinkage increased up to 105 days for both concretes. The average change in shrinkage values between 7 and 105 days of the 100NFA and 10RHA was of the order of 183 and 253 με, respectively. A higher rate of increment was noted in 10RHA when compared with 100NFA. A slight reduction was observed in both concretes from 105 to 126 days. Beyond 126 days, the overall drying shrinkage for concrete slightly increased until 365 days. However, a further small peak was observed at 189 and 203 days in the 100NFA and 10RHA concretes.

DISCUSSION

The process of polymerization takes place when reactive aluminosilicates are rapidly dissolved and free $[SiO_4]$- and $[AlO_4]$-tetrahedral units are released into the solution. Under highly alkaline conditions, a three-dimensional polymeric aluminosilicate gel network is formed, which governs the performance of alkali-activated concrete. Water provides the medium for the dissolution of aluminosilicates and the transfer of ions, hydrolysis of Al^{3+} and Si^{4+} compounds, and polycondensation of aluminate and silicate hydroxyl species. Hence, the absorption of water will result in reduced solvation of aluminosilicate species during the dissolution stage. The higher unburnt carbon content (~6%) in RHA absorbs

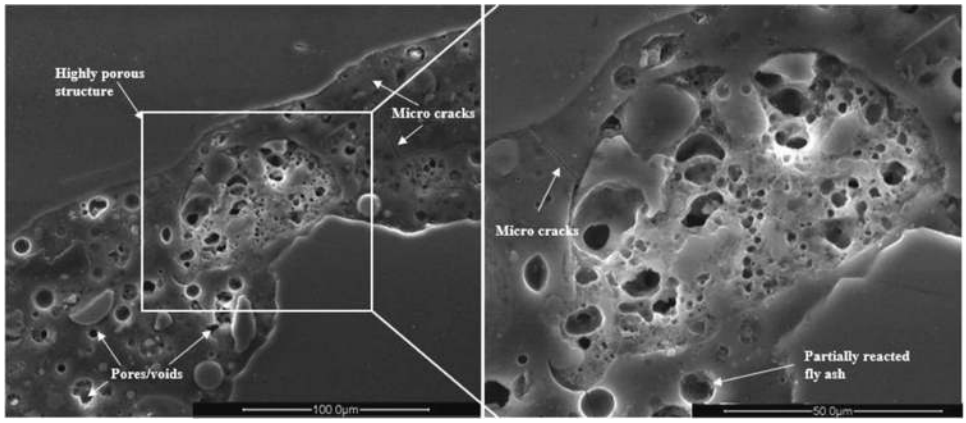

Fig. 6—Highly porous microstructure observed in 10RHA concrete at 28 days.

the available water and activator solution. Due to the higher surface area of the RHA particles compared with fly ash particles, more water molecules are absorbed by the surface of the RHA particles. This is supported by the flowability of both concretes (refer to Table 4), where 10RHA (456 mm) is 14% lower than 100NFA (530 mm). The lower liquid content in 10RHA leads to difficulties obtaining uniform mixing and compaction but also less activator availability within the mixture. In turn, this could hinder the dissolution of aluminosilicate species during the dissolution stage, inhibiting the gelation of the alkali-activation process. This is consistent with the lower compressive strength values displayed by 10RHA. The rate of dissolution of the alumina and silica species is crucial in controlling the synthesis process of alkali activation and development of the aluminosilicate gel matrix. The availability of aluminum in the binder material and a high initial dissolution rate of silicate are identified to accelerate the conversion of aluminosilicate materials to alkali-activated binders.[33,34] The addition of RHA leads to a lower quantity of fly ash, 10% by weight, in the concrete mixture. As RHA does not contain substantial alumina, the quantity of aluminum in 10RHA is lower compared to 100NFA. Furthermore, the dissolution rate of RHA is much higher than that of fly ash.[35] Therefore, it is hypothesized that the imbalance in the dissolution rate of the raw materials in the blended system (10RHA) could negatively influence the strength properties, which leads to poor matrix integrity and a highly porous structure when compared with 100NFA, as shown in Fig. 6. Therefore, a negative synergistic effect of blended RHA and fly ash is hypothesized as contributing to the strength reduction observed.

The Si/Al ratio increased with the substitution of RHA into the fly ash alkali-activated concrete as the addition of RHA effectively replaces aluminum with silicon. The aluminum is directly connected to the kinetics of gel formation.[19] It has been reported that the addition of excess reactive silica leads to a reduction in the rate of the reaction in an alkali-activated gel binder,[33,34] such that in high-concentration silica, solidification takes place prior to the completion of the reaction process. The Si/Al ratio shows a reduction from 28 to 365 days, as illustrated in Fig. 7. This indicates the formation of a gel matrix with the incorporation of alumina into the silicate backbone; thus, ongoing alkali activation occurs in the period from 28 to 365 days. Therefore, it can be inferred that the increase in the Si/Al ratio in 10RHA is one of the factors contributing to the lower strengths achieved compared to 100NFA.

It is interesting to note that beyond 28 days, compressive strength declined at both 180 and 365 days despite the evidence of ongoing gel formation from the change in the Si/Al ratio data. It is hypothesized that this could be the result of the degradation of the matrix due to crack propagation. The SEM images obtained for the 100NFA and 10RHA specimens for 28 and 365 days are illustrated in Fig. 7. The images show that the inclusion of RHA resulted in a looser structure with wider cracks compared to 100NFA. Overall, the 10RHA microstructure had a nonhomogeneous, loosely packed gel matrix with higher porosity at 28 days, while a relatively less porous structure was observed at early age in 100NFA at 28 days. At 365 days, increased crack propagation and efflorescence are evident in the 10RHA concrete, as shown in Fig. 8. Needle-type efflorescence products are identified in the SEM images and EDS spectrum (principally sodium) (Fig. 8(c), (f), and (g)). A similar finding was reported in Temuujin and van Riessen.[36] Formation of efflorescence has a negative influence on strength development. The 100NFA concrete showed a lower intensity of efflorescence products (Fig. 8(c)), while 10RHA displayed a higher intensity of efflorescence products (Fig. 8(f)). The addition of RHA tended to increase the formation of efflorescence. It is hypothesized that the widening of cracks and further propagation of microcracks (which were initiated during the heat curing) were due to the formation of efflorescence products in the period from 28 to 365 days. The formation of efflorescence products within the pores/voids creates internal stresses, which widen and propagate the cracks. The combined effect of this crack propagation, efflorescence, and the more loosely packed structure in 10RHA correlates with the lower strength and higher creep strain noted when compared to the 100NFA concrete.

The interfacial transition zone (ITZ) is one of the primary factors that influence the creep and shrinkage behavior of concrete. The ITZ is formed by the interconnection between the binder gel matrix and aggregate, which are considered heterogeneous and nonuniform matter.[32] The ITZ is likely to be the weakest link within the microstructure of

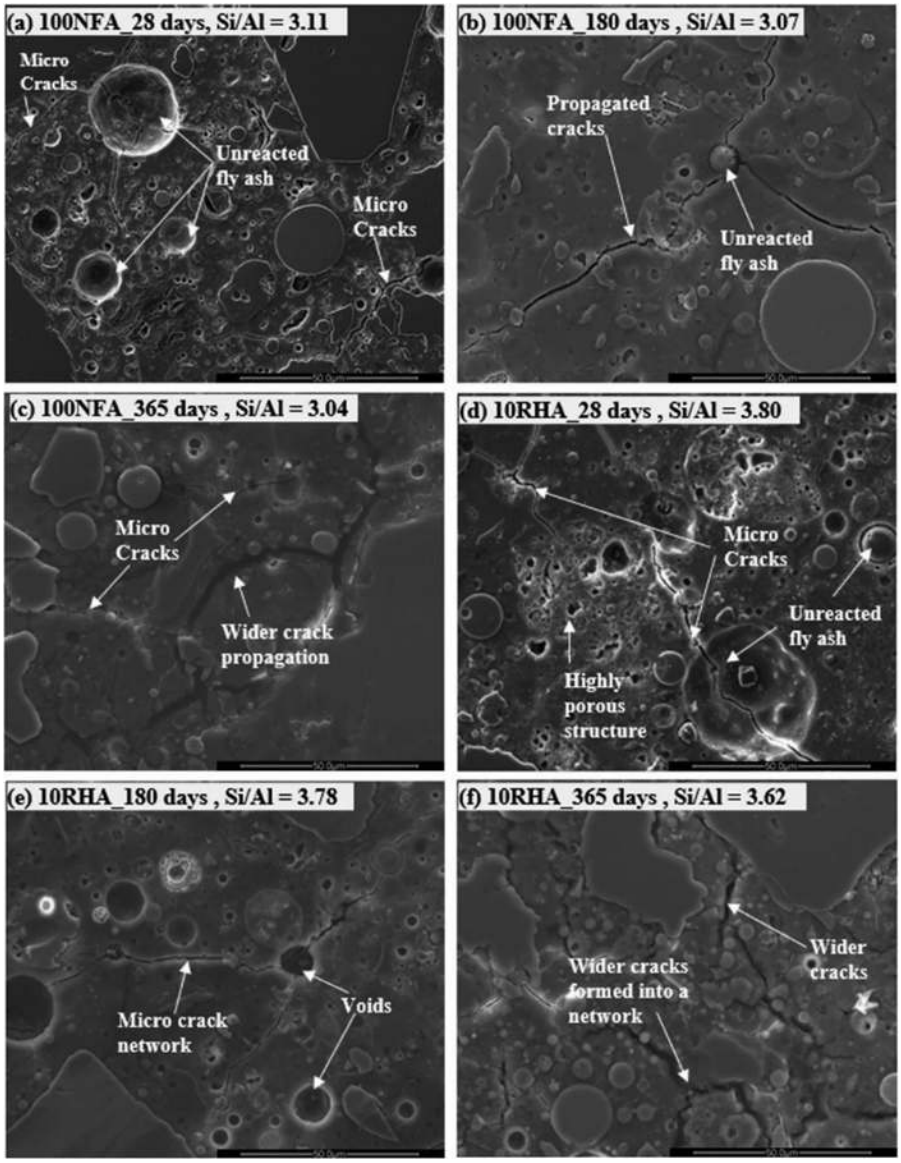

Fig. 7—SEM images and Si/Al ratio of 100NFA and 10RHA alkali-activated concretes up to 365 days.

the concrete due to its high heterogeneity.[37] A strong bond between alkali-activated paste and aggregate enhances the strength properties within the concrete matrix. Hence, the tendency of failure by cracking will depend on the strength of the ITZ. Figure 8 illustrates the ITZ of the 100NFA and 10RHA alkali-activated concretes at 28 and 365 days. The 100NFA concrete appears to have a stronger ITZ compared to 10RHA throughout the period. The broader ITZ, which contained cracks, observed in the 10RHA contributes to the higher creep compared to the 100NFA concrete, which displays a more compact and smaller ITZ. The SEM images show cracks propagated toward the aggregate near the ITZ at 365 days (Fig. 8(b) and (e)). Efflorescence products are observed adjacent to the ITZ in both concretes (with a greater quantity in the 10RHA concrete) (Fig. 8(c) and (f)). These efflorescence products are hypothesized as accelerating the propagation of cracks near the ITZ over time. This crack propagation has a highly detrimental impact on the ITZ, contributing to the reduced strength properties in the long-term specimens (365 days) for both concretes. This is attributed as the reason for the lower creep strength for both alkali-activated concretes at 365 days.

The total porosity (open and closed porosity) of the 100NFA and 10RHA alkali-activated concretes are calculated based on the images obtained from micro-CT analysis. Specific software was applied for further analysis of the micro-CT data: NRecon software for reconstructing projection images to form cross-section images, and CTAn software for characterizing the porous internal structures of specimens, either open or closed pores. The total porosity of 100NFA was 3.2%, 2.2%, and 2.8% at 28, 180, and 365 days, respectively, while the similar values for 10RHA were 5.3%, 3.4%, and 2.6%.

Figure 9 illustrates the percentage of macropore volume distribution for 100NFA and 10RHA. The 10RHA contained larger pores throughout (pore diameter of more than 1000 μm). These were more pronounced at 28 days when compared with 180 and 365 days and when compared with 100NFA. This is due to the formation of efflorescence products over time in the larger pores, which resulted in a reduction in the

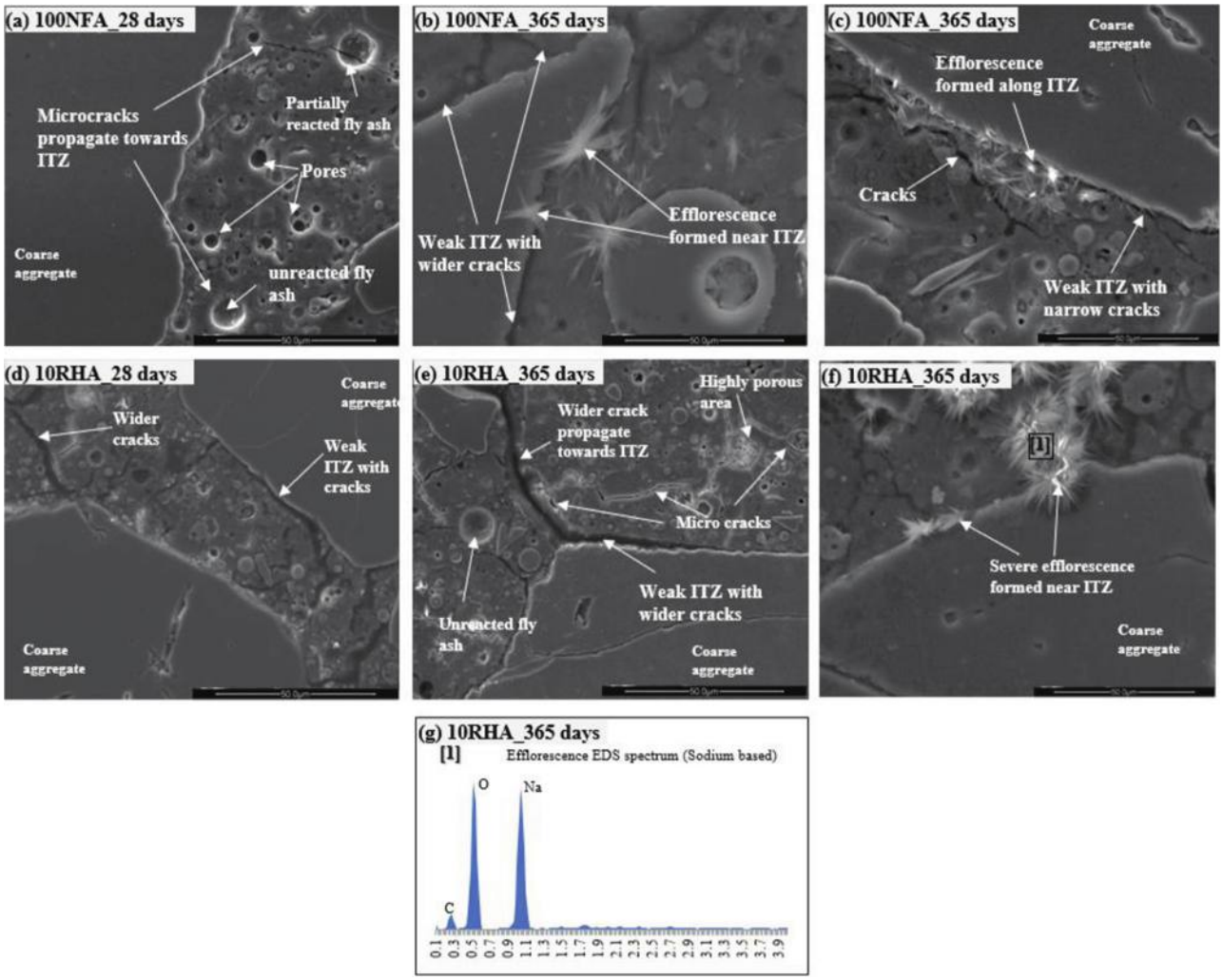

Fig. 8—SEM images of ITZ, efflorescence products, and EDS spectrum of 100NFA and 10RHA alkali-activated concretes.

number of larger pores at 180 and 365 days in the 10RHA concrete.

The aggregate content in concrete has a direct impact on the creep behavior of concrete: creep strain decreases with higher aggregate content.[38] However, it has been found that the creep strains of fly ash-based alkali-activated concrete may exhibit block polymerization and lead to favorable creep behavior when compared with traditional PC concrete.[39] Silicon and aluminum atoms in the precursor materials (that is, fly ash) are not entirely dissolved in the alkaline medium, as alumina-silica species are mainly leached from the dissolution of the amorphous phase rather than the crystalline phases.[3] In addition, the alkali-fly ash reaction takes place primarily at the particle-liquid interface.[40] Hence, the interior of the atoms is not completely dissolved and remains stable. This can act as micro-aggregates in the alkali-activated system, and as such, increase the aggregate content. The replacement with RHA will reduce the fly ash content in the mixture and hence will reduce the quantity of micro-aggregates. This is hypothesized as one of the reasons for the increased creep in the 10RHA alkali-activated concrete.

Alkali-activated concrete has a similar mechanism to PC for drying shrinkage, that is, an increase in negative pressure in the capillary network of cement/gel paste. The stresses developed lead to a contraction of concrete.[41] During heat curing of alkali-activated specimens, the condensation reaction accelerates moisture loss from the capillary pores. This has been attributed as the cause of the lower shrinkage strain for alkali-activated concrete when compared with the values generally obtained for PC concrete.[41] Furthermore, during the heat curing of alkali-activated concrete, most of the water released during the chemical reaction is lost through evaporation. Therefore, only a small amount of water remains contained in the micropores of the hardened alkali-activated concrete.[25] This is attributed as also contributing to the lower drying shrinkage observed in alkali-activated concrete (100NFA and 10RHA) compared to PC concrete.

Overall, the 10RHA concrete displayed higher creep strain and drying shrinkage when compared with 100NFA. The major factor that determines the creep and shrinkage behavior in the 100NFA and 10RHA alkali-activated concretes is crack propagation due to the formation of efflorescence products.

The reported creep and shrinkage values for 100NFA and 10RHA are significantly higher (more than double) than some of the values reported for low-calcium fly ash alkali-activated concrete reported in the literature.[3,13,25] However, a similar value to the creep coefficient of 100NFA has been

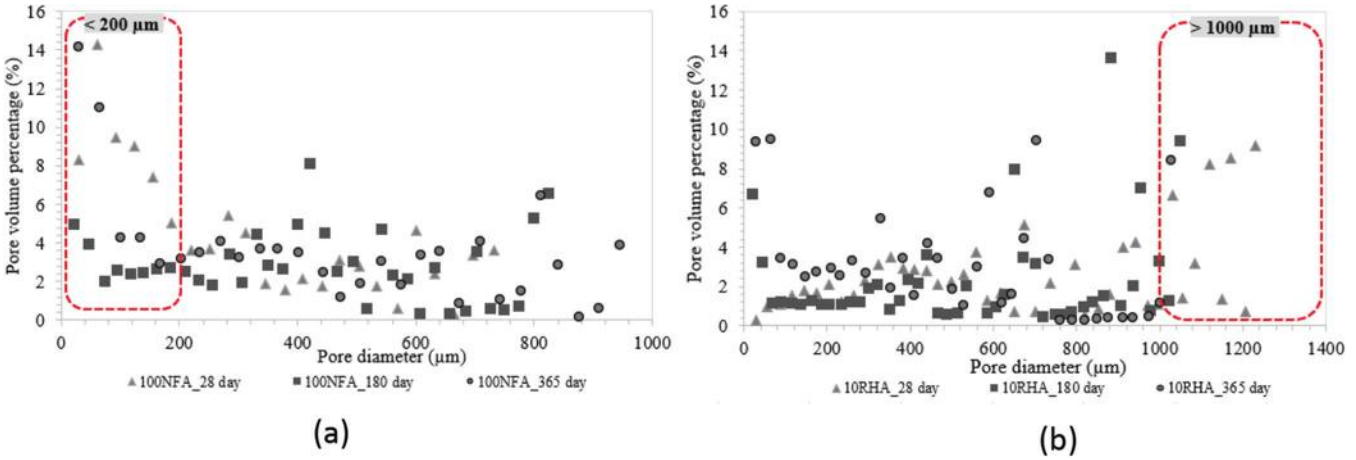

Fig. 9—Pore volume distribution of: (a) 100NFA; and (b) 10RHA alkali-activated concretes.

reported in the literature for 100% low-calcium fly ash alkali-activated concrete (Tarong Power Station, Australia), which is approximately 4.0 at 365 days.[3] This indicates that the long-term creep and shrinkage of each alkali-activated concrete should be evaluated to ensure that the creep and shrinkage behavior falls within the required conditions to use as a construction material.

CONCLUSIONS

The present study investigates the long-term creep and shrinkage properties of blended low-calcium fly ash-rice husk ash (RHA) (that is, 10RHA corresponds to 10% RHA replacement with fly ash) alkali-activated concrete for a period of up to 1 year. The following conclusions can be made from the experimental results:

1. The addition of 10% RHA to low-calcium fly ash alkali-activated concrete increases the creep strain and rate of creep development over time. The 100% low-calcium fly ash alkali-activated concrete (100NFA) showed a creep strain of 2139 µm, while 10RHA had a creep strain of 2713 µm at 365 days.

2. The negative synergistic effect due to the imbalance in the dissolution rate of the raw materials in the blended system in 10RHA negatively influences the strength properties, which leads to poor matrix integrity and a highly porous structure when compared with 100NFA.

3. The major influencing factor that determines the creep and shrinkage behavior in the 100NFA and 10RHA alkali-activated concretes is the effect of crack propagation due to the formation of efflorescence production.

4. The combined effect of crack propagation, efflorescence, and the more loosely packed structure in 10RHA correlates with the lower strength and high creep strain noted when compared to 100NFA.

5. The presence of the micro-aggregates due to the block polymerization provides the effect of increasing the aggregate content in the 100NFA concrete compared with the 10RHA concrete, which is hypothesized as one of the reasons the creep and shrinkage properties declined in 10RHA.

6. The observed drying shrinkage values of the 100NFA and 10RHA concretes are lower than the maximum permitted value for concrete recommended by the AS 3600 standard in Australia and the CEB-FIP model. The values predicted by these standards overestimate the drying shrinkage of both the 100NFA and 10RHA alkali-activated concretes.

AUTHOR BIOS

Sarah Fernando *is a PhD Student in civil and infrastructure engineering at RMIT University, Melbourne, VIC, Australia, and the Faculty of Engineering at the University of Peradeniya, Peradeniya, Sri Lanka. She received her BSc Eng (Hons) from the University of Peradeniya. Her research interests include concrete materials and the engineering properties of rice husk ash-blended alkali-activated concretes.*

Chamila Gunasekara *is a Lecturer of civil and infrastructure engineering at RMIT University. He received his BSc Eng (Hons) from the University of Peradeniya, and his MEng from Saitama University, Saitama, Japan. His research interests include concrete materials and engineering properties of geopolymer concretes.*

David W. Law *is a Senior Lecturer of civil and infrastructure engineering at RMIT University, having previously worked at Heriot-Watt University in Edinburgh, UK. His research interests include the durability and performance of reinforced concrete structures.*

M. C. M. Nasvi *is a Senior Lecturer in the Department of Civil Engineering, Faculty of Engineering, University of Peradeniya. His research interests include the wellbore integrity of carbon capture and sequestration (CCS) wells, well cementing, flow and mechanical behavior of geopolymers, ground improvement, and the adaptability of Eurocode 7 for geotechnical design.*

Sujeeva Setunge *is a Professor of civil engineering and the Associate Deputy Vice Chancellor for Research and Innovation in health, engineering and science at RMIT University. Her research interests include mechanical behavior, strengthening and creep, and shrinkage of reinforced concrete structures.*

Ranjith Dissanayake *is a Senior Professor in the Department of Civil Engineering, Faculty of Engineering, University of Peradeniya. His research interests include disaster mitigation, structural health monitoring of structures, structural optimization, and sustainable built environments.*

ACKNOWLEDGMENTS

The authors wish to acknowledge the X-Ray Facility and the Microscopy and Microanalysis Facility (RMMF) provided by RMIT University and the scientific and technical assistance. Scholarship provided by the School of Engineering, RMIT University; Faculty of Engineering, University of Peradeniya; and Tokyo Cement Company (Lanka) PLC to the first author is gratefully acknowledged. This project is funded by an ARC-ITRH (Australian Research Council Industrial Transformation Research Hub) research grant (IH200100010) allocated for Transformation of Reclaimed Waste Resources to Engineered Materials and Solutions for a Circular Economy (TREMS).

REFERENCES

1. Garside, M., "Global Cement Production 1995-2021," Statista, 2022.

2. Chen, C.; Habert, G.; Bouzidi, Y.; and Jullien, A., "Environmental Impact of Cement Production: Detail of the Different Processes and Cement Plant Variability Evaluation," *Journal of Cleaner Production*, V. 18, No. 5, Mar. 2010, pp. 478-485. doi: 10.1016/j.jclepro.2009.12.014

3. Gunasekara, C.; Setunge, S.; and Law, D. W., "Creep and Drying Shrinkage of Different Fly-Ash-Based Geopolymers," *ACI Materials Journal*, V. 116, No. 1, Jan. 2019, pp. 39-49. doi: 10.14359/51706941

4. Hwang, C.-L., and Huynh, T.-P., "Effect of Alkali-Activator and Rice Husk Ash Content on Strength Development of Fly Ash and Residual Rice Husk Ash-Based Geopolymers," *Construction and Building Materials*, V. 101, Part 1, Dec. 2015, pp. 1-9. doi: 10.1016/j.conbuildmat.2015.10.025

5. Fernando, S.; Gunasekara, C.; Law, D. W.; Nasvi, M. C. M.; Setunge, S.; and Dissanayake, R., "Life Cycle Assessment and Cost Analysis of Fly Ash–Rice Husk Ash Blended Alkali-Activated Concrete," *Journal of Environmental Management*, V. 295, Oct. 2021, Article No. 113140. doi: 10.1016/j.jenvman.2021.113140

6. Khale, D., and Chaudhary, R., "Mechanism of Geopolymerization and Factors Influencing Its Development: A Review," *Journal of Materials Science*, V. 42, No. 3, Feb. 2007, pp. 729-746. doi: 10.1007/s10853-006-0401-4

7. Huynh, T.-P.; Hwang, C.-L.; and Lin, K.-L., "Performance and Microstructure Characteristics of the Fly Ash and Residual Rice Husk Ash-Based Geopolymers Prepared at Various Solid-to-Liquid Ratios and Curing Temperatures," *Environmental Progress & Sustainable Energy*, V. 36, No. 1, Jan. 2017, pp. 83-92. doi: 10.1002/ep.12445

8. Khan, R.; Jabbar, A.; Ahmad, I.; Khan, W.; Khan, A. N.; and Mirza, J., "Reduction in Environmental Problems Using Rice-Husk Ash in Concrete," *Construction and Building Materials*, V. 30, May 2012, pp. 360-365. doi: 10.1016/j.conbuildmat.2011.11.028

9. Fernando, S.; Nasvi, M. C. M.; Gunasekara, C.; Law, D. W.; Setunge, S.; and Dissanayake, R., "Systematic Review on Alkali-Activated Binders Blended with Rice Husk Ash," *Journal of Materials in Civil Engineering*, ASCE, V. 33, No. 9, Sept. 2021, p. 04021229. doi: 10.1061/(ASCE)MT.1943-5533.0003825

10. Provis, J. L., "Alkali-Activated Materials," *Cement and Concrete Research*, V. 114, Dec. 2018, pp. 40-48. doi: 10.1016/j.cemconres.2017.02.009

11. Wallah, S. E., "Creep Behaviour of Fly Ash-Based Geopolymer Concrete," *Civil Engineering Dimension*, V. 12, No. 2, Sept. 2010, pp. 73-78.

12. Hardjito, D.; Wallah, S. E.; Sumajouw, D. M. J.; and Rangan, B. V., "On the Development of Fly Ash-Based Geopolymer Concrete," *ACI Materials Journal*, V. 101, No. 6, Nov.-Dec. 2004, pp. 467-472.

13. Sagoe-Crentsil, K.; Brown, T.; and Taylor, A., "Drying Shrinkage and Creep Performance of Geopolymer Concrete," *Journal of Sustainable Cement-Based Materials*, V. 2, No. 1, 2013, pp. 35-42. doi: 10.1080/21650373.2013.764963

14. AS 3582.1-1998, "Supplementary Cementitious Materials for Use with Portland and Blended Cement Fly Ash – Part 1: Fly Ash," Standards Australia, Sydney, NSW, Australia, 1998, 9 pp.

15. Hardjito, D., and Rangan, B. V., "Development and Properties of Low-Calcium Fly Ash-Based Geopolymer Concrete," Research Report GC 1, Curtin University, Perth, WA, Australia, 2005, 103 pp.

16. Khodr, M.; Law, D. W.; Gunasekara, C.; Setunge, S.; and Brkljaca, R., "Compressive Strength and Microstructure Evolution of Low Calcium Brown Coal Fly Ash-Based Geopolymer," *Journal of Sustainable Cement-Based Materials*, V. 9, No. 1, 2020, pp. 17-34. doi: 10.1080/21650373.2019.1666061

17. Fernando, K. S. D. M.; Nasvi, M. C. M.; Gunasekara, M. C. M.; Law, D. W.; Setunge, S.; and Dissanayake, P. B. R., "Mix Optimization of Geopolymer Mortar Produced with Low Calcium Fly Ash in Sri Lanka," *Proceedings*, 10th International Conference on Structural Engineering and Construction Management (ICSECM 2019), Kandy, Sri Lanka, Dec. 2019, pp. 292-299.

18. Gunasekara, C.; Law, D. W.; Setunge, S.; and Sanjayan, J. G., "Zeta Potential, Gel Formation and Compressive Strength of Low Calcium Fly Ash Geopolymers," *Construction and Building Materials*, V. 95, Oct. 2015, pp. 592-599. doi: 10.1016/j.conbuildmat.2015.07.175

19. Fernando, S.; Gunasekara, C.; Law, D. W.; Nasvi, M. C. M.; Setunge, S.; Dissanayake, R.; and Ismail, M. G. M. U., "Investigation of the Reaction Mechanism of Blended Fly Ash and Rice Husk Ash Alkali-Activated Binders," *Archives of Civil and Mechanical Engineering*, V. 22, No. 1, Feb. 2022, Article No. 24. doi: 10.1007/s43452-021-00349-6

20. AS 1012.9:2014, "Methods of Testing Concrete – Method 9: Compressive Strength Tests—Concrete, Mortar and Grout Specimens," Standards Australia, Sydney, NSW, Australia, 2014, 11 pp.

21. AS 1012.16-1996, "Methods of Testing Concrete – Method 16: Determination of Creep of Concrete Cylinders in Compression," Standards Australia, Sydney, NSW, Australia, 1996, 7 pp.

22. AS 1012.13:2015, "Methods of Testing Concrete – Method 13: Determination of the Drying Shrinkage of Concrete for Samples Prepared in the Field or in the Laboratory," Standards Australia, Sydney, NSW, Australia, 2015, 9 pp.

23. Hardjito, D.; Wallah, S. E.; Sumajouw, D. M. J.; and Rangan, B. V., "Fly Ash-Based Geopolymer Concrete," *Australian Journal of Structural Engineering*, V. 6, No. 1, 2005, pp. 77-86. doi: 10.1080/13287982.2005.11464946

24. Silva, R. V.; de Brito, J.; and Dhir, R. K., "Comparative Analysis of Existing Prediction Models on the Creep Behaviour of Recycled Aggregate Concrete," *Engineering Structures*, V. 100, Oct. 2015, pp. 31-42. doi: 10.1016/j.engstruct.2015.06.004

25. Wallah, S. E., and Rangan, B.V., "Low-Calcium Fly Ash-Based Geopolymer Concrete: Long-Term Properties," Research Report GC 2, Curtin University, Perth, WA, Australia, 2006, 107 pp

26. Castel, A.; Foster, S. J.; Ng, T.; Sanjayan, J. G.; and Gilbert, R. I., "Creep and Drying Shrinkage of a Blended Slag and Low Calcium Fly Ash Geopolymer Concrete," *Materials and Structures*, V. 49, No. 5, May 2016, pp. 1619-1628. doi: 10.1617/s11527-015-0599-1

27. AS 3600:2018, "Concrete Structures," Standards Australia, Sydney, NSW, Australia, 2018, 256 pp.

28. *fib*, "CEB-FIP Model Code 1990," CEB Bulletin No. 213/214, International Federation for Structural Concrete, Lausanne, Switzerland, 1993, 460 pp.

29. ACI Committee 209, "Guide for Modeling and Calculating Shrinkage and Creep in Hardened Concrete (ACI 209.2R-08)," American Concrete Institute, Farmington Hills, MI, 2008, 45 pp.

30. Neville, A. M.; Dilger, W. H.; and Brooks, J. J., *Creep of Plain and Structural Concrete*, Construction Press, London, UK, 1983.

31. Allena, S., and Newtson, C. M., "State-of-the-Art Review on Early-Age Shrinkage of Concrete," *The Indian Concrete Journal*, V. 85, No. 7, July 2011, pp. 14-20.

32. Herath, C.; Gunasekara, C.; Law, D. W.; and Setunge, S., "Long Term Creep and Shrinkage of Nano Silica Modified High Volume Fly Ash Concrete," *Journal of Sustainable Cement-Based Materials*, V. 11, No. 3, 2022, pp. 202-222.

33. Fernández-Jiménez, A.; Palomo, A.; Sobrados, I.; and Sanz, J., "The Role Played by the Reactive Alumina Content in the Alkaline Activation of Fly Ashes," *Microporous and Mesoporous Materials*, V. 91, No. 1-3, Apr. 2006, pp. 111-119. doi: 10.1016/j.micromeso.2005.11.015

34. De Silva, P.; Sagoe-Crenstil, K.; and Sirivivatnanon, V., "Kinetics of Geopolymerization: Role of Al_2O_3 and SiO_2," *Cement and Concrete Research*, V. 37, No. 4, Apr. 2007, pp. 512-518. doi: 10.1016/j.cemconres.2007.01.003

35. Hajimohammadi, A., and van Deventer, J. S. J., "Dissolution Behaviour of Source Materials for Synthesis of Geopolymer Binders: A Kinetic Approach," *International Journal of Mineral Processing*, V. 153, Aug. 2016, pp. 80-86. doi: 10.1016/j.minpro.2016.05.014

36. Temuujin, J., and van Riessen, A., "Effect of Fly Ash Preliminary Calcination on the Properties of Geopolymer," *Journal of Hazardous Materials*, V. 164, No. 2-3, May 2009, pp. 634-639. doi: 10.1016/j.jhazmat.2008.08.065

37. Gunasekara, C.; Law, D. W.; and Setunge, S., "Long Term Engineering Properties of Fly Ash Geopolymer Concrete," *Proceedings*, Fourth International Conference on Sustainable Construction Materials and Technologies (SCMT4), Las Vegas, NV, Aug. 2016, 10 pp.

38. Neville, A. M., and Brooks, J. J., *Concrete Technology*, Longman Scientific & Technical, Essex, UK, 1987.

39. Davidovits, J., ed., "Geopolymer Chemistry and Sustainable Development. The Poly(sialate) Terminology: A Very Useful and Simple Model for the Promotion and Understanding of Green-Chemistry," *Geopolymers, Green Chemistry and Sustainable Development Solutions: Proceedings of the World Congress Geopolymer 2005*, Saint-Quentin, France, 2005, pp. 9-16.

40. Diaz, E. I.; Allouche, E. N.; and Eklund, S., "Factors Affecting the Suitability of Fly Ash as Source Material for Geopolymers," *Fuel*, V. 89, No. 5, May 2010, pp. 992-996. doi: 10.1016/j.fuel.2009.09.012

41. Bissonnette, B.; Pierre, P.; and Pigeon, M., "Influence of Key Parameters on Drying Shrinkage of Cementitious Materials," *Cement and Concrete Research*, V. 29, No. 10, Oct. 1999, pp. 1655-1662. doi: 10.1016/S0008-8846(99)00156-8

JOIN AN ACI Chapter!

The American Concrete Institute has Chapters and Student Chapters located throughout the world. Participation in a local chapter can be extremely rewarding in terms of gaining greater technical knowledge and networking with leaders in the concrete community.

Because chapters are distinct and independent legal entities, membership includes both ACI members and non-ACI members and is made up of a diverse blend of architects, engineers, consultants, contractors, educators, material suppliers, equipment suppliers, owners, and students—basically anyone interested in concrete. Many active ACI members initially became involved in ACI through their local chapter. In addition to technical programs and publications, many chapters sponsor ACI Certification programs, ACI educational seminars, project award recognition programs, and social events with the goal of advancing concrete knowledge.

Check out the Chapters Special Section from the November 2020 *Concrete International*: www.concrete.org/publications/concreteinternational.aspx

---

Student Chapters

Join or form an ACI Student Chapter to maximize your influence, knowledge sharing, and camaraderie! ACI has 240+ student chapters located throughout the world, each providing opportunities for students to:

- Connect with their peers and participate in concrete-related activities such as: student competitions, ACI Conventions, ACI Certification Programs, ACI Educational Seminars, local chapter meetings, social events, and community service projects;
- Network with members of local chapters, many of whom have been in the industry for decades and can help to develop professional relationships and offer career advice;
- Win recognition for their universities through the University Award; and
- Learn about the many scholarships and fellowships offered by the ACI Foundation and by ACI's local chapters.

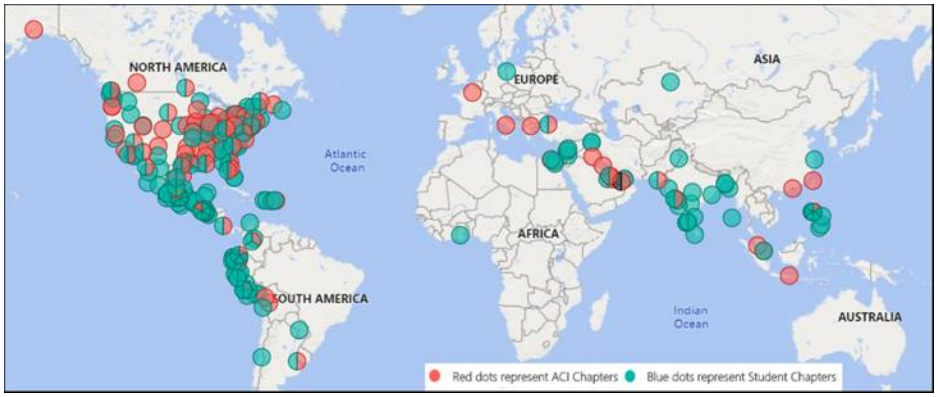

ACI MATERIALS JOURNAL TECHNICAL PAPER

Title No. 120-M55

Self-Healing Efficiency of Concretes through Permeability to Chlorides

by C. F. Hollmann, L. Zucchetti, D. C. C. Dal Molin, and A. B. Masuero

Self-healing is a process by which concrete is able to recover its properties after the appearance of cracks, which can improve mechanical properties and durability and reduce the permeability of concrete. Self-healing materials can be incorporated into concrete to contribute to crack closure. This study aims to evaluate the influence of crystalline admixtures and silica fume on the self-healing of concrete cracks. The rapid chloride penetration test was performed on cracked and uncracked samples, from which it was possible to estimate the service life of concretes. The concretes were characterized by tests of compressive strength and water absorption by capillarity. The use of crystalline admixtures did not have a negative influence on concrete properties, but did not favor the chloride penetration resistance. The concrete with silica fume showed the lowest charge passed and highest values of estimated service life.

Keywords: chloride penetration resistance; crystalline admixture (CA); self-healing; service life prediction; silica fume.

INTRODUCTION

The low tensile strength of concrete makes the material susceptible to cracking. Structures are designed with steel bars to resist tensile strength, which helps to avoid crack formation. However, in most cases, the reinforcement is not able to completely prevent the crack opening, only restricting the crack width.[1]

In this context, the concept of self-healing emerges, a process by which concrete is able to recover its properties after the appearance of cracks. Crack closure through self-healing can improve mechanical properties and durability and reduce the permeability of concrete.[2,3]

Self-healing materials can be incorporated into the concrete to contribute to crack closure.[4] Crystalline admixtures (CAs) have been studied for this purpose, being evaluated mainly through microscopy techniques and image analysis.[5-12] In the presence of water, these admixtures react according to Eq. (1) to form calcium silicate hydrates (C-S-H) and/or pore-blocking precipitates in the existing microcracks and capillaries.[8,13]

$$3CaO\text{-}SiO_2 + M_xR_x + H_2O \rightarrow Ca_xSi_xO_xR\text{-}(H_2O)_x + M_xCaR_x\text{-}(H_2O)_x \quad (1)$$

(Calcium silicate + crystalline promoter + water → modified calcium silicate hydrate + pore-blocking precipitate)

Silica fume can also contribute to the self-healing of cracks due to the pozzolanic reaction, which consumes $Ca(OH)_2$ and produces C-S-H.[14,15]

The rapid chloride penetration test (RCPT), specified by ASTM C1202-19,[16] is a method used in several studies, mainly to evaluate the durability of concrete.[17-19] Nonetheless, its application can also be interesting to assess the self-healing of concrete, to verify if the crack closure was enough to prevent the ingression of aggressive agents. Therefore, this study aims to evaluate the influence of CAs (two different commercial brands) and silica fume on the self-healing of cracks through the RCPT.

RESEARCH SIGNIFICANCE

Cracking is the most common pathological manifestation in concrete structures, which facilitates the ingress of aggressive agents such as chloride ions. Self-healing provided by the use of CAs and silica fume may be an option to prevent the deterioration of structures by cracking.

Most of the research on self-healing uses microscopy and image analysis techniques to assess crack closure. In this paper, the recovery of cracked concretes in relation to their chloride penetration resistance was evaluated. To achieve this objective, cracked and uncracked concrete specimens were tested by the RCPT, seeking to evaluate the self-healing of cracks and thus estimate the service life.

EXPERIMENTAL INVESTIGATION

Materials and mixture proportions

The cement used was portland cement composed with filler (CP II-F 40), conforming to ABNT NBR 11578/1991,[20] equivalent to Type II cement of ASTM C150/C150M-20.[21] The cement used was obtained before the replacement of ABNT NBR 11578[20]; therefore, its chemical composition is as specified by this standard. The chemical composition of the cement, the CAs (CA1 and CA2), and the silica fume (SF) used were determined by X-ray fluorescence (XRF) analysis (Table 1). CA1 and CA2 were also characterized by X-ray diffraction (XRD) (Fig. 1) and laser granulometric analysis (Fig. 2). The characterization of the aggregates is presented in Table 2, and the particle-size distribution is presented in Fig. 3. A high-range water-reducing admixture

ACI Materials Journal, V. 120, No. 5, September 2023.
MS No. M-2022-221.R2, doi: 10.14359/51738892, received April 22, 2023, and reviewed under Institute publication policies.

(HRWRA) was employed to achieve the desired workability (220 ± 20 mm). Potable water was used for the concrete casting.

Four different concretes were investigated in this study: two concretes with CAs from different brands (1% of the cement weight) (CCA1 and CCA2), a concrete with the addition of silica fume (5% of the cement weight) (CSF), and a control concrete without admixtures (Fig. 4). The composition of all concretes was 1:1.37:2.18 by mass (cement:fine aggregate:coarse aggregate), with CAs and silica fume being used as an addition and not as a replacement for cement. The water-cement ratio (*w*/*c*) of 0.40 was fixed for all concretes. Table 3 shows the composition of the concretes.

Table 1—Chemical composition of raw materials

	Chemical compositions, %			
	Cement	CA1	CA2	SF
SiO_2	12.78	8.94	12.64	88.35
Al_2O_3	3.77	2.67	2.95	1.72
Fe_2O_3	4.13	2.24	2.50	0.10
CaO	66.48	64.07	58.45	0.68
MgO	1.46	0.55	5.54	4.30
K_2O	1.19	0.56	1.04	0.91
Cl	—	0.15	0.09	0.23
TiO_2	—	0.19	0.18	—
MnO	—	0.06	0.06	0.05
SrO	—	0.28	0.24	—
P_2O_5	—	—	—	0.57
SO_3	6.84	2.44	3.43	0.13
Loss on ignition	5.20	17.81	12.87	2.91

Note: CA1 is crystalline admixture 1; CA2 is crystalline admixture 2; SF is silica fume.

The concretes' slump and specific mass were determined according to ABNT NBR NM 67:1998[22] and ABNT NBR 9833:2008,[23] respectively. The properties of fresh concretes are shown in Table 4.

Cylindrical specimens (100 x 200 mm) were molded for the tests of compressive strength and water absorption by capillarity, and cylindrical specimens (95 x 190 mm) were molded for the RCPT, which are smaller in diameter due to the limited size of the test equipment. All specimens were compacted on a vibrating table. The specimens were demolded after 24 hours and placed in a humidity chamber (25°C and 95% relative humidity [RH]).

Compressive strength

The compressive strength test was performed according to ABNT NBR 5739:2018.[24] Three cylindrical specimens (100 x 200 mm) cured in a humidity chamber were tested at the ages of 3 and 28 days to determine the compressive strength of each concrete.

Water absorption by capillarity

The water absorption by capillarity was determined according to ABNT NBR 9779:2012.[25] Four cylindrical specimens (100 x 200 mm) cured in a humidity chamber were tested at the age of 28 days. Before the test, the specimens were oven-dried at 100°C for 3 days. The specimens were placed in a container with a 5 mm layer of water, and their weights were determined at the beginning of the test and after 3, 6, 24, 48, and 72 hours. The water absorption in each test time is the ratio between the mass of water absorbed

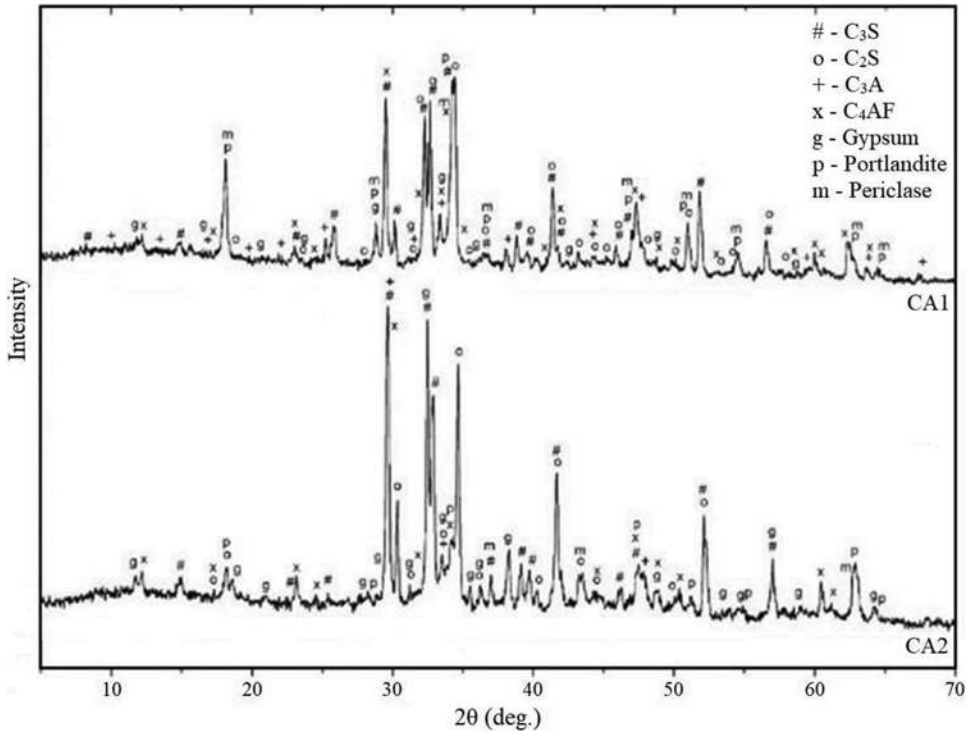

Fig. 1—XRD analysis of crystalline admixtures.

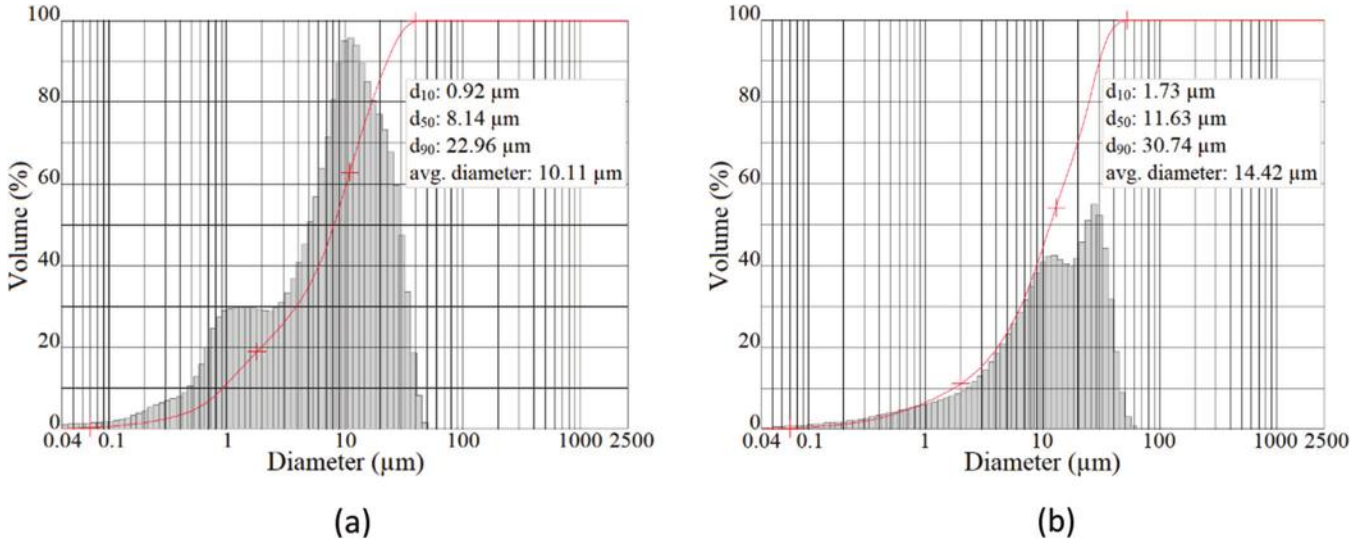

Fig. 2—Laser granulometry of crystalline admixtures: (a) CA1; and (b) CA2.

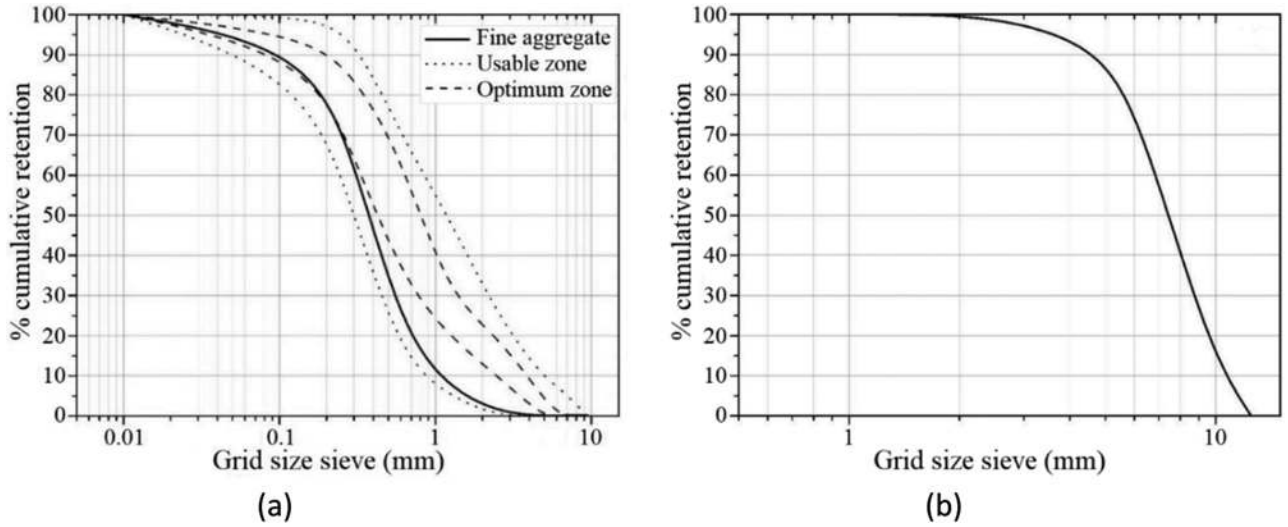

Fig. 3—Particle-size distribution: (a) fine aggregate; and (b) coarse aggregate.

Table 2—Characterization of coarse and fine aggregates

	Fine aggregate	Coarse aggregate
Fineness modulus	1.89	6.10
Maximum size, mm	2.36	12.50
Specific gravity, g/cm^3	2.54	3.01
Water absorption, %	1.30	1.20

since the beginning of the test and the cross-sectional area of the test sample.

Rapid chloride penetration test (RCPT)

The RCPT was carried out according to ASTM C1202[16] to evaluate the charge passed in cracked and uncracked specimens. Cylindrical specimens (95 x 190 mm) were cured in a humidity chamber for 3 days. This age was chosen for the crack opening because, in real situations, it is common for concrete to crack at early ages and, as there is a greater amount of anhydrous cement in the cementitious matrix, the process of autogenous self-healing is favored. Each specimen was sawn into four slices, using the central slices of the specimens, with a thickness of 50 ± 3 mm each (Fig. 5).

After sawing, the crack opening was carried out by the splitting tensile strength test.[26] A constant loading of 0.45 ± 0.15 MPa/s was applied to the specimens, being automatically stopped when there was a load drop that indicated the rupture and visual crack opening. A patent-pending rupture apparatus was used to prevent the specimen from breaking completely (Fig. 6). The surface crack widths were measured by optical microscopy, on the face where the crack was visually thicker, to select the cracks with a thickness less than 0.4 mm in its entire length.

The specimens were exposed to wetting-and-drying cycles with 2 days of immersion in potable water that was changed each cycle and 12 days of drying, with the wetting-and-drying periods having the same duration as used by Cappellesso et al.[27] and Ziegler et al.[28] The wetting-and-drying cycles were defined to simulate common situations of concrete structures in contact with water, with the immersion periods simulating wet days and the drying period

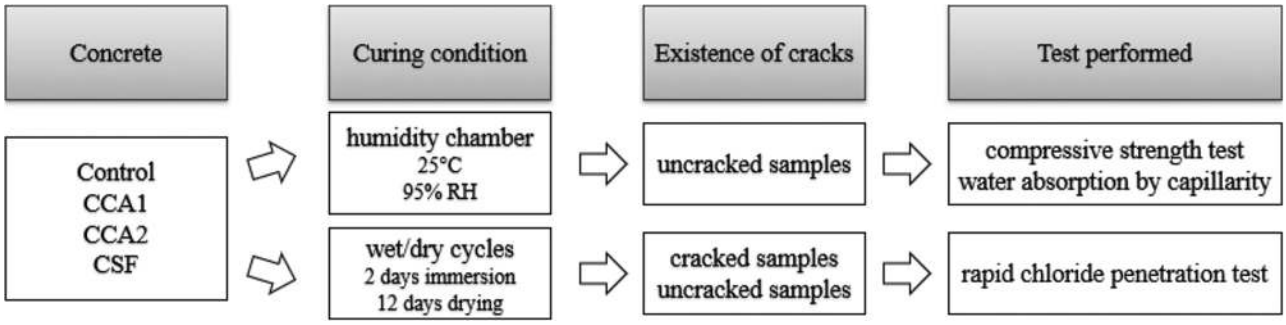

Fig. 4—Experimental program.

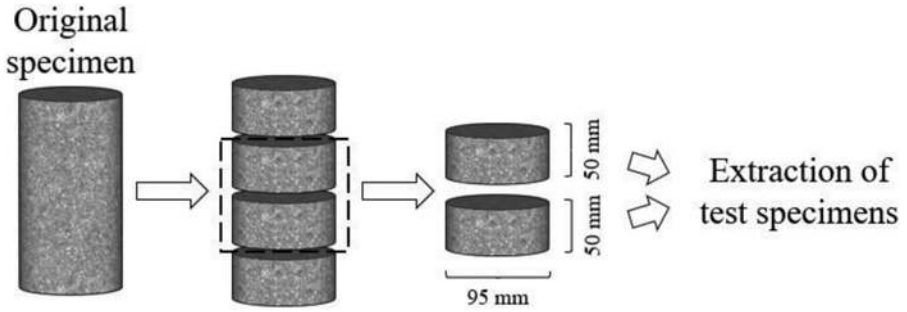

Fig. 5—Specimens cutting procedure.

Table 3—Concrete mixture design

Material	Control	CCA1	CCA2	CSF
Cement, kg/m^3	485.76	487.96	493.24	467.26
Water, kg/m^3	194.30	195.18	197.30	186.91
HRWRA, L/m^3	0.40	0.58	0.72	0.72
Coarse aggregate, kg/m^3	1060.90	1065.70	1077.24	1020.50
Fine aggregate, kg/m^3	663.55	666.55	673.77	638.28
Crystalline admixture, kg/m^3	—	4.88	4.93	—
Silica fume, kg/m^3	—	—	—	23.36
w/c	0.40	0.40	0.40	0.40
w/b	0.40	0.40	0.40	0.38

Table 4—Fresh concrete properties

Concrete	Slump, mm	Specific mass, kg/m^3
Control	200	2404.52
CCA1	200	2420.26
CCA2	200	2446.49
CSF	200	2336.32

simulating a hot and dry period. The RCPT was carried out at two ages, after two and six wetting-and-drying cycles, corresponding to 28 and 91 days, respectively. At each age, three cracked and three uncracked samples were tested.

After the defined curing periods, the samples were epoxy-coated to isolate the concrete from the external environment (Fig. 7). The next day, the vacuum saturation procedure was performed as specified by ASTM C1202,[16] so the chloride-ion penetration process would not occur by absorption. This procedure consists of placing the specimens in the vacuum desiccator, with both end faces of the specimens

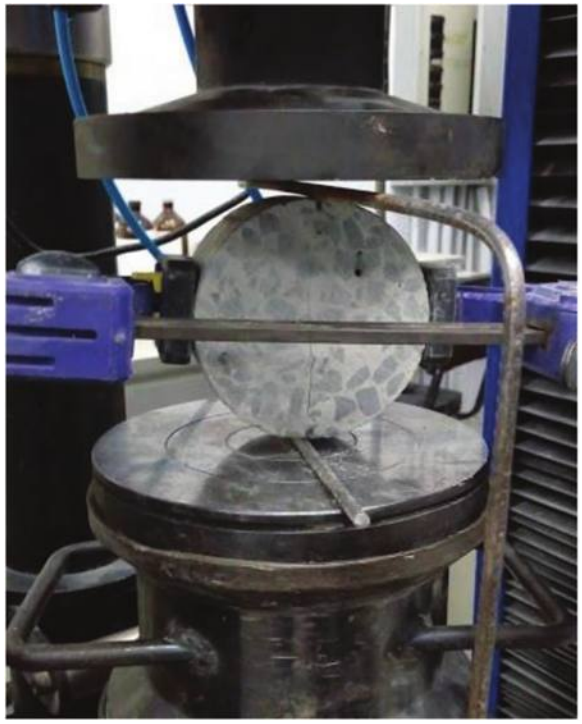

Fig. 6—Crack opening procedure.

exposed. A vacuum pump was connected to the desiccator for 2 hours to remove all the air present in the pores of the concrete. Then, the desiccator was sealed, and the samples remained submerged in deionized water for another 18 ± 2 hours.

The specimens were coupled between two cells using a polyurethane adhesive. One of the cells was filled with 0.3N sodium hydroxide (NaOH) solution and the other with 3% sodium chloride (NaCl) solution. Each pair of cells

Table 5—Compressive strength and water absorption by capillarity of concretes

Concrete	Compressive strength, MPa				Water absorption by capillarity after 72 hours of testing, g/cm²	
	3 days		28 days			
	Average	Standard deviation	Average	Standard deviation	Average	Standard deviation
Control	29,7	1.5	34.9	3.6	0.76	0.05
CCA1	34,1	0.2	40.3	1.8	0.71	0.10
CCA2	35,7	1.0	45.7	1.2	0.54	0.03
CSF	30,3	1.7	44.8	2.2	0.48	0.04

was individually connected to a multimeter, all of which were connected to a power supply capable of holding the voltage constant at 60 V between the cells. The electrical current passing through each specimen was recorded every 30 minutes using the multimeter, for 6 hours. The charge passed was calculated from the results of current versus time according to ASTM C1202[16] (Eq. (2))

$$Q = 900(I_0 + 2I_{30} + 2I_{60} + \ldots 2I_{300} + 2I_{330} + I_{360}) \quad (2)$$

where Q is the charge passed (coulombs); I_0 is the current (amperes) immediately after the voltage is applied; and I_t is the current (amperes) at t minutes after the voltage is applied.

Service life prediction

To estimate the service life from the RCPT, the model proposed by Berke and Hicks[29] was used, which is not standardized; however, it was adopted in other studies.[30-33] From the charge passed measured in the RCPT, the model uses Eq. (3) to estimate the chloride diffusion coefficient in concrete. This coefficient characterizes the concrete's resistance to the passage of chlorides and is used to assess the durability of the material in relation to reinforcement depassivation by chlorides[28,31]

$$C_{da} = 0.0103 \times 10^{-8} Q^{0.84} \quad (3)$$

where C_{da} is the chloride apparent diffusion coefficient (cm²/s); and Q is the total charge passed (coulombs) obtained in the RCPT.

Equations (4) and (5), developed from Fick's second law, allow the service life to be estimated. The proposal enables a correlation between the concrete cover and the time to initiate corrosion. Because the proposed method is based on Fick's second law, it represents a more realistic situation for the passage of chloride ions through concrete, as it considers non-steady-state diffusion, which means that the flow is dependent on both time and penetration depth, unlike Fick's first law, which assumes that ion flow is constant[34,35]

$$P_{Cl} = 2(z)\sqrt{Dt} \quad (4)$$

$$\text{erf}(z) = 1 - \frac{C_{Cl} - C_0}{C_s - C_0} \quad (5)$$

where P_{Cl} is the chloride penetration depth in which the chloride concentration reached a critical point for depassivation of reinforcement (cm); D is the chloride apparent diffusion coefficient (cm²/year); t is the service life (years); erf(z) is the Gaussian error function; C_{Cl} is the chloride concentration limit for depassivation of reinforcement by chloride attack over the P_{Cl} depth and time t (defined as 0.4%[31-33]); C_0 is the initial chloride concentration inside the concrete component (considered as 0%); and C_s is the chloride concentration in the surface of the concrete component, admitted as constant (fixed at 0.63%, value used for concrete with w/c less than 0.48, f_{ck} above 35 MPa, and exposed to salt spray[36]).

Fig. 7—Coating of specimens with epoxy.

EXPERIMENTAL RESULTS AND DISCUSSION

Compressive strength

The compressive strength test was performed at 3 days (age of crack opening) and at 28 days (Table 5). As expected, all concretes showed an increase in compressive strength from the age of 3 to 28 days. The concrete that showed the greatest increase in compressive strength between the test ages was the concrete with silica fume (CSF), being 48% higher at 28 days compared to 3 days, which probably occurred due to the filler effect and pozzolanic reaction of the silica fume.[37]

The concretes with CAs (CCA1 and CCA2) showed compressive strength higher than the control concrete for both test ages. The increase in compressive strength provided by the use of these admixtures may have occurred

due to their reaction, which contributes to the increase in the density of C-S-H in the matrix.[8]

Some authors who incorporated CAs into concrete also found superior compressive strength when compared to control concrete,[5,8,38] while others observed similar compressive strength values with and without the use of these admixtures.[31,39] Therefore, CAs do not have a negative influence over the compressive strength.

At the age of 3 days, the CSF and control concrete showed similar results for compressive strength, while at the age of 28 days, the compressive strength of CSF was 28% higher than the compressive strength of the control concrete. Thus, the addition of silica fume influenced the compressive strength only at 28 days, because the pozzolanic reaction has more influence at a later age of the concrete and was not significant at the age of 3 days. Furthermore, the fine particles of the silica fume contribute to a higher packing density (filler effect) and a consequent increase in the compressive strength of the concrete.[18,38] It should also be noted that although the *w*/*c* of concretes are equal, the water-binder ratio (*w*/*b*) of concrete with silica fume is 0.38, while that of the reference concrete is 0.40.

Water absorption by capillarity

The results of water absorption by capillarity over the duration of the test are shown in Fig. 8. To facilitate the comparison between the concretes, only the results obtained after 72 hours of testing were considered (Table 5).

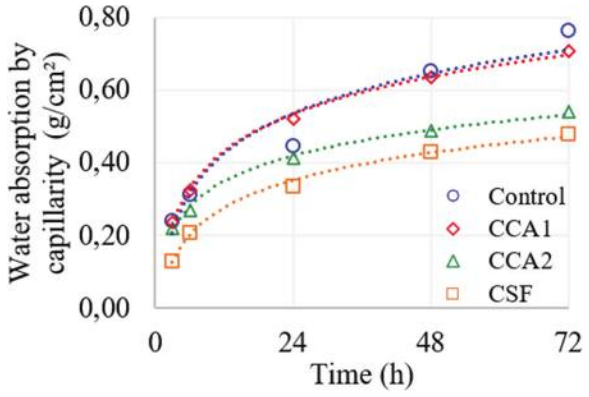

Fig. 8—Water absorption by capillarity of concretes.

The concretes that showed less water absorption by capillarity were CSF and CCA2. The control concrete was the one with the highest water absorption by capillarity after 72 hours of testing, the value being very close to that obtained for the CCA1.

In general, the water absorption by capillarity was lower in concretes with higher compressive strength, a fact that may be related to the capacity of the admixtures to fill the capillary pores of the concrete, thus contributing to both properties.

CAs have the ability to fill the capillary pores of the cementitious matrix, making the concrete less permeable, which may have contributed to the reduction in water absorption in the concretes with the admixtures in relation to the control concrete.[31,40]

Cappellesso et al.[38] observed the greater efficiency of silica fume in reducing water absorption compared to CAs and the control concrete, as in the present work. The incorporation of silica fume contributes to a denser microstructure, which reduces the permeability of the cementitious matrix.[41]

Rapid chloride penetration test (RCPT)

The RCPT results obtained at 28 and 91 days for the concretes are shown in Table 6. To verify the significance of the use of CAs and silica fume, the age, and the presence of cracks in the concrete, an analysis of variance (ANOVA) was carried out (Table 7). Then, the multiple comparisons were performed by Fisher's least significant difference (LSD) test to verify which results belong to the same homogeneous group (Fig. 9).

In all combinations of concrete type and the presence of cracks, there was a decrease in the charge passed at 91 days compared to 28 days. This result was expected because the chloride penetration resistance in concrete increases with age, due to the continuity of cement hydration reactions.[5,37,42,43] The uncracked CSF showed the greatest reduction in the charge passed between the ages of 28 and 91 days (47%), which possibly occurred because of the pozzolanic reaction provided by the addition of silica fume, which occurs over time.

In the case of CSF and the control concrete, the results of charge passed obtained for the cracked concretes at 91 days were similar to those obtained for the uncracked concretes at

Table 6—Chloride-ion penetrability at 28 and 91 days

	Concrete	28 days		91 days	
		Average charge passed, coulombs	Chloride-ion penetrability[16]	Average charge passed, coulombs	Chloride-ion penetrability[16]
Cracked	Control	3982.70	Moderate	2987.31	Moderate
	CCA1	4630.48	High	2984.79	Moderate
	CCA2	4277.07	High	2712.19	Moderate
	CSF	2522.89	Moderate	1600.61	Low
Uncracked	Control	3218.74	Moderate	2470.06	Moderate
	CCA1	3739.20	Moderate	2259.05	Moderate
	CCA2	3748.08	Moderate	2319.61	Moderate
	CSF	1673.57	Low	891.56	Very low

Table 7—Analysis of variance (ANOVA) for charge passed results obtained in RCPT

Effect	SS	DF	MS	*F*	*p*	Sig.
Concrete	23,537,329	3	7,845,776	124.340	0.000000	S
Crack	5,423,357	1	5,423,357	85.949	0.000000	S
Age	17,163,374	1	17,163,374	272.005	0.000000	S
Concrete crack	227,158	3	75,719	1.200	0.325507	N
Concrete age	1,344,681	3	448,227	7.104	0.000865	S
Crack age	88,990	1	88,990	1.410	0.243744	N
Concrete crack age	5923	3	1974	0.031	0.992409	N
Error	2,019,183	32	63,099	—	—	—

Note: SS is sum of squares; DF is degrees of freedom ($n - 1$); MS is mean squares; *F* is calculated value of *F*; *p* is significance level ($p < 5\%$ denotes a significant effect); S is significant effect; N is nonsignificant effect.

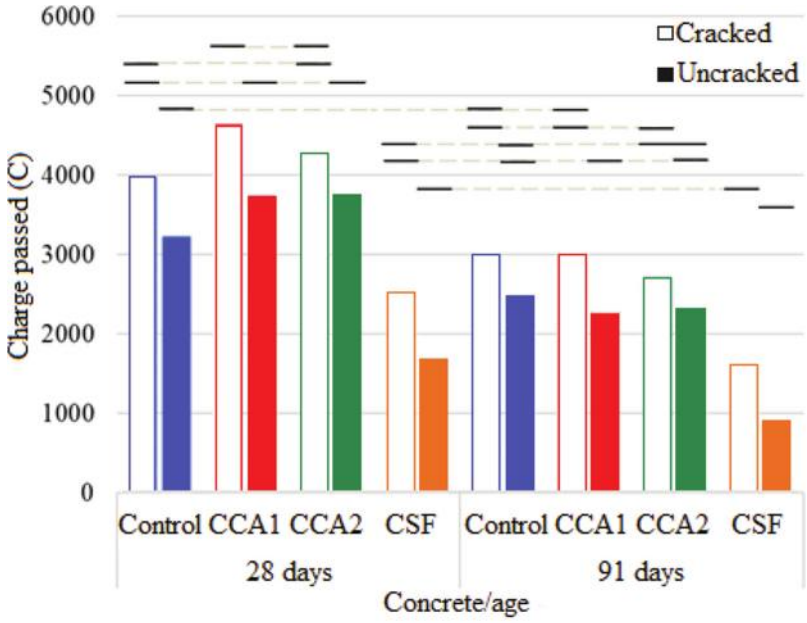

Fig. 9—Homogenous groups by Fisher's LSD test for charge passed results obtained in RCPT.

28 days. This indicates that cracked concrete can achieve the same chloride penetration resistance as uncracked concrete, as long as it has a longer curing time.

Comparing cracked and uncracked concretes, the existence of cracking allowed greater charge passed in the tested specimens, which probably occurred due to the fact that the cracks act as a preferential path for the ingression of aggressive agents into the concrete.[44-47] However, this result indicates that the cracks were not completely closed until the age of 91 days, because their presence had an influence on the charge passed. Only in the case of CCA2, there was no statistically significant difference between cracked and uncracked concrete at the age of 91 days. Even so, the reduction in the charge passed at 91 days shows that the self-healing probably occurred internally.

CSF showed the lowest charge passed under all conditions analyzed. At the age of 28 days, the use of silica fume provided a reduction of 37% and 48%, respectively, for cracked and uncracked concrete, in relation to the control concrete. At 91 days, this reduction was 46% for cracked concrete and 63% for uncracked concrete. The greater reduction in charge passed at later ages can be attributed to the pozzolanic reaction due to the use of silica fume, which occurs over time.[37]

One of the main advantages of using pozzolanic materials in concrete is the increase in its durability because the reduced capillary porosity of the cement paste with their addition makes the ingress of aggressive agents into the concrete difficult, which justifies the lower charge passed values obtained for CSF.[48] The results obtained in the water absorption by capillarity tests corroborate this statement, because less permeable concretes generally have higher durability.[49]

The use of CAs did not contribute to preventing the ingress of chloride ions into the tested concretes. For cracked concretes, at the age of 28 days, CCA1 showed a charge passed 16% higher than the control concrete, while the charge passed in CCA2 was similar to the control concrete. For uncracked concretes, a 16% higher charge passed was observed in both CCA1 and CCA2 compared to the control

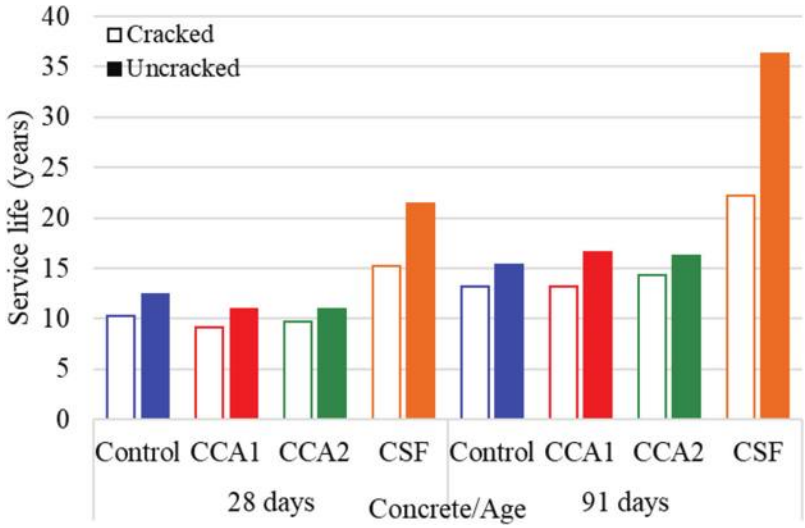

Fig. 10—Service life prediction after 28 and 91 curing days.

concrete. At the age of 91 days, the charge passed in CCA1, CCA2, and the control concrete was similar, for both cracked and uncracked concretes.

Although it was expected that the use of CAs would provide greater chloride penetration resistance than the control concrete, the results obtained may be due to the adopted wetting-and-drying cycle, which lasted 14 days, but only 2 days were of water immersion. However, contact with humidity is necessary for the CA to react.[11] Possibly, the wetting-and-drying cycles adopted did not provide enough moisture time for the reactions of CAs to occur; thus, they did not contribute to the chloride penetration resistance.

Ziegler et al.[28] adopted cycles with the wetting-and-drying periods having the same duration as in this study. The authors also verified that the short wetting period the specimens were exposed to impaired the crack closure. However, the concretes were in direct contact with water during the diffusion test carried out for a long period, which may have positively influenced the reduction in the passage of chloride ions, due to the continuous hydration reaction of the CAs with the water in the test. Borg et al.[6] verified that the crack closure occurs in samples submerged in seawater and can be more efficient than in distilled water. Helene et al.[31] obtained lower values of charge passed for the concrete with CA, and the specimens were cured in a moist chamber until the test age, which may have favored the results obtained.

The selection of the samples considering only the superficial crack width may have contributed to a greater variation in the RCPT results. The internal morphology of the cracks influences the occurrence of self-healing because the zones with smaller crack widths might be more suitable to start the precipitation of crack-healing products.[8]

Service life prediction

The service life of a reinforced concrete structure, with respect to the corrosion of reinforcement in marine environments, corresponds to the time to initiate the reinforcement depassivation by chlorides. To estimate the service life, a 4 cm reinforcement depth was adopted, recommended by ABNT NBR 6118:2014[50] for the class of environmental aggressiveness III (strong aggressiveness, marine environment, and great risk of deterioration of the structure), considering beams and columns. Figure 10 shows the estimated service life for all conditions analyzed.

The service life was estimated from the results of charge passed; therefore, the results are equivalent, that is, a concrete that presents higher chloride penetration resistance also has a longer estimated service life. Therefore, the concretes with the highest charge passed had a higher chloride diffusion coefficient and, consequently, a shorter estimated service life.

In general, the concretes presented a very low estimated service life, except for the CSF. Helene et al.[31] obtained an estimated service life of approximately 20 years for the uncracked concretes, with the RCPT performed at the age of 28 days, a result superior to that obtained in this study. However, Helene et al.[31] used slag-blended cement, sulfate resistant (CP III-40 RS), which contributes to the reduction in porosity and the increase in durability of the concrete. In this research, the cement used, CP II-F 40, may have impaired the results, as it has only filler addition, a material that has no chemical action and therefore reduces the binder content, consequently increasing the *w*/*b*. The main crack-sealing process promoted by the cement used is the leaching of calcium hydroxide, with the consequent formation of $CaCO_3$, which can impoverish the matrix by the release of $Ca(OH)_2$ crystals.[51]

In the same way as in the RCPT, CCA1 and CCA2 showed a similar or inferior result of service life when compared to the control concrete. Even when the service life was similar between CCA2 and the control concrete, the result was not satisfactory because the CAs were incorporated into the concrete with the function of contributing to the crack closure and, consequently, increasing the service life of the concretes.

CSF had the longest estimated service life, as was already expected because the use of silica fume provided the lowest charge-passed values in the RCPT. At the age of 28 days, the increase provided was 47% and 73%, respectively, for cracked and uncracked concrete, compared to the control

concrete. At 91 days, the increase was 69% and 135% for cracked and uncracked concrete, respectively. The addition of silica fume to the concrete contributed to the increase in its durability due to the reduction in the capillary porosity of the cement paste and in the aggregate-cement paste transition zone, which makes it difficult for aggressive agents to enter the concrete.[48]

It is important to note that the service life prediction presented is only valid in the following conditions: reinforced concrete is at the beginning of its service life (initiation period); the fastest aggressive agent is the ingression of chloride ions, disregarding the others; concrete is subjected to salt spray or immersion in water contaminated with chloride ions, and no other accidental external factors would affect the properties of the concrete cover.[31,32]

CONCLUSIONS

This study aimed to evaluate the influence of the use of crystalline admixtures (CAs) and silica fume on the self-healing of concrete, with the focus being the rapid chloride penetration test (RCPT). To characterize the different concretes, compressive strength and water absorption by capillarity tests were performed. The conclusions of this study are as follows:

1. The use of CAs did not impair the compressive strength and water absorption by capillarity of the concrete, while the concrete with the addition of silica fume showed the best results for these properties.

2. The incorporation of CAs did not contribute to the increase in chloride penetration resistance for either cracked or uncracked concretes in relation to the control concrete.

3. The concrete with silica fume showed the best results, reducing the charge passed up to 63% at the age of 91 days for uncracked concrete compared to uncracked control concrete, which led to an increase of 135% in the estimated service life for this concrete.

4. Subjecting concrete to a greater number of wetting-and-drying cycles improved its resistance to chloride penetration, regardless of whether the concrete was cracked or uncracked.

5. The cracks were not completely healed until the age of 91 days because the charge passed in the cracked concretes was higher in relation to the uncracked concretes.

AUTHOR BIOS

Camila Frank Hollmann *received her BS in civil engineering from the State University of Western Paraná, Cascavel, PR, Brazil, in 2018, and her MS in civil engineering from the Federal University of Rio Grande do Sul, Porto Alegre, RS, Brazil, in 2021. Her research interests include self-healing concretes.*

Lais Zucchetti *is a Professor at the Federal University of Rio Grande do Sul. She received her BS in architecture and urbanism from the University of Passo Fundo, Passo Fundo, RS, Brazil, in 2007, and her MS and PhD in civil engineering from the Federal University of Rio Grande do Sul in 2010 and 2016. Her research interests include architecture, urbanism, and civil engineering, mainly the following topics: civil construction, performance evaluation of building systems, and the development of building components.*

Denise Carpena Coitinho Dal Molin *is a Professor at the Federal University of Rio Grande do Sul. She received her BS and MS in civil engineering from the Federal University of Rio Grande do Sul in 1982 and 1988, and her PhD in civil engineering from the University of São Paulo, São Paulo, SP, Brazil, in 1995. Her research interests include civil engineering, with an emphasis on civil construction.*

Angela Borges Masuero *is a Professor at the Federal University of Rio Grande do Sul. She received her BS and MS in civil engineering and her PhD in material and metallurgical engineering from the Federal University of Rio Grande do Sul in 1988, 1993, and 2001. Her research interests include civil engineering, focusing on materials and components of construction.*

REFERENCES

1. Van Tittelboom, K., and De Belie, N., "Self-Healing in Cementitious Materials—A Review," *Materials (Basel)*, V. 6, No. 6, June 2013, pp. 2182-2217. doi: 10.3390/ma6062182

2. de Rooij, M.; Van Tittelboom, K.; De Belie, N.; and Schlangen, E., eds., *Self-Healing Phenomena in Cement-Based Materials: State-of-the-Art Report of RILEM Technical Committee 221-SHC: Self-Healing Phenomena in Cement-Based Materials*, Springer, Dordrecht, the Netherlands, 2013.

3. Kan, L.-L.; Lv, J.-W.; Duan, B.-B.; and Wu, M., "Self-Healing of Engineered Geopolymer Composites Prepared by Fly Ash and Metakaolin," *Cement and Concrete Research*, V. 125, Nov. 2019, Article No. 105895. doi: 10.1016/j.cemconres.2019.105895

4. Ravitheja, A.; Reddy, T. C. S.; and Sashidhar, C., "Self-Healing Concrete with Crystalline Admixture—A Review," *Journal of Wuhan University of Technology-Materials Science Edition*, V. 34, No. 5, Oct. 2019, pp. 1143-1154. doi: 10.1007/s11595-019-2171-2

5. Azarsa, P.; Gupta, R.; and Biparva, A., "Assessment of Self-Healing and Durability Parameters of Concretes Incorporating Crystalline Admixtures and Portland Limestone Cement," *Cement and Concrete Composites*, V. 99, May 2019, pp. 17-31. doi: 10.1016/j.cemconcomp.2019.02.017

6. Borg, R. B.; Cuenca, E.; Gastaldo Brac, E. M.; and Ferrara, L., "Crack Sealing Capacity in Chloride-Rich Environments of Mortars Containing Different Cement Substitutes and Crystalline Admixtures," *Journal of Sustainable Cement-Based Materials*, V. 7, No. 3, 2018, pp. 141-159. doi: 10.1080/21650373.2017.1411297

7. Reddy, T. C. S.; Ravitheja, A.; and Sashidhar, C., "Micromechanical Properties of Self-Healing Concrete with Crystalline Admixture and Silica Fume," *ACI Materials Journal*, V. 117, No. 3, May 2020, pp. 63-74. doi: 10.14359/51722395

8. Roig-Flores, M.; Moscato, S.; Serna, P.; and Ferrara, L., "Self-Healing Capability of Concrete with Crystalline Admixtures in Different Environments," *Construction and Building Materials*, V. 86, July 2015, pp. 1-11. doi: 10.1016/j.conbuildmat.2015.03.091

9. Cuenca, E.; Tejedor, A.; and Ferrara, L., "A Methodology to Assess Crack-Sealing Effectiveness of Crystalline Admixtures under Repeated Cracking-Healing Cycles," *Construction and Building Materials*, V. 179, Aug. 2018, pp. 619-632. doi: 10.1016/j.conbuildmat.2018.05.261

10. Escoffres, P.; Desmettre, C.; and Charron, J.-P., "Effect of a Crystalline Admixture on the Self-Healing Capability of High-Performance Fiber Reinforced Concretes in Service Conditions," *Construction and Building Materials*, V. 173, June 2018, pp. 763-774. doi: 10.1016/j.conbuildmat.2018.04.003

11. Sisomphon, K.; Copuroglu, O.; and Koenders, E. A. B., "Self-Healing of Surface Cracks in Mortars with Expansive Additive and Crystalline Additive," *Cement and Concrete Composites*, V. 34, No. 4, Apr. 2012, pp. 566-574. doi: 10.1016/j.cemconcomp.2012.01.005

12. Wang, X.; Fang, C.; Li, D.; Han, N.; and Xing, F., "A Self-Healing Cementitious Composite with Mineral Admixtures and Built-in Carbonate," *Cement and Concrete Composites*, V. 92, Sept. 2018, pp. 216-229. doi: 10.1016/j.cemconcomp.2018.05.013

13. ACI Committee 212, "Report on Chemical Admixtures for Concrete (ACI 212.3R-16)," American Concrete Institute, Farmington Hills, MI, 2016, 76 pp.

14. De Belie, N.; Gruyaert, E.; Al-Tabbaa, A.; Antonaci, P.; Baera, C.; Bajare, D.; Darquennes, A.; Davies, R.; Ferrara, L.; Jefferson, T.; Litina, C.; Miljevic, B.; Otlewska, A.; Ranogajec, J.; Roig-Flores, M.; Paine, K.; Lukowski, P.; Serna, P.; Tulliani, J.-M.; Vucetic, S.; Wang, J.; and Jonkers, H. M., "A Review of Self-Healing Concrete for Damage Management of Structures," *Advanced Materials Interfaces*, V. 5, No. 17, Sept. 2018, Article No. 1800074. doi: 10.1002/admi.201800074

15. Moffatt, E. G.; Thomas, M. D. A.; and Fahim, A., "Performance of High-Volume Fly Ash Concrete in Marine Environment," *Cement and Concrete Research*, V. 102, Dec. 2017, pp. 127-135. doi: 10.1016/j.cemconres.2017.09.008

16. ASTM C1202-19, "Standard Test Method for Electrical Indication of Concrete's Ability to Resist Chloride Ion Penetration," ASTM International, West Conshohocken, PA, 2019, 8 pp.

17. Banu, S. S.; Karthikeyan, J.; and Jayabalan, P., "Effect of Agro-Waste on Strength and Durability Properties of Concrete," *Construction and Building Materials*, V. 258, Oct. 2020, Article No. 120322. doi: 10.1016/j.conbuildmat.2020.120322

18. Sujay, H. M.; Nair, N. A.; Sudarsana Rao, H.; and Sairam, V., "Experimental Study on Durability Characteristics of Composite Fiber Reinforced High-Performance Concrete Incorporating Nanosilica and Ultra Fine Fly Ash," *Construction and Building Materials*, V. 262, Nov. 2020, Article No. 120738. doi: 10.1016/j.conbuildmat.2020.120738

19. Zahedi, M.; Jafari, K.; and Rajabipour, F., "Properties and Durability of Concrete Containing Fluidized Bed Combustion (FBC) Fly Ash," *Construction and Building Materials*, V. 258, Oct. 2020, Article No. 119663. doi: 10.1016/j.conbuildmat.2020.119663

20. ABNT NBR 11578/1991, "Cimento Portland Composto," Brazilian Association of Technical Standards, Rio de Janeiro, RJ, Brazil, 1991, 5 pp.

21. ASTM C150/C150M-20, "Standard Specification for Portland Cement," ASTM International, West Conshohocken, PA, 2020, 9 pp.

22. ABNT NBR NM 67:1998, "Concreto — Determinação da Consistência Pelo Abatimento do Tronco de Cone," Brazilian Association of Technical Standards, Rio de Janeiro, RJ, Brazil, 1998, 8 pp.

23. ABNT NBR 9833:2008, "Concreto Fresco — Determinação da Massa Específica, do Rendimento e do Teor de Ar Pelo Método Gravimétrico," Brazilian Association of Technical Standards, Rio de Janeiro, RJ, Brazil, 2008, 11 pp.

24. ABNT NBR 5739:2018, "Concreto — Ensaio de Compressão de Corpos de Prova Cilíndricos," Brazilian Association of Technical Standards, Rio de Janeiro, RJ, Brazil, 2018, 13 pp.

25. ABNT NBR 9779:2012, "Argamassa e Concreto Endurecidos — Determinação da Absorção de Água por Capilaridade," Brazilian Association of Technical Standards, Rio de Janeiro, RJ, Brazil, 2012, 3 pp.

26. ABNT NBR 7222:2011, "Concreto e Argamassa — Determinação da Resistência à Tração por Compressão Diametral de Corpos de Prova Cilíndricos," Brazilian Association of Technical Standards, Rio de Janeiro, RJ, Brazil, 2011, 5 pp.

27. Cappellesso, V.; Silva, D.; Petry, N.; Arndt, J.; Masuero, A.; and Dal Molin, D., "Self-Healing Approach on Early Age Cracked Concretes with Smart Admixture," *Durable Concrete for Infrastructure under Severe Conditions: Smart Admixtures, Self-Responsiveness and Nano-Additions – Proceedings*, M. A. Pereira Gomes de Araújo, N. De Belie, and K. Van Tittelboom, eds., Ghent, Belgium, Sept. 2019, 4 pp.

28. Ziegler, F.; Masuero, A. B.; Pagnussat, D. T.; and Dal Molin, D. C. C., "Evaluation of Internal and Superficial Self-Healing of Cracks in Concrete with Crystalline Admixtures," *Materials (Basel)*, V. 13, No. 21, Nov. 2020, Article No. 4947. doi: 10.3390/ma13214947

29. Berke, N. S., and Hicks, M. C., "Estimating the Life Cycle of Reinforced Concrete Decks and Marine Piles Using Laboratory Diffusion and Corrosion Data," *Corrosion Forms and Control for Infrastructure*, ASTM STP 1137, V. Chaker, ed., ASTM International, West Conshohocken, PA, 1992, pp. 207-231.

30. Andrade, C., and Whiting, D., "A Comparison of Chloride Ion Diffusion Coefficients Derived from Concentration Gradients and Non-Steady State Accelerated Ionic Migration," *Materials and Structures*, V. 29, No. 8, Oct. 1996, pp. 476-484. doi: 10.1007/BF02486282

31. Helene, P.; Guignone, G.; Vieira, G.; Roncetti, L.; and Moroni, F., "Evaluation of the Chloride Penetration and Service Life of Self-Healing Concretes Activated by Crystalline Catalyst," *IBRACON Structures and Materials Journal*, V. 11, No. 3, June 2018, pp. 544-563. doi: 10.1590/s1983-41952018000300007

32. Farias de Medeiros, M. H.; Gobbi, A.; Groenwold, J. A.; and Helene, P., "Previsão da Vida Útil de Concreto Armado de Alta Resistência com Adição de Metacaulim e Sílica Ativa em Ambientes Marinhos," *Revista Escola de Minas*, V. 66, No. 1, Jan.-Mar. 2013, pp. 59-65. doi: 10.1590/S0370-44672013000100008

33. Wally, G. B.; Sell, F. K. Jr.; and Magalhães, F. C., "Ensaios Acelerados de Penetração de Cloretos Aplicados à Estimativa do Coeficiente de Difusão do Concreto e à Vida Útil de Estruturas em Ambiente Marinho," *Revista Técnico-Científica do CREA-PR*, V. 21, 2019, pp. 1-14. doi: 10.4322/2526-7248.027

34. Silvestro, L., "Validação de Modelo para Previsão de Vida Útil de Estruturas de Concreto Armado: Iniciação da Corrosão por Cloretos," master's dissertation, Federal University of Rio Grande do Sul, Porto Alegre, RS, Brazil, 2018, 158 pp. (in Portuguese)

35. Ziegler, F., "Avaliação da Autocicatrização de Fissuras em Concretos com Aditivos Cristalizantes," master's dissertation, Federal University of Rio Grande do Sul, Porto Alegre, RS, Brazil, 2020, 187 pp. (in Portuguese)

36. Helene, P., "Contribuição ao Estudo da Corrosão em Armaduras de Concreto Armado," thesis, University of São Paulo, São Paulo, SP, Brazil, 1993, 248 pp. (in Portuguese)

37. Ibrahim, M., and Issa, M., "Evaluation of Chloride and Water Penetration in Concrete with Cement Containing Limestone and IPA," *Construction and Building Materials*, V. 129, Dec. 2016, pp. 278-288. doi: 10.1016/j.conbuildmat.2016.10.085

38. Cappellesso, V. G.; dos Santos Petry, N.; Dal Molin, D. C. C.; and Masuero, A. B., "Use of Crystalline Waterproofing to Reduce Capillary Porosity in Concrete," *Journal of Building Pathology and Rehabilitation*, V. 1, No. 1, Dec. 2016, Article No. 9. doi: 10.1007/s41024-016-0012-7

39. Pazderka, J., and Hájková, E., "Crystalline Admixtures and Their Effect on Selected Properties of Concrete," *Acta Polytechnica*, V. 56, No. 4, 2016, pp. 306-311. doi: 10.14311/AP.2016.56.0306

40. Jo, B. W.; Sikandar, M. A.; Baloch, Z.; and Khan, R. M. A., "Effect of Incorporation of Self-Healing Admixture (SHA) on Physical and Mechanical Properties of Mortars," *Journal of Ceramic Processing Research*, V. 16, No. S1, Nov. 2015, pp. 138-143.

41. de Castro, A. L., and Pandolfelli, V. C., "Revisão: Conceitos de Dispersão e Empacotamento de Partículas para a Produção de Concretos Especiais Aplicados na Construção Civil," *Cerâmica*, V. 55, Mar. 2009, pp. 18-32. doi: 10.1590/S0366-69132009000100003

42. Thomas, R. J.; Ariyachandra, E.; Lezama, D.; and Peethamparan, S., "Comparison of Chloride Permeability Methods for Alkali-Activated Concrete," *Construction and Building Materials*, V. 165, Mar. 2018, pp. 104-111. doi: 10.1016/j.conbuildmat.2018.01.016

43. Şahmaran, M.; Yıldırım, G.; Noori, R.; Ozbay, E.; and Lachemi, M., "Repeatability and Pervasiveness of Self-Healing in Engineered Cementitious Composites," *ACI Materials Journal*, V. 112, No. 4, July-Aug. 2015, pp. 513-522. doi: 10.14359/51687308

44. Kan, L.-L.; Shi, H.-S.; Sakulich, A. R.; and Li, V. C., "Self-Healing Characterization of Engineered Cementitious Composite Materials," *ACI Materials Journal*, V. 107, No. 6, Nov.-Dec. 2010, pp. 617-624. doi: 10.14359/51664049

45. Lee, H. X. D.; Wong, H. S.; and Buenfeld, N. R., "Self-Sealing of Cracks in Concrete Using Superabsorbent Polymers," *Cement and Concrete Research*, V. 79, Jan. 2016, pp. 194-208. doi: 10.1016/j.cemconres.2015.09.008

46. Otieno, M.; Beushausen, H.; and Alexander, M., "Chloride-Induced Corrosion of Steel in Cracked Concrete – Part I: Experimental Studies under Accelerated and Natural Marine Environments," *Cement and Concrete Research*, V. 79, Jan. 2016, pp. 373-385. doi: 10.1016/j.cemconres.2015.08.009

47. Cuenca, E.; Cislaghi, G.; Puricelli, M.; and Ferrara, L., "Influence of Self-Healing Stimulated via Crystalline Admixtures on Chloride Penetration," *Durability and Sustainability of Concrete Structures*, SP-326, V. Falikman, R. Realfonzo, L. Coppola, P. Hàjek, and P. Riva, eds., American Concrete Institute, Farmington Hills, MI, 2018, 10 pp. doi: 10.14359/51710987

48. de Araújo Vasconcelos, M. C., "Avaliação da Atividade Pozolânica da Cinza do Bagaço de Cana-de-Açúcar Utilizando Métodos Físicos," master's dissertation, Federal University of Pernambuco, Recife, PE, Brazil, 2013, 134 pp. (in Portuguese)

49. Ramezanianpour, A. A.; Pilvar, A.; Mahdikhani, M.; and Moodi, F., "Practical Evaluation of Relationship between Concrete Resistivity, Water Penetration, Rapid Chloride Penetration and Compressive Strength," *Construction and Building Materials*, V. 25, No. 5, May 2011, pp. 2472-2479. doi: 10.1016/j.conbuildmat.2010.11.069

50. ABNT NBR 6118:2014, "Projeto de Estruturas de Concreto – Procedimento," Brazilian Association of Technical Standards, Rio de Janeiro, RJ, Brazil, 2014, 238 pp.

51. Cappellesso, V. G., "Avaliação da Autocicatrização de Fissuras em Concretos com Diferentes Cimentos," master's dissertation, Federal University of Rio Grande do Sul, Porto Alegre, RS, Brazil, 2018, 295 pp. (in Portuguese)

ACI MATERIALS JOURNAL TECHNICAL PAPER

Title No. 120-M56

Pertinent Surface Moisture of Concrete for Water Ingress Assessment

by Uwazuruonye Raphael Nnodim

This study clarifies the effects of moisture (expressed as percentage saturation degree of permeable pore voids, PSD) on water ingress properties of concrete and establishes a region where PSD does not affect the quantitative water absorption. Experimental measurements and finite element model (FEM) simulation results for ordinary portland cement (OPC) concretes preconditioned to equilibrium moisture formed plateaus between 21 and 58% PSD. Non-continuous finer capillary pores (ϕ10 nm [3.937 × 10^{-4} mil, thou] to ϕ100 nm [3.937 × 10^{-3} mil, thou]) constitute the empty pores within the plateau region before tests. Water sorptivity of OPC and slag cement concrete blocks at several degrees of surface moisture with internal moisture gradients validate the existence of the plateau within the PSD range. Measuring short-term water absorption within this plateau region eliminates the effects of initial surface moisture content on the measured properties and evaluates the continuity and connectivity of pores, which is the major indicator of the durability of concrete.

Keywords: durability; permeability; pore size distribution; transport properties.

INTRODUCTION

To what degree the cover zone of concrete resists moisture ingress is of paramount importance regarding durability of in-place concrete structures. Notwithstanding that there is no universally accepted quantifier for the general durability performance of concrete, the resistance to water ingress is arguably one of the greatest quantifiers in durability design and assessment of concrete structures against the ingress of deleterious materials as well as the initiation of concrete deterioration.[1] Regardless of the deterioration mechanism, water is needed to initiate almost all deterioration processes of concrete structures. Even the deteriorations that are inherent in the materials require water to begin.[2,3]

Many durability test standards such as ASTM C1585,[4] BS 1881 Part 207,[5] and JSCE-G 582[6] appropriately consider and evaluate the resistance to water ingress. Nonetheless, the quality of concrete in actual structures always differs from the design assumptions due to several effects resulting from concreting works; therefore, durability assessment of in-service concrete structures is important. The aforementioned test standards require drying concrete to a sufficiently steady weight and cannot be applied in-place. Resistance to water absorption has not been appropriately considered in the durability assessment of in-place concrete structures due to the ambiguous effects of moisture conditions. Moreover, covercrete, which is the channel for water infiltration, is also the most affected part by concreting works and is always different from the inner concrete.[2,3,7,8]

Surface water absorption largely depends on the action of the capillary pores resulting from the pore diameters, pore continuity/connectivity, tortuosity, and the degree of saturation. Furthermore, surface tension and viscosity, which are influenced by factors such as temperature, contribute a great deal to water permeability.[9-11] Short-term water penetration depth of concrete has an approximately linear relationship with the square root of immersion time.[12] However, this is for concrete that is dried to a steady weight, seemingly unable to experience further moisture loss. In the literature, it is difficult to find an appropriate initial saturation degree of the pore system for effective evaluation of resistance to water ingress of in-place concrete structures. Also, the coupled influence of capillary pore size distribution and saturation degree on moisture transfer has not been clarified.

In an investigation of the relationship among the permeation rate of water into concrete, mixture design, curing, and degree of drying, Sakai et al.[13] propounded a simple equation to evaluate the water absorption in concrete. The equation assumed that water-binder ratio (*w*/*b*), curing, and degree of drying are dominant in water absorption. "As long as the amount of aggregate and mineral admixture are common, the sorptivity of concrete can be evaluated with the *w*/*b*, curing, and the degree of drying,"[13] indicating an assumption of a linear relation. Parrott[14] showed that sorptivity was linearly correlated with the amount of water loss by drying. Maruyama[15] indicated the influence of dried C-S-H on water absorption. The C-S-H is said to shrink on drying and swells on water absorption and its amount may considerably affect sorptivity. This might not be far from the finding that during water uptake in relatively dry concrete, water redistributes to smaller pores and at the same time results in more internal swelling, which reduces the connectivity of the capillary pore system, thereby lowering the water uptake.[12] Using a nuclear magnetic resonance (NMR) test, Rucker-Gramm and Beddoe[12] revealed that water in gel pores decisively affected the transport of water in larger capillary pores.

Yokoyama et al.[16] concluded that "water absorbency of concrete slabs is affected by the quantity of pores with diameters of approximately 10^{-7} m (100 nm [3.937 × 10^{-3} mil, thou]) and larger, while water content depends on the quantity of pores with diameters of approximately 10^{-8} m (10 nm [3.937 × 10^{-4} mil, thou]) and smaller." In a study of the relationship between the degree of drying and oxygen diffusion coefficient in hardened cement paste, results showed

ACI Materials Journal, V. 120, No. 5, September 2023.
MS No. M-2022-340.R1, doi: 10.14359/10.14359/51739018, received May 30, 2023, and reviewed under Institute publication policies.

that between 15 and 45% relative humidity (RH), RH had no virtual effect on the oxygen diffusion coefficient (D_e–m^2/s).[17]

Surface water absorption of in-place concrete is highly affected by the moisture condition before the measurement and specimen preconditioning influences sorptivity.[18,19] Also, moisture content of in-place concrete is not uniform and always exhibits moisture gradient. The effect of moisture content on measured properties of concrete is the greatest challenge and limitation for all the in-place measurement devices[2,3] such as Autoclam water/air permeability, double-chamber air permeability, electrical resistivity, surface water absorption test (SWAT), and so on. In this study, experimental investigations and numerical simulations are conducted and the surface moisture content is expressed as a percentage saturation degree of permeable pore voids (*PSD*), which is directly related to the volume of pore voids of the concrete.

RESEARCH SIGNIFICANCE

Many design methods evaluate the resistance of concrete to water ingress, but none have been effective for in-place concrete durability assessment due to the complex effects of moisture conditions. The effects of initial moisture contents on surface water absorption tests have been deeply researched without any proposal of the appropriate initial moisture contents for effective nondestructive assessment. This is the first detailed study clarifying the effects of moisture content on the resistance to surface water absorption for in-place concrete with a proposal of an appropriate initial surface moisture content that excludes the effect of moisture contents on the measured properties.

EXPERIMENTAL INVESTIGATION

Materials

Table 1 summarizes the different types of concretes used in this study, which were selected from among commonly used concretes in Japan. Prismatic concrete specimens with 300 x 300 mm (11.811 x 11.811 in.) area and 150 mm (5.91 in.) thickness were prepared with ordinary portland cement (OPC) and slag cement (JIS Type B slag cement). The concrete specimens were prepared in two sets and were kept in a controlled room condition of 20°C (68°F) and 60% RH after curing until the absorption test preparation time. The first set is composed of three concrete types and is marked "‡" in Table 1, while the second set is composed of eight concrete types. The names of the specimens were coded to portray cement type, water-cement ratio (*w*/*c*), and type of curing. The curing conditions applied were 7D: 7 days sealed in mold, 10D: 10 days sealed in mold, and 10W: 1 day sealed in mold + 9 days in water after removing the mold. The procedure for fabricating the concrete test specimens in the laboratory followed the ASTM C192/C192M-02 standard practice. The concrete specimens were rodded with tamping rods while the molds were made of nonabsorbent smooth wooden form. All tests were conducted on the formwork finished surface of the concrete specimens.

Experimental methods

Preconditioning of moisture condition—To investigate the effects of saturation degree of pore voids on the resistance to water ingress, concrete cores of ϕ100 mm (ϕ3.94 in.) were taken along the 150 mm (5.91 in.) thickness at the age of 510 days from selected prismatic specimens (marked with "‡" in Table 1). The concrete needed a sufficient hydration degree to eliminate the possibility of microstructural change during preconditioning. The extracted cores were sliced, and two specimens were provided with 45 mm height and with the formwork-finished face (Fig. 1). To achieve moisture equilibrium inside the specimens at several saturation degrees of pore voids, the sliced specimens were preconditioned in a controlled humidity chamber (40°C [104°F] and

Table 1—Summary of concrete mixture proportions and curing conditions

Name of specimen	*w*/*c*, %	*s*/*a*, %	Mixture composition, kg/m³				Admixtures		Curing
			Cement		Aggregate				
			Amount	Type	Fine	Coarse	Type*	Dosage†	
N40-7D‡	40	45	400	N	777	950	Ad-AE	1.1875	7D
N50-7D‡	50	47	320	N	841	948	Ad-AE	1.1985	7D
N60-7D‡	60	48.5	267	N	890	945	Ad-AE	1.3	7D
N40-10D	40	45	400	N	776	948	Ad-AE	1.1025	10D
N50-10D	50	47	320	N	840	947	Ad-AE	1.0025	10D
N60-10D	60	48.5	267	N	890	945	Ad-AE	1.0025	10D
BB50-10D	50	47	320	BB	831	937	Ad-AE	1.025	10D
N40-10W	40	45	400	N	776	948	Ad-AE	1.1025	10W
N50-10W	50	47	320	N	840	947	Ad-AE	1.0025	10W
N60-10W	60	48.5	267	N	890	945	Ad-AE	1.0025	10W
BB50-10W	50	47	320	BB	831	937	Ad-AE	1.025	10W

*Admixture types: Ad is water-reducing admixture; AE is air-entraining agent.

†Admixture dosage: percentage of admixtures to binder, weight-to-weight ratio.

‡Specimens from which cores were taken and preconditioned to equilibrium moisture distribution.

Note: N is ordinary portland cement, BB is slag cement (JIS Type B slag cement).

50% RH). The sealing materials and preconditioning steps have previously been established by the author[20] and can be summarized as follows:

- Saturating specimen by total immersion into water;
- Sealing the lateral sides with vinyl electric insulation tape;
- Drying the specimen to obtain the desired weight;
- Sealing the two faces of the specimen with a layer of polythene sheet;
- Returning the specimen to the controlled chamber to attain moisture equilibrium; and
- Storing the specimen in a different closed chamber to allow natural heat loss until the specimen is cooled down to approximately 20 to 25°C (68 to 77°F).

To investigate the sorptivity of concrete with moisture gradient such as in in-place concrete structures, eight kinds of prismatic specimens (without the "‡" mark in Table 1) were provided without the preconditioning mentioned previously. During the placement of concrete, moisture sensors were embedded (in pairs, 10 mm apart) at 5, 10, 20, 30, and 50 mm (0.197, 0.394, 0.787, 1.181, and 1.969 in.) depths from the surface (Fig. 2) to monitor the moisture gradient in the specimens by attaching a moisture meter (electric resistance type) to the sensors. A moisture sensor is a set of stainless direct-current-type (φ 4 mm [0.157 in.]) threaded rods that are embedded in pairs into the concrete to serve as the connecting electrodes to the moisture meter. It has an effective area of 4 mm diameter. To eliminate cracks due to the embedding of the moisture sensor in the very shallow concrete cover of 5 mm (0.197 in.), the moisture sensor for the 5 mm (0.197 in.) depth was embedded from the back (Fig. 2). The output of the moisture meter is expressed in moisture content or in "count values," and the investigated relationship between the two outputs is shown in Fig. 3. It was previously confirmed that count values have an inverse relationship with electric resistance.[21]

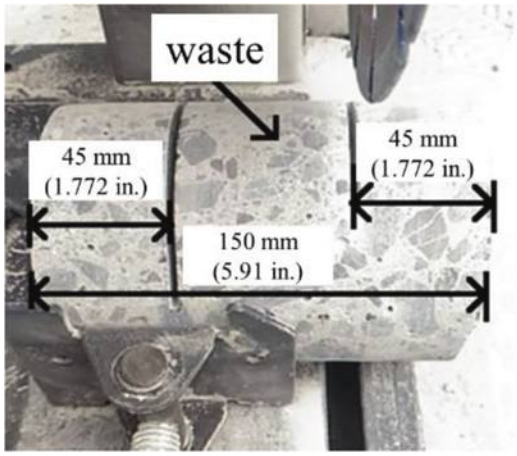

Fig. 1—Extraction of test samples used in preconditioned state.

To simulate many kinds of complicated internal moisture distribution and surface moisture contents for concrete in outdoor environments, at 90 days after the placement, the second set of concrete blocks were exposed to 60, 80, and 99% RH for a varying number of days. Three same specimens were provided for eight types of concretes shown in Table 1, and three specimens were exposed to different RH to obtain various kinds of moisture distribution. Measurements of surface moisture content and surface water absorption were conducted daily until 14 days from the exposure date using a surface moisture meter and SWAT device, respectively.

Measurement of percentage saturation degree of pore voids, PSD—*PSD* is measured using an electric resistance moisture meter by pressing the device onto the concrete surface; the results are expressed in count values. The surface moisture tester has an built-in hard-rubber-type sensor that measures when in contact with the surface of concrete. The advantages of this surface moisture meter over others is the ability to access both the pore water and the pore connectivity during measurements and the capacity to measure moisture content up to the depth of 5 mm from the surface.[22] Figure 4 shows the relationship between *PSD* and count values measured with the surface moisture meter in a documented preliminary investigation.[20] The scatter plot showed a strong positive correlation between *PSD* and

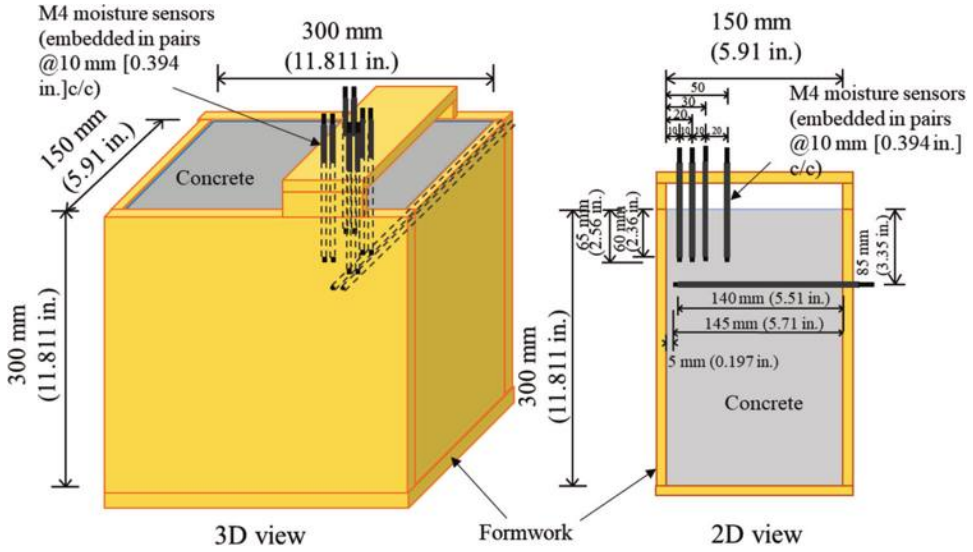

Fig. 2—Details of M4 moisture sensor locations in concrete blocks.

moisture meter count values. The scatter plot was obtained from many kinds of concretes preconditioned to equilibrium internal moisture distribution.

Surface water absorption test procedure—For the samples preconditioned to equilibrium moisture distribution, two replicate samples (Fig. 5(a)) were tested by the SWAT to investigate the resistance to water ingress. Similarly, for the second set of concrete blocks without equilibrium moisture preconditioning, the average result from four measurement points (Fig. 5(b)) is used to obtain both the water sorptivity and count values.

The resistance against water absorption is expressed as the coefficient of surface water absorption, *CSWA* (mL/m^2/s$^{1/2}$). *CSWA* can be obtained from the slope of the approximate linear regression between water absorption amount and the square root of time. The author recently introduced the *CSWA* index and confirmed its correlations with the JSCE-G 582 sorptivity test results.[8]

SWAT (Appendix A) is a nondestructive device that evaluates the quality of covercrete in 10 minutes under natural water suction.[23,24] SWAT is composed of a fully automatic machine unit, an absorption cup (80 mm inner diameter and 100 mm outer diameter) with a calibrated cylindrical tube, water inlet and tap, a sensor, a framed vacuum pump for fixing or fixing clamp for small specimens, and a water container. The SWAT system does not require a constant water head throughout the testing time and the time for injecting water into the water absorption cup before test is 10 seconds. SWAT has been proven to be effective in detecting the influences of curing conditions, mixture proportions, and the adverse effects of microcracks in covercrete quality within 10 to 20 mm (0.394 to 0.787 in.), which is the most affected by concreting works.[8,22-26] The rate of surface water absorption at 10 minutes (where the time for injecting water into the cup for measurement preparation is 10 seconds) measured by SWAT is termed p_{600} (mL/m^2/s) and the criterion for the conventional quality grading is shown in Table A1 of Appendix A. *CSWA* has a good correlation with p_{600}.[8] Besides, good correlations have been demonstrated between p_{600} and long-term water penetration depth,[25] as well as the carbonation rate coefficient of concrete.[27]

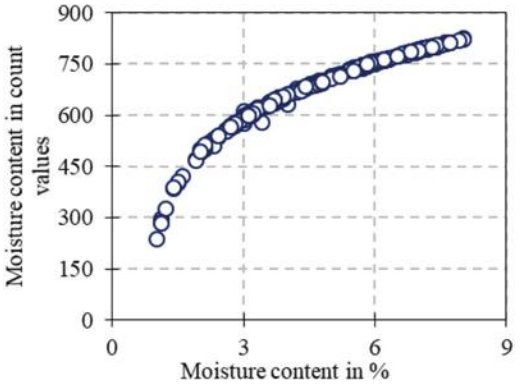

Fig. 3—Relationship between count values and percentage values of HI-800 moisture meter.

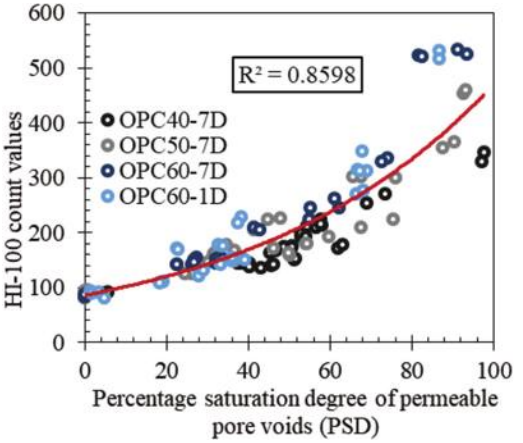

Fig. 4—Relationship between PSD *and HI-100 moisture meter count values.*

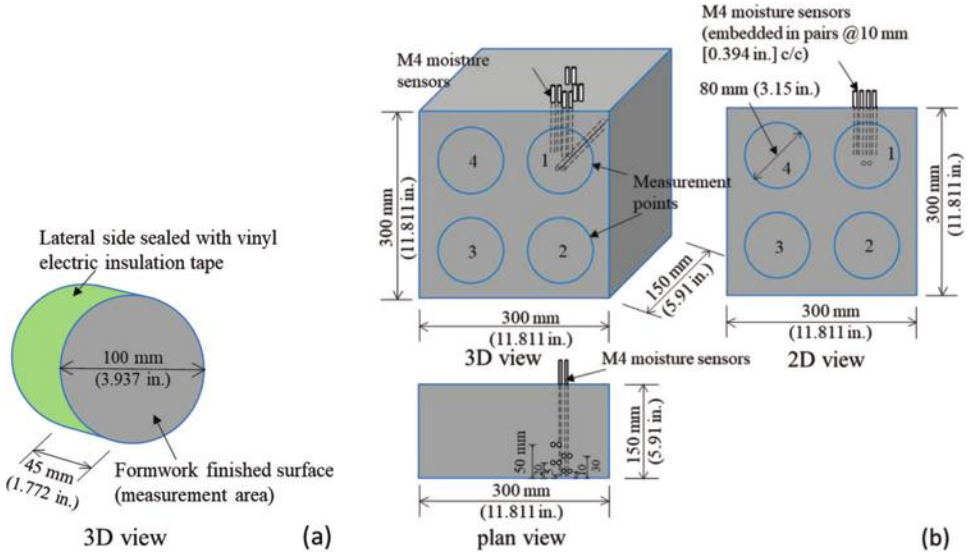

Fig. 5—Measurement of water sorptivity of concrete by SWAT device: (a) sample pre-conditioned to equilibrium moisture distribution; and (b) concrete block with internal moisture gradient.

NUMERICAL SIMULATION

Simulation tool—To investigate the effective pore diameter available for water transport at different percentage saturation degrees of pore voids, numerical simulation was used. A commercial, multi-scale and thermo-hygro dynamics analysis software, Durability of COncrete Model (DuCOM),[28,29] is used to model water absorption and is thereafter applied in the porosity estimation and pore size distribution of the samples preconditioned to equilibrium moisture. DuCOM is capable of predicting the hydration of cement and its densification by continuous hydration of the unhydrated cement particles.[28,29] The hydration of cement particles and moisture transport are inherently coupled during microstructure development and pore structure formation.[29] DuCOM applies the computational prediction of the pore structure of the matrix as a basis for moisture transport computation. Each capillary and gel porosity distribution, $\phi_{cp}(r)$ and $\phi_{gl}(r)$, is represented as

$$V = 1 - \exp(-Br),\ dV = Br\exp(-Br)\,d\ln r \quad (1)$$

where V is the fractional pore volume of the distribution up to pore radius r; and B is the peak distribution in a logarithmic scale of the sole porosity distribution parameter.

The overall microstructure is represented as a bimodal porosity distribution through the combination of the inner and outer product contribution to the total porosity function $\phi(r)$ as

$$\phi(r) = \phi l_r + \phi g_l(1 - \exp(-B_{gl}r)) + \phi_{cp}(1 - \exp(-B_{cp}r)) \quad (2)$$

where B_{gl} and B_{cp} correspond, respectively, to the gel and capillary porosity components.

Boundary conditions for water movement in DuCOM—To establish effective modeling, appropriate meshing and boundary conditions in numerical simulation are necessary. In this research, at first, one-dimensional (1-D) dominant water movement was simulated and validated by experimental results for calibrating appropriate boundary conditions. One-dimensional water sorptivity results from cylindrical samples (ϕ100 x 200 mm) were used to determine appropriate boundary conditions for water movement during absorption by simulation. The measurements were conducted based on JSCE-G 582.[6] Twenty-five mm (0.984 in.) surface zone from the bottom of the specimen was removed and the final test sample was ϕ100 mm × 175 mm (ϕ3.937 x 8.890 in.). Second, three-dimensional (3-D) water movement by SWAT—that is, the water penetration depth at 10 minutes of absorption, which cannot be measured experimentally—was simulated using the established and validated meshing and boundary conditions from the 1-D dominant water movement results. In the DuCOM system, a magnification factor is applied (especially in short-time water movement) for the vapor transfer coefficient. Based on the parametric investigations for the surface water absorption, four times the magnification factor of the vapor transfer coefficient for RH = 99.99% is selected to account for the transference of condensed water from the surface to the concrete.

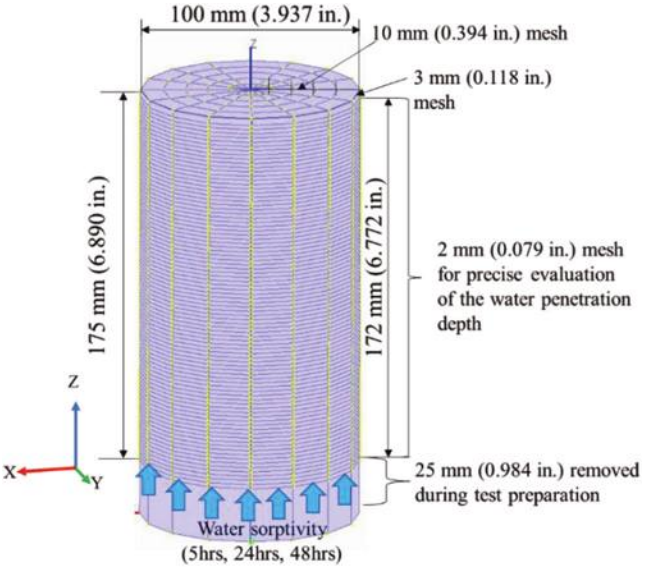

Fig. 6—Model of JSCE-G 582 test specimen.

Three types of concrete prepared with OPC and slag cement (JIS Type B slag cement) were used. The amount of water (kg/m^3 [lb/ft^3]) for mixing was kept constant at 160 kg/m^3 (9.988 lb/ft^3) for all the concrete types. Two different *w*/*c* contents (40 and 50%) for the OPC concretes were obtained by varying the amount of cement. The curing type was sealing in the mold for 28 days. The specimens were named N40-28D for OPC + 40% *w*/*c*, N50-28D for OPC + 50% *w*/*c*, and BB50-28D for slag cement + 50% *w*/*c*. The concrete mixture proportions are:

- N40-28D – sand/aggregate ratio = 45%, cement = 400 kg/m^3 (24.971 lb/ft^3), fine aggregate = 796 kg/m^3 (49.693 lb/ft^3), coarse aggregate = 973 kg/m^3 (60.742 lb/ft^3), Ad is water-reducing admixture = 1.0, AE is air-entraining agent = 0.0015 entrained air content 5.6%.
- N50-28D – sand/aggregate ratio = 47%, cement = 320 kg/m^3 (19.977 lb/ft^3), fine aggregate = 865 kg/m^3 (54.0 lb/ft^3), coarse aggregate = 975 kg/m^3 (60.876 lb/ft^3), Ad is water-reducing admixture = 1.0, AE is air-entraining agent = 0.0015 entrained air content 4.9%.
- BB50-28D – sand/aggregate ratio = 46.7%, cement = 320 kg/m^3 (19.977 lb/ft^3), fine aggregate = 854 kg/m^3 (53.313 lb/ft^3), coarse aggregate = 975 kg/m^3 (60.867 lb/ft^3), Ad is water-reducing admixture = 0.8, AE is air-entraining agent = 0.0015 entrained air content 3.5%.

Sample preparations according to JSCE-G 582 started 60 days after casting. Details of the experimental steps, conditions, test preparations, and results are documented by the author.[8] Figure 6 shows the meshing details of the model.

COMPARISON OF SIMULATIONS AND EXPERIMENTAL RESULTS

Water penetration depths at 5, 24, and 48 hours for BB50-28D are shown in Fig. 7(a) through (c) while the effectiveness of the boundary condition on the 5 hours of water penetration depth is shown in Fig. 7(d). The penetration depth is determined as the first point where the difference in saturation degree of pore voids before and after water

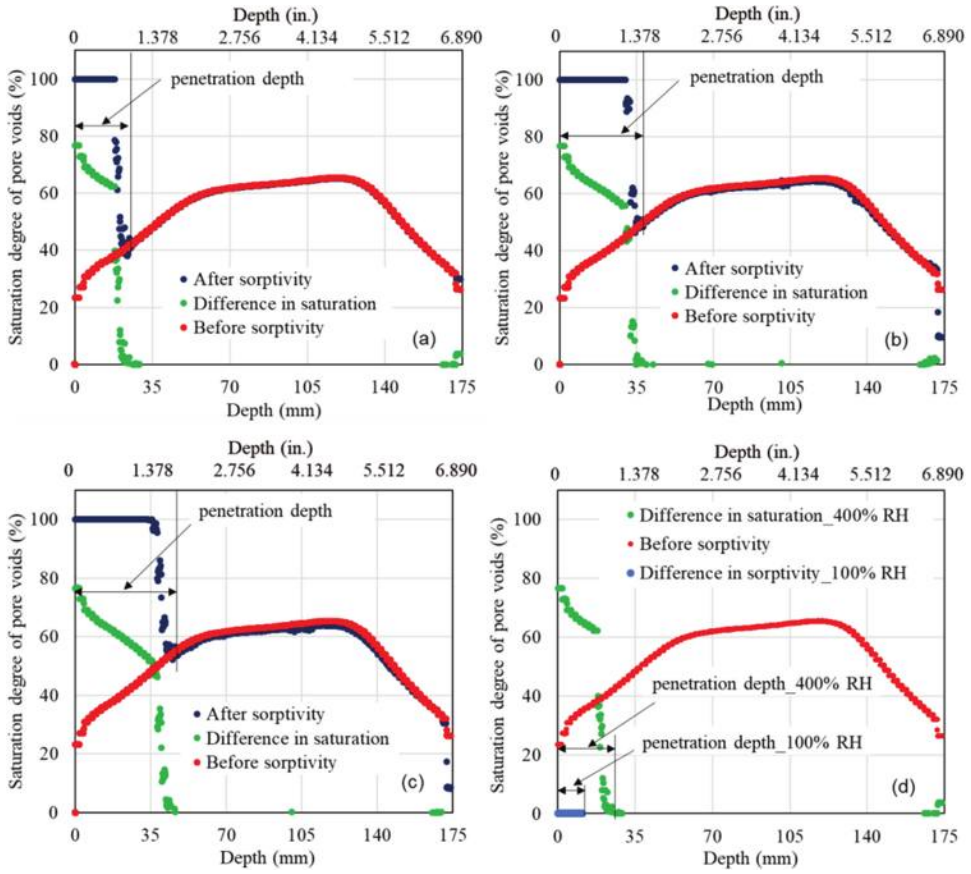

Fig. 7—Numerical modeling of water sorptivity—depth of water penetration for BB50-28D specimen: (a) 5 hours; (b) 24 hours; (c) 48 hours; and (d) effects of RH.

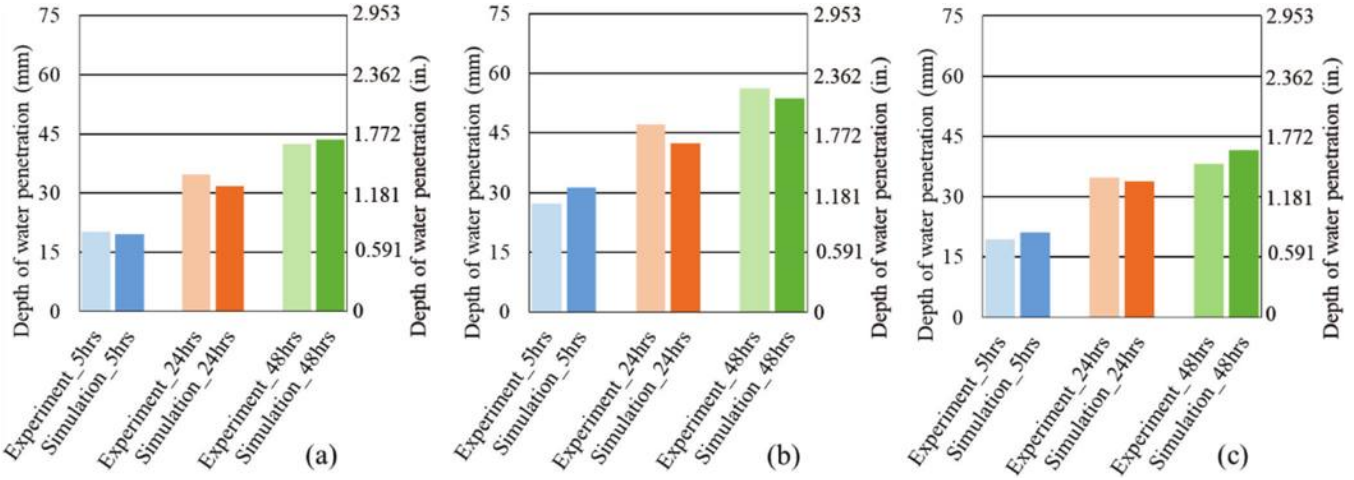

Fig. 8—Average depth of water penetration of concrete from experiment and numerical simulation: (a) N40-28D; (b) N50-28D; and (c) BB50-28D.

absorption equals zero. As for experiments, moisture penetration depth is determined by spraying a color-differentiating water detector that conforms to NDIS 3423 specifications. The measured and simulated results for the three concrete types (N40-28D, N50-28D, and BB50-28D) are compared in Fig. 8(a) through (c). A high coefficient of determination, $R^2 = 0.9438$ (Fig. 9), was obtained from the approximation of the relationship between measured and simulated results for water penetration depth by a linear function. This high correlation validates the simulation model for evaluating water penetration depth in a 1-D dominant water movement.

The simulation model was applied to investigate the 3-D water ingress of the concrete samples (preconditioned to uniform moisture distributions and measured at several *PSD*s). The meshing was shown in Fig. 10 where 2 mm thick meshes were used up to 10 mm from the surface in the depth direction (z-direction) for a precise simulation of absorption amount. Also, 2 mm thick mesh sizes in the y-direction were made beyond the inner ϕ80 mm circle (which represents the

SWAT water cup) to evaluate the effect of 3-D water ingress. For the experiments, *CSWA* is the slope from an approximate linear regression obtained by plotting the cumulative water absorption per unit area against the square root of time (in seconds), whereas *CSWA* in the numerical simulation is deduced from the cumulative water absorption calculated by considering all the output parameters (physically adsorbed water, free water, and water fixed in hydrates) for moisture transfer in the DuCOM tool.

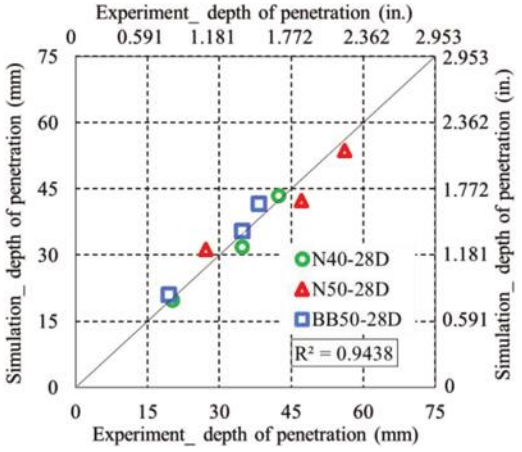

Fig. 9—Relationship between measured and simulated results for depth of water penetration.

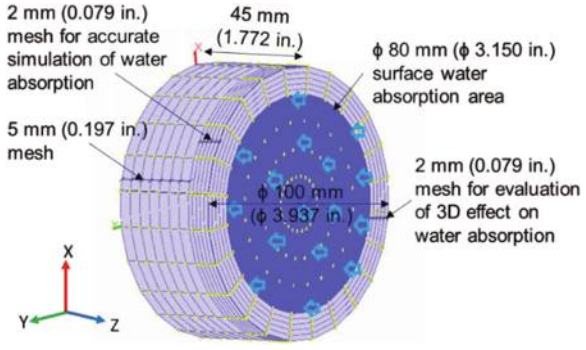

Fig. 10—Model of sample preconditioned to equilibrium moisture distribution.

RESULTS AND DISCUSSION

Influence of pore void saturation degree on water absorption for concrete with uniform moisture distribution

The effects of *PSD* on water sorptivity for the simulated and measured values are shown in Fig. 11(a) and (b). A good agreement is observed when values obtained from the simulation model are compared to the experimental results. It is seen that three regions are formed (indicated as A, B, and C) as illustrated in Fig. 12. Similar trends were seen in regions A and C. It was revealed that the water sorptivity obtained from 10 minutes of measurement exhibited a near-linear inverse relationship with *PSD* for all the samples in the two regions. From the experimental results, region A was between 0 and 20% *PSD* for all the concrete types, whereas region C was 46% *PSD* and above for N60-7D, 51% *PSD* and above for N50-7D, and 59% *PSD* and above for N40-7D. According to the increase in *PSD*, water sorptivity decreased in regions A and C. On the other hand, from simulation results, while all the concrete types revealed 0 to 20% *PSD* in region A, region C for N40-7D was 51% *PSD* and above, and region C for N50-7D and N60-7D was 54% *PSD* and above.

A different trend from regions A and C was observed in region B. From the experimental results, between 21% *PSD* and 45% *PSD*, *PSD* was seen to have almost no influence on water sorptivity for N60-7D. In the same way, the plateau zone was observed between 21% *PSD* and 50% *PSD* for N50-7D, and 21% PSD and 58% *PSD* for N40-7D. The simulation results showed a plateau zone at 21% *PSD* to 50% *PSD* for N40-7D, and 21% *PSD* to 53% *PSD* for N50-7D and N60-7D. Experimental results revealed that the range of region B (plateau zone) increases with a decrease in the *w*/*c*. This means that the volume of pore diameters related to the plateau region increases with a decrease in the *w*/*c* content, indicating an increase as the quality of concrete improves. The plateau region is caused by the discontinuity in the pore connections that resulted from instant rapid absorption and moisture redistribution during water absorption at region A. The discontinuous pores require a longer time for the saturation of pore voids. This is evident in Fig. 13, where the simulation results of 6 hours of surface water absorption revealed the disappearance of the plateau region. More discussion on different water absorption mechanisms that resulted in the three regions is in the subsection that follows.

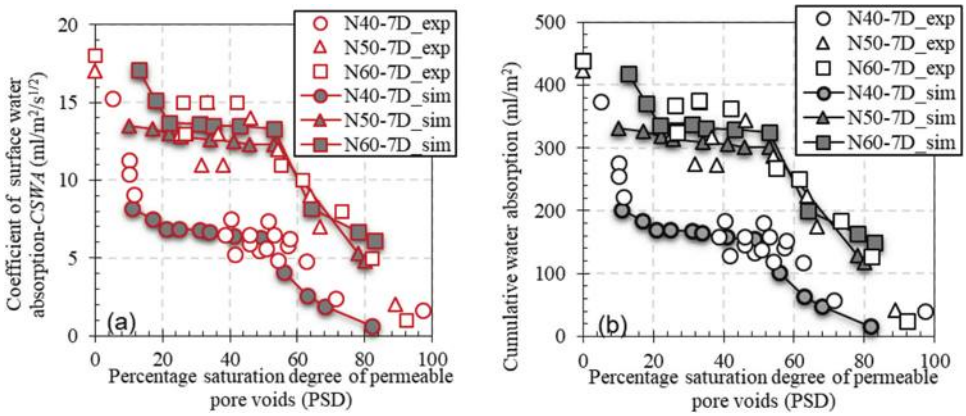

Fig. 11—Water sorptivity of concrete against PSD*: (a) CSWA versus* PSD*; and (b)* p_{600} *versus* PSD.

The estimated pore size distributions from numerical simulations are shown in Fig. 14(a). Validations of the pore size distributions obtained by the simulation tool were not conducted as many experimental validations for many kinds of concrete have previously been documented by researchers.[28-33] The dominant pore diameters empty for absorption and saturation during the 10 minutes of water absorption in region B (plateau region) is the shaded areas shown in Fig. 14(b), (c) and (d) for N40-7D, N50-7D, and N60-7D, respectively. It revealed that for all concrete types in this study, the maximum pore diameter corresponding to the upper limit of the plateau region is equivalent to 10^{-7} m (100 nm [3.937×10^{-3} mil, thou]). The range of dominant pore diameters differs in the three regions; thus, different water absorption mechanisms contributed to the pattern (A, B, and C regions) in the relationship between water sorptivity and *PSD*. In estimating the empty capillary pores available for water uptake, the saturation is taken in the order of the pore diameter starting from the smallest while neglecting ink-bottle effects because the water absorption measurements were conducted at the condition of equilibrium moisture distribution. It has been confirmed that at an equilibrium moisture distribution state only the pores of specific diameter and smaller diameter sizes are saturated; thus, the effects of the ink-bottle neck on water absorption are negligible.[12]

Absorption mechanism for water movement in regions A and C—In region A (predominately 0 to 20% *PSD*), which could be seen as an extremely dry region, the pore system is empty; thus, rapid surface water absorption occurs when concrete is placed in contact with water. Because the bigger gel pores are not filled, as water enters the large capillary pores, instant-rapid-partial redistribution into the smaller empty pores occurs allowing for an increase in internal swelling that reduces the pore connectivity, lowering the amount of absorption. This is similar to Rucker-Gramm and Beddoe's revelation on the influence of gel pore water in the transport of water in much larger capillaries.[12] For this reason, surface water absorption in this region has a

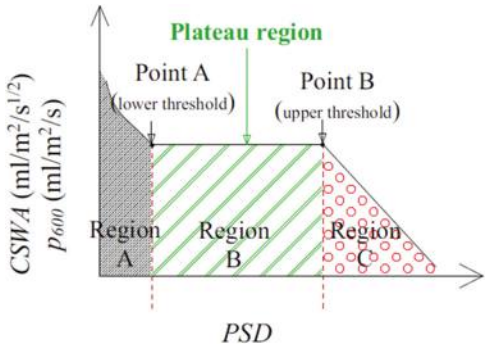

Fig. 12—Pattern diagram for relationship between sorptivity and PSD.

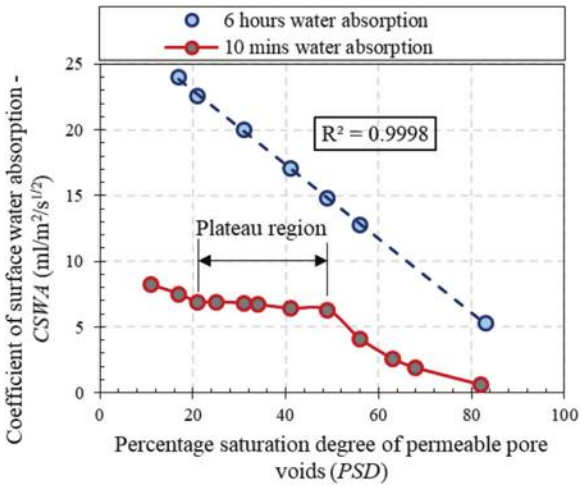

Fig. 13—Effect of long-term absorption on plateau region for N40-7D concrete by numerical simulation.

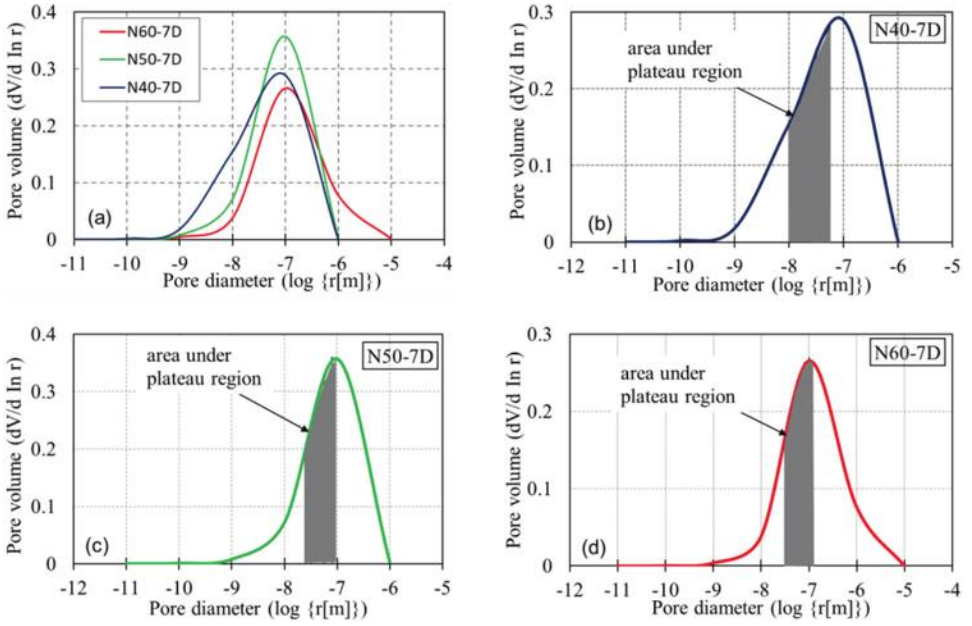

Fig. 14—Porosity estimation of pore size distribution for OPC concretes showing effective pore diameters for plateau regions from simulation: (a) pore size distribution; (b) N40-7D; (c) N50-7D; and (d) N60-7D.

near-linear inverse relationship with the saturation degree of permeable pore voids until the critical pore diameters that aid in the instant moisture redistribution are filled up. The critical pore diameter is seemingly within 20% *PSD* and below.[34]

Region C, which could be seen as a wet region, similarly shows a water absorption relationship with *PSD* as a near-linear inverse relation. In this region, only big capillary pores that have sole water absorbency[16] are empty. As absorption proceeds, smaller pores are filled, reducing the volume of the available empty pores for absorption.

Absorption mechanism for water movement in region B (the plateau region)—Nearly zero influence of *PSD* on water absorption is observed in this region; thus, a plateau in the pattern diagram exists. Here, the critical pore diameters that contribute to the instant-rapid-partial redistribution of moisture have already been filled. The pore diameters in this region do not directly contribute to water absorption. Capillary water absorption in this region requires a longer time (as shown in Fig. 13) for saturation of the pores due to the presence of noncontinuous finer capillary pores, less connectivity, and discontinuity in the pore system, together with the tortuous property of concrete. Because SWAT is measured only at 10 minutes, the saturation of the pores could not be attained. As seen in Fig. 14(b) through (d), the empty capillary pore diameters in this region are between 10^{-8} m (10 nm [3.937×10^{-4} mil, thou]) and 10^{-7} m (100 nm [3.937×10^{-3} mil, thou]). The pore diameters could have strong relations with the threshold pore size by the mercury intrusion porosimetry (MIP) test. When short-time water absorption measurements such as SWAT are conducted in this *PSD* region (plateau zone), it assesses the continuity and connectivity of the pore systems, which is the major indicator of the durability of concrete.

The threshold for the saturation degree of permeable pore voids for effective evaluation of surface water absorption is the plateau region because nearly zero effects of moisture were observed and every concrete quality was distinct. Where the quality of the mixture proportion of concrete is unknown, the upper threshold *PSD*, which is the most important, could be taken as "210 counts" of surface moisture meter equivalent to 58% *PSD*. The general water absorption mechanism, including the formation of the plateau, is represented in the schematic diagram shown in Fig. 15.

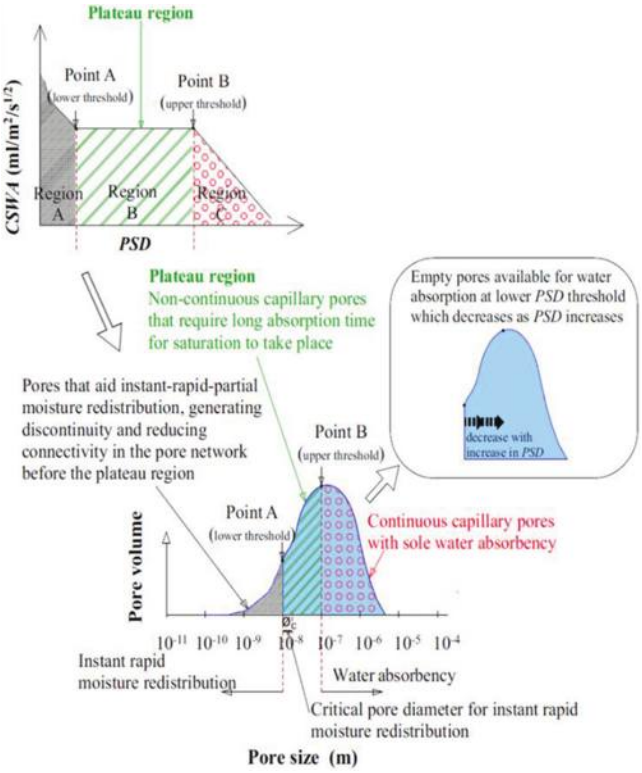

Fig. 15—Schematic diagram of water absorption mechanism for formation of plateau zone.

Influence of pore void saturation degree on water absorption for concrete with moisture gradient

In actual concrete structures, moisture condition inside concrete is not uniform. In many cases, there is a moisture gradient from the surface of concrete into the depth direction. Here, the effects of *PSD* with moisture gradient on water absorption are investigated.

The effects of surface *PSD* on water sorptivity were investigated using concrete blocks with internal moisture gradients. Moisture distribution in the concrete blocks exposed to 60, 80, and 99% RH was measured with embedded sensors at several depths. The count values by the moisture meter (as explained in Fig. 3) are shown in Fig. 16. The N40, N50, N60, and BB50 concretes are shown in Fig. 16(a), (b), (c), and (d), respectively, which are typical to different internal moisture gradients in real concrete structures.

Simultaneous measurements for surface *PSD* and water sorptivity are conducted with the recordings of the internal moisture gradient. The plotting of *CSWA* against moisture meter count values is shown in Fig. 17. Figure 17(a) shows the results for the 10D series of the concrete blocks, whereas Fig. 17(b) is for the 10W series. In Fig. 17, hollow circles represent surface *PSD* above the threshold whereas solid circles represent surface *PSD* within the threshold (plateau region) as per the upper threshold defined by 210 count value of the moisture meter.

In general, the results strongly revealed that below the 210 count value, surface *PSD* has almost no effect on water sorptivity for in-place concrete. Clear, acceptable grading and covercrete quality variations are seen among the eight different concrete types. It revealed visible influences of cement type, *w*/*b* content, and curing conditions on the plateau range, as well as the water sorptivity results. For all the 10D series, a near-linear inverse relation is seen above 210 count values. For some 10W series, the plateau range extended beyond 210 count values, indicating better quality of concrete with a larger volume of pores within 10 to 100 nm (3.937×10^{-4} to 3.937×10^{-3} mil, thou) diameters. It confirmed the different ranges of the plateau region observed in experiments for the preconditioned OPC samples. Where information on the *w*/*b* and curing condition of in-place concrete is available, the upper threshold *PSD* value could appropriately be adjusted and considered before SWAT measurement. This validates the acceptability of the proposed assessment method using an upper-threshold *PSD* as the maximum surface moisture content for effective

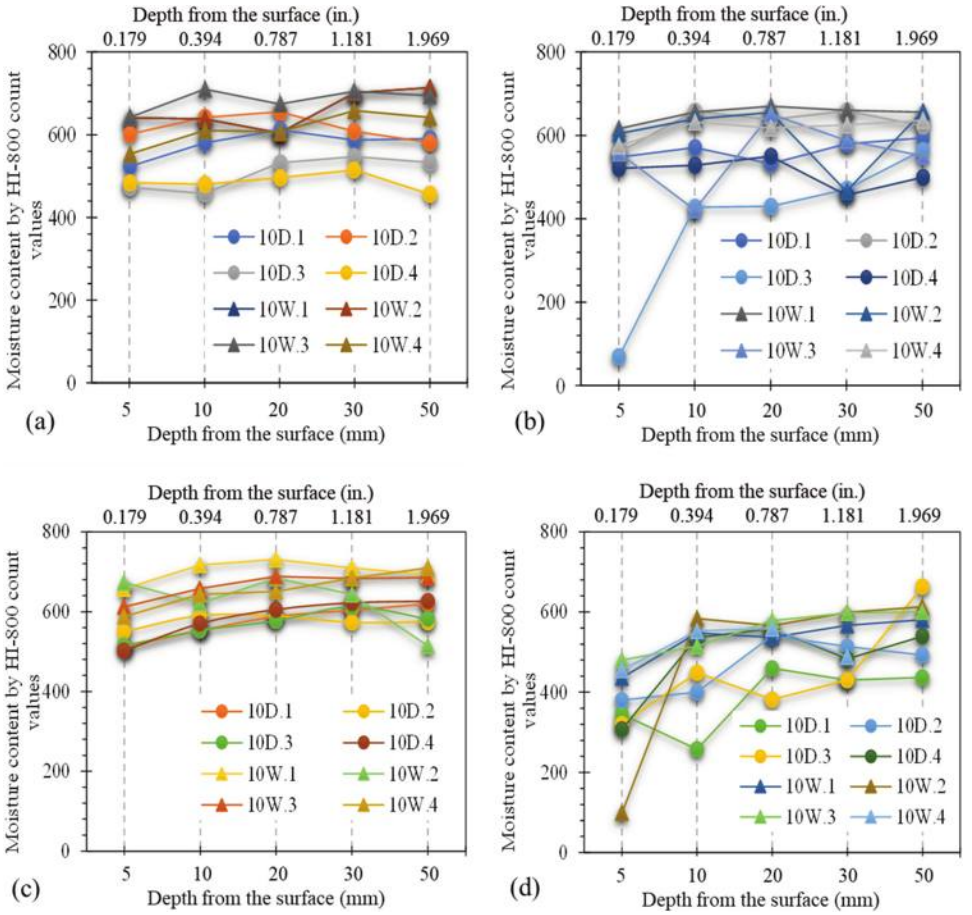

Fig. 16—Typical internal moisture distribution of concrete blocks exposed to different RH.

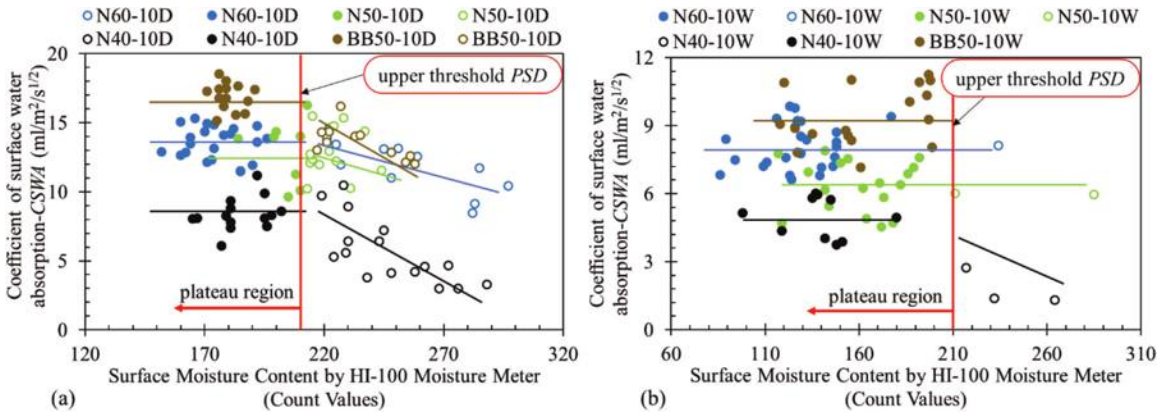

Fig. 17—Coefficient of surface water absorption—CSWA versus surface moisture content by HI-100 count values: (a) 10D series; and (b) 10W series.

durability assessment of in-place concrete structures when measuring the resistance to water ingress.

CONCLUSIONS

This study investigated the effect of saturation degree in concrete pore voids on water sorptivity, with quantitative and a clear correlation, showing the region where the degree of saturation of pore voids has almost no effect on the water resistance measurement results by the surface water absorption test. The conclusions derived from this study can be summarized as follows:

1. The initial pore void saturation degree at the cover zone of concrete for effective evaluation of the resistance to water absorption during durability assessment of in-place concrete structures was proposed based on the region where the degree of saturation has almost no effect on the measured results. Ordinary portland cement (OPC) 40, 50, and 60% water-cement ratio (*w*/*c*) concrete specimens preconditioned to uniform moisture distribution showed almost no effect of the saturation degree of permeable pore voids (*PSD*) on coefficient of surface water absorption (*CSWA*) within a particular *PSD* region (plateau region) for both the measured and simulated results. Moreover, the water sorp-

tivity of OPC and BB concrete blocks with internal moisture gradients confirmed the existence of the plateau region within the same *PSD* region for various patterns of internal moisture gradients.

2. When a short-term resistance to water absorption test is conducted with an initial surface moisture content within the plateau region, the measurement estimates the volume of noncontinuous finer capillary pores and evaluates the continuity and connectivity of the pore system. Continuity and connectivity of the pore system are known as the major indicator of the durability of concrete. The effective pore diameter relevant to the plateau zone is 10 to 100 nm (3.937×10^{-4} to 3.937×10^{-3} mil, thou). Measurement at this region eliminates the effects of initial surface moisture content on the measured properties.

3. To ensure the evaluation of resistance to water absorption at the noncontinuous finer capillary pore void saturation degree, the upper threshold for initial surface moisture content of concrete could be appropriately considered as equivalent to the "210 counts" of the surface moisture meter. This is the least value of the upper threshold and could be applied when information about the in-place concrete structure (such as *w*/*c* content and curing condition) is unknown. Where this information is available, the upper threshold may be appropriately adjusted upwards.

AUTHOR BIO

Uwazuruonye Raphael Nnodim *is a Postdoctoral Researcher at the Concrete Laboratory, Civil Engineering Department, Institute of Urban Innovation of Yokohama National University, Yokohama, Japan. He received his bachelor's degree from Federal Polytechnic Nekede Owerri, Nekede, Nigeria; his PGD from National Centre for Technology Management, Ife, Nigeria; and his MPhil and PhD from Yokohama National University. He is a World Bank Scholar and a one-time recipient of the prestigious MEXT scholarship. His research interests include nondestructive durability assessment of concrete structures.*

ACKNOWLEDGMENTS

This research was partly funded by the technology research and development system of The Committee on Advanced Road Technology established by the Ministry of Land, Infrastructure, Transport and Tourism (MLIT), Japan, as "Research development on quality and durability attainment system for concrete structures in various regions utilizing curing techniques and admixtures", the commissioned research of the National Institute for Land and Infrastructure Management.

NOTATION

B	=	peak distribution in logarithmic scale of sole porosity distribution parameter
B_{cp}	=	capillary porosity component
B_{gl}	=	gel porosity component
CSWA	=	coefficient of surface water absorption
DuCOM	=	Durability of COncrete Model simulation tool
PSD	=	percentage saturation degree of permeable pore voids of concrete
r	=	pore radius
SWAT	=	surface water absorption test
V	=	fractional pore volume of the distribution up to pore radius r
ϕ_{cp}	=	capillary porosity function
ϕ_{gl}	=	gel porosity function
ϕ_{lr}	=	interlayer porosity function

REFERENCES

1. Ueda, H.; Sakai, Y.; Kinomura, K.; Watanabe, K.; Ishida, T.; and Kishi, T., "Durability Design Method Considering Reinforcement Corrosion due to Water Penetration," *Journal of Advanced Concrete Technology*, V. 18, No. 1, 2020, pp. 27-38. doi: 10.3151/jact.18.27

2. Claisse, A. P., *Transport Properties of Concrete: Measurements and Applications*, Elsevier, Amsterdam, the Netherlands, 2014.

3. Long, A. E.; Henderson, G. D.; and Montgomery, F. R., "Why Assess the Properties of Near-surface Concrete?" *Construction and Building Materials*, V. 15, No. 2-3, 2001, pp. 65-79. doi: 10.1016/S0950-0618(00)00056-8

4. ASTM C1585-04, "Standard Test Method for Measurement of Rate of Absorption of Water by Hydraulic-Cement Concretes," ASTM International, West Conshohocken, PA, 2007.

5. BS 1881, Part 207, "Testing Concrete − Recommendations for the Assessment of Concrete Strength by Near-to-Surface Tests," British Standards Institution, London, UK, 1992.

6. JSCE-G 582, "Test Method for Water Penetration Rate Coefficient of Concrete Subjected to Water in Short-Term," Japan Society of Civil Engineers, Tokyo, Japan, 2018. (in Japanese)

7. Nakarai, K.; Shitama, K.; Nishio, S.; Sakai, Y.; Ueda, H.; and Kishi, T., "Long-Term Permeability Measurements on Site-Cast Concrete Box Culverts," *Construction and Building Materials*, V. 198, No. 8, 2019, pp. 777-785. doi: 10.1016/j.conbuildmat.2018.11.263

8. Uwazuruonye, R. N., and Hosoda, A., "Investigation on Correlation between Surface Water Absorption Test and JSCE Sorptivity Test," *Proceedings of JCI*, V. 42, No. 1, 2020, pp. 1726-1731.

9. Castro, J.; Bentz, D.; and Weiss, J., "Effect of Sample Conditioning on the Water Absorption of Concrete," *Cement and Concrete Composites*, V. 33, No. 8, 2011, pp. 805-813. doi: 10.1016/j.cemconcomp.2011.05.007

10. Gummerson, R. J.; Hall, C.; and Hoff, W. D., "Water Movement in Porous Building Materials—II. Hydraulic Suction and Sorptivity of Brick and Other Masonry Materials," *Building and Environment*, V. 15, No. 2, 1980, pp. 101-108. doi: 10.1016/0360-1323(80)90015-3

11. Hall, C., "Water Sorptivity of Mortars and Concretes: A Review," *Magazine of Concrete Research*, V. 41, No. 147, 1989, pp. 51-61. doi: 10.1680/macr.1989.41.147.51

12. Rucker-Gramm, P., and Beddoe, R. E., "Effect of Moisture Content of Concrete on Water Uptake," *Cement and Concrete Research*, V. 40, No. 1, 2010, pp. 102-108. doi: 10.1016/j.cemconres.2009.09.001

13. Sakai, Y.; Yokoyama, Y.; and Kishi, T., "Relationship Among the Permeation Rate of Water into Concrete, the Mix Design, Curing, and the Degree of Drying," *Journal of Advanced Concrete Technology*, V. 15, No. 10, 2017, pp. 595-602. doi: 10.3151/jact.15.595

14. Parrott, L. J., "Water Absorption in Cover Concrete," *Materials and Structures*, V. 25, No. 5, 1992, pp. 284-292. doi: 10.1007/BF02472669

15. Maruyama, I., "Multi-Scale Review for Possible Mechanisms of Natural Frequency Change of Reinforced Concrete Structures under an Ordinary Drying Condition," *Journal of Advanced Concrete Technology*, V. 14, No. 11, 2016, pp. 691-705. doi: 10.3151/jact.14.691

16. Yokoyama, Y.; Yokoi, T.; and Ihara, J., "The Effects of Pore Size Distribution and Working Techniques on the Absorption and Water Content of Concrete Floor Slab Surfaces," *Construction and Building Materials*, V. 50, 2014, pp. 560-566. doi: 10.1016/j.conbuildmat.2013.10.013

17. Shirakawa, T.; Shimazoe, Y.; Aso, M.; Nagamatsu, S.; and Sato, Y., "Relationship between Degree of Drying and Gas Diffusion Coefficient in Hardened Cement," *Transactions of AIJ*, V. 64, No. 524, 1999. pp. 7-12. doi:10.3130/aijs.64.7_410.3130/aijs.64.7_4

18. Dias, W. P. S., "Reduction of Concrete Sorptivity with Age through Carbonation," *Cement and Concrete Research*, V. 30, No. 8, 2000, pp. 1255-1261. doi: 10.1016/S0008-8846(00)00311-2

19. Dias, W. P. S., "Influence of Drying on Concrete Sorptivity," *Magazine of Concrete Research*, V. 56, No. 9, 2004, pp. 537-543. doi: 10.1680/macr.2004.56.9.537

20. Uwazuruonye, R. N., and Hosoda, A., "Investigation of the Effects of Saturation Degree of Permeable Pore Voids for Appropriate Covercrete Quality Evaluation by SWAT," *Internet Journal of Society for Social Management Systems*, V. 12, No. 2, 2020, pp. 87-96.

21. Hayashi, K.; Akmal, U.; and Hosoda, A., "Analysis of Moisture Transfer is Surface Water Absorption Test of Concrete using Embedded Sensors," *Proceedings of JCI*, V. 35, No. 1, 2013, pp. 1791-1794. (in Japanese)

22. Komatsu, S.; Tajima, R.; and Hosoda, A., "Proposal of Quality Evaluation Method for Upper Surface of Concrete Slab with Surface Water Absorption Test," *Concrete Research and Technology*, V. 29, 2018, pp. 33-40. doi: 10.3151/crt.29.33

23. Hayashi, K., and Hosoda, A., "Development of Surface Water Absorption Test Applicable to Actual Structures," *Proceedings of JCI*, V. 33, No. 1, 2011, pp. 1769-1774. (in Japanese)

24. Hayashi, K., and Hosoda, A., "Fundamental Study on Evaluation Method of Covercrete Quality of Concrete Structures by Surface Water Absorption Test," *Journal of Japan Society of Civil Engineers, Ser. E2, Materials and Concrete Structures*, V. 69, No. 1, 2013, pp. 82-97. (in Japanese)

25. Nam, H. P., and Hosoda, A., "Improvement of Water and Chloride Penetration Resistance of Slag Concrete by Using High Alite Cement," *Proceedings of JCI*, V. 37, No. 1, 2015, pp. 661-666.

26. Ngo, V. T.; Hosoda, A.; Komatsu, S.; and Ikawa, N., "Effect of Moisture Content on Surface Water Absorption Test and Air Permeability Test," *Proceedings of JCI*, V. 40, No. 1, 2018, pp. 1725-1730

27. Hosoda, A., and Hayashi, K., "Evaluation of Covercrete Quality of Concrete Structures by Surface Water Absorption Test," *Proceedings of the IOS2016 Symposium*, 2016.

28. Maekawa, K.; Chaube, T.; and Kishi, T., *Modelling of Concrete Performance: Hydration Microstructure Formation and Mass Transport*, Spon Press, London, UK, 1999.

29. Maekawa, K.; Ishida, T.; and Kishi, T., *Multi-Scale Modeling of Structural Concrete*, Taylor & Francis, London, UK, 2009.

30. Ishida, T.; Maekawa, K.; and Kishi, T., "Enhanced Modeling of Moisture Equilibrium and Transport in Cementitious Materials under Arbitrary Temperature and Relative Humidity History," *Cement and Concrete Research*, V. 37, No. 4, 2007, pp. 565-578. doi: 10.1016/j.cemconres.2006.11.015

31. Maekawa, K.; Pimanmas, A.; and Okamura, H., *Nonlinear Mechanics of Reinforced Concrete*, Spon Press, London, UK, 2003.

32. Nakarai, K.; Ishida, T.; Kishi, T.; and Maekawa, K., "Enhanced Modeling of Microstructure Formation of Cement Hydrates Coupled with Thermodynamics." *Proceedings of Monte Verità*, Switzerland, 2005, 6 pp.

33. Nakarai, K.; Ishida, T.; Kishi, T.; and Maekawa, K., "Enhanced Thermodynamic Analysis Coupled with Temperature-dependent Microstructures of Cement Hydrates," *Cement and Concrete Research*, V. 37, No. 2, 2007, pp. 139-150. doi: 10.1016/j.cemconres.2006.10.006

34. Uwazuruonye, R. N., "Effects of Pore Void Saturation Degree on Nondestructive Tests for Durability Assessment of Concrete Structures," PhD thesis, Yokohama National University, Yokohama, Japan, 2020, 155 pp. doi: 10.18880/00013481

APPENDIX A

Figure A1 shows the detailed geometry of the SWAT device, while Table A1 shows the conventional grading of covercrete quality by SWAT.

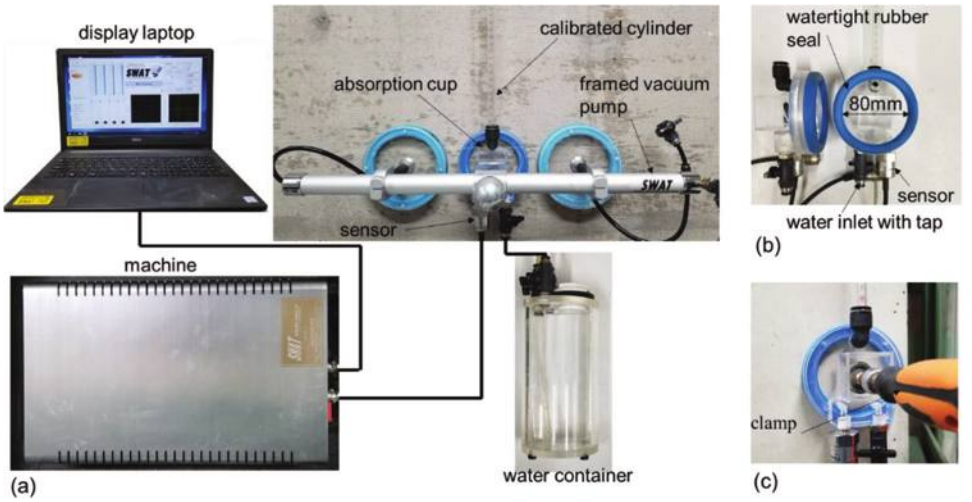

Fig. A1—Detailed geometry of SWAT device: (a) system; (b) details of absorption cup; and (c) detail of attachment onto small specimen.

Table A1—Grading of covercrete quality by SWAT

Water absorption rate at 10 minutes (600 seconds)	Quality		
	Good	Ordinary	Poor
p_{600}, mL/m^2/s	<0.25	0.25 to 0.50	>0.50

ACI MATERIALS JOURNAL TECHNICAL PAPER

Title No. 120-M57

Multi-Step Slotting Method for Evaluating In-Place Stress in Concrete

by Zhao-Dong Xu, Yi Zhang, Jin-Bao Li, Xing-Huai Huang, and Ying-Qing Guo

The slotting method is a nondestructive detection method based on the stress release principle to evaluate in-place stress in concrete. By measuring the change in strain of the slotting area using a strain gauge, the in-place stress within the concrete member can be calculated by elastic theory. This paper proposes a multi-step slotting method that combines experimental strain measurements with numerical simulation results. For concrete specimens under unidirectional stress, the effects of compressive stress, slotting spacing, slotting length, and slotting depth on the degree of stress release were analyzed using finite element analysis, and a normalized fitting equation was proposed that can be quickly and accurately applied in engineering detection. The excellent agreement between the experimental results and the numerical simulation (fitted equation) results shows that the slotting method can facilitate the accurate evaluation of the in-place stress in concrete, and the relative error can be reduced to less than 10% when it is calculated using the optimized multi-step experimental data.

Keywords: experimental study; in-place stress; numerical analysis; slotting method; stress measurement.

INTRODUCTION

With the emergence of super high-rise buildings and large-span bridge structures, the health monitoring and damage identification of engineering structures have garnered significant attention among scholars in recent years.[1,2] Throughout the service life of concrete structures, various factors such as stress decay, concrete creep, construction deviations, and differential settlements contribute to stress changes within these structures. Consequently, the theoretically calculated stress often significantly deviates from the actual stress. Therefore, accurate evaluation of in-place stress is of great importance to ensure the safety and reliability of structures. The measurement of in-place stress in existing concrete structures has been a difficult problem. The inhomogeneity and randomness of concrete materials, strain measurement techniques, and other factors contribute to the large dispersion and errors of stress measurement results.

The stress release method was initially proposed for measuring residual stress in steel members.[3] A hole is drilled in the measurement area of the material so that the stress around the hole is released and the change in strain at the measured point before and after the stress release is measured to calculate the residual stress.[4,5]

Stress release methods can be divided into the hole-drilling method (HDM), core-drilling method (CDM), and slotting method according to the drilling or slotting format employed. HDM is normally applied to the measurement of metals,[6-9] and the elastic modulus of the material can be accurately measured by coring, so CDM is more suitable for stress measurement in concrete and rocks.[10-14] The core-drilling machine used in CDM typically has a core diameter ranging from 100 to 250 mm, which allows for practical handling while meeting strain measurement requirements. Both HDM and CDM have been extensively studied and analyzed by scholars.[15-19] The change in strain at the edge of the hole before and after drilling is measured to calculate the in-place stress in concrete. In recent decades, researchers have conducted numerous studies on stress release methods and gradually applied them to stress detection in concrete.[20-28] The influence function based on surface displacements has been applied to concrete structures.[29,30] While the theoretical accuracy of these results was good, their practical application was hindered by the extremely small magnitude of the released displacements. In 2015, a nondestructive method for identifying the uniaxial in-place stress in concrete components for existing bridges using CDM based on influence functions was proposed.[31] An open-hole technique for evaluating in-place stress was proposed using a three-dimensional strain gauge wreath to measure the strain release during core drilling, and the reliability of the technology was evaluated through laboratory research.[32]

However, in CDM, it is not possible to measure the strain information inside the hole due to the limitation of the core-drilling machine. Additionally, the strain measurement in the area outside the hole is unstable, and the change in strain is dependent on the distance from the hole edge. The measurement results are further disturbed when the distance is too close, while the change in strain is minimal when the distance is too far.[33] Therefore, researchers have proposed an improved and innovative slotting method based on CDM, which can be divided into the linear slotting method (horizontal slot) and the square slotting method (square slot) according to the shape of the slots. The slotting method offers convenience in practical engineering applications and resolves the issue of discontinuous strain information within the coring area of CDM. In particular, the slotting method causes less damage to the concrete structure when unidirectional stress is involved. The slotting method is ideal for measuring in-place stress in structures such as piers and pile foundations with large unidirectional load-bearing capacity.

ACI Materials Journal, V. 120, No. 5, September 2023.

MS No. M-2022-356.R1, doi: 10.14359/51738893, received June 15, 2023, and reviewed under Institute publication policies.

Consequently, it effectively addresses the challenge of quickly and efficiently evaluating concrete stresses in the field of health monitoring research.[34]

This paper proposes a multi-step slotting method that combines experimental strain measurements with numerical simulation results. For concrete specimens under unidirectional stress, the effects of compressive stress, slotting spacing, slotting length, and slotting depth on the degree of stress release were analyzed using finite element analysis. According to the conclusion of numerical simulation analysis, the influence of different slotting lengths was reduced by controlling the aspect ratio of the slotting area. Two main influencing factors of slotting spacing and slotting depth were innovatively normalized into a fitting equation, which can be used to quickly calculate the stress release rate under different working conditions without complicated modeling calculations in practical engineering applications. Finally, the applicability and accuracy of the multi-step slotting method were evaluated by experiment on concrete specimens, and the relative error between the measured results and the real results was 10 to 15%, which could be reduced to below 10% by using the optimized multi-step experimental data for calculation.

RESEARCH SIGNIFICANCE

Traditional measurement methods cannot be applied to engineering measurement quickly and accurately. The strain information in the hole cannot be output continuously in CDM and the strain measurement in the area outside the hole is unstable. The authors firmly believe that this comprehensive study on the multi-step slotting method represents the first attempt of its kind and holds immense value for concrete technology. The findings and insights have the potential to significantly enhance the understanding of in-place stress evaluation, thereby benefiting the broader domain of concrete technology.

MULTI-STEP SLOTTING METHOD

Fundamental theory

The slotting method is a local damage detection method used to evaluate in-place stress in concrete. The concrete is elastically deformed during the slotting process as the stress in the slotting area is gradually released. The strain gauge is attached to the measurement points according to in-place stress direction, and as slotting depth increases, the strain gauge begins to measure the elastic strain released by concrete. The in-place stress at the measurement point is completely released when the slotting depth reaches a certain defined value. The in-place stress can be calculated from the stress-strain relationship in the elastic stage based on the strain change measured by the strain gauge and the modulus of elasticity of concrete.

Multi-step slotting method

First, it is important to define the relevant parameters in the slotting method to facilitate subsequent analysis and discussion. Dimension parameters such as slotting spacing S, slotting length L, central measurement point, and aspect ratio λ of the slotting area are defined, as shown in Fig. 1.

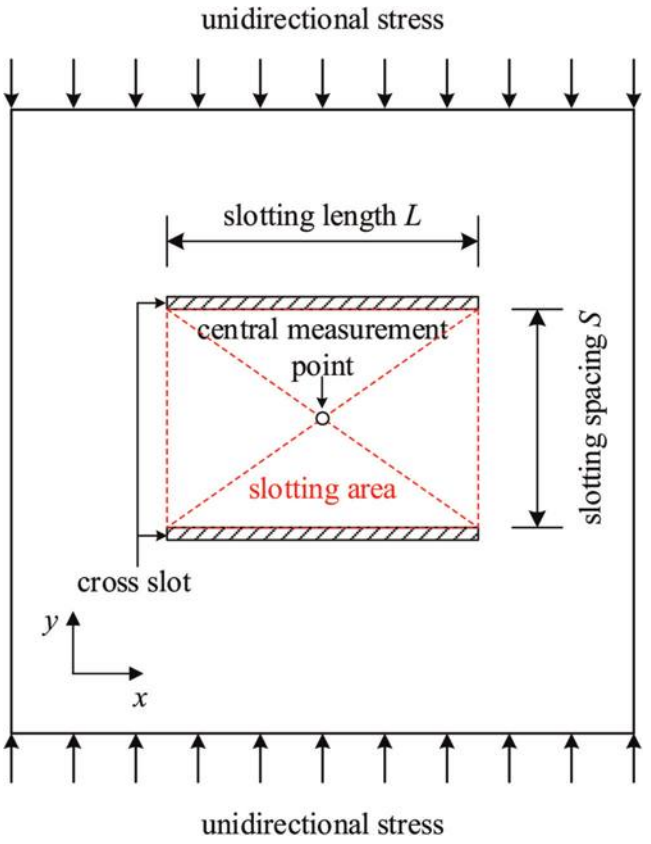

Fig. 1—Model schematic.

The aspect ratio λ of the stress release area is the ratio of slotted length L and slotted spacing S (L/S).

The stress release rate α_i at slotting step i is calculated as

$$\alpha_i = \frac{\sigma_0 - \sigma_i}{\sigma_0} = \frac{\varepsilon_0 - \varepsilon_i}{\varepsilon_0} = \frac{\Delta\varepsilon_i}{\varepsilon_0} \quad (1)$$

where α_i is the stress release rate of slotting step i; σ_0 is the initial y-directional stress; σ_i is the y-directional stress at slotting step i; ε_0 is the initial y-directional strain; ε_i is the y-directional strain at slotting step i; and $\Delta\varepsilon_i$ is the difference between the initial y-directional strain and the y-directional strain at slotting step i.

The traditional measurement method involves slotting concrete to a sufficient depth to fully release the stress at the measurement point. However, the in-place stress measured using this traditional method often exhibits a significant error. The following reasons are analyzed to explain this phenomenon: first, the zero-stress depth is closely related to factors such as slotting shape, slotting spacing, and slotting length. These factors are prone to change during the slotting process, leading to variations in the zero-stress depth and resulting in a large error. Second, it is difficult to precisely control the slotting depth to just reach the zero-stress depth. To address these limitations, this paper proposes a multi-step slotting method that combines experimental strain measurements with numerical simulation results. The in-place stress can be calculated as

$$\sigma = \frac{E}{n}\sum_{1}^{n}\frac{\Delta\varepsilon_i}{\alpha_i} \quad (2)$$

where σ is the in-place stress; E is the modulus of elasticity; n is the number of slotting steps; α_i is the stress release rate of the numerical simulation at slotting step i; and $\Delta\varepsilon_i$ is the difference between the initial strain and the strain of the experiment at slotting step i.

It is important to note that change in measured strain $\Delta\varepsilon_i$ can be measured in engineering detection. However, the true values of the initial strain ε_0 and the strain ε_i after each slotting step on the concrete surface cannot be directly measured (they can only be measured and analyzed in experimental studies). In Eq. (2), the calculation of the in-place stress does not involve the true values of the initial strain and the strain after each slotting step, but rather focuses on the change in measured strain without slotting and with slotting. Therefore, the inability to measure the true values of strains on the concrete surface during engineering detection does not affect the calculation of in-place stress.

By setting a reasonable slotting step depth, the change in strain at the measurement point under multiple step depths can be measured, and the in-place stress can be calculated by combining numerical simulation results. The multi-step slotting method offers the significant advantage of not requiring precise attention to the variation of the zero-stress depth. Instead, it uses a rational analysis step and a suitable number of analysis steps to minimize errors.

NUMERICAL ANALYSIS

Calculation model

To study the effects of various factors on stress release, the finite element method was employed to conduct numerical simulations on compressed members subjected to unidirectional stress. A finite element model of concrete with dimensions of 500 x 500 x 250 mm (19.69 x 19.69 x 9.84 in.) was created in Abaqus/CAE. The model was analyzed using a direct solver with static conditions and an implicit form of integration. Because the multi-step slotting method involves a progressive slotting process with incremental depths, individual models were generated at each slotting depth: 0, 5, 10, 15, 20, 25, 30, 35, 40, 45, and 50 mm (0, 0.20, 0.39, 0.59, 0.79, 0.98, 1.18, 1.38, 1.58, 1.78, and 1.97 in.). The material properties of the concrete were assumed to exhibit elastic behavior, with a strength grade of C30, modulus of elasticity of 30,000 MPa (4,350,000 psi), and a Poisson's ratio of 0.20 assigned to the model. The element type employed in the model was an eight-node hexahedral linearly reduced integration element (C3D8R). The model was meshed using a structured mesh with a global size of 10 x 10 mm (0.39 x 0.39 in.), with appropriate size reduction near the slotting area. The load was uniformly applied from the top surface as a pressure distribution, and all degrees of freedom at the bottom of the model were constrained.

Effect of slotting length

The effect of the slotting length on the degree of stress release was analyzed. For this purpose, a slotting spacing of 100 mm (3.94 in.) was chosen, and eight different slotting lengths were selected: 60, 80, 100, 120, 140, 160, 180, and 200 mm (2.36, 3.15, 3.94, 4.72, 5.51, 6.30, 7.09, and 7.87 in.), corresponding to aspect ratios of 0.6, 0.8, 1.0, 1.2, 1.4, 1.6, 1.8, and 2.0, respectively. The y-directional stress values at the central measurement point for different slotting depths were calculated and presented in Fig. 2.

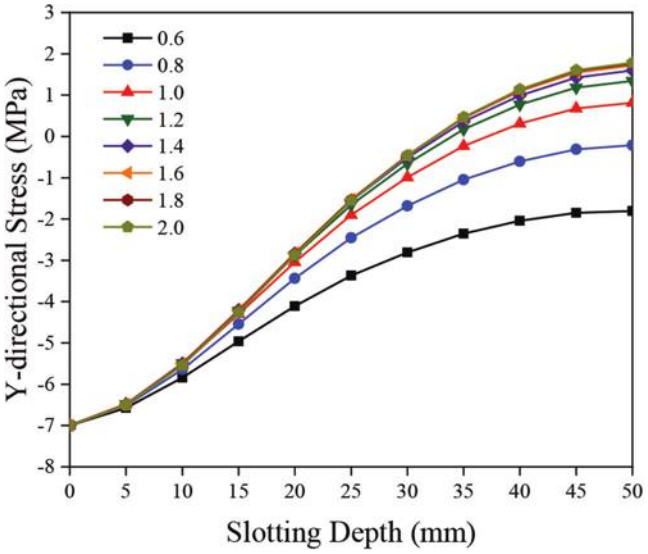

Fig. 2—Variation of y-directional stress with slotting depth at different slotting lengths. (Note: 1 MPa = 145 psi; 1 mm = 0.039 in.)

As the slotting depth increased, the y-directional stress gradually decreased and eventually stabilized at a certain value. The variation trend of y-directional stress with slotting depth remained consistent across different aspect ratios, but the degree of discrepancy varied among the working conditions. The effect of aspect ratio can be analyzed in two cases: $\lambda \leq 1$ and $\lambda > 1$.

Aspect ratio $\lambda \leq 1$ (slotted length L *≤ slotted spacing* S*)*—The significant differences of y-directional stress were observed among different aspect ratios at the same slotting depth. Longer slotting lengths resulted in faster stress release, and smaller slotting depths were required to achieve complete stress release. When $\lambda = 0.6$, the y-directional stress at the central measurement point was not completely released, regardless of the slotting depth.

Aspect ratio $\lambda > 1$ (slotted length L *> slotted spacing* S*)*—The minimal differences of y-directional stress were observed among different aspect ratios at the same slotting depth. The maximum difference of y-directional stress among the five working conditions with $\lambda > 1$ was observed at the slotting depth of 50 mm (1.97 in.), and the ratio of the maximum difference to the initial y-directional stress was 6.30%. The average ratio of the maximum difference of y-directional stress to the initial y-directional stress at each slotting depth was 2.52%. Therefore, as long as the aspect ratio is greater than 1 ($\lambda > 1$), the error resulting from variations in slotting length caused by factors such as saw blade shape or slotting disturbances is minimal, ensuring accurate measurement results.

Effect of slotting spacing

The effect of the slotting spacing on the degree of stress release was analyzed by selecting slotting spacings of 50, 60, 70, 80, 90, and 100 mm (1.97, 2.36, 2.76, 3.15, 3.54,

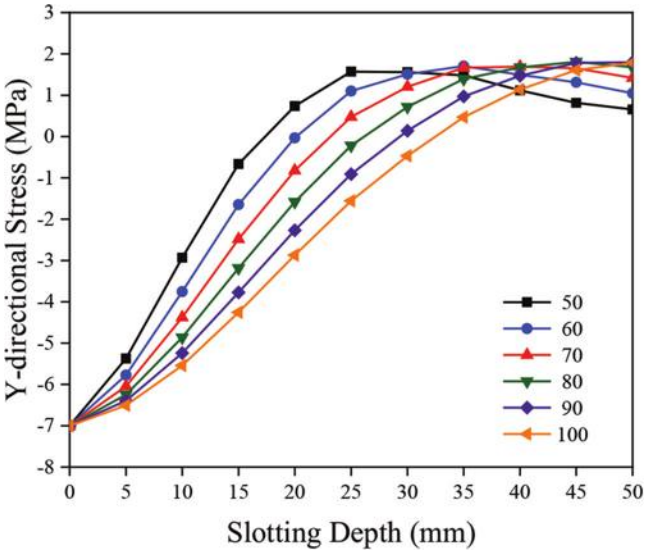

Fig. 3—Variation of y-directional stress with slotting depth at different slotting spacings. (Note: 1 MPa = 145 psi; 1 mm = 0.039 in.)

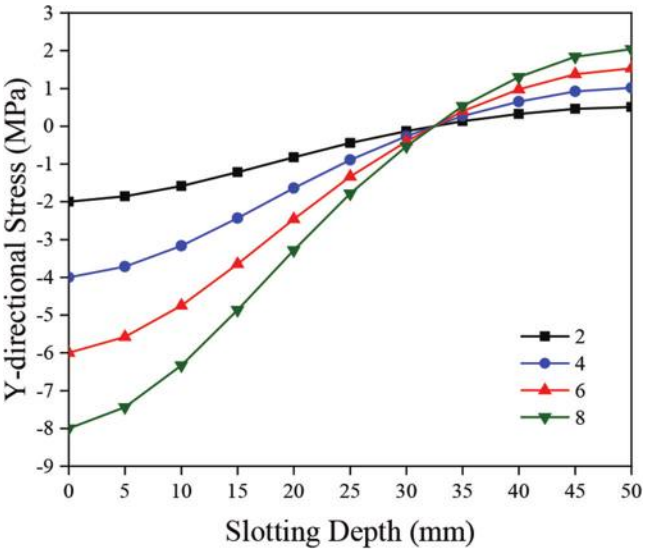

Fig. 4—Variation of y-directional stress with slotting depth at different stresses. (Note: 1 MPa = 145 psi; 1 mm = 0.039 in.)

and 3.94 in.) for a total of six working conditions. To ensure consistency and avoid the influence of different slotting lengths on the results, an aspect ratio of 2 ($L = 2S$) was maintained for all six working conditions. The variation of y-directional stress with slotting depth at different slotting spacings is shown in Fig. 3.

As observed in Fig. 3, the variation trend of y-directional stress with slotting depth remained consistent across different slotting spacings. A longer slotting spacing resulted in a slower release of stress, requiring a larger slotting depth for complete stress release. During the slotting process, the y-directional stress at the center measurement point would undergo three stages. In the first stage, as the slotting depth increased, the y-directional stress gradually decreased until the stress was completely released and the slotting depth reached the zero-stress depth, which was first reached at the end of the first stage. The slotting depth continued to increase and the stress release entered the second stage. At this stage, the stress increased in the opposite direction until it reached the maximum value (much less than the initial y-directional stress). Finally, the third stage was entered, and the y-directional stress gradually approached 0 again from the reverse maximum. In practical stress measurements, particular attention should be given to the first stage of stress release.

Effect of initial stress

The effect of the initial stress on the degree of stress release was analyzed. Figure 4 shows the variation of y-directional stress with slotting depth at different initial stresses, and Fig. 5 shows the results of the stress release rate. A slotting spacing of 100 mm (3.94 in.), slotting length of 200 mm (7.87 in.) with an aspect ratio of 2, and four initial stress levels (2, 4, 6, and 8 MPa [290, 580, 870, and 1160 psi]) were considered for analysis.

In Fig. 4, the y-directional stress gradually decreased from the initial value as the slotting depth increased.

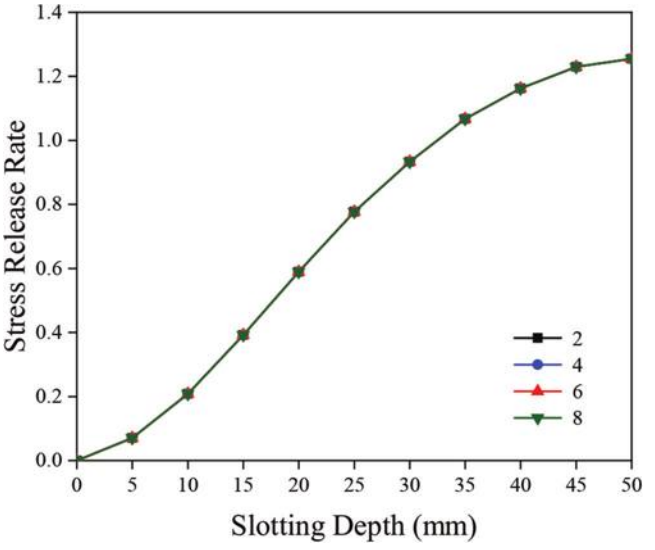

Fig. 5—Variation of stress release rate with slotting depth at different stresses. (Note: 1 mm = 0.039 in.)

The y-directional stress of four working conditions was completely released at a slotting depth of 32 mm (1.26 in.). Beyond the point of stress release, as the slotting depth continued to increase, the y-directional stress reversed and increased in magnitude. Notably, the greater the initial stress, the higher the maximum value of the reverse stress observed. Figure 5 illustrates that the stress release rate remained consistent at the same slotting depth across all four compressive stress conditions. The magnitude of the stress only influenced the initial y-directional stress value at the measurement point and the stress release value at each step. It had no impact on the stress release rate at each step or the zero-stress depth. Consequently, the slotting method can be widely used to detect the in-place stress in concrete. The degree of stress release at different slotting depths is independent of the magnitude of the current in-place stresses in concrete.

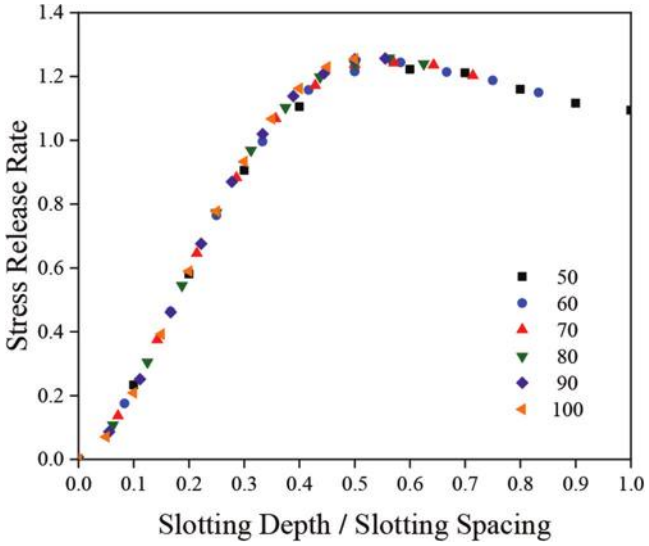

Fig. 6—Variation of stress release rate with ratio of slotting depth to slotting spacing.

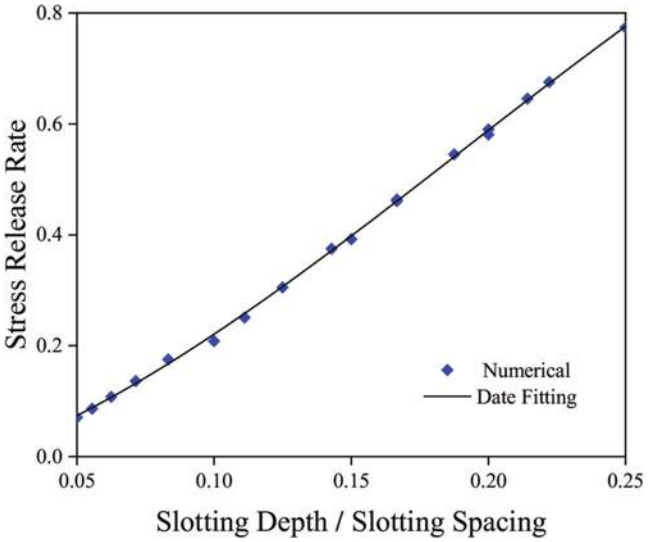

Fig. 7—Fitted stress release rate curve.

Normalized analysis of factors

In the previous analysis, factors such as slotting depth, slotting length, slotting spacing, and initial stress were found to affect the stress release rate in the slotting method. It was observed that the magnitude of the initial stress does not impact the stress release rate, and the influence of the slotting length can be mitigated by ensuring that the aspect ratio is greater than 1 ($\lambda > 1$). Consequently, a normalized equation incorporating slotting depth and slotting spacing was proposed to calculate the stress release rate, enabling quick application for theoretical stress release rate calculation in practical engineering detection. To account for the effect of slotting spacing, the y-directional stress data at different slotting depths in Fig. 3 were processed. Figure 6 illustrates the variation of the stress release rate with the ratio of slotting depth to slotting spacing.

The data points were primarily clustered around a single curve, allowing for the calculation of stress release rates at different slotting spacings and depths based on this curve. In practical engineering applications and experiments, particular attention should be paid to the variation of stress release rates in the first stage (from 0 to 1) due to limitations in slotting depth and the use of long-scale strain gauges. For subsequent experiments, a large slotting spacing was employed in conjunction with long-scale strain gauges. To ensure the accuracy of the fitting equation, data points corresponding to slotting depth to slotting spacing ratios ranging from 0.05 to 0.25 in Fig. 6 were selected for curve fitting. The resulting fitted stress release rate curve is depicted in Fig. 7. The fitting equation is

$$\alpha = -22.4736\left(\frac{H}{S}\right)^3 + 12.8042\left(\frac{H}{S}\right)^2 + 1.4089\left(\frac{H}{S}\right) - 0.0257 \quad (3)$$

Equation (3) has correlation coefficient $R^2 = 0.9982$; α is the stress release rate; H is the slotting depth; and S is the slotting spacing.

Equation (3) is valid for any level of stress and concrete grade provided that the applied load is within the elastic range (linear variation of stress and strain).

EXPERIMENTAL STUDY

To evaluate the accuracy of the slotting method in assessing in-place stress in real concrete structures, experiments were conducted taking into account various slotting depths and slotting spacings.

Preparation of concrete specimen

The experimental study was performed on plain cement concrete members with a cross-sectional area of 500 x 250 mm (19.69 x 9.84 in.) and a length of 500 mm (19.69 in.). The experimental study was limited to plain cement concrete, while the effect of reinforcement remains a part of future studies.

To ensure quality control and consistency in the experimental study, concrete specimens of strength class C30 were prepared using concrete supplied by a commercial concrete company. The specimens were cured under natural conditions, and standard test blocks were prepared to measure the physical properties of the concrete. The test block method is used in experimental study to detect the grade of concrete. In engineering detection, the concrete grade can be determined through various methods, including consulting available information, using the rebound method, or conducting core drilling, depending on the specific circumstances. Table 1 shows the physical properties of concrete. The age of the concrete at slotting from the date of casting was 195 days (Specimens 1 and 2) and 196 days (Specimens 3, 4, and 5). A total of six concrete specimens were prepared for the experimental study, with one specimen initially used for a pretest to verify the accuracy of the experimental setup and instrumentation. The remaining five specimens were used for the formal experiments.

Experimental setup

Figure 8 illustrates the experimental setup used in the study. An electro-hydraulic servo pressure tester with a

Table 1—Physical properties of concrete

Number	Compressive strength, MPa	Average, MPa	Numerical, MPa	Number	Modulus of elasticity, MPa	Average, MPa	Numerical, MPa
S-1	30.8	30.6	30	S-4	29,500	30,233	30,000
S-2	31.1			S-5	30,200		
S-3	29.9			S-6	31,000		

Note: 1 MPa = 145 psi.

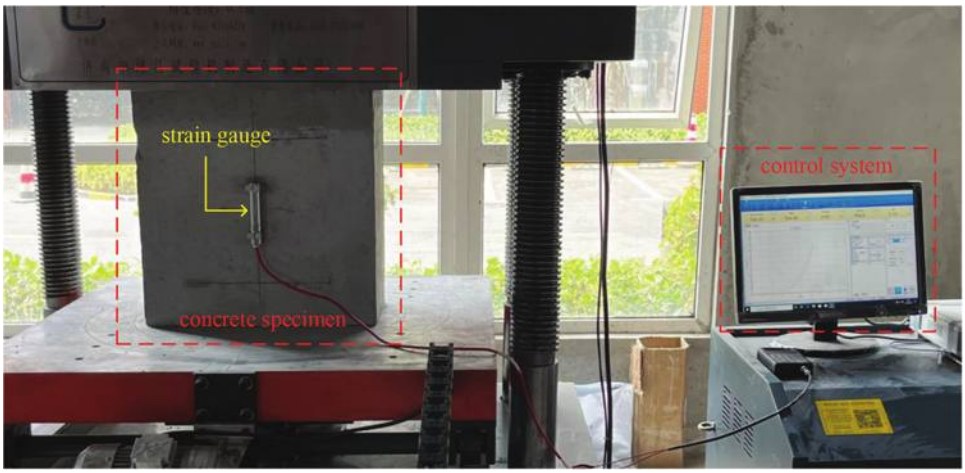

Fig. 8—Experimental setup.

maximum load capacity of 2000 kN (449.62 kip) was employed to apply the load. The digital control system was used to regulate the pressure tester, enabling precise control of the applied load to reach the desired value and maintain it at different loading speeds. The real-time load values were displayed on the control system screen, ensuring accurate monitoring of the applied load during the experiments.

Figures 9 and 10 show the vibrating wire surface strain gauge system used to measure the changes in concrete strain within the slotting area. To ensure reliable measurements, the concrete surface was thoroughly cleaned and polished before attaching the strain gauge using epoxy resin adhesive. Clamp supports were installed at both edges of the strain gauge to facilitate accurate attachment to the concrete surface. Experiments were performed after a minimum drying period of 24 hours to ensure the firm attachment of the strain gauge. A reading instrument was connected to the strain gauge through a cable, allowing real-time monitoring of the gauge's frequency. The strain calculation equation is

$$\varepsilon = A\left(f_i^2 - f_0^2\right) \quad (4)$$

where ε is the measured strain; A is the calibration factor; f_0 is the initial frequency; and f_i is the measured frequency.

Experimental conditions and procedures

It is important to note that the slotting method is applicable within the elastic working stage of concrete. When concrete enters the plastic stage and undergoes plastic deformation, the released strain measured through the slotting method may be lower than the actual strain, leading to inaccurate measurement of the concrete stress. The in-place stress of actual structural concrete typically falls within the range of 0.4 to 0.5f_c. It is crucial to consider variations between experiments and actual situations, such as potential loading eccentricity, uneven force distribution on specimens, and the potential weakening of the specimen section due to the

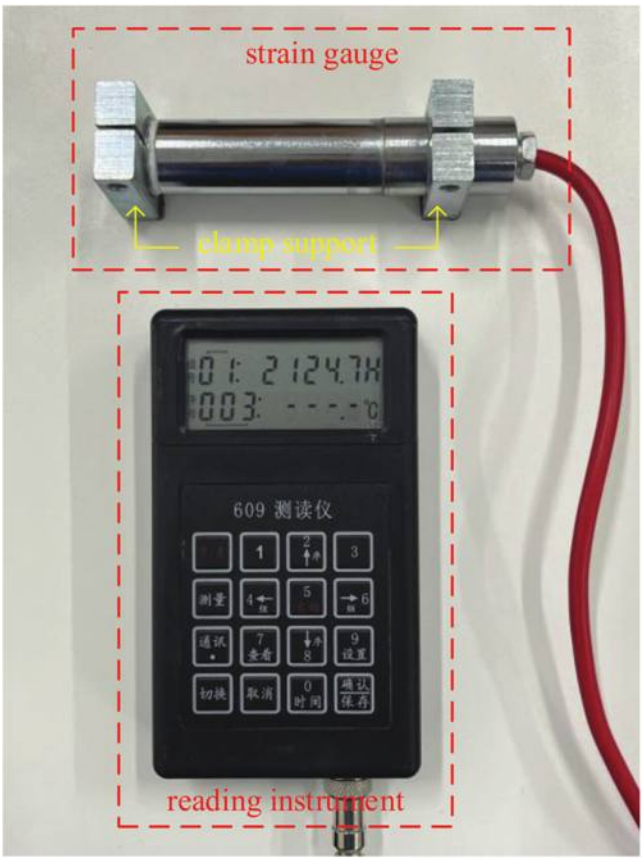

Fig. 9—Strain gauge system.

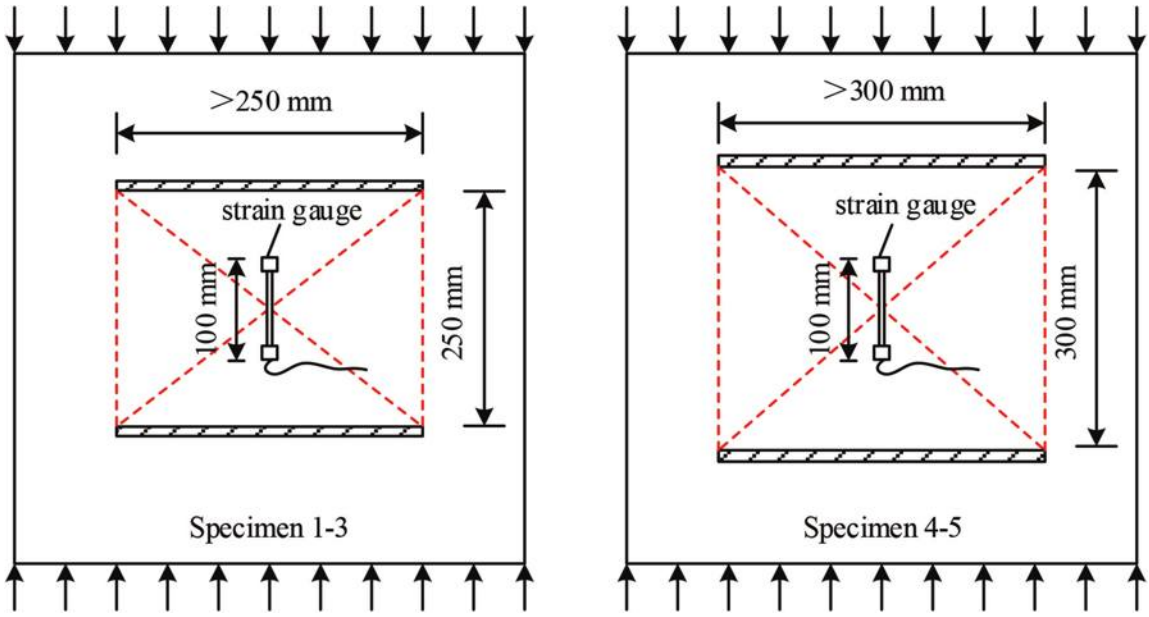

Fig. 10—Diagram of experimental conditions. (Note: 1 mm = 0.039 in.)

Table 2—Experimental conditions

Number	Slotting spacing, mm	Slotting spacing, mm	Load, kN	Stress, MPa
1	250	>250	500	4
2			750	6
3			1000	8
4	300	>300	500	4
5			750	6

Note: 1 mm = 0.039 in.; 1 kN = 0.2248 kip; 1 MPa = 145 psi.

slotting process. Therefore, it is advisable to avoid excessive loading stress to ensure accurate measurements and account for these factors.

Table 2 shows the specific working conditions of five specimens in the experiments considering various slotting depths and slotting spacings. Figure 11 demonstrates the effect of a circular saw blade on a handheld cutter, with a corresponding increase in slotting length as the slotting depth increases. The effect of slotting length on results was minimized by ensuring that the slotting lengths were greater than the corresponding slotting spacings—that is, the aspect ratio $\lambda > 1$.

The experimental procedures in this this study were conducted as follows: the specimen was positioned on the pressure tester, and the initial reading of the strain gauge was recorded prior to the application of any load. Subsequently, the load was gradually increased to the predetermined design load at a rate of 5 kN/s (1.12 kip/s). Once the load reached a stable state, the reading of the strain gauge was recorded. To ensure result stability, a holding time of 10 minutes was selected, during which the strain gauge reading was recorded at intervals of 30 seconds. Upon completion of the data recording phase, the designated area of the specimen was slotted using a handheld cutter. The depth of each slot was measured meticulously with a steel ruler to ensure that it reached the desired target. Following stabilization, the strain gauge reading was recorded within 10 minutes. This process was repeated for each subsequent slotting depth until a depth of 50 mm (1.97 in.) was reached. The slotting depths in the experiments were incrementally increased in five steps, ranging from 0 to 50 mm (0 to 1.97 in.), with a step size of 10 mm (0.39 in.).

Results and error analysis

Figures 12 and 13 show the comparison of the stress release rates of the experimental specimens at various slotting depths with the results obtained from numerical simulations, along with Eq. (3). The experimental results indicated a gradual increase in the stress release rate as the slotting depth increased. Moreover, for specimens with the same slotting depth, a smaller slotting spacing was associated with a lower stress release rate. The comparison of the stress release rate among specimens subjected to different levels of initial stress indicated that the magnitude of compressive stress did not significantly impact the stress release rate. These experimental results corroborated the validity of several conclusions drawn from the earlier numerical simulation analysis.

Meanwhile, it can be observed from Fig. 12 and 13 that the experimental results generally exhibited higher values compared to the numerical simulation results. This discrepancy can be attributed to the length of the strain gauge used in the experiment, which was 100 mm (3.94 in.), whereas the stress release rate calculated by the numerical simulation was only determined at the central measurement point. To explore the impact of strain gauge length, a preliminary analysis was conducted using numerical simulation. It was found that when the strain gauge length was approximately one-third of the slotted spacing, the average strain within the length of the strain gauge slightly exceeded the strain at the central measurement point, although the difference was small. For the purposes of this paper, the data obtained from the central measurement point was used for subsequent analysis. As the effect of strain gauge length will be a focal point in future studies, numerical simulation can be employed to

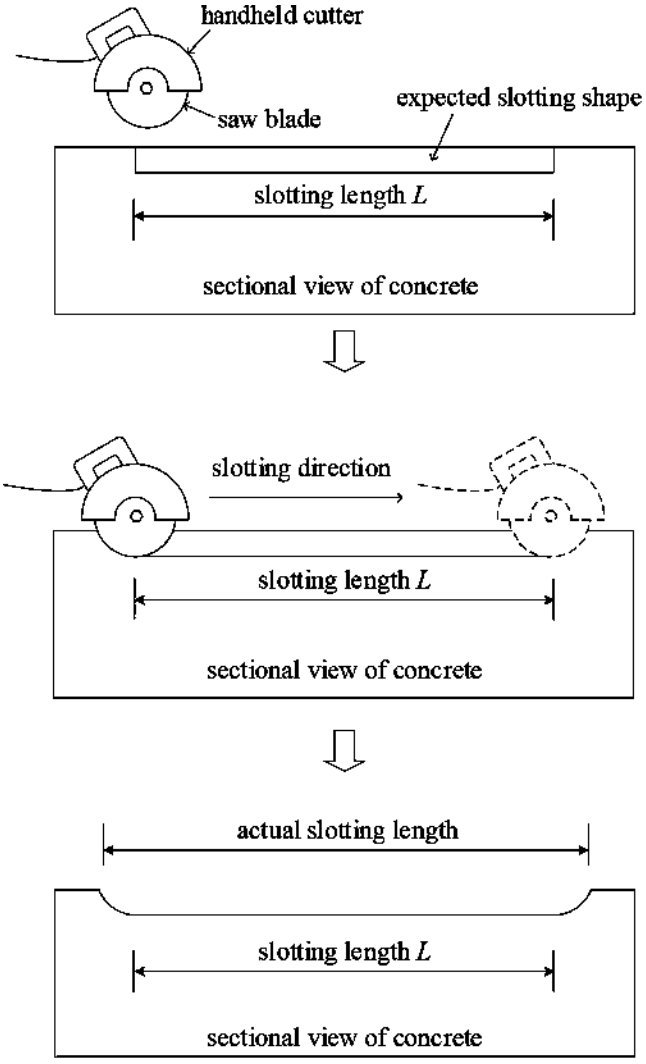

Fig. 11—Schematic diagram of slotting process.

extract the strain values of each node within the length of the strain gauge. The average strain can then be calculated using the method of integrating over the standard distance length.

The discrepancy between the numerical simulation results obtained by modeling the experimental conditions and the results derived from Eq. (3) for the corresponding experimental conditions was found to be minimal. This proves the applicability and reasonableness of the fitting equation, which can be easily and quickly applied in engineering detection. The difference between experimental results and numerical simulation results was the focus of attention. Although the trend of the stress release rate obtained from both experiments and numerical simulations was consistent, there still existed a certain degree of difference. To quantify the magnitude of this difference, a relative error factor K was defined. The error factor could not be simply expressed in terms of the difference between results, so it returned to the derivation of the equation of in-place stress

$$\sigma = \frac{E}{n}\sum_{1}^{n}\frac{\Delta\varepsilon_i}{\alpha_i} = \frac{E}{n}\sum_{1}^{n}\frac{\Delta\varepsilon_i \cdot \varepsilon_0}{\alpha_i \cdot \varepsilon_0} = \frac{E\varepsilon_0}{n}\sum_{1}^{n}\frac{\Delta\varepsilon_i}{\alpha_i \cdot \varepsilon_0} = \frac{E\varepsilon_0}{n}\sum_{1}^{n}\frac{\alpha_i'}{\alpha_i} \quad (5)$$

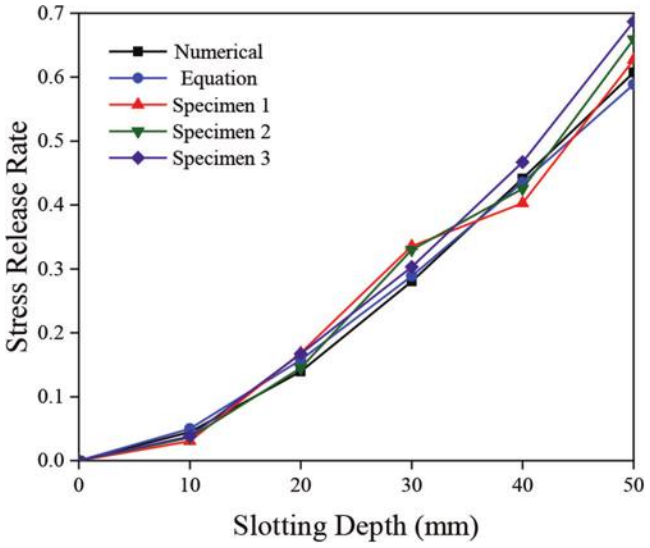

Fig. 12—Stress release rate with depth of slotting. (Note: Slotting spacing of 250 mm; 1 mm = 0.039 in.)

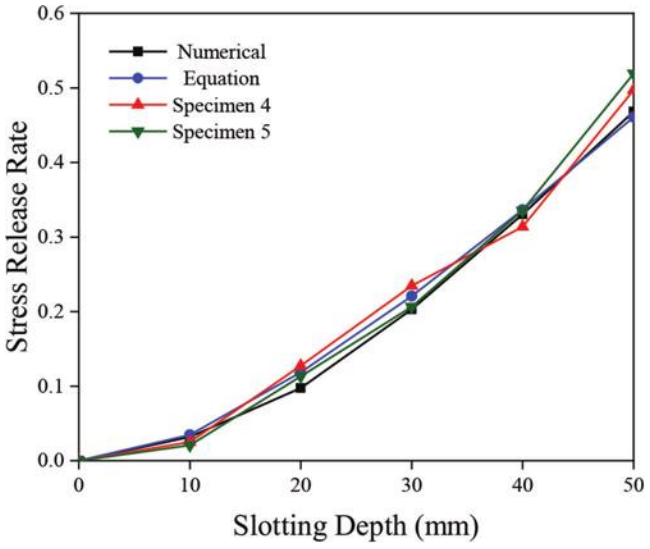

Fig. 13—Stress release rate with depth of slotting. (Note: Slotting spacing of 300 mm; 1 mm = 0.039 in.)

where σ is in-place stress; E is the modulus of elasticity; n is the number of slotting steps; α_i is stress release rate of the numerical simulation at slotting step i; α_i' is the stress release rate of the experiment at slotting step i; ε_0 is the initial strain at the measurement point; and $\Delta\varepsilon_i$ is the difference between the initial strain and the strain of the experiment at slotting step i.

In theory, the in-place stress $\sigma = E\varepsilon_0$, so the equation of total relative error K can be obtained as

$$K = \frac{1}{n}\sum_{1}^{n}k_i = \frac{1}{n}\sum_{1}^{n}\left|\frac{\alpha_i' - \alpha_i}{\alpha_i}\right| \quad (6)$$

where K is the total relative error; and k_i is the relative error at slotting step i.

Table 3 shows the relative errors of experimental data with numerical simulation and Eq. (3). It is evident that the relative error exhibited significant variations at different

Table 3—Error factor

Number	Numerical						Fitting equation					
	k_1	k_2	k_3	k_4	k_5	K	k_1	k_2	k_3	k_4	k_5	K
1	0.318	0.206	0.197	0.087	0.032	0.168	0.387	0.068	0.161	0.075	0.065	0.151
2	0.195	0.04	0.177	0.036	0.085	0.107	0.276	0.079	0.140	0.023	0.119	0.127
3	0.145	0.199	0.082	0.059	0.131	0.123	0.232	0.062	0.049	0.073	0.167	0.117
4	0.215	0.306	0.154	0.051	0.062	0.158	0.279	0.073	0.062	0.068	0.079	0.112
5	0.35	0.162	0.016	0.015	0.1069	0.130	0.403	0.045	0.065	0.003	0.127	0.129

slotting depths. The error was larger for small depths (10 mm [0.39 in.]). This can be attributed to factors such as the large size of the specimen, shallow slotting depth, and limited stress release, which resulted in minimal strain changes and subsequently smaller measurement outcomes. As the slotting depth increased, the relative error decreased. Notably, at depths of 20 and 30 mm (0.79 and 1.18 in.), where the strain exhibited substantial changes, the error was relatively small. However, when the slotting depth was 50 mm (1.97 in.), the relative error became large. It is because the depth of the slotting is large, and the weakening of the cross section is too great.

The relative errors observed in the experiments for the five specimens were predominantly within the range of 10 to 15%. These errors fall within an acceptable range and further validate the applicability and accuracy of the multi-step slotting method for concrete stress measurement. Notably, the relative error was reduced to 9.4% when using data from slotting depths ranging from 20 to 40 mm (0.79 to 1.58 in.), which significantly improved the accuracy of the results. Follow-up studies and engineering measurements can improve the accuracy of results by using the experimental data from appropriate slotting depths.

CONCLUSIONS

The average relative error of 13.2% for all specimen experiments described in Table 3 was reduced to 9.4% when data from appropriate slotting depths was used, indicating the effective use of the multi-step slotting method for evaluating in-place stress in concrete. The main conclusions can be drawn as follows:

1. The excellent consistency between experimental results and numerical simulations (or fitting equation results) demonstrates that the multi-step slotting method can be conveniently and accurately employed to evaluate the in-place stress in concrete structures.

2. The slotting method effectively addresses the limitation of discontinuous strain information in the hole of the core-drilling method (CDM). When stress is released, the stress change in the slotting area is more sensitive and accurate than that in the area outside the slot, and the measurement results are stable.

3. The finite element method is used to analyze the relevant factors affecting the degree of stress release of the slotting method. The main influencing factors are normalized and incorporated into a fitting equation, enabling rapid and precise calculation of the stress release rate under different working conditions without the need for complex modeling calculations.

4. According to the multi-step slotting method combined with numerical simulation (or fitting equation), the calculation equation of in-place stress is proposed. By employing multi-step slotting and optimizing the selection of data intervals, measurement errors can be minimized.

AUTHOR BIOS

Zhao-Dong Xu *is a Professor at Southeast University, Nanjing, Jiangsu, China. He received his BS, MS, and PhD in civil engineering from Xi'an University of Architecture and Technology, Xi'an, Shaanxi, China. His research interests include structural seismic disaster prevention and vibration control, structural health monitoring, and intelligent materials and structures.*

Yi Zhang *is a Master's Student at Southeast University, where he received his BS in civil engineering. His research interests include concrete stress measurement and structural health monitoring.*

Jin-Bao Li *is a Senior Engineer at Jiangsu Dongnan Special Engineering & Technology Co., LTD, Nanjing, Jiangsu Province, China. He received his BS in civil engineering from Yangzhou University, Yangzhou, Jiangsu Province, China. His research interests include rectification and reinforcement technology of buildings.*

Xing-Huai Huang *is an Associate Professor at Southeast University, where he received his BS, MS, and PhD in civil engineering. His research interests include engineering structure disaster prevention and structural vibration control.*

Ying-Qing Guo *is a Professor at Nanjing Forestry University, Nanjing, Jiangsu Province, China. She received her BS from Xi'an University of Architecture and Technology, and her MS and PhD from Southeast University. Her research interests include intelligent control technology, intelligent materials, and structural vibration control.*

ACKNOWLEDGMENTS

This research is financially supported by the National Key R&D Programs of China with Grant No. 2019YFE0121900, the National Natural Science Foundation of China with Grant No. 52130807, and the Key R&D Program for Anhui Province with Grant No. 202104G01020002. These supports are gratefully acknowledged.

REFERENCES

1. Xu, Z. D., and Wu, Z. S., "Energy Damage Detection Strategy Based on Acceleration Responses for Long-Span Bridge Structures," *Engineering Structures*, V. 29, No. 4, 2007, pp. 609-617. doi: 10.1016/j.engstruct.2006.06.004

2. Xu, Z. D., and Wu, K. Y., "Damage Detection for Space Truss Structures Based on Strain Mode under Ambient Excitation," *Journal of Engineering Mechanics*, ASCE, V. 138, No. 10, 2012, pp. 1215-1223. doi: 10.1061/(ASCE)EM.1943-7889.0000426

3. Mathar, J., "Determination of Initial Stresses by Measuring the Deformations around Drilled Holes," *Transactions of the American Society of Mechanical Engineers*, V. 56, No. 3, 1934, pp. 249-254. doi: 10.1115/1.4019712

4. Rendler, N., and Vigness, I., "Hole-Drilling Strain-Gage Method of Measuring Residual Stresses," *Experimental Mechanics*, V. 6, No. 12, 1966, pp. 577-586. doi: 10.1007/BF02326825

5. ASTM E837-08e1, "Standard Test Method for Determining Residual Stresses by the Hole-Drilling Strain-Gage Method," ASTM International, West Conshohoken, PA, 2008.

6. Schajer, G. S., "Hole-Drilling Residual Stress Measurements at 75: Origins, Advances, Opportunities," *Experimental Mechanics*, V. 50, No. 2, 2010, pp. 245-253. doi: 10.1007/s11340-009-9285-y

7. Nau, A., and Scholtes, B., "Evaluation of the High-Speed Drilling Technique for the Incremental Hole-Drilling Method," *Experimental Mechanics*, V. 53, No. 4, 2013, pp. 531-542. doi: 10.1007/s11340-012-9641-1

8. Pan, L.; Ge, H.; and Wang, B., "Effects of Poisson's Ratio on the Calibration Coefficients of Hole-Drilling Strain-Gauge Method for Measuring Residual Stresses," *Strength of Materials*, V. 53, No. 4, 2021, pp. 566-572. doi: 10.1007/s11223-021-00318-7

9. Pisarev, V.; Odintsev, I.; Eleonsky, S.; and Apalkov, A., "Residual Stress Determination by Optical Interferometric Measurements of Hole Diameter Increments," *Optics and Lasers in Engineering*, V. 110, 2018, pp. 437-456. doi: 10.1016/j.optlaseng.2018.06.022

10. McGinnis, M., and Pessiki, S., "Review of the Core-Drilling Method for Evaluating Concrete Stresses," *International Conference on Health Monitoring of Structure, Materials and Environment*, V. 1, 2007, 632 pp.

11. Pessiki, S., and Turker, H., "Theoretical Formulation of the Core Drilling Method to Evaluate Stresses in Concrete Structures," *Review of Progress in Quantitative Nondestructive Evaluation*, V. 509, 2000, pp. 1731-1737. doi: 10.1063/1.1306241

12. Siddig, O. M.; Al-Afnan, S. F.; Elkatatny, S. M.; and Abdulraheem, A., "Drilling Data-Based Approach to Build a Continuous Static Elastic Moduli Profile Utilizing Artificial Intelligence Techniques," *Journal of Energy Resources Technology-Transactions of the ASME*, V. 144, No. 2, 2022, p. 023001. doi: 10.1115/1.4050960

13. Wang, Q.; Gao, H. K.; Jiang, B.; Li, S. C.; He, M. C.; and Qin, Q., "In-Situ Test and Bolt-Grouting Design Evaluation Method of Underground Engineering Based on Digital Drilling," *International Journal of Rock Mechanics and Mining Sciences*, V. 138, 2021, p. 104575. doi: 10.1016/j.ijrmms.2020.104575

14. Gao, M. Z.; Hao, H. C.; Xue, S. N.; Lu, T.; Cui, P. F.; Gao, Y. N.; Xie, J.; Yang, B. G.; and Xie, H. P., "Discing Behavior and Mechanism of Cores Extracted From Songke-2 Well at Depths Below 4500 m," *International Journal of Rock Mechanics and Mining Sciences*, V. 149, 2022, p. 104976. doi: 10.1016/j.ijrmms.2021.104976

15. Beghini, M., and Bertini, L., "Analytical Expressions of the Influence Functions for Accuracy and Versatility Improvement in the Hole-Drilling Method," *Journal of Strain Analysis for Engineering Design*, V. 35, No. 2, 2000, pp. 125-135. doi: 10.1243/0309324001514071

16. McGinnis, M. J., and Pessiki, S., "Experimental Study of the Core-Drilling Method for Evaluating In Situ Stresses in Concrete Structures," *Journal of Materials in Civil Engineering*, ASCE, V. 28, No. 2, 2016, p. 04015099. doi: 10.1061/(ASCE)MT.1943-5533.0001294

17. Rickert, T., "Residual Stress Measurement by ESPI Hole-Drilling," *Procedia CIRP*, V. 45, 2016, pp. 203-206. doi: 10.1016/j.procir.2016.02.256

18. Deng, N. C., and Tang, P. F., "Research on In Situ Stress Measurements in Reinforced Concrete Beams Based on the Core-Drilling Method," *Advances in Civil Engineering*, V. 2020, 2020, p. 8832614. doi: 10.1155/2020/8832614

19. Dabli, A. G.; Bambole, A. N.; and Bajoria, K. M., "Evaluation of In-Place Stress in Concrete by Incremental Hole Drilling," *ACI Materials Journal*, V. 117, No. 4, July 2020, pp. 27-35. doi: 10.14359/51724612

20. McGinnis, M. J., and Pessiki, S., "Water-Induced Swelling Displacements in Core Drilling Method," *ACI Materials Journal*, V. 104, No. 1, Jan.-Feb. 2007, pp. 13-22.

21. Campione, G., and Minafo, G., "Applicability of Over-Coring Technique to Loaded RC Columns," *Structural Engineering and Mechanics*, V. 51, No. 1, 2014, pp. 181-197. doi: 10.12989/sem.2014.51.1.181

22. Beghini, M.; Bertini, L.; and Mori, L. F., "Evaluating Non-Uniform Residual Stress by the Hole-Drilling Method With Concentric and Eccentric Holes. Part II: Application of the Influence Functions to the Inverse Problem," *Strain*, V. 46, No. 4, 2010, pp. 337-346. doi: 10.1111/j.1475-1305.2009.00684.x

23. Beghini, M.; Bertini, L.; and Mori, L. F., "Evaluating Non-Uniform Residual Stress by the Hole-Drilling Method with Concentric and Eccentric Holes. Part I. Definition and Validation of the Influence Functions," *Strain*, V. 46, No. 4, 2010, pp. 324-336. doi: 10.1111/j.1475-1305.2009.00683.x

24. McGinnis, M. J.; Pessiki, S.; and Turker, H., "Application of Three-Dimensional Digital Image Correlation to the Core-Drilling Method," *Experimental Mechanics*, V. 45, No. 4, 2005, pp. 359-367. doi: 10.1007/BF02428166

25. McGinnis, M. J., and Pessiki, S., "Differential Shrinkage Effects in the Core-Drilling Method," *Magazine of Concrete Research*, V. 59, No. 3, 2007, pp. 155-164. doi: 10.1680/macr.2007.59.3.155

26. Schajer, G. S., "Hole-Drilling Residual Stress Profiling with Automated Smoothing," *Journal of Engineering Materials and Technology-Transactions of the ASME*, V. 129, No. 3, 2007, pp. 440-445. doi: 10.1115/1.2744416

27. Beghini, M.; Bertini, L.; Mori, L. F.; and Rosellini, W., "Genetic Algorithm Optimization of the Hole-Drilling Method for Non-Uniform Residual Stress Fields," *Journal of Strain Analysis for Engineering Design*, V. 44, No. 1, 2009, pp. 105-115. doi: 10.1243/03093247JSA457

28. Castaneda, D. I., "New Field Testing Procedure For Measuring Residual Stress in Plain Concrete Pavements and Structures," PhD dissertation, University of Illinois Urbana-Champaign, Urbana, IL, 2010, pp. 52-80.

29. Trautner, C.; McGinnis, M.; and Pessiki, S., "Analytical and Numerical Development of the Incremental Core-Drilling Method of Non-Destructive Determination of In-Situ Stresses in Concrete Structures," *Journal of Strain Analysis for Engineering Design*, V. 45, No. 8, 2010, pp. 647-658. doi: 10.1177/030932471004500801

30. Trautner, C.; McGinnis, M.; and Pessiki, S., "Application of the Incremental Core-Drilling Method to Determine In-Situ Stresses in Concrete," *ACI Materials Journal*, V. 108, No. 3, May-June 2011, pp. 290-299.

31. Ruan, X., and Zhang, Y., "In-Situ Stress Identification of Bridge Concrete Components Using Core-Drilling Method," *Structure and Infrastructure Engineering*, V. 11, No. 2, 2015, pp. 210-222. doi: 10.1080/15732479.2013.862729

32. Parivallal, S.; Ravisankar, K.; Nagamani, K.; and Kesavan, K., "In Situ Stress Assessment in Concrete Structures Under Bi-Axial Condition by Trepanning Technique," *Experimental Techniques*, V. 39, No. 4, 2015, pp. 57-63. doi: 10.1111/j.1747-1567.2012.00860.x

33. Zhang, F., and Qiu, Z., "Analysis of Measuring Existing Stresses in Concrete Structure by Hole Drilling Core Surface Strain Gauge Method," *Materials Research Innovations*, V. 15, 2011, pp. S601-S604. doi: 10.1179/143307511X12858957677118

34. Xu, Z. D.; Liu, M.; Wu, Z. S.; and Zeng, X., "Energy Damage Detection Strategy Based on Strain Responses for Long-Span Bridge Structures," *Journal of Bridge Engineering*, ASCE, V. 16, No. 5, 2011, pp. 644-652. doi: 10.1061/(ASCE)BE.1943-5592.0000195

ACI MATERIALS JOURNAL TECHNICAL PAPER

Title No. 120-M58

Influence of Aggregate on Fresh Pore Solution Resistivity

by K. S. T. Chopperla, A. Tuinukuafe, J. H. Biever, O. B. Isgor, and W. J. Weiss

This study examines the influence of fine aggregates on early-age mortar pore solution chemistry and electrical resistivity. Specifically, this paper considers the potential adsorption of Na^+ and K^+ on the aggregate. Ten aggregates from various locations in the United States were used in this study. It was shown that fine aggregates can adsorb Na^+ and K^+ ions, which can change the ionic concentration of the pore solution and increase the pore solution resistivity. The resistivity is also influenced by the absorbed water in the aggregate, which dilutes the pore solution. A test methodology was proposed to characterize the aggregate adsorption of Na^+ and K^+ from the pore solution. The alkali adsorption was quantified by developing adsorption isotherms for each aggregate. Using the adsorption isotherms, the concentrations of Na^+ and K^+ adsorbed on aggregates in mortars were estimated.

Keywords: adsorption isotherms; alkali adsorption; fine aggregates; fresh mortar; pore solution; resistivity.

INTRODUCTION

Resistivity testing of concrete has been gaining popularity as a quality control/quality assurance (QC/QA) tool. ASTM International and the American Association of State Highway and Transportation Officials (AASHTO) provide standardized procedures (ASTM C1876-19,[1] AASHTO TP 119-22,[2] AASHTO T 358-21,[3] and AASHTO R 101-22[4]) for determining the resistivity of hardened concrete cylinders. While the electrical resistivity of hardened concrete has been used as a surrogate transport measurement,[5-8] a number of studies[9-13] have examined the use of electrical properties as a potential QA/QC tool. For example, the resistivity of fresh paste has been studied as a potential indicator of the water-cementitious materials ratio (*w*/*cm*) and supplementary cementitious material (SCM) content.[10,12,14,15] Additionally, variations in electrical responses due to added water or admixture volumes have also been investigated in fresh mixtures.[9,11,16] Also, there are ongoing efforts to develop fast, effective, and practical field measurement techniques for the determination of the bulk and pore solution resistivity of fresh mixtures.[17-24]

The electrical resistivity can be described by using the modified parallel law[25] as described in Eq. (1).

$$\frac{1}{\rho_c} = \frac{1}{\rho_{ps}}\phi_{ps}\beta_{ps} + \frac{1}{\rho_{cm}}\phi_{cm}\beta_{cm} + \frac{1}{\rho_{agg}}\phi_{agg}\beta_{agg} + \frac{1}{\rho_{air}}\phi_{air}\beta_{air} \quad (1)$$

where ρ_c is the resistivity of the mortar or concrete; $\rho_{(i)}$ is the resistivity of phase *i*; $\phi_{(i)}$ is the volume fraction of phase *i*; and $\beta_{(i)}$ is the connectivity parameter of phase *i*. As shown in Eq. (1), each phase of concrete (that is, pore solution [ps], cementitious materials [cm], aggregate [agg], and air) impacts the electrical resistivity of the system based on their volume fraction. Phases other than pore solution have significantly higher resistivity, by several orders of magnitude than that of pore solution, which has a resistivity in the range of 1 to 100 ohm·cm. For example, concrete aggregates typically have a resistance in the order of 10^4 to 10^8 ohm·cm[26]; therefore, aggregates are typically assumed to be electrically insulating, with the exception of conductive aggregates that contain metals and connected pores.[17,26] Similarly, the vapor phase and cementitious binder have typical resistivities of 10^{19} ohm·cm and 10^7 ohm·cm, respectively.[27] Thus, it can be assumed that the ratios of pore solution resistivity to resistivity of cementitious material, aggregate, and air approach zero and can be ignored. Therefore, Eq. (1) can be simplified to Eq. (2).

$$\frac{1}{\rho_c} = \frac{1}{\rho_{ps}}\phi_{ps}\beta_{ps} \quad (2)$$

While aggregates do not contribute significantly to electrical conduction, they may still have indirect effects on the electrical properties of fresh concrete. It is well established that aggregates may dilute the pore solution system as their absorbed water dilutes the pore solution,[28,29] and some aggregates, especially the ones containing feldspar, may release alkalies into the pore solution over time.[30-34] Both processes can influence the pore solution composition and pore solution resistivity.

Several past studies have focused on studying the effect of different aggregates, aggregate contents, and the interfacial transition zone (ITZ) on the resistivity of hardened mortar or concrete (based on the assumption of nonconductive and non-alkali-silica-reactive aggregate).[26,28,29,35-40] However, limited work[41] has been done comparing paste and mortar or concrete pore solution in terms of their chemistry and resistivity in light of the potential aggregate alkali adsorption. Therefore, the need exists to determine the role of aggregates in comparing paste and mortar pore solutions' composition and resistivity.

While the dilution of the pore solution due to absorbed water and alkali release from the aggregates may affect the resistivity of the pore solution, the aggregates could also adsorb any ions from the surrounding pore solution.[42,43] There is evidence from several studies from other fields such as chemistry and geosciences showing that particles containing quartz

ACI Materials Journal, V. 120, No. 5, September 2023.
MS No. M-2023-024, doi: 10.14359/51738894, received January 31, 2023, and reviewed under Institute publication policies.

could adsorb alkali and alkaline-earth cations.[44-47] Adsorption of alkali cations such as Na^+ and K^+ from concrete pore solution by aggregates would reduce the pH of the pore solution and increase the pore solution resistivity. The effect of alkali-cation adsorption by aggregates on concrete pore solution properties has not been studied in depth.

This study investigates the effect of different fine aggregates on the pore solution composition and resistivity of fresh mortars, specifically relating to aggregate porosity and potential surface adsorption of alkali cations from pore solutions. This study presents a practical method to characterize aggregates that alter fresh mortar pore solution resistivity.

RESEARCH SIGNIFICANCE

The electrical properties of concrete are increasingly being used in the QC/QA of concrete. The assumption that the aggregates are inert, while often appropriate, may not always be true. As such, the aggregates may impact the electrical resistivity of the pore solution in concrete or mortar, causing it to differ from the paste. This study presents a method to quantify the ion adsorption behavior of aggregates. This can then be used to quantify the effect of the aggregate on the pore solution chemistry and resistivity. The proposed methods will lead to a more reliable interpretation of the pore solution resistivity and may be useful for quantifying the formation factor.

MATERIALS AND MIXTURES

Materials

Ten fine aggregates that meet ASTM C33/C33M-18[48] were studied. The fine aggregate properties such as fineness modulus (FM), absorption capacity (AC), and saturated-surface-dry (SSD) specific gravity (SG) are summarized in Table 1.

For the mortar experiments, an ASTM C150/C150M-22[49] Type I ordinary portland cement (OPC) was used in this study[50]; Table 2 lists the chemical composition of this OPC. The SG and the Blaine fineness were 3.15 and 420 m^2/kg, respectively. The water used in all mixtures was ASTM D1193-06[51] Type II deionized (DI) water.

Mortar mixtures

Mortar mixtures were made with all the aggregates in the study. The mixtures were prepared to have a *w*/*cm* of 0.45. Fine aggregates at the SSD condition were used for mortar mixing. Approximately 247.0 cm^3 of fine aggregate was used for each mortar mixture. A cement paste volume to fine aggregate volume ratio of 0.93 was used for all the mixtures. The mortars were mixed for approximately 30 minutes from the initial contact of cement with water and then transferred to plastic cylinders with dimensions of 7.6 (diameter) x 15.2 cm (length) for bulk electrical resistivity measurements.

Simulated pore solution

A simulated pore solution (SPS) was prepared for testing the dilution and surface adsorption effects on the solution resistivity. Table 3 shows the chemical composition of the prepared SPS.

Table 1—Summary of fine aggregates properties used in this study

Origin of fine aggregate	Sample ID	Fineness modulus	Absorption capacity, %	Specific gravity (SSD)
Western Oregon	A-1	2.96	3.6	2.59
Southern Oregon	A-2	2.78	3.8	2.57
Florida	A-3	2.76	0.6	2.64
Central California	A-4	3.31	1.1	2.65
Eastern California	A-5	3.51	0.8	2.55
Idaho	A-6	2.62	2.5	2.59
Minnesota	A-7	2.75	1.0	2.65
Indiana	A-8	2.41	1.3	2.66
Kansas	A-9	2.78	0.6	2.63
North Carolina	A-10	2.83	0.5	2.64

Table 2—Chemical composition of OPC

Cement oxides and LOI	Percent by mass, %
Silicon dioxide (SiO_2)	19.9
Aluminum oxide (Al_2O_3)	4.6
Ferric oxide (Fe_2O_3)	3.2
Calcium oxide (CaO)	62.0
Magnesium oxide (MgO)	3.8
Sulfur trioxide (SO_3)	2.8
Alkalies ($Na_2O + 0.658K_2O$)	0.57
LOI	1.6
Bogue phase composition	
Phase	Percent by mass, %
Tricalcium silicate (C_3S)	57.0
Dicalcium silicate (C_2S)	14.0
Tricalcium aluminate (C_3A)	7.0
Tetracalcium aluminoferrite (C_4AF)	10.0

Note: LOI is loss on ignition.

Table 3—Composition of simulated pore solution

Label	NaOH	KOH	$Ca(OH)_2$
SPS	0.19 M	0.19 M	0.10 M

Sodium and potassium hydroxide solutions

Three different concentrations of NaOH and KOH solutions were prepared for the alkali-cation adsorption isotherm tests. The purity of chemicals used was 95% and 98% for NaOH and KOH, respectively. The solutions were prepared using DI water. Table 4 summarizes the molar concentrations measured using an X-ray fluorescence (XRF) spectrometer, the pH, and the resistivity of NaOH and KOH solutions prepared in the study.

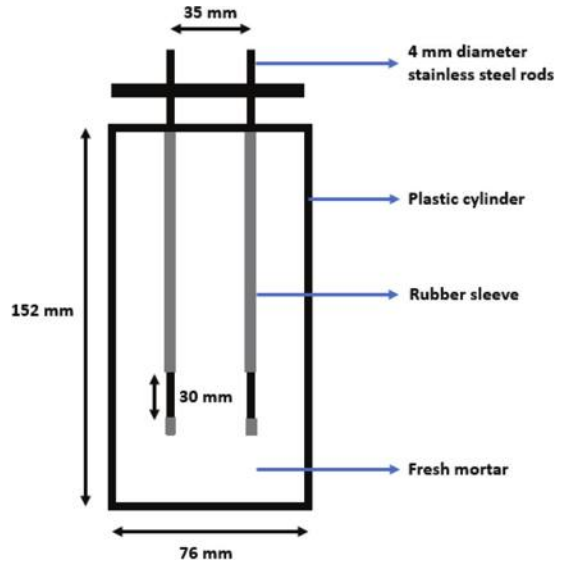

Fig. 1—Bulk electrical resistivity setup (not to scale).

METHODS

Mortar bulk electrical resistivity

The bulk resistivity was measured for fresh mortar samples using an advanced nondestructive laboratory tool that was connected to two embedded electrodes, as shown in Fig. 1. The measurements were performed using a 7.6 cm (diameter) x 15.2 cm (length) plastic cylinder filled with fresh mortar or cement paste with two 4 mm diameter stainless steel electrodes spaced at a distance of 35 mm in the vertical direction. The measurements were taken 30 minutes after the water and cement were mixed.

The geometry factor of the assembly was found using Eq. (3) using two solutions of known conductivity (41 and 84 mS/cm).

$$G_f = \frac{R_{ST}}{\rho_{ST}} \tag{3}$$

where G_f is the geometry factor; R_{ST} is the resistance of the solution; and ρ_{ST} is the resistivity of the solution. The geometry factor of the assembly was 41.6 m^{-1}.

Two samples per mixture were prepared for the resistivity measurement and the average of the values is reported. After measuring the resistivity of the mortar mixtures, the pore solution resistivity was found by using a centrifuge to extract the pore solution from the fresh mortar.[24] The extracted pore solution was decanted and placed into vials to use for the resistivity and ion concentration measurements.

Solution resistivity and chemical composition

The resistivity of each solution was measured with a three-pole platinum conductivity electrode for an electrochemistry benchtop meter, as shown in Fig. 2. Before every experiment in this study, the conductivity electrode was calibrated using a single 25 mS/cm (40 ohm·cm) buffer solution as per the manufacturer's recommendation.

A benchtop energy-dispersive XRF spectrometer was used to analyze the chemical composition of each solution. A description of the calibration technique used for this particular device can be found in the literature.[52] Solutions were filtered using a 45 μm filter syringe prior to XRF testing.

Table 4—Measured composition, pH, and resistivity of solutions used for adsorption isotherm tests

Label	C_{Na^+}, mmol/L	C_{K^+}, mmol/L	pH	Resistivity, ohm·cm
DI water	0.9	0.4	8.74	13.4×10^3
50 mM NaOH	37.1	0.3	12.46	78.7
100 mM NaOH	79.6	0.4	12.66	41.5
200 mM NaOH	170.2	0.4	12.81	21.0
100 mM KOH	1.0	85.2	12.81	41.8
200 mM KOH	7.9	169.4	13.08	20.8
400 mM KOH	4.2	334.4	13.39	11.3

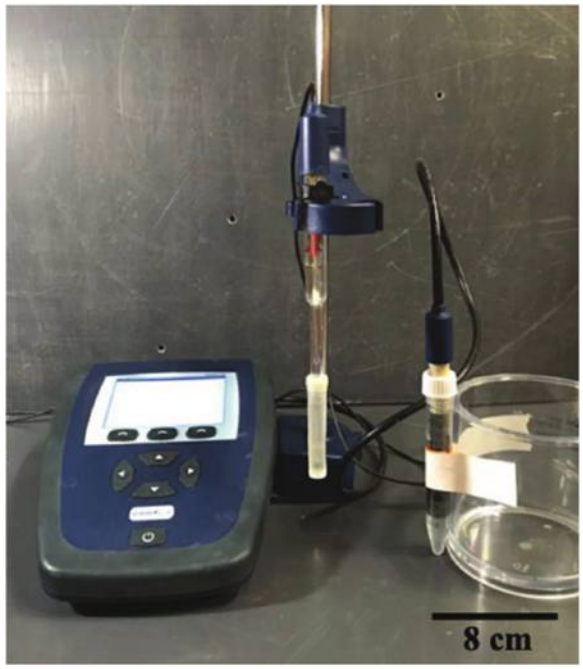

Fig. 2—Electrochemistry benchtop meter with pH probe (left); and resistivity probe testing specimen (right).

Simulated pore solution tests

The SSD aggregates were exposed to the SPS (the composition is shown in Table 3) to determine the effect of aggregate moisture (dilution) and surface adsorption of alkali on solution resistivity. Approximately 20 cm^3 of fine aggregate at the SSD condition was measured into sealed 50 mL centrifuge tubes for testing. Approximately 15 mL of the SPS was added to each centrifuge tube containing the sample, and the tubes were shaken by hand for 1 minute to ensure all aggregate particles were exposed to the SPS. The samples were then tested 30 minutes after the initial fine aggregate contact with the solution.

To extract the solution, the test specimens in the 50 mL centrifuge tubes were inserted into a centrifuge and spun at 4000 revolutions per minute (rpm) for 2 minutes. The solution was then decanted from the top of the centrifuge tubes and placed into smaller 10 mL centrifuge tubes for the resistivity.

Effect of dilution by aggregate moisture on solution resistivity—The water contained in the pores of an aggregate at SSD will come to equilibrium with the pore solution in a concrete and dilute the ionic concentration of the pore solution system.[53] To determine the corrected concentration and resistivity of the SPS, resistivity-ion concentration relationships from Snyder et al. were used.[54] The relationship between ionic concentrations and the resistivity of the solution is represented by Eq. (4).

$$\frac{1}{\rho_{ps}} = \sum_i C_i z_i \lambda_i \quad (4)$$

where ρ_{ps} is the resistivity of the pore solution; C_i represents the molar concentration of each ion i; z_i is the number of valence electrons for each ion; and λ_i is the equivalent conductivity of each ion. The equivalent conductivity is simplified by Eq. (5)[54]

$$\lambda_i = \frac{\lambda_i^\circ}{1 + G_i I_M^{1/2}} \quad (5)$$

where λ° represents the equivalent conductivity of the ionic species at infinite dilution; G_i is the conductivity coefficient; and I_M is the ionic strength of the solution. The values of λ° and G_i can be found in Table 5.[54] The ionic strength, I_M, can be calculated with Eq. (6)[54]

$$I_M = \frac{1}{2}\sum_i z_i^2 C_i \quad (6)$$

To create a function of these variables that relate the change in conductivity of the alkali solution in terms of water added to the system by aggregate water content, a dilution term can be introduced, as shown in Eq. (7),[24] which quantifies the change in ion concentration due to the addition of DI water to the system

$$C_{i.dil} = \frac{C_i}{1 + \frac{V_{Aw}}{V_{OS}}} \quad (7)$$

where $C_{i.dil}$ represents the new ionic concentration after the dilution due to the fine aggregate water content; V_{Aw} represents the volume of added water due to the fine aggregate water content; and V_{OS} represents the original volume of alkali solution, which was kept constant throughout testing. The resulting function for the resistivity ρ_{dil} can be obtained by merging Eq. (4) to (7), and is shown as Eq. (8).

$$\frac{1}{\rho_{dil}} = \sum_i \left[\frac{C_i z_i}{1 + \frac{V_{Aw}}{V_{OS}}}\right]\left[\frac{\lambda_i^\circ}{1 + G_i\sqrt{\frac{1}{2}\cdot\frac{C_K + C_{Na} + C_{OH} + C_{Ca}}{1 + \frac{V_{Aw}}{V_{OS}}}}}\right] \quad (8)$$

Table 5—Equivalent conductivity at infinite dilution (λ°) and conductivity coefficient (G) at 25°C

Ionic species	$z\lambda^\circ$, cm²·S/mol	G, mol/L$^{-1/2}$
OH^-	198.0	0.353
K^+	73.5	0.548
Na^+	50.1	0.733
Cl^-	76.4	0.548
Ca^{2+}	59.0	0.771
SO_4^{2-}	79.0	0.877

To obtain the dilute resistivity, the concentrations of ions in the SPSs can be substituted in Eq. (8), where V_{Aw} is calculated by multiplying the mass of fine aggregate in each sample by the water content as tested. The resulting resistivities are reported as the predicted resistivity of the SPS.

Effect of aggregate surface area on solution resistivity—The impact of the surface area of the aggregate on solution resistivity was studied using the A-1 aggregate source. Oven-dry A-1 aggregate was sieved using No. 4, 8, 16, 30, 50, and 100 sieves (including a pan). Each sieved fraction was prepared using DI water to reach the SSD condition for the testing. The same absorption and SG were assumed for every gradation. To estimate the surface area of each gradation, the particles were assumed to be spherical and have a normal distribution of particle size on every sieve. The average radius was used to solve for the number of particles in each sieve gradation using Eq. (9)

$$n = \frac{V}{\frac{4}{3}\pi r_a^3} \quad (9)$$

where V is the total volume of the particles (20 cm³) in each gradation; and r_a is the average radius of the particles. The number of particles (n) was then used in Eq. (10) to estimate the total surface area of each gradation tested

$$A = n(4\pi r_a^2) \quad (10)$$

where A is the total surface area of the particles.

Alkali-adsorption isotherm tests

Each of the 10 aggregates was exposed to DI water, 50 mM NaOH, 100 mM NaOH, 200 mM NaOH, 100 mM KOH, 200 mM KOH, and 400 mM KOH solutions. The selected concentration ranges of NaOH and KOH solutions for the adsorption tests were based on pore solution concentrations at 30 minutes of several OPC pastes reported in Vollpracht et al.[55] Aggregates at the SSD condition were used in the test. SSD aggregates of 20 cm³ volume were exposed to 18.6 cm³ of testing solution in a 50 mL centrifuge tube for 30 minutes. The mentioned volumes of SSD aggregate and solution were chosen to maintain the solution-to-aggregate volume ratio of 0.93, which is the same as the cement paste-to-aggregate volume ratio in the mortar mixtures to maintain the same exposure of mortar pore solution to the aggregates. After adding both aggregate

and solution to the tubes, they were shaken by hand for 1 minute to ensure all aggregate particles were exposed to the prepared solutions. After every 15 minutes from the start of the aggregate exposure to the solution, the centrifuge tubes were shaken by hand for 30 seconds. Two replicates were prepared for each aggregate-solution combination. After 30 minutes of exposure, the centrifuge tubes were then placed in a centrifuge and spun at 4000 rpm for 2 minutes. The separated solution in the centrifuge tube was decanted into 10 mL vials for further measurements of resistivity and ionic composition.

The concentration of ions in the solutions after dilution from the SSD aggregate's moisture can be calculated using Eq. (7). Therefore, the initial ion concentration of solutions would be as shown in Eq. (11).

$$C_{i,initial} = \frac{C_{i,sol}}{1 + \frac{\left(\frac{AC}{100}\right) \cdot V_{agg} \cdot SG}{V_{sol}}} \quad (11)$$

where $C_{i,initial}$ is the concentration of ions in the alkali test solution after dilution from the aggregate moisture (mmol/L); $C_{i,sol}$ is the concentration of ions in the prepared alkali test solution (mmol/L); V_{agg} is the volume of SSD aggregates; and V_{sol} is the volume of test solution. The concentration of alkali cations adsorbed per gram of aggregate was calculated using Eq. (12)

$$C_{i,ads} = \frac{(C_{i,initial} - C_{i,final}) \cdot V_{sol}}{V_{agg} \cdot SG} \quad (12)$$

where $C_{i,ads}$ is the concentration of ions adsorbed per gram of aggregate (mol/g of aggregate); and $C_{i,final}$ is the concentration of ions in the alkali test solution after 30 minutes of aggregates exposure to the alkali test solution (mmol/L). To determine the correlation between the adsorbed ions and the concentration of ions in the test solution, the Langmuir isotherm was used, as shown in Eq. (13).

$$C_{i,ads} = \frac{Q_o K_L C_{i,initial}}{1 + K_L C_{i,initial}} \quad (13)$$

where K_L is the Langmuir constant; and Q_o is the theoretical adsorption capacity.

RESULTS AND DISCUSSION

Influence of aggregates on fresh mortar bulk resistivity

To determine the effect of aggregates on fresh mortar bulk resistivity, cement paste bulk resistivity was determined, and it was measured to be 60.7 ohm·cm. As the volume ratio of fine aggregate to cement paste was kept constant for all the mortars, the Maxwell effective medium model[26,56] was used to find the expected bulk resistivity of the mortar using Eq. (14).

$$\frac{\rho_p}{\rho_m} = \frac{2v_p}{3 - v_p} \quad (14)$$

Table 6—Summary of mortar resistivity measurements

Mortar sample ID	Bulk resistivity ρ_m, ohm·cm
A-1	339.4
A-2	267.5
A-3	148.1
A-4	178.6
A-5	160.9
A-6	183.9
A-7	167.5
A-8	153.3
A-9	155.8
A-10	176.3

where ρ_m is the bulk resistivity of the mortar; ρ_p is the bulk resistivity of the cement paste; and v_p is the volume fraction of paste in the mortar. The volume fraction of paste in the mortar was calculated to be 0.482. Therefore, the calculated bulk resistivity of the mortar was found to be 158.5 ohm·cm. Table 6 shows the measured bulk resistivities of the mortars with all the fine aggregates.

The measured bulk resistivities of the mortars varied from 148.1 to 339.4 ohm·cm, whereas the expected mortar bulk resistivity when the aggregates are considered inert was 158.5 ohm·cm. The mortars with A-1 and A-2 aggregates had the highest influence in terms of an increase in bulk resistivity among all the aggregates. To investigate the overall increase in measured bulk resistivity of mortars, the mortar pore solutions were examined.

Influence of aggregates on fresh mortar pore solution chemistry and resistivity

Aggregates A-1 to A-10 were tested in mortars at equal volumes from which pore solution was extracted, and its resistivity was measured. Table 7 shows the measured pore solution resistivities and Na^+ and K^+ concentrations in the pore solutions of the mortars.

Cement paste pore solution 30 minutes after mixing was composed of 15.2 mM Na^+ and 155.5 mM K^+, and it had a resistivity of 25.0 ohm·cm. Mortars prepared with an inert and dry aggregate are expected to have similar paste pore solution composition to cement paste (prepared with the same *w*/*cm* as mortar). However, mortar pore solutions were observed to have a wide range of Na^+ and K^+ concentrations, as shown in Table 7. It was observed that Na^+ concentration in mortar pore solutions varied from 9.9 to 25.8 mM, and K^+ concentration in mortar pore solutions varied from 29.3 to 146.0 mM with different aggregates. It is hypothesized that the difference in the alkali-cation concentrations of the mortar pore solutions compared to cement paste pore solution is mainly attributed to dilution from aggregate moisture and adsorption of ions on the aggregates.

The measured mortar pore solution resistivities ranged from 25.9 to 61.3 ohm·cm, implying a higher pore solution resistivity that ranged from 4 (A-3) to 145% (A-1) more than the expected value of 25.0 ohm·cm. Apart from A-3, every

Table 7—Measured resistivity and Na^+ and K^+ concentrations of mortar pore solutions

Sample ID	ρ_{ps}, ohm·cm	C_{Na^+}, mmol/L	C_{K^+}, mmol/L
Cement paste	25.0	15.2	155.5
A-1	61.3	11.3	29.3
A-2	58.9	9.9	47.7
A-3	25.9	24.0	146.0
A-4	32.3	14.5	110.6
A-5	33.2	20.1	120.1
A-6	32.1	14.8	115.2
A-7	34.7	16.5	122.0
A-8	32.6	15.0	118.9
A-9	31.6	15.6	130.6
A-10	29.1	25.8	138.8

aggregate increased the pore solution resistivity by more than 10%. The mortars with A-1 and A-2 aggregates had the lowest Na^+ and K^+ ions in the pore solution and the highest pore solution resistivities among the tested mortars. The mortar with A-3 aggregate had a pore solution resistivity closer to the expected value of 25 ohm·cm.

Effect of aggregate moisture (dilution) on solution resistivity

Moisture in aggregate pores dilutes the ion concentration of the pore solution proportional to their absorption capacity. Equation (8) calculates the resistivity of the pore solution due to this added water. Figure 3 illustrates the resistivity computed from Eq. (8) as a function of the absorption capacity of the SSD aggregates when the SPS was used.

As shown in Fig. 3, depending on the volume of aggregate, the absorption capacity can affect the resistivity of a pore solution if the absorbed water is not taken into account. It was determined that an SSD aggregate with an absorption capacity of 2.3% exposed to SPS increases its resistivity by 10% due to the dilution effect. Similarly, when an SSD aggregate with an absorption capacity of 4.7% is exposed to SPS, moisture from the aggregate increases the solution resistivity by 20%.

To give an example of the effect of dilution on concrete pore solution, an aggregate with an absorption capacity of just 0.9% in a concrete mixture with a *w*/*cm* of 0.35 and 70% aggregate by volume will impact the pore solution resistivity by 10%. Similarly, a mixture of the same characteristics containing an aggregate with 2.5% absorption will increase pore solution resistivity by 25%. These changes to resistivity can be even larger when lightweight aggregates are used, as they can have absorption capacities of 15% or greater.[57] A lightweight aggregate with an absorption capacity of 20% will impact the resistivity by 137%. A correction for the dilution by the moisture in the aggregate must be taken into consideration, especially when examining early-age pore solutions.

Table 8 shows the Na and K ion concentrations in mortar pore solutions calculated from paste ion concentrations after accounting for the dilution effect using Eq. (11). By comparing Tables 7 and 8, it was observed that even after

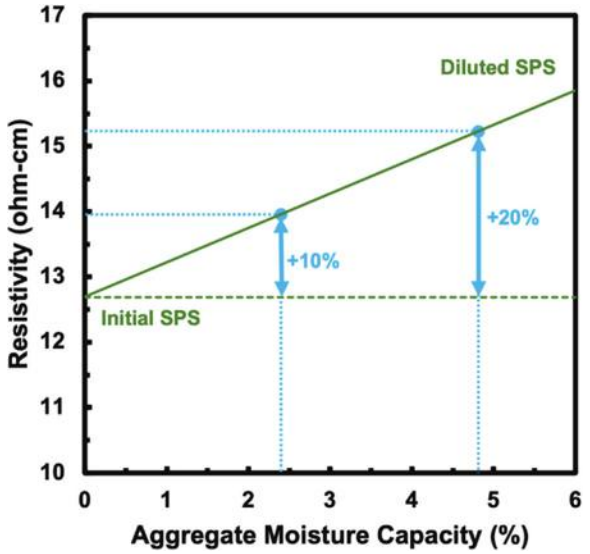

Fig. 3—Calculated resistivity of simulated pore solution (considering dilution effect) after testing with SSD aggregates with different absorption capacities.

Table 8—Calculated Na^+ and K^+ concentrations of mortar pore solutions after accounting for dilution effect, and remaining difference in ion concentrations from measured values

Sample ID	C_{Na^+}, mmol/L	C_{K^+}, mmol/L	Remaining difference from measurement	
			ΔC_{Na^+}, mmol/L	ΔC_{K^+}, mmol/L
A-1	11.49	117.53	0.19	88.23
A-2	11.36	116.19	1.46	68.49
A-3	14.41	147.41	–9.59	1.41
A-4	13.81	141.24	–0.69	30.64
A-5	14.20	145.23	–5.9	25.13
A-6	12.41	127.01	–2.39	11.81
A-7	13.92	142.42	–2.58	20.42
A-8	13.57	138.86	–1.43	19.96
A-9	14.41	147.44	–1.19	16.84
A-10	14.54	148.70	–11.26	9.9

accounting for the dilution effect, the calculated ion concentrations of the mortar pore solutions do not match the measured ion concentrations of the mortars. For example, the remaining difference in K ion concentration of mortar pore solution between the measured and calculated values (after accounting for the dilution effect) ranged from 1.4 mmol/L (A-3) to 88.2 mmol/L (A-1), or 0.9% to 56.7% of the measured value, respectively.

Effect of aggregate surface area on solution resistivity

Figure 4 shows the change in the resistivity of the SPS due to a change in the estimated surface area of A-1. It was observed that the surface area of the particles exposed to SPS was proportional to the measured resistivity of the solution. When the surface area of 20 cm^3 of A-1 was 3.4 m^2,

the resistivity of the pore solution increased by 56%. When the same volume of A-1 had a surface area of 53.5 m^2, the resistivity increased by 147%. The results showed that the increase in mortar pore solution resistivity was not a phenomenon of a certain fraction of A-1 aggregate, and the increase in resistivity was clearly correlated to an increase in surface area, suggesting that there was a surface adsorption effect. Figure 4 also shows the estimated resistivity (in open circles) after accounting for dilution from the aggregate moisture. It was observed that for A-1 aggregate, surface alkali adsorption was a dominating effect compared to the dilution effect in terms of an increase in solution resistivity.

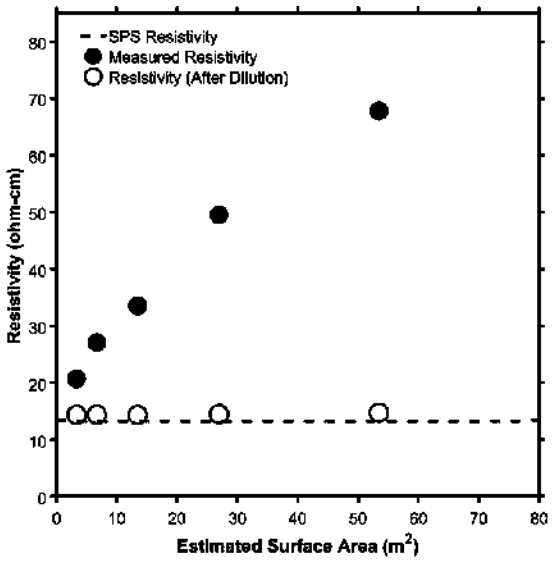

Fig. 4—Measured resistivity of simulated pore solution exposed to different gradations of A-1. Maximum difference between two resistivity measurements of sample was found to be 0.46 ohm·cm; therefore, average values are reported.

Alkali-adsorption isotherms

Figures 5 and 6 show the adsorption isotherms of Na^+ and K^+, respectively, for all the aggregates tested using their gradation as received. Estimated alkali adsorption in the mortars was also plotted in Fig. 5 and 6 to compare with the predicted alkali adsorption from the isotherm tests. The aggregates were observed to release a small concentration of alkalies when tested in DI water for 30 minutes, and this baseline was accounted for in the isotherms.

It was observed that all aggregates followed the Langmuir adsorption behavior for Na^+ and K^+. Similar surface adsorption behavior was observed for Na^+ and K^+. Table 9 lists the Langmuir isotherm coefficients, Q_o and K_L, for Na and K ions. For the majority of the aggregates, K ions had higher theoretical adsorption capacity (Q_o) than Na ions; however, it was observed that the theoretical adsorption capacity differed for Na and K with some aggregates. This suggests that preferences for the adsorption of Na or K may be different between aggregates, but the different ranges of [Na] and [K] tested make it difficult to make a direct comparison. It was observed that A-1 and A-2 had the highest theoretical adsorption capacity for both Na and K ions, whereas A-3 had the least theoretical adsorption capacity for the ions among the tested aggregates.

From Fig. 5 and 6, it was observed that the adsorption isotherms predicted the adsorbed ion concentrations in mortars reasonably well. Table 10 shows the comparison of estimated ions adsorbed on aggregate in mortars and predicted ions adsorbed on aggregate in mortars using the adsorption isotherms.

It was observed that isotherms predicted Na^+ adsorption with less than 4 mol/(g of sand) difference and K^+ adsorption with less than 6 mol/(g of sand) difference from the adsorbed ion concentration in mortar tests. Because of the low concentration of Na^+ in the fresh pore solution, a reliable comparison to the isotherm predictions could not be made. Table 11 shows the effect of K^+ adsorption on resistivity. The

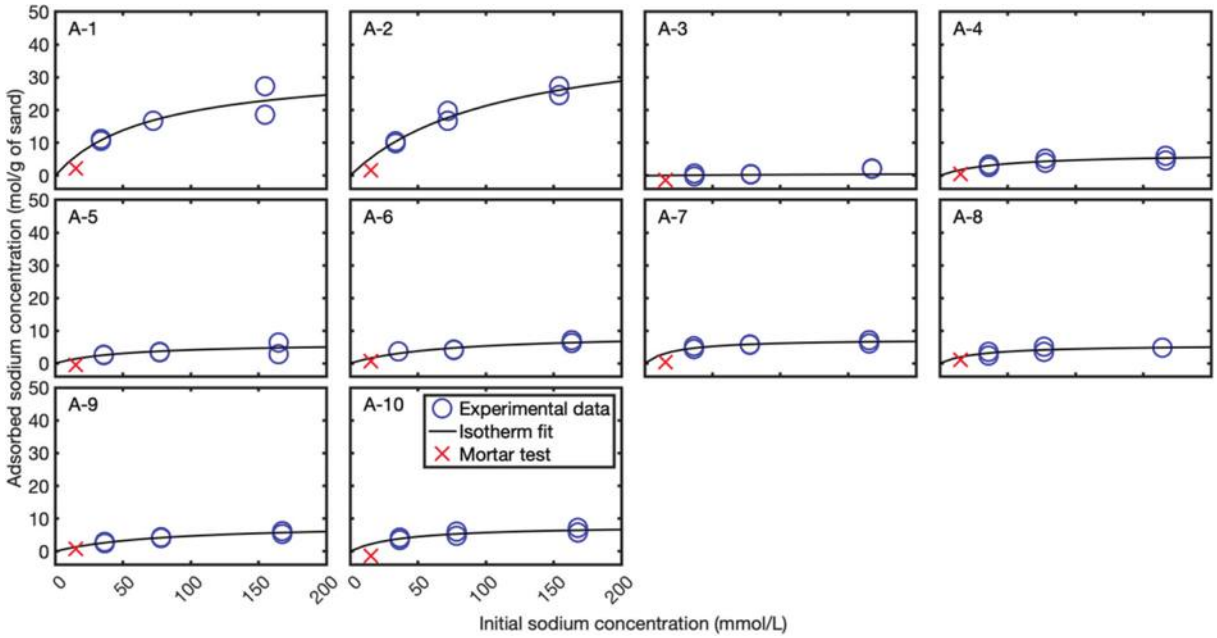

Fig. 5—Adsorption isotherms of Na^+ for all aggregates.

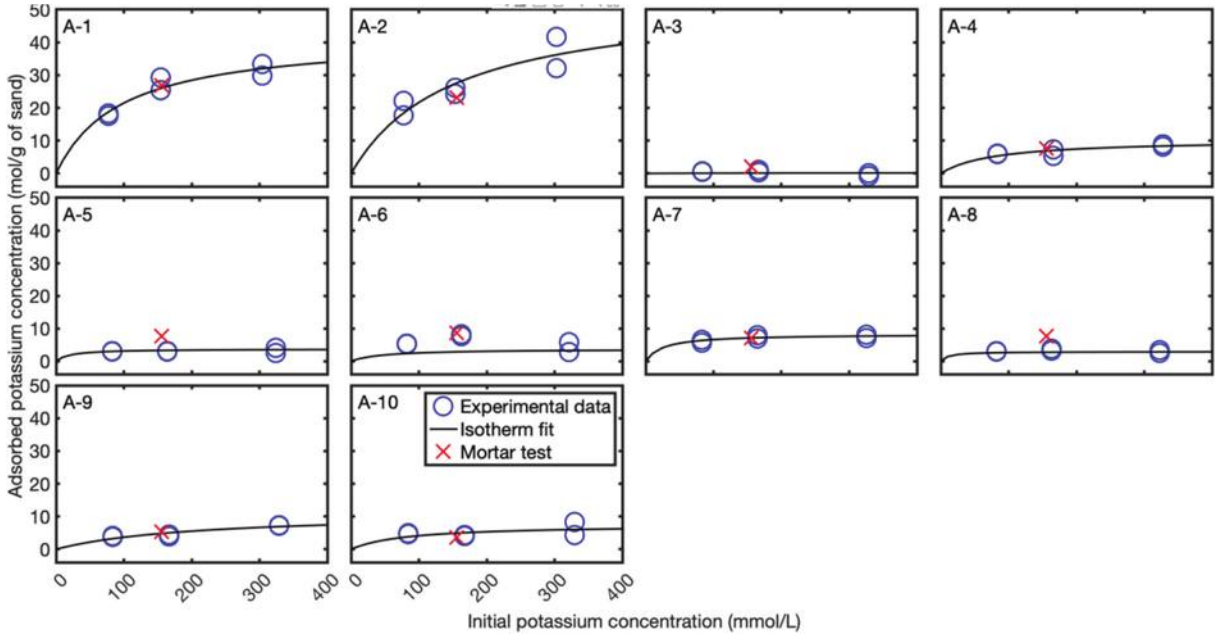

Fig. 6—Adsorption isotherms of K^+ for all aggregates.

Table 9—Langmuir isotherm coefficients for Na and K ions

Sample	Na^+		K^+	
	Q_o, mol/g of sand	K_L	Q_o, mol/g of sand	K_L
A-1	33.20	1.42×10^{-2}	42.00	1.05×10^{-2}
A-2	44.90	9.02×10^{-3}	54.10	6.69×10^{-3}
A-3	2.99	3.01×10^{-3}	1.98	1.82×10^{-2}
A-4	6.74	2.33×10^{-2}	1.04	1.27×10^{-2}
A-5	6.30	1.85×10^{-2}	3.72	4.91×10^{-2}
A-6	9.08	1.40×10^{-2}	3.73	2.09×10^{-2}
A-7	7.44	4.62×10^{-2}	8.25	3.98×10^{-2}
A-8	9.55	1.53×10^{-2}	9.78	8.12×10^{-2}
A-9	8.47	1.25×10^{-2}	11.20	4.84×10^{-2}
A-10	7.91	2.63×10^{-2}	7.52	1.22×10^{-2}

isotherms were able to predict the mortar pore solution resistivity within ±18% for nine out of 10 aggregates tested.

The possible adsorption of Ca^{+2} in pore solution on aggregates was not considered as its concentration at 30 minutes in pore solution is expected to be lower than Na^+.[55] In addition, Ca^{+2} has lower ion conductivity than Na^+,[54] and therefore any adsorption of Ca^{+2} is expected to have a negligible effect on the solution resistivity.

CONCLUSIONS

This paper discussed the influence of fine aggregates on early-age mortar pore solution chemistry and the electrical resistivity of the pore solution. Specifically, two effects of fine aggregates on pore solution in fresh mortar were discussed: pore solution dilution from aggregate moisture and surface adsorption of Na^+ and K^+ on aggregates. Due to both dilution and surface adsorption effects, the mortar pore solution resistivity increased by 4 to 145% depending on the aggregate. A-1 and A-2 aggregates had the most influence on the pore solution by increasing the pore solution resistivity by 145 and 136%, respectively, and they also had the highest influence on the bulk resistivity of mortar.

A simple experimental approach was proposed to characterize the aggregate surface adsorption of Na^+ and K^+ from the surrounding pore solution. The proposed approach involved determining the alkali-adsorption isotherms when the aggregates are exposed to varying concentrations of NaOH and KOH solutions. The developed Langmuir adsorption isotherms were used to estimate the Na and K ions adsorption on aggregates. The concentrations of alkalies adsorbed on aggregates in mortars were predicted reasonably well using the isotherms. Adsorption concentration of Na and K ions above 4 mol/g of sand resulted in an increase in the mortar pore solution resistivity of 20%. Therefore, it is recommended to use the developed test methodology to identify aggregates that influence fresh mortar pore solution chemistry and correct for the change in alkali concentration due to dilution and alkali-adsorption effects.

AUTHOR BIOS

ACI member **Krishna Siva Teja Chopperla** *is a Postdoctoral Scholar at Oregon State University, Corvallis, OR. His research interests include concrete durability and the characterization of cementitious materials.*

ACI member **Atolo Tuinukuafe** *is a Postdoctoral Researcher at Oregon State University. His research interests include alternative cements and concrete durability.*

ACI member **Joseph H. Biever** *received his MS and BS from Oregon State University. His research interests include fresh concrete properties and pore solution chemistry.*

O. Burkan Isgor, *FACI, is a Professor in the School of Civil and Construction Engineering at Oregon State University. His research interests include corrosion of steel in concrete, service life modeling of concrete, and thermodynamic modeling of cementitious systems.*

W. Jason Weiss, *FACI, is the Edwards Distinguished Professor of Engineering in the School of Civil and Construction Engineering at Oregon State University. He is Editor in Chief of the* ACI Materials Journal, *a*

Table 10—Comparison of estimated ions adsorbed on aggregates in mortar test and predicted ions adsorbed on aggregate in mortar from adsorption isotherms

Sample	Na^+ adsorbed, mol/g of sand			K^+ adsorbed, mol/g of sand		
	Mortar test	Isotherm prediction	Difference	Mortar test	Isotherm prediction	Difference
A-1	2.14	5.92	3.78	26.83	26.04	–0.80
A-2	1.67	5.41	3.74	23.13	27.57	4.45
A-3	–1.31	0.06	1.36	2.13	0.09	–2.03
A-4	–0.77	1.76	2.54	7.63	6.88	–0.75
A-5	–0.51	1.38	1.89	7.69	3.29	–4.40
A-6	0.62	1.59	0.97	8.71	2.85	–5.86
A-7	0.34	3.07	2.72	7.04	7.10	0.06
A-8	1.06	1.95	0.89	7.58	2.73	–4.84
A-9	0.80	1.35	0.55	5.28	4.83	–0.45
A-10	–1.43	2.26	3.70	3.56	4.92	1.36

Table 11—Comparison of calculated mortar pore solution resistivity and solution resistivity predicted from adsorption isotherm considering only K^+ and OH^- ions in pore solution

Sample	Mortar extraction, ohm·cm	Isotherm prediction, ohm·cm	Difference, %
A-1	135.1	119.0	12
A-2	84.0	144.9	72
A-3	29.2	27.4	6
A-4	35.0	34.0	3
A-5	35.0	30.2	14
A-6	36.4	29.8	18
A-7	34.5	34.5	0
A-8	35.3	29.9	16
A-9	32.4	31.8	2
A-10	30.5	31.9	5

member of the ACI Technical Activities Committee, and on the ACI Board of Direction.

ACKNOWLEDGMENTS

The authors would like to thank R. Campbell for assisting with the laboratory experiments. The authors would like to acknowledge that this study was partly funded by the Transportation Pooled Fund—TPF-5(368): Performance-Engineered Concrete Paving Mixtures. A. Tuinukuafe's participation was funded by the National Science Foundation under Grant No. EEC-2127509, administered by the American Society for Engineering Education.

REFERENCES

1. ASTM C1876-19, "Standard Test Method for Bulk Electrical Resistivity or Bulk Conductivity of Concrete," ASTM International, West Conshohocken, PA, 2019, 7 pp.

2. AASHTO TP 119-22, "Standard Method of Test for Electrical Resistivity of a Concrete Cylinder Tested in a Uniaxial Resistance Test," American Association of State Highway and Transportation Officials, Washington, DC, 2022, 18 pp.

3. AASHTO T 358-21, "Standard Method of Test for Surface Resistivity Indication of Concrete's Ability to Resist Chloride Ion Penetration," American Association of State Highway and Transportation Officials, Washington, DC, 2021, 10 pp.

4. AASHTO R 101-22, "Standard Practice for Developing Performance Engineered Concrete Pavement Mixtures," American Association of State Highway and Transportation Officials, Washington, DC, 2022, 14 pp.

5. Weiss, W. J.; Spragg, R. P.; Isgor, O. B.; Ley, M. T.; and Van Dam, T., "Toward Performance Specifications for Concrete: Linking Resistivity, RCPT and Diffusion Predictions Using the Formation Factor for Use in Specifications," *High Tech Concrete: Where Technology and Engineering Meet: Proceedings of the 2017* fib *Symposium, held in Maastricht, The Netherlands, June 12-14, 2017*, D. A. Hordijk and M. Luković, eds., Springer, Cham, Switzerland, 2018, pp. 2057-2065.

6. Weiss, W. J..; Ley, M. T.; Isgor, O. B.; Van Dam, T., "Toward Performance Specifications for Concrete Durability: Using the Formation Factor for Corrosion and Critical Saturation for Freeze-Thaw," Transportation Research Board 96th Annual Meeting, Washington, DC, 2017, 20 pp.

7. Moradllo, M. K.; Qiao, C.; Isgor, O. B.; Reese, S.; and Weiss, W. J., "Relating Formation Factor of Concrete to Water Absorption," *ACI Materials Journal*, V. 115, No. 6, Nov. 2018, pp. 887-898. doi: 10.14359/51706844

8. Isgor, O. B., and Weiss, W. J., "A Nearly Self-Sufficient Framework for Modelling Reactive-Transport Processes in Concrete," *Materials and Structures*, V. 52, No. 1, Feb. 2019, Article No. 3. doi: 10.1617/s11527-018-1305-x

9. Sant, G.; Rajabipour, F.; Fishman, P.; Lura, P.; and Weiss, W. J., "Electrical Conductivity Measurements in Cement Paste at Early Ages: A Discussion of the Contribution of Pore Solution Conductivity, Volume, and Connectivity to the Overall Electrical Response," *Proceedings*, International RILEM Workshop on Advanced Testing of Fresh Cementitious Materials, Stuttgart, Germany, 2006, 10 pp.

10. Sallehi, H.; Ghods, P.; and Isgor, O. B., "Formation Factor of Fresh Cementitious Pastes," *Cement and Concrete Composites*, V. 91, Aug. 2018, pp. 174-188. doi: 10.1016/j.cemconcomp.2018.05.011

11. Castro, J.; Spragg, R.; Kompare, P.; and Weiss, W. J., "Portland Cement Concrete Pavement Permeability Performance," Report No. FHWA/IN/JTRP-2010/29, Joint Transportation Research Program, Indiana Department of Transportation and Purdue University, West Lafayette, IN, 2010, 258 pp.

12. Li, Z.; Xiao, L.; and Wei, X., "Determination of Concrete Setting Time Using Electrical Resistivity Measurement," *Journal of Materials in Civil Engineering*, ASCE, V. 19, No. 5, May 2007, pp. 423-427. doi: 10.1061/(ASCE)0899-1561(2007)19:5(423)

13. Tang, S. W.; Yao, Y.; Andrade, C.; and Li, Z. J., "Recent Durability Studies on Concrete Structure," *Cement and Concrete Research*, V. 78, Part A, Dec. 2015, pp. 143-154. doi: 10.1016/j.cemconres.2015.05.021

14. Wei, X., and Li, Z., "Early Hydration Process of Portland Cement Paste by Electrical Measurement," *Journal of Materials in Civil Engineering*, ASCE, V. 18, No. 1, Feb. 2006, pp. 99-105. doi: 10.1061/(ASCE)0899-1561(2006)18:1(99)

15. Mancio, M.; Moore, J. R.; Brooks, Z.; Monteiro, P. J. M.; and Glaser, S. D., "Instantaneous In-Situ Determination of Water-Cement Ratio of Fresh Concrete," *ACI Materials Journal*, V. 107, No. 6, Nov.-Dec. 2010, pp. 586-592.

16. Kompare, P. L., "Electrical and Relative Humidity Measurements of Concrete and Their Relation to Transport Properties," master's thesis, Purdue University, West Lafayette, IN, 2015.

17. Whittington, H. W.; McCarter, J.; and Forde, M. C., "The Conduction of Electricity through Concrete," *Magazine of Concrete Research*, V. 33, No. 114, Mar. 1981, pp. 48-60. doi: 10.1680/macr.1981.33.114.48

18. Chrisp, T. M.; Starrs, G.; McCarter, W. J.; Rouchotas, E.; and Blewett, J., "Temperature-Conductivity Relationships for Concrete: An Activation Energy Approach," *Journal of Materials Science Letters*, V. 20, No. 12, June 2001, pp. 1085-1087. doi: 10.1023/A:1010926426753

19. Liu, Y., and Presuel-Moreno, F. J., "Normalization of Temperature Effect on Concrete Resistivity by Method Using Arrhenius Law," *ACI Materials Journal*, V. 111, No. 4, July-Aug. 2014, pp. 433-442. doi: 10.14359/51686725

20. McCarter, W. J.; Chrisp, T. M.; Starrs, G.; Basheer, P. A. M.; and Blewett, J., "Field Monitoring of Electrical Conductivity of Cover-Zone Concrete," *Cement and Concrete Composites*, V. 27, No. 7-8, Aug.-Sept. 2005, pp. 809-817. doi: 10.1016/j.cemconcomp.2005.03.008

21. Morsy, M. S., "Effect of Temperature on Electrical Conductivity of Blended Cement Pastes," *Cement and Concrete Research*, V. 29, No. 4, Apr. 1999, pp. 603-606. doi: 10.1016/S0008-8846(98)00198-7

22. Villagrán Zaccardi, Y. A.; Fullea García, J.; Huélamo P.; and Di Maio Á. A., "Influence of Temperature and Humidity on Portland Cement Mortar Resistivity Monitored with Inner Sensors," *Materials and Corrosion*, V. 60, No. 4, Apr. 2009, pp. 294-299.

23. Obla, K.; Hong, R.; Sherman, S.; Bentz, D. P.; and Jones, S. Z., "Relating the Electrical Resistance of Fresh Concrete to Mixture Proportions," *Advances in Civil Engineering Materials*, V. 7, No. 1, 2018, pp. 71-86. doi: 10.1520/ACEM20170126

24. Biever, J. H.; Chopperla, K. S. T.; Isgor, O. B.; and Weiss, W. J., "Practical Measurement of Pore Solution Resistivity in Fresh Mixtures," *ACI Materials Journal*. V. 120, No. 5, 2023. doi: 10.14359/51738903

25. Rajabipour, F., "Insitu Electrical Sensing and Material Health Monitoring in Concrete Structures," PhD dissertation, Purdue University, West Lafayette, IN, 2006.

26. Princigallo, A.; van Breugel, K.; and Levita, G., "Influence of the Aggregate on the Electrical Conductivity of Portland Cement Concretes," *Cement and Concrete Research*, V. 33, No. 11, Nov. 2003, pp. 1755-1763. doi: 10.1016/S0008-8846(03)00166-2

27. van Beek, A., and Hilhorst, M. A., "Dielectric Measurements to Characterize the Microstructural Changes of Young Concrete," *HERON*, V. 44, No. 1, 2000, pp. 3-17.

28. Barrett, T. J., "Improving Service Life of Concrete Structures through the Use of Internal Curing: Impact on Practice," PhD dissertation, Purdue University, West Lafayette, IN, 2015, 484 pp.

29. Castro, J., "Moisture Transport in Cement Based Materials: Application to Transport Tests and Internal Curing," PhD dissertation, Purdue University, West Lafayette, IN, 2011.

30. Bérubé, M. A.; Duchesne, J.; and Rivest, M., "Alkali Contribution by Aggregates to Concrete," *Proceedings*, 10th International Conference on Alkali-Aggregate Reaction in Concrete (10th ICAAR), Melbourne, VIC, Australia, A. Shayan, ed., 1996, pp. 899-906.

31. Constantiner, D., and Diamond, S., "Alkali Release from Feldspars into Pore Solutions," *Cement and Concrete Research*, V. 33, No. 4, Apr. 2003, pp. 549-554. doi: 10.1016/S0008-8846(02)01001-3

32. Ferraz, A. R.; Fernandes, I.; Soares, D.; Santos Silva, A.; and Quinta-Ferreira, M., "Assessment of the Alteration of Granitic Rocks and Its Influence on Alkalis Release," *IOP Conference Series: Earth and Environmental Science*, V. 95, No. 2, 2017, Article No. 022001.

33. Poulsen, E.; Hansen, T. S.; and Sørensen, H. E., "Release of Alkalies from Feldspar in Concrete and Mortar," *2000 CANMET/ACI International Conference on Durability of Concrete*, SP-192, American Concrete Institute, Farmington Hills, MI, 2000, pp. 807-824.

34. van Aardt, J. H. P., and Visser, S., "Reaction of $Ca(OH)_2$ and of $Ca(OH)_2 + CaSO_4.2H_2O$ at Various Temperatures with Feldspars in Aggregates Used for Concrete Making," *Cement and Concrete Research*, V. 8, No. 6, Nov. 1978, pp. 677-681. doi: 10.1016/0008-8846(78)90076-5

35. Shane, J. D.; Mason, T. O.; Jennings, H. M.; Garboczi, E. J.; and Bentz, D. P., "Effect of the Interfacial Transition Zone on the Conductivity of Portland Cement Mortars," *Journal of the American Ceramic Society*, V. 83, No. 5, May 2000, pp. 1137-1144. doi: 10.1111/j.1151-2916.2000.tb01344.x

36. Garboczi, E. J.; Schwartz, L. M.; and Bentz, D. P., "Modeling the Influence of the Interfacial Zone on the DC Electrical Conductivity of Mortar," *Advanced Cement Based Materials*, V. 2, No. 5, Sept. 1995, pp. 169-181. doi: 10.1016/1065-7355(95)90001-2

37. Garboczi, E. J., and Berryman, J. G., "New Effective Medium Theory for the Diffusivity or Conductivity of a Multi-Scale Concrete Microstructure Model," *Concrete Science and Engineering*, V. 2, June 2000, pp. 88-96.

38. Hou, T.-C.; Nguyen, V. K.; Su, Y.-M.; Chen, Y.-R.; and Chen, P.-J., "Effects of Coarse Aggregates on the Electrical Resistivity of Portland Cement Concrete," *Construction and Building Materials*, V. 133, Feb. 2017, pp. 397-408. doi: 10.1016/j.conbuildmat.2016.12.044

39. Spragg, R.; Jones, S.; Bu, Y.; Lu, Y.; Bentz, D.; Snyder, K.; and Weiss, W. J., "Leaching of Conductive Species: Implications to Measurements of Electrical Resistivity," *Cement and Concrete Composites*, V. 79, May 2017, pp. 94-105. doi: 10.1016/j.cemconcomp.2017.02.003

40. Wei, X., and Xiao, L., "Influence of the Aggregate Volume on the Electrical Resistivity and Properties of Portland Cement Concretes," *Journal of Wuhan University of Technology-Materials Science Edition*, V. 26, No. 5, Oct. 2011, pp. 965-971. doi: 10.1007/s11595-011-0346-6

41. Chopperla, K. S. T., and Ideker, J. H., "A Study on the Effect of Aggregate Type on Pore Solution Composition," *Proceedings*, 16th International Conference on Alkali-Aggregate Reaction in Concrete (16th ICAAR), Lisbon, Portugal, A. Lopes Batista, ed., 2022, 12 pp.

42. Revil, A., and Glover, P. W. J., "Theory of Ionic-Surface Electrical Conduction in Porous Media," *Physical Review B: Condensed Matter and Materials Physics*, V. 55, No. 3, Jan. 1997, pp. 1757-1773. doi: 10.1103/PhysRevB.55.1757

43. Rodrigues, F. A.; Monteiro, P. J. M.; and Sposito, G., "The Alkali–Silica Reaction: The Effect of Monovalent and Bivalent Cations on the Surface Charge of Opal," *Cement and Concrete Research*, V. 31, No. 11, Nov. 2001, pp. 1549-1552. doi: 10.1016/S0008-8846(01)00578-6

44. Allen, N.; Machesky, M. L.; Wesolowski, D. J.; and Kabengi, N., "Calorimetric Study of Alkali and Alkaline-Earth Cation Adsorption and Exchange at the Quartz-Solution Interface," *Journal of Colloid and Interface Science*, V. 504, Oct. 2017, pp. 538-548. doi: 10.1016/j.jcis.2017.06.005

45. Estefan, S. F., and Malati, M. A., "Adsorptive Behaviour of Alkali and Alkaline-Earth Cations onto Quartz," *Recent Advances in Science and Technology of Materials: Volume 1*, A. Bishay, ed., Springer, Boston, MA, 1974, pp. 351-364.

46. Malati, M. A.; Mazza, R. J.; Sherren, A. J.; and Tomkins, D. R., "The Mechanism of Adsorption of Alkali Metal Ions on Silica," *Powder Technology*, V. 9, No. 2-3, Feb.-Mar. 1974, pp. 107-110. doi: 10.1016/0032-5910(74)85014-X

47. Rimsza, J. M.; Jones, R. E.; and Criscenti, L. J., "Interaction of NaOH Solutions with Silica Surfaces," *Journal of Colloid and Interface Science*, V. 516, Apr. 2018, pp. 128-137. doi: 10.1016/j.jcis.2018.01.049

48. ASTM C33/C33M-18, "Standard Specification for Concrete Aggregates," ASTM International, West Conshohocken, PA, 2018, 8 pp.

49. ASTM C150/C150M-22, "Standard Specification for Portland Cement," ASTM International, West Conshohocken, PA, 2022, 9 pp.

50. ASTM C150/C150M-19, "Standard Specification for Portland Cement," ASTM International, West Conshohocken, PA, 2019, 10 pp.

51. ASTM D1193-06(2018), "Standard Specification for Reagent Water," ASTM International, West Conshohocken, PA, 2018, 6 pp.

52. Tsui Chang, M.; Suraneni, P.; Isgor, O. B.; Trejo, D.; and Weiss, W. J., "Using X-Ray Fluorescence to Assess the Chemical Composition and Resistivity of Simulated Cementitious Pore Solutions," *International Journal of Advances in Engineering Sciences and Applied Mathematics*, V. 9, No. 3, Sept. 2017, pp. 136-143. doi: 10.1007/s12572-017-0181-x

53. Spragg, R.; Jones, S.; Bu, Y.; Lu, Y.; Bentz, D.; Snyder, K.; and Weiss, J., "Leaching of Conductive Species: Implications to Measurements of Electrical Resistivity," *Cement and Concrete Composites*, V. 79, May 2017, pp. 94-105. doi: 10.1016/j.cemconcomp.2017.02.003

54. Snyder, K. A.; Feng, X.; Keen, B. D.; and Mason, T. O., "Estimating the Electrical Conductivity of Cement Paste Pore Solutions from OH^-, K^+ and Na^+ Concentrations," *Cement and Concrete Research*, V. 33, No. 6, June 2003, pp. 793-798. doi: 10.1016/S0008-8846(02)01068-2

55. Vollpracht, A.; Lothenbach, B.; Snellings, R.; and Haufe, J., "The Pore Solution of Blended Cements: A Review," *Materials and Structures*, V. 49, No. 8, Aug. 2016, pp. 3341-3367. doi: 10.1617/s11527-015-0724-1

56. Bharadwaj, K.; Glosser, D.; Moradllo, M. K.; Isgor, O. B.; and Weiss, W. J., "Toward the Prediction of Pore Volumes and Freeze-Thaw Performance of Concrete Using Thermodynamic Modelling," *Cement and Concrete Research*, V. 124, Oct. 2019, Article No. 105820. doi: 10.1016/j.cemconres.2019.105820

57. Barrett, T. J.; Miller A. E.; and Weiss W. J., "Documentation of the INDOT Experience and Construction of the Bridge Decks Containing Internal Curing in 2013," Report No. FHWA/IN/JTRP-2015/10, Joint Transportation Research Program, Indiana Department of Transportation and Purdue University, 2015, 108 pp.

ACI MATERIALS JOURNAL

The American Concrete Institute (ACI) is a leading authority and resource worldwide for the development and distribution of consensus-based standards and technical resources, educational programs, and certifications for individuals and organizations involved in concrete design, construction, and materials, who share a commitment to pursuing the best use of concrete.

Individuals interested in the activities of ACI are encouraged to explore the ACI website for membership opportunities, committee activities, and a wide variety of concrete resources. As a volunteer member-driven organization, ACI invites partnerships and welcomes all concrete professionals who wish to be part of a respected, connected, social group that provides an opportunity for professional growth, networking, and enjoyment.

American Concrete Institute